An STM and Photocatalysis Study of Single Crystal and Ultrathin Films of Rutile and Anatase TiO_2

George Timothy Harrison

Thesis submitted for the degree of Doctor of Philosophy

of the University College London

Supervised by
Prof. Geoff Thornton

Department of Chemistry

UNIVERSITY COLLEGE LONDON

2017

I, George Timothy Harrison, confirm that the work presented in this thesis is my own. Where information has been derived from other sources, I confirm that this has been indicated in the thesis.

Abstract

Synthesis of two ultrathin TiO_2 films: model rutile / anatase TiO_2(101) and rutile TiO_2 / lepidocrocite-like TiO_2 / W(100) interfaces:

Scanning tunneling microscopy (STM) tip-pulse modification of a well characterised e-beamed single crystal anatase TiO_2(101) surface composed of a high step edge density, resulted in the formation of a new crystalline ordered rutile structure, characterised in real space by STM. This region was embedded in a ~400 Å diameter, ~50 Å tall mound in a surface hole surrounded by a ca. pristine (0.035 ML water) outer area of anatase TiO_2(101)-(1 × 1). One area of the modified surface had an atomically resolved unit mesh of (3.1 ± 0.2 Å × 14.2 ± 0.5 Å) and saw-tooth structure consistent with the surface structure of (1 × 3) reconstructed rutile TiO_2(100) surface. In-situ adsorption of acetic acid resulted in a monolayer coverage (2 adsorbates per (1 × 3)) of adsorbates resulting in a (2 × 3) (6.1 ± 0.4 Å × 14.7 ± 0.4 Å) unit mesh. Analysis of the STM images allowed this to be precisely assigned as the reduced rutile TiO_2(100)-(1 × 3)-β surface structure [Phys. Rev. Lett. Vol. 82, 26, 5265-5268]. This presents a novel methodology to form a system composed of two single crystal variants of anatase and rutile in close enough contact ~30 Å to study the interfaces influence on the electronic properties of rutile and anatase with scanning tunnelling microscopy (STS) and photochemical properties with a photo-active molecule.

Ultrathin films of TiO_2 were grown on a W(100)-O-(2 × 1) substrate and characterised using a combination of STM and low energy electron diffraction (LEED). In addition to islands of rutile TiO_2(110) with (1 × 1) termination that have been reported previously, rutile TiO_2(110) islands with a (1 × 2) film termination were observed. A lepidocrocite-like TiO_2 nanosheet, of 5 Å height was observed; closely related structurally to an anatase (001) bi-layer, was also observed on the W(100) surface in combination with rutile islands. High-resolution STM images show that the nanosheet grows in the principal orthogonal directions of the W(100)

substrate and forms a commensurate (1 × 7) coincident cell. This two phase titania ultrathin film system of rutile TiO_2(110)/lepidocrocite-like TiO_2 provides a suitable model system to study a model interface between an anatase derived and rutile TiO_2. Here macroscopic bulk averaging techniques can be utilised to study the interface.

Photooxidation study on single crystal anatase TiO_2(101):

As little mechanistic information of a photooxidation reaction has yet to be derived from single-crystal studies on anatase TiO_2(101) surface with photo-active probe molecules a study is required prior to the investigation of a tip modified rutile / anatase TiO_2(101) surface. The photooxidation of ethanol (as a prototype hole-scavenger organic molecule) adsorbed on the anatase TiO_2(101) surface was studied by STM and online mass spectrometry to determine the adsorbate species in the dark and under UV illumination in the presence of O_2 and to extract kinetic reaction parameters under photo-excitation.

Here, the reaction rate for the photooxidation of ethanol to acetaldehyde was found to depend on the O_2 partial pressure and surface coverage. An order of the reaction with respect to O_2 was found to be close to 0.15. Carbon−carbon bond dissociation leading to the formation of CH_3 radicals in the gas phase was found to be a minor pathway, which is contrary, to the case of the rutile TiO_2(110) single-crystal. Our STM images distinguished two types of surface adsorbates upon ethanol exposure that can be attributed to its molecular and dissociative modes. A mixed adsorption is also supported by DFT calculations performed by SABIC, in which they determined similar energies of adsorption (E_{ads}) for the molecular (1.11 eV) and dissociative (0.93 eV) modes. Upon UV exposure at (and above) 3 × 10^{-8} mbar O_2, a third species was identified on the surface as a reaction product that can be tentatively attributed to acetate/formate species on the basis of C 1s XPS results. The kinetics of the initial oxidation steps were evaluated using the STM and mass spectrometry data.

Acknowledgements

I would like to thank my supervisor Prof. Geoff Thornton for his guidance and constant support during my studies and for providing the opportunity to study in such an interesting field. I benefitted immensely from past and present Thornton research group members including: Dr. Chi Lun Pang, Dr. David C. Grinter, Dr Chi Yim and Dr. Axel Wilson; who gave an enormous amount of guidance in surface science research the technical UHV and scientific aspects of the work. Others frequently provided assistance or advice in the Lab. including: Dr. Andrew Mellor, Dr. Daniel T. Payne, Immad Nadeem, Michael Allan, Dr. Bobbie-Jean Shaw and Dr. Yu Zhang. Proof reading and corrections to the manuscript was kindly provided by all of the above including Dr. Hu Ya. In addition Dr. Maria-Chiara Spadaro was very helpful during her COST action supported visit in 2014. My second supervisor Dr. Matt Blunt was also supportive during the project.

I am immensely thankful to Prof. Hicham Idriss, for allowing me to visit the SABIC CRI hydrogen group lab in KAUST during my studies, his support was vital during the analysis, preparation and submission of work. The SABIC Senior Scientist Dr. Khabiboulakh Katsiev was instrumental for the work presented in Chapters 6: setting up the STM/Photoreaction chamber, recording some of the measurements and providing advice. All other members of the SABIC hydrogen group were extremely hospitable; including Yahya Alsalik who helped with the XPS measurements during my visit to KAUST and provided additional data.

Within the UCL department: the MAPS workshop and the technical support were helpful during repairs and kit modifications. Dewi Lewis was helpful, assisting in reading parts of the manuscript and to other colleagues within the department.

Lastly, to my family and friends for their constant support.

Publication List

Mechanism of Ethanol Photooxidation on Single-Crystal Anatase TiO_2(101)

K. Katsiev, G. Harrison, H. Alghamdi, Y. Alsalik, A. Wilson, G. Thornton and H. Idriss

The Journal of Physical Chemistry C, **2017**, Volume 121, Issue 5, pp 2940-2950

Lepidocrocite-like TiO_2 and TiO_2-(110)-(1×2) supported on W(100)

G. Harrison, M.C. Spadaro, C.L. Pang, D.C. Grinter, C.M Yim, P.L. Luches and G. Thornton

Material Science and Technology, **2016**, Volume 32, Issue 3, pages 203-205

In preparation:

Switch in photocatalytic reaction selectivity: the effect of oxygen partial pressure on carbon-carbon bond dissociation over rutile TiO_2(110) single crystal

G. Harrison, K. Katsiev, A. Wilson, G. Thornton, and H. Idriss

Au/TiO_2 (110) model photocatalyst for hydrogen production: Particle size effect

K. Katsiev, G. Harrison, G. Thornton and H. Idriss

Glossary

AES	Auger Electron Spectroscopy
AFM	Atomic Force Microscopy
BGS	Band Gap State
CB	Conduction Band
CBM	Conduction Band Minimum
CF	Correction Factor
DFT	Density Functional Theory
DOS	Density Of States
DSSC	Dye Sensitised Solar Cells
EPR	Electron Paramagnetic Resonance
ET	Electron Transfer
FEL	Fast Entry Loadlock
FFT	Fast Fourier Transform
FWHM	Full Width Half Maximum
GIXRD	Grazing incident X-ray diffraction
GGA	Generalized Gradient Approximation
IMFP	Inelastic Mean Free Path
JDOS	Joint Density Of States
LEED	Low Energy Electron Diffration
LDOS	Local Density Of States
LT	Low Temperature
MD	Molecular Dynamics
ML	Monolayer
MLE	Monolayer Equivalent

NC-AFM	Non-Contact Atomic Force Microscopy
VO	Oxygen Vacancy
PBE	Perdew−Burke−Ernzerhof
PSD	Photon Stimulated Desorption
QM/MM	Quantum Mechanical / Molecular Mechanical
QMS	Quadrupole Mass Spectrometry
RAIRS	Reflection Absorption Infra-Red Spectroscopy
RFA	Retarding Field Analyser
RGA	Residual Gas Analysis
RT	Room Temperature
SEM	Scanning Electron Microscopy
SPM	Scanning Probe Microscopy
STS	Scanning Tunneling Spectroscopy
STM	Scanning Tunneling Microscopy
SHE	Standard Hydrogen Electrode
TMO	Transition Metal Oxide
TEM	Transmission Electron Microscopy
TPD	Temperature Programmed Desorption
TMA	Trimethyl Acetic Acid
TSP	Titanium Sublimation Pump
UHV	Ultrahigh Vacuum
UV	Ultra-Violet
VB	Valence Band
VBM	Valence Band Maximum
WKB	Wentzel-Kramers-Brillouin
XPS	X-ray Photoelectron Spectroscopy

Table of Contents

List of Figures

topographic image (green, light blue, dark blue). Bottom inset: the principal (101) azimuths. (**C**) Height line profiles as indicated in (**B**). (**D**) A high resolution 220 × 120 $Å^2$ image with resolution along the rows, green height line profile. The principal rutile TiO_2(100) azimuths are shown. (**E**) A zoomed-in of 125 × 125 $Å^2$ of a region of terrace as indicated by the blue square in (**B**), black dashed lines indicate ridges, a light blue height profile is drawn across the rows. The white lines indicate the off-set between the upper and lower terrace. The principal rutile TiO_2(100) azimuths are shown. (**F**) Line profiles perpendicular to the row direction in **(E)**. (**G**) A green line profile along the row in (**D**). 120

Figure 4.14: Structural filled ball models of two rutile TiO_2(100)-(1 × 3) models from reference.[42] (**A**) The tilted view rutile TiO_2(100)-(1 × 3) microfacet model. (**B**) The side view model of (**A**). (**C**) The tilted view rutile TiO_2(100)-(1 × 3)-β microfacet model. (**D**) The side view model of (**C**). Indicated by the black arrows are the rows *a* , *b* and *c* of Ti_{5c}/Ti_{3c}. The (2.96 × 13.77 Å) unit cell is indicated by the black rectangle. The Ti_{3c}/Ti_{5c} rows are identified by the black arrows. The inter-row separation of Ti_{5c}/Ti_{3c} (dotted lines) for both models are shown. **(E)** A 300 K STM image (79 × 76 $Å^2$) (+1.6 V, 0.1 nA). Indicated are the three repeating rows *a*, *b* and *c* by the white lines. A blue line profile is drawn across the repeating structure. (**F**) A blue line height profile indicates a maximum corrugation of 1.5 Å. The distances between, |*b*-*a*|, |*c*-*a'*|, |*c*-*b*| and |*a*-*c*| are indicated. The TiO_2(100) principal azimuths are shown for both the STM image and model. 122

Figure 4.15: 300 K STM images (+1.6 V, 0.1 nA) of the same area of the surface-modified anatase TiO_2(101) surface imaged in **Figure 4.13** after exposure of acetic acid (22 L) at 300 K. **(A)** Large-area image (400 × 400 $Å^2$) of the region, where black dashed ovals indicate pristine TiO_2(101). Lower inset: the principal (101) azimuths are indicated. (**B**) Zoomed-in (140 × 140 $Å^2$) of the terrace identified by the green box in (**A).** Blue and green dashed lines correspond to the line profiles in (**D**) along and across the rows. The distances between rows and bright features are indicated. **(C)** 300 × 150 $Å^2$ region of densely packed acetic acid 0.25 ML. Overlaid are a green line profile in the $[1\bar{1}\bar{1}]$ direction and a blue line profile in the $[\bar{1}\bar{1}1]$ direction. **(D)** STM height line profiles across (blue dashed) and along (green dashed) the rows of protrusions in **B**. The distances12 representative of a rutile (100)-(2 × 3) are indicated. (**E**) STM height line profile along the rows of adsorbates from the lines in (**C**). (**F**) The alignment of the rutile TiO_2(100) (4.59 Å × 2.96 Å) (blue) and the anatase TiO_2(101) (10.24 × 3.78 Å) (red) unit cells. An angle of 65° is between rutile [001] and anatase [010] directions. 126

Figure 4.16: STM images (+1.6V, 0.1 nA) of the modified region of anatase TiO_2(101) before and after exposure to acetic acid. (**A**) 91 × 83 $Å^2$ image of the modified 100-(1 × 3)-β region. Identified: three rows *a*, *b* and *c* (black parallel line). Top inset: the (100) azimuths. (**B**) A 91 × 73 $Å^2$ image of the modified 100-(1 × 3)-β-acetate region. Identified: three rows *a*, *b* and *c* by black parallel lines; the adsorbate rows (black parallel lines) assigned as *a** and *c**; circles overlaid on top of the upper (blue) and lower rows (green); parallel line profiles on the upper (green) and lower (blue) rows; black rhomboids overlaid on four nearest neighbours. (**C**) Line profiles displaying the phase difference of 1.8 Å ± 0.3 Å between the parallel rows of adsorbates. 128

Figure 4.17: (A)(B) Tilted structural ball and stick models of the rutile TiO_2(100)-(1 × 3)-β and rutile TiO_2(100)-(1 × 3) with acetate molecules binding in a bi-dentate mode along the [001] direction to the Ti_{5c}. Inset (**A**): acetate in a second possible co-ordination position. Lattice is represented by red spheres (oxygen atoms) and blue spheres (titanium atoms). The carboxylic acid are represented by green spheres (oxygen atoms) the black spheres (carbon) and white spheres (hydrogen. Rows of Ti_{5c} labelled *a*, *b* and *c* are identified. (**C**) **(D)** Top view of the upper respective structural models. Blue circles are overlaid on top of rows *a** and *c** and yellow on *b** co-incident halfway between the –COO-Ti atoms. Black rhomboids identify geometry of four nearest neighbours and separation along is shown. The distances between the

(**C**) Computed peak areas from panel A as a function of O_2 pressure in mbar. Lower inset: computed areas of the exponential fitted function, slow (red) and fast (blue) processes. (**D**) ln(reaction rate) taken from panel A as a function of ln(P_{O2}). [The QMS mass spectrometry data was collected by Dr. K. Katsiev]_____183

Figure 6.8: (A) Acetaldehyde formation upon photooxidation of ethanol on TiO_2(101) at 1 × 10^{-7} mbar O_2 pressure, 300 K, and ethanol exposure between 2.3 and 32 L. **(B)** Ethanol coverage plot as a function of exposure in Langmuir. **(C)** Initial rate of reaction (in ML_{EtOH} s-1) with respect to the initial ethanol coverage (in ML), with a linear regression fit. UV excitation flux ≈ 5 mW/cm^2. **(D)** ln(rate) vs ln(θ_{EtOH}) plot. [The mass spectrometry traces were collected by Dr. K Katsiev]_____185

Figure A.1: The centre of the anatase TiO_2(101) surface after electron bombardment for 5 minutes at a flux of 2-3 × 10^{15} electrons $s^{-1}cm^{-2}$ (**A**) A 700 × 700 Å^2 image (+1.6 V, 0.1 nA) Shown in the inset are azimuths with respect to the (101) surface. (**B**) A zoomed-in area 190 × 150 Å^2 image where dark depressions (black dashed circles) and protrusions (green circles) are identified. _____193

Figure A.2: STM image of the outer edge of the anatase TiO_2(101) after e-beaming with an electron flux of 5-7 × 10^{14} electrons $s^{-1}cm^{-2}$ for 5 + 10 minutes. (**A**) A 250 × 250 Å^2 (+1.6 V sample bias, 0.1 nA), dark strips are present elongated in the [$\bar{1}$01] direction. (**B**) A 250 × 250 Å^2 (-1.0 V, 0.1 nA) with identical dark strips. In both images several representative depressions are identified by the green dashed lines in the blue ovals._____194

Figure A.3: An example of the calibration procedure performed on the tip modified STM images in Chapter 4. A 300 K 388.3 × 388.3 Å^2 STM tunneling current image (+1.6 V, 0.1 nA) of a tip modified region of anatase TiO_2(101). The green square is the region zoomed in image (**E**). The red square is the region zoomed-in in image (**B**). The green arrows identify the angle between the [010] anatase direction and the horizontal image direction (vertical is 21°). (**B**) Zoomed-in image of the anatase TiO_2(101)-(1 × 1) surface. Pink and blue line profiles are overlaid in the [10$\bar{1}$] and [010] direction respectively. (**C**) A line profile in the [10$\bar{1}$] direction. (**D**) A line profile in the [010] direction. (**E**) A zoomed-in image of the modified region defined by green square in (**A**). Overlaid are lines across the length of four unit cells of the (1 × 3) from which the maximum (pink line) and minimum (blue line) can determine a (1 × 3) lattice parameter 14.2 Å ± 0.4 Å._____195

Figure A.4: 300 K STM images (+1.6 V, 0.1 nA) of a tip modified (+10 V 200 ms, 50 nA) anatase TiO_2(101) surface. **(A)** A (730 × 730 Å^2) STM image, white cross indicates the centre of pulse. Top inset: the anatase TiO_2(101) azimuths are identified. Blue box identifies an area zoomed-in in (**B**). The green rectangle indicates the area zoomed in in (**C**) **(B)** A (125× 125 Å^2) STM image of an outer 'healed' region. Blue ovals identify bright-dark-bright point defects. Black rectangle identifies the anatase (101) unit cell. **(C)** A 280 × 190 Å^2 area of the surface identified by the green box in (**A**). Blue circles identify bright-dark-bright point defects. Pink and green lines profiles are overlaid. **(D)** Line profile of step height (4 Å) in (**C**). **(E)** Pink line profile as defined in (**C**), where rows (5.2 Å) are identified. **(F)** Height line profiles from lines in (**A**) an angle of 10° ± 1° (green) [101] an angle of 6° ±1° (dark blue) [010] and substrate 0° (light blue) are shown._____196

Figure A.5: STM images (+1.6 V, 0.1 nA) of a (+8 V 100 ms, 50 nA) tip pulse modified e-beamed (35 minutes total) anatase TiO_2(101) surface. **(A)** 1400 × 1200 Å^2 large scale image of the tip pulse, black dashed circle identifies the outer effected area, black cross depicts the centre of the pulse and the dark blue line a height line profile over a region of crystalline surface of the outer 'healed' surface. **(B)** An STM image of the tip pulsed region where multiple crystalline areas can be observed (black dashed circle). Inset: region defined by the green box zoom

CHAPTER 1

1.0 Introduction

1.1 Transition Metal Oxides

Transition metal oxides (TMO) are of universal importance in a wide range of practical and future applications from electronics to catalysis, such as catalysts for the efficient photocatalytic production of hydrogen from renewable sources.[1] These are based on the large variety of physical properties of TMO.[2] For example, the bonding ranges from ionic to covalent and the conductivity from insulating to super-conducting.[3] These unique properties are related to the outer valence d-electrons. In certain applications the bulk properties determine the functionality, in others such as in catalysis, the surface bonding with molecules and metals play the important role. The ability to support multiple oxidation states, and therefore participate in reduction and oxidation chemical processes, dictates much of the behaviour.

The surface of TMO may be regarded as a two dimensional defect of its bulk structure. This surface is often not a simple truncation of the bulk structure. Complex structural modifications can occur, for example by the surface's desire to eliminate a dipole or to accommodate a departure from the metal oxide stoichiometry. This great variety of the potential surface structure is one factor for the delay in progress regarding their understanding compared to metal surfaces.[2,4] Since the development of the necessary instrumentation, such as Scanning Tunneling Microscopy (STM) by Binnig and Rohrer[5], the link between their surface structure and chemical activity relationships has been intensely investigated.[6]

TMO in nature are usually semiconductors with a band gap up to a few electron volts (eV). These materials absorb light when the photon energy is equal to or larger than the band

gap. This may lead to the spatial and energetic separation of electrons from the hole: resulting in highly reducing and oxidising species, respectively. Interactions with surface adsorbed species can lead to photochemical reduction and oxidation. For example on the TiO_2 surface, water can be converted into its component elements O_2 and H_2 under UV irradiation.

1.2 Titanium Dioxide TiO_2

Titanium dioxide (TiO_2) crystallises in three common stable polymorphs; anatase (a = b = 3.782 Å, c = 9.502 Å), rutile (a = b = 4.584 Å, c = 2.953 Å) and brookite (a = 5.436 Å, b = 9.166 Å, c = 5.135 Å).[6] By far, the polymorphs anatase and rutile constitute the most widely studied TiO_2 structures, due to their ease of synthesis and are the forms of titania used in many applications, such as in photocatalysis.[6,7] Structural models of anatase and rutile unit cells are displayed in **Figure 1.1**. Although both structures contain repeating octahedron units, the rutile unit cell contains a slightly distorted octahedron, as shown by the X-ray Diffraction (XRD) determined bond lengths and angles.[6] In anatase the distortion of the octahedron (grey oval) is more significant. This increased structural distortion is implicated in calculations to result directly in the band structure alignment of rutile and anatase discussed later.[8,9] Rutile is the most thermodynamically stable phase, but anatase crystallites are those typically formed initially in synthetic chemical methods,[10-12] due to the greater free energy of anatase surfaces. This favours anatase particles of < 10 nm diameter.[1314] Bulk anatase undergoes an irreversible phase transition to rutile in the temperature range of 850 K-1250 K,[14] depending on many factors including initial particle size,[15] presence or absence of deposited metals,[16] pressure and gas phase composition as well as bulk doping.

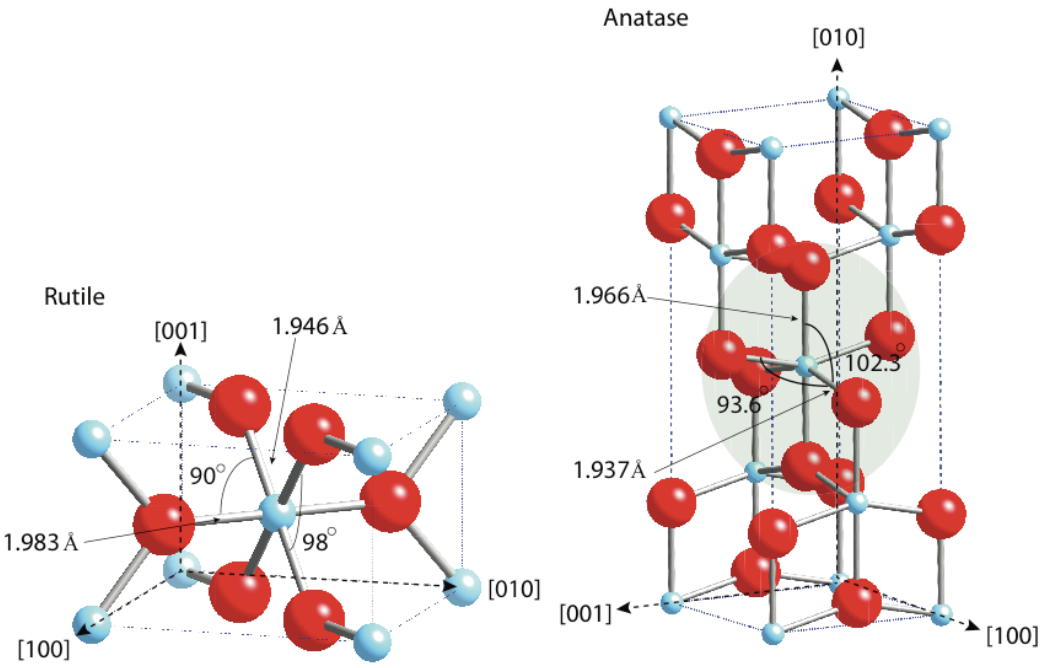

Figure 1.1: Diagram showing the structural models of the unit cells of rutile (left) and anatase (right) TiO_2. Lattice parameters of the unit cell of rutile are a = b = 4.584 Å, c = 2.953 Å, and those of the unit cell of anatase are a = b = 3.782 Å, c = 9.502 Å. Blue spheres represent Ti ions and red spheres are O ions. The bond angles and bond lengths are labelled. Azimuth directions are shown. This figure was adapted from reference.[6]

The large band gaps of anatase and rutile would make the two phases insulators. However, they generally form semi-conducting materials without doping, due to non-stoichiometry introduced by ultrahigh vacuum (UHV) preparation, that gives rise to Ti interstitials and oxygen vacancies (VO).[6] This conductive property of the anatase and rutile surfaces allows for scanning probe microscopy (SPM) as well as other electron-based surface science techniques.[4] The presence of VO and Ti interstitials gives rise to electronic states lying between the valence band (VB) and the Fermi level (E_F) of anatase and rutile; which results in an n-semiconductor and pinning of E_F slightly below the conduction band minimum (CBM).[6] These electronic states are detectable by photoemission measurements, and are often referred to as the band-gap states (BGS).[17] Surface VO can be created by a variety of techniques including ion sputtering, electron bombardment and heating in vacuum.[18]

The surfaces of single crystalline rutile and anatase can be easily prepared and cleaned in UHV. In addition, single crystalline films of rutile and anatase can be grown epitaxially, in

the form of ultrathin (defined as up to 20 Å thickness) or thin films, on near lattice-matched substrates.[19-21] Epitaxial growth is defined here as the growth of a crystalline layer which has a definite crystallographic orientation and registry with respect to the substrate crystal structure. In practice this epitaxial growth occurs most favourably when the two-dimensional unit cell of the substrate and epitaxial layer supercell are closely matched (~1-3% mismatched).[22] Ultrathin films of TiO_2 form a core component of this thesis; supported on the metal W(100) surface in Chapter 5 and grown *in-situ* by the action of a high sample biased STM tip pulse (during imaging) on single crystalline anatase TiO_2(101) in Chapter 4.

The W(100) supported ultrathin film allows the implementation of all surface science characterisation techniques which use charged particles, such as STM and XPS.[23] This allows, in principal the investigation of TiO_2 in a non-reduced (TiO_2-x) state and at a size relevant to metal–metal oxide catalytic systems.[24] Additionally, new TiO_2 phases only present at a reduced dimensionality with no equivalent bulk comparison can be studied. In the STM tip pulse fabricated ultrathin film; the novel formation of an ultrathin rutile film on top of an anatase TiO_2 single crystal surface, provides a means to form an interface between two different TiO_2 polymorphs (rutile/anatase).

There exists a good understanding of the surface structure and reactivity of the low index crystal planes of rutile in the single crystalline form, and to a lesser extent in thin film form (< 100 Å).[25] There is a moderate understanding of the surfaces of single crystalline anatase compared to rutile.[6] This is in part due to the difficulty in growing large single crystals of anatase TiO_2. The anatase (101) Miller index surface plane is the most stable surface, representing a significant fraction of surfaces in commercial TiO_2 nanomaterials.[26] An atomic understanding of the surface chemistry and physics of the single crystalline surface is needed to support the work on nanomaterials. Work on this latter surface comprises a large fraction of the study presented here. The rutile TiO_2(110) is the proto-typical model metal oxide surface for which a vast quantity of research has been published in single crystal studies. Topics include

surface reconstructions, molecular adsorption and point defect dynamics, analysis of photo-reaction products and hole-electron initiated kinetics.[7]

1.3 TiO_2 as a Photocatalyst

Fujishima and Honda reported the ultra-violet (UV) induced photo-electrochemical splitting of water into hydrogen and oxygen.[27] In their electrochemical cell an n-type TiO_2 material constituted the anode and Pt metal the cathode. Upon UV light exposure in the absence of a bias voltage, a photocurrent flowed from the Pt electrode to the TiO_2 electrode through the external circuit. This was explained by the generation of holes at the anode by excitation of VB electrons, leading to a lower electrochemical oxidation potential. As the conduction band minimum (CBM) in TiO_2 is higher than the redox potential of $2H+/H_2$ 0 V (SHE) and the valence band maximum (VBM) lower than the redox potential O_2/H_2O +1.23 V (SHE), water splitting occurs spontaneously.[28]

The photo-electrochemical activity of TiO_2 has stimulated four decades of TiO_2 research to improve and understand heterogeneous photocatalysis;[29] however the photochemical quantum yields (Φ) are low (~1 %),[30] due in part to fast recombination rates for the charge carriers, electron and holes.[31]

Despite the poor quantum yields, TiO_2 formulations are still widely used in photocatalysis.[29] For example, TiO_2 is used in the photocatalytic degradation of organic pollutants, due to the chemical stability and benign biological properties of TiO_2.[29]

Anatase and rutile TiO_2 have bulk optical band gaps of 3.2 (indirect) and 3.02 eV (direct), respectively. The highest joint densities of states (JDOS) in the conduction band (CB) and VB actually leads to an excitation energy requirement of ~3.3 eV for both polymorphs.[32] Therefore, the photo-absorption of anatase and rutile TiO_2 is almost completely limited to the UV region, with rutile absorbing a small amount of visible light, presenting a problem for effectively harvesting solar radiation for photocatalytic applications.

Shown in **Figure 1.2** is a schematic of the relevant photophysical and photochemical processes involved in photocatalysis of TiO_2. Step one (1) involves the photo-induced formation of electron-hole pairs, with the electrons (holes) lying at the bottom (top) of the conduction (valence) band.[33] This process can take place both at the surface and within the bulk with differing transport consequences.[32] Carrier (electron/holes) migration (2) to the surface is required for photocatalysis after which electron transfer (ET) with a stable adsorbed species at the surface takes place (3)(4). Reduced/oxidised species can then initiate further reactions, such as organic molecular degradation or generation of OH.[34] In addition, poisoning by adsorption at active sites is possible.

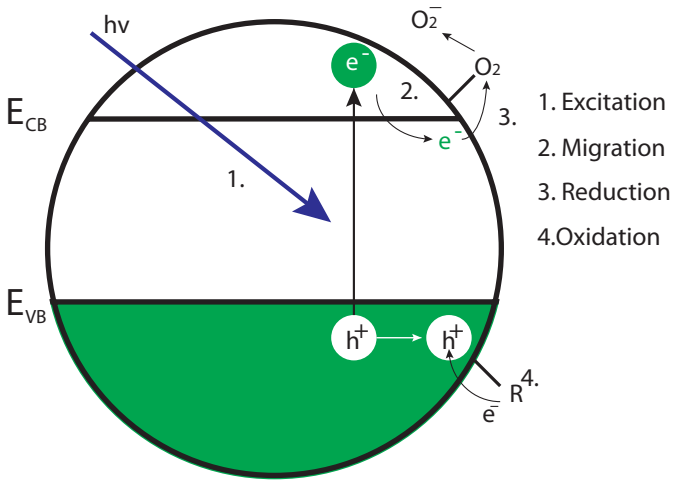

Figure 1.2: Schematic model illustrating the four fundamental processes associated with TiO_2 photocatalysis. The maximum valence band energy E_{VB} and minimum conduction band E_{CB} are labelled. The key processes: (1) UV light excites an electron into the CB. (2) The photo-excited electron migrates to the surface. (3) The O_2 surface molecule is reduced by the photo-excited electron. (4) A species R is oxidised by the interaction with a h+. Adapted from reference.[32]

The choice of TiO_2 polymorph is an important factor in photocatalysis of the many stable forms of TiO_2. Anatase is thought to be the most active for the photodecomposition of organic molecules.[35-38] Rutile is considered to have the highest photooxidation activity water splitting to form O_2.[37-39]

To directly compare the polymorphs, one example study correlated the charge carrier lifetime of electron-hole pairs with the photo-oxidation of CO to CO_2 on rutile TiO_2(110) and anatase TiO_2(101), with anatase having the higher activity. This result was explained by the in-

direct band gap and a greater upward band bending in anatase.[40] The extent of the band bending, the potential height (VBM (CBM) at surface – VBM (CBM) at bulk) and depletion length (length of band bending influence) is thought to depend inversely on a materials dielectric constant, which is higher in rutile than anatase.[41] The increased band-bending in anatase results in less hindered migration of electrons from the surface to the bulk and holes from the bulk to the surface in anatase compared to rutile.[42] The lifetime of holes in films of anatase and rutile nanoparticles have been measured by a ultrafast pump-probe laser technique, resulting in hole lifetimes of ~1 ps and ~100 ps respectively; in the former holes were quickly trapped at anatase surface states.[43] Overall, a steeper upward band-bending in anatase leads to a quicker spatial separation of holes and electrons and explains the higher activity determined for some surface reactions.

The surface of the polymorph can drastically influence the photocatalytic properties of the TiO_2 material. The optical absorption, work function, and adsorption properties are all very surface sensitive. In addition the band bending and depletion length have been shown to be surface plane dependent on rutile.[44] Different photocatalytic activities are observed for different lattice planes.[32] For instance, anatase TiO_2 crystals with controlled percentages of the (001), (101) and (010) low index crystal planes, were characterised with respect to the photocatalytic production of hydrogen from water. The order of photocatalytic rate followed (010) > (001) > (101).[45] For rutile TiO_2 single-crystals, the order for the rate of oxidation of an organic reactant was found to be (101) > (110) > (001) > (100).[46] An overall trend observed from these experiments is that a higher percentage of five-coordinated surface Ti atoms increases the photocatalytic activity.[32]

1.4 Mixed Phase TiO_2 Photocatalysis

TiO_2 nanomaterials consisting of a mixed-phase of anatase and rutile are the most successful photocatalysts; one example is the benchmark photocatalyst Degussa P25 Aeroxide TiO_2, formed by the hydrolysis of $TiCl_4$, which contains a 70/30 % mixture of anatase (rutile)

nano-crystallites of ~30 nm diameter (~80 nm diameter).[47] Degussa P25 is used in many applications, either modified for example in Dye Sensitised Solar Cells (DSSC) or unmodified in commercial water purification systems. Research analysing Degussa P25 and other mixed-phase anatase/rutile materials (with good contact between the phases) indicates a comparatively higher activity, compared to the pure forms of anatase and rutile, suggesting a synergistic effect.[48-50] However there is disagreement about the origin of the high activity of these mixed-phase materials. Some propose that it is due to a combined microstructure leading to synergistic catalytic effects;[51] where in general catalytic activity is enhanced at the interface of crystalline solid materials.[47] Others suggest that the particles exist as separated particles of anatase and rutile and therefore behave independently. A recent review on the synergism of these two phases in photocatalysis summarised most of the work in the last two decades.[26] A complete understanding of the possible synergistic effect in the anatase/rutile mixed-phase is, however, still lacking.

One major requirement for efficient photocatalysis is a hindered charge recombination;[47] as instant recombination of the hole-electron pair results in no redox activity. The dispersion of metal (Au, Pd, Pt) nanoparticles provides an electron sink to achieve this. Electron transfer (ET) between anatase and rutile phases in contact is hypothesised to also lead to reduced recombination by the spatial separation of electrons and holes.[51] However, with respect to the ET direction, previous experimental studies indicate both possibilities; some indicate ET from rutile to anatase.[42,52-55] Notable examples, such as electron Paramagnetic Resonance (EPR) measurements of Degussa P25 under visible light indicate the movement of electrons from rutile to anatase.[42,54] In addition, Parkin and co-workers fabricated a layered anatase and rutile film interface of 1-2 μm thickness to analyse a photochemical reaction and the photochemical reduction of Ag.[52] This study also indicated the transfer of electrons from rutile to anatase under photo-excitation. Other studies indicate the reverse ET direction from anatase to rutile.[56-58] The preferred photo-deposition of Ag on rutile close to the anatase/rutile interface, on a prepared surface junction, indicated the movement of electrons from anatase to rutile.[57] The

experimental variation in the direction of electron transfer stems from the difficulty in creating a well defined anatase/rutile interface.[59]

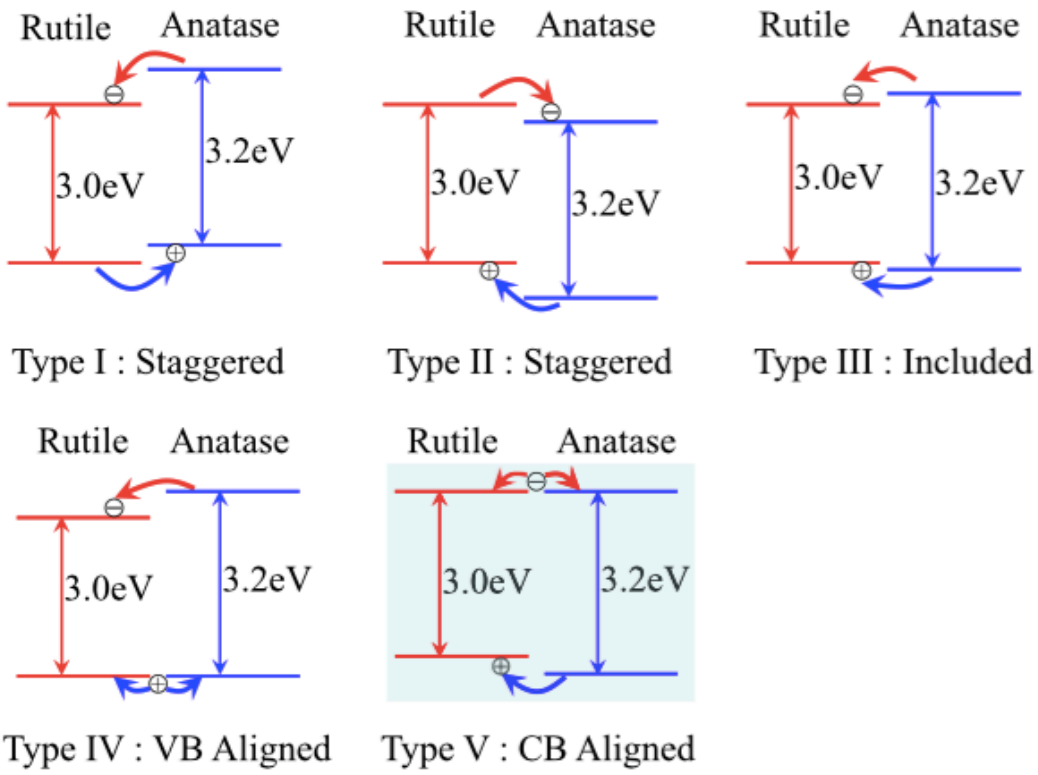

Figure 1.3: Schematic diagrams showing five (I-V) possible bulk band alignments between rutile and anatase. The band gaps of 3.0 eV for rutile and 3.2 eV for anatase are depicted. The red arrows indicate the migration direction of photo-excited electrons and blue arrows the migration of photo-excited holes based on the stability conferred by the conduction band minimum (CBM) and valence band maximum (VBM) positions. Adapted from reference.[59]

To explain photocatalytic synergy Bickley proposed an included type III alignment (see **Figure 1.3**) with a space charge layer created at the interface between anatase and rutile phases. This results in favourable VB hole migration from anatase to rutile.[60] In this model, thermodynamically, photo-excited electrons cannot move in the opposite direction and it is referred to as the rutile 'sink' model. Trapping sites below the CBM of anatase (and CBM of rutile) were later proposed to explain EPR evidence of photo-excited electron migration from rutile to anatase.[42]

Experimental investigations into the explicit relative band gap alignment of anatase (3.2 eV) and rutile (3.0 eV) have been carried out. This requires an accessible shared reference

energy level. The mid-gap transition of Ti^{3+},[59] electrochemical reference level,[61] XPS core levels,[62] or shared vacuum level,[63] have all been used, affording a direct comparison between isolated or mixed phases.[62] A summary of the existing models proposed in the literature is shown in **Figure 1.3**,[42,54,57,64-66] where the energetically controlled migration of hole/electrons is indicated by the red and blue arrows. In one example Pfeifer et al., used XPS to measure rutile/RuO_2 and anatase/RuO_2 interfaces separately and determined a type II band alignment, with 0.5-0.39 eV CB and 0.70-0.63 eV VB differences.[9] A type V alignment where the CBM are equal has been proposed by Mi, studying nanocrystalline mixed phase TiO_2.[59] Here the relative speed of electron transfer determines the electron flow direction between anatase and rutile. Xiong also determined a type V alignment studying rutile nanocrystals embedded in anatase film with photoemission.[63] A recent kelvin probe microscopy study conducted on anatase and rutile nanoparticles, indicated an electrical field across an interfacial rutile/anatase region of 450 nm length, with a type II alignment.[67]

The rutile/anatase band alignment can be determined theoretically.[64] Deák determined a generic alignment of the bulk band structures at the Fermi level and concluded the presence of a type II alignment with the VB (CB) of rutile is 0.35 eV (0.55 eV) higher.[64] Scanlon et al. also investigated this theoretically using a combination of quantum mechanical and molecular mechanical (QM/MM) calculations performed on a core-shell model. A VB offset (0.47 eV) and CB offset (0.3 eV) with respect to the vacuum level was determined, also indicating a type II alignment.[62] Explicit rutile/anatase interfaces have been modelled such as single crystalline R(100)/A(100) and R(110)/A(101).[68] Here Kullgren et al. determined a type II, using the calculated electrostatic potential at the interface as a reference.[68] Further more, the influence of the dissociated water leading to H^+ and OH^- ions at the interface has also been modelled for close (10 nm) interfaces, resulting in a higher anatase CB; resolving the discrepancy between results obtained in wet or humid environments, while solid interfaces generally indicate a type II.[69]

Notably, as considered by Nosaka et al.[70] the direct band gap of anatase of 3.8 eV profoundly influences the alignment of the VB and CB of rutile and anatase. For example when

this is taken into account the type II alignment (indirect band gap) modelled[62] results in a type III arrangement (anatase CBM above rutile CBM).

Given the contradictions in previous work, the study of a well-defined anatase/rutile system would seem to be necessary as a means to understand the rutile-anatase interface.

It is intrinsically difficult to grow anatase on rutile or vice versa. Existing fabricated model systems include: anatase (001) grown on $LaAlO_3$(001) or $SrTiO_3$(001), where rutile co-exists.[71] In the latter STM and electron microscopy confirmed the presence of rutile TiO_2(100)-(1 × 3) domains embedded in the polycrystalline anatase film. In addition, rutile TiO_2 has been grown in conjunction with a lepidocrocite-like bilayer (formally derived from an anatase (001) bi-layer) on Ni(110) and Ag(100).[25,72] These two systems constitute the most relevant previously studied anatase/rutile thin films.

Modelling of rutile/anatase interfaces composed of Miller interfaces of rutile and anatase planes have been considered. Deskins employed molecular dynamics (MD) simulations using near-coincidence-site lattice (NCSL) theory to analyse interfaces of rutile (110), (100) and (001) with anatase (101), (100) and (001) (rectangular unit cells matched).[73] This resulted in favourable adhesion energies of -1 to -3 J/m^2, with unsaturated Ti_{5c} becoming bulk like Ti_{6c} at the interface and an observed partial disordering at the interface of a single layer ~4 Å. The most favourable interfaces were constructed from rutile (110)/anatase (101) and rutile (100)/ anatase (100). In addition, in a separate studies, Kullgren et al. identified Ti_{4c} within the interfacial region of rutile (110)/ anatase (101) and rutile (100) and anatase (100) interfaces[68] and Ju modelled a rutile (111) / anatase (101) interface analysing the electronic properties of the interface.[8] Recently Nolan et al. used DFT simulations to investigate the interfacial region of anatase (101) / rutile (110) and anatase (100) / rutile (001). This latter study also confirmed the disordered nature of the interface and presence of low coordinated Ti_{4c} and VO, where the former were associated with electron localisation and the latter formed more easily formed compared to the bulk. Holes were shown to be distributed across the interface.[74]

In addition, theoretical work has also studied a more complicated indirect rutile/anatase interfaces, where an intermediate TiO_2-II phase has a favourable contact with the anatase

TiO_2(112) plane and can support a rutile phase. This intermediate phase reduces the epitaxial mismatch between rutile and anatase. Experimental evidence for such a system is provided by electron microscopy of nanoparticles.[75,76]

1.5 Research Question and Thesis Structure

A photocatalytic synergism between anatase and rutile has been hypothesised to explain the general higher activity of mixed-phase rutile and anatase systems than either pure anatase or rutile.[42,54,77] However, fundamental knowledge of how the anatase and rutile interact during photocatalysis is still lacking. Therefore the research question is, can a model rutile/anatase single-crystalline system, which can be studied by STM and STS by synthesised? The study of such a system would be invaluable to understand the properties and possible photocatalytic synergism resulting from the two-phase interface.

A surface science approach, with STM being the principal means of characterisation for the investigation of the interface of anatase and rutile has been employed. The objective is to grow an ultrathin film of anatase and rutile in contact with each other on a viable substrate, with clear distinguishable domains of ~100-300 Å width/length.[25,78] A viable substrate could be one that supports either anatase or rutile, with the potential to grow the other phase. This substrate would be expected to have a good lattice match with either anatase or rutile. An alternative strategy would involve utilising single crystal anatase (rutile) and transforming a region to rutile (anatase).

Obtaining the described model system will facilitate an understanding of the anatase/rutile phase interface on the atomic scale, where both reactivity (photocatalytic synergism) and electronic structure can be probed concomitantly. Using STM, the geometrical and electronic structure can be probed while monitoring adsorbates and point defects such as VO and hydroxyls. Furthermore, although not included here, future studies can use STS to map the local density of states (LDOS) and band structure of the film. This latter method will allow

the band alignment and bending at the formed interface between anatase and rutile to be investigated.

The layout of this thesis is as follows:

Auxiliary Chapters: Chapter 2: Theoretical aspects relevant to the techniques studied will be presented. Chapter 3: This thesis relies heavily on instrumentation for the preparation and analysis/characterisation of the single crystal an ultrathin film samples, therefore these will be presented and discussed.

The original experimental work is divided into two chapters concerned with the fabrication of an rutile ultrathin film /anatase TiO_2(101) interface and a ultrathin film rutile/ lepidocrocite-like TiO_2/W(100) interface. In addition an ethanol photochemical study was performed on anatase TiO_2(101). These consist of:

Chapter 4: A novel preparation methodology employing the electrical effects of an STM tip to modify the structure of a surface of anatase TiO_2(101) and characterise the resulting crystalline surfaces with STM. An ultrathin film terminated with the rutile TiO_2(100)-(1 × 3) surface was fabricated and characterised using the surface adsorption of a carboxylic acid (CH_3COOH).

Chapter 5: A study of ultrathin titania films grown on W(100). Here STM indicates the presence of a ultrathin island structure of rutile TiO_2(110) in conjunction with the (anatase (001) derived) lepidocrocite-like TiO_2 bilayer (5 Å). These were structurally characterised by STM and LEED, where the epitaxial registry with the W(100) surface of the lepidocrocite-like TiO_2 bi-layer was identified.

Chapter 6: A photooxidation study of ethanol adsorbed on single crystalline anatase TiO_2(101) surface in the presence of O_2. A mass spectrometry and STM study (dark and post UV exposure) was conducted, with a reaction mechanism proposed and photoreaction cross-section extracted.

In each individual Chapter (4-6) the significance of the experimental work with respect to the research question is considered and details of perspective future work are given.

References

(1) Connelly, K. A.; Idriss, H. The Photoreaction of TiO_2 And Au/TiO_2 Single Crystal and Powder Surfaces with Organic Adsorbates. Emphasis on Hydrogen Production From Renewables. *Green Chem.* **2012**, *14*, 260–280.

(2) Henrich, V. E.; Cox, P. A. The Surface Science of Metal Oxides; Cambridge University Press, 1996.

(3) Freund, H.-J.; Kuhlenbeck, H.; Staemmler, V. Oxide Surfaces. *Rep. Prog. Phys.* **1996**, *59*, 283–347.

(4) Pang, C. L.; Lindsay, R.; Thornton, G. Structure of Clean and Adsorbate-Covered Single-Crystal Rutile TiO_2 Surfaces. *Chem. Rev.* **2013**, *113*, 3887–3948.

(5) Binnig, G.; Smith, D. P. E. Single-Tube Three-Dimensional Scanner for Scanning Tunneling Microscopy. *Rev. Sci. Instrum.* **1986**, *57*, 1688–1689.

(6) Diebold, U. The Surface Science of Titanium Dioxide. *Surf. Sci. Rep.* **2003**, *48*, 53–229.

(7) Pang, C. L.; Lindsey, R.; Thornton, G. Chemical Reactions on Rutile TiO_2(110). *Chem. Soc. Rev.* **2008**, *37*, 2328–2353.

(8) Ju, M.-G.; Sun, G.; Wang, J.; Meng, Q.; Liang, W. Origin of High Photocatalytic Properties in the Mixed-Phase TiO_2: A First-Principles Theoretical Study. *ACS Appl. Mater. Interfaces* **2014**, *6*, 12885–12892.

(9) Pfeifer, V.; Erhart, P.; Li, S.; Rachut, K.; Morasch, J.; Brötz, J.; Reckers, P.; Mayer, T.; Rühle, S.; Zaban, A.; et al. Energy Band Alignment Between Anatase and Rutile TiO_2. *J. Phys. Chem. Lett.* **2013**, *4*, 4182–4187.

(10) Shin, H.; Jung, H. S.; Hong, K. S.; Lee, J.-K. Crystal Phase Evolution of TiO_2 Nanoparticles with Reaction Time in Acidic Solutions Studied via Freeze-Drying Method. *J. Solid State Chem.* **2005**, *178*, 15–21.

(11) Liu, L.; Zhao, H.; Andino, J. M.; Li, Y. Photocatalytic CO_2 Reduction with H_2O on TiO_2 Nanocrystals: Comparison of Anatase, Rutile, and Brookite Polymorphs and Exploration of Surface Chemistry. *ACS Catal.* **2012**, *2*, 1817–1828.

(12) Ohno, T.; Sarukawa, K.; Tokieda, K.; Matsumura, M. Morphology of a TiO_2 Photocatalyst (Degussa, P-25) Consisting of Anatase and Rutile Crystalline Phases. *J. Catal.* **2001**, *203*, 82–86.

(13) Ghosh, T. B.; Dhabal, S. On Crystallite Size Dependence of Phase Stability of Nanocrystalline TiO_2. *J. Appl. Phys.* **2003**, *94*, 4577–4582.

(14) Hanaor, D. A. H.; Sorrell, C. C. Review of the Anatase to Rutile Phase Transformation. *J. Mater. Sci.* **2011**, *46*, 855–874.

(15) Bashir, S.; Wahab, A. K.; Idriss, H. Synergism and Photocatalytic Water Splitting to Hydrogen Over M/TiO_2 Catalysts: Effect of Initial Particle Size of TiO_2. *Catal. Today* **2015**, *240, part B*, 242–247.

(16) Cardenenas-Lizana, F.; Gomez-Quero, S.; Idriss, H.; Keane, M. A. Gold Particle Size Effects in the Gas-Phase Hydrogenation of M-Dinitrobenzene Over Au/TiO_2. *J. Catal.* **2009**, *268*, 223–234.

(17) Papageorgiou, A. C.; Beglitis, N. S.; Pang, C. L.; Teobaldi, G.; Cabailh, G.; Chen, Q.; Fisher, A. J.; Hofer, W. A.; Thornton, G. Electron Traps and Their Effect on the Surface Chemistry of TiO_2(110). *Proc. Natl. Acad. Sci. U.S.A.* **2010**, *107*, 2391–2396.

(18) Pang, C. L.; Bikondoa, O.; Humphrey, D. S.; Cabailh, G.; Ithnin, R.; Chen, Q.; Muryn, C. A.; Onishi, H.; Thornton, G. Tailored TiO_2(110) Surfaces and Their Reactivity. *Nanotechnology* **2006**, *17*, 5397–5405.

(19) Pacchioni, G.; Valeri, S. Oxide Ultrathin Films; Pacchioni, G.; Valeri, S., Eds.; John Wiley & Sons: Weinheim, Germany, 2012.

(20) Lotnyk, A.; Senz, S.; Hesse, D. Epitaxial Growth of TiO_2 Thin Films on $SrTiO_3$, $LaAlO_3$ And Yttria-Stabilized Zirconia Substrates by Electron Beam Evaporation. *Thin Solid Films* **2007**, *515*, 3439–3447.

(21) Matharu, J.; Cabailh, G.; Thornton, G. Synthesis of TiO_2(110) Ultra-Thin Films on W(100) and Their Reactions with H_2O. *Surf. Sci.* **2013**, *616*, 198–205.
(22) Venables, J. Introduction to Surface and Thin Film Processes; Cambridge University Press, 2000.
(23) Bowker, M.; Davies, P. R. Scanning Tunneling Microscopy in Surface Science, Nanoscience and Catalysis; John Wiley & Sons, 2009.
(24) Kuhlenbeck, H.; Shaikhutdinov, S.; Freund, H.-J. Well-Ordered Transition Metal Oxide Layers in Model Catalysis–a Series of Case Studies. *Chem. Rev.* **2013**, *113*, 3986–4034.
(25) Papageorgiou, A. C.; Cabailh, G.; Chen, Q.; Resta, A.; Lundgren, E.; Anderson, J. N.; Thornton, G. Growth and Reactivity of Titanium Oxide Ultrathin Films on Ni(110). *J. Phys. Chem. C* **2007**, *111*, 7704–7710.
(26) Connelly, K. A.; Idriss, H. Photoreaction of Au/TiO_2 For Hydrogen Production From Renewables: a Review on the Synergistic Effect Between Anatase and Rutile Phases of TiO_2. *Mater. Renew. Sustain. Energy* **2012**, *1*, 1–12.
(27) Fujishma, A.; Honda, K. Electrochemical Photolysis of Water at a Semiconductor Electrode. *Nature* **1972**, *238*, 37–38.
(28) Fujishima, A.; Rao, T. N.; Tryk, D. A. Titanium Dioxide Photocatalysis. *J. Photochem. Photobiol. C: Photochem. Rev.* **2000**, *1*, 1–21.
(29) Fujishima, A.; Zhang, X.; Tryk, D. A. TiO_2 Photocatalysis and Related Surface Phenomena. *Surf. Sci.* **2008**, *63*, 515–582.
(30) Emeline, A. V.; Zhang, X.; Jin, M.; Murakami, T.; Fujishima, A. Application of a "Black Body" Like Reactor for Measurements of Quantum Yields of Photochemical Reactions in Heterogeneous Systems. *J. Phys. Chem. B* **2006**, *110*, 7409–7413.
(31) Cong, S.; Xu, Y. Explaining the High Photocatalytic Activity of a Mixed Phase TiO_2: A Combined Effect of O_2 And Crystallinity. *J. Phys. Chem. C* **2011**, *115*, 21161–21168.
(32) Henderson, M. A. A Surface Science Perspective on TiO_2 Photocatalysis. *Surf. Sci.* **2011**, *66*, 185–297.
(33) Nakata, K.; Fujishma, A. TiO_2 Photocatalysis: Design and Applications. *J. Photochem. Photobiol. C: Photochem. Rev.* **2012**, *13*, 169–189.
(34) Schneider, J.; Matsuoka, M.; Takeuchi, M.; Zhang, J.; Horiuchi, Y.; Anpo, M.; Bahnemann, D. W. Understanding TiO_2 Photocatalysis: Mechanisms and Materials. *Chem. Rev.* **2014**, *114*, 9919–9986.
(35) Ahmed, A. Y.; Kandiel, T. A.; Oekermann, T.; Bahnemann, D. Photocatalytic Activities of Different Well-Defined Single Crystal TiO_2 Surfaces: Anatase Versus Rutile. *J. Phys. Chem. Lett.* **2011**, *2*, 2461–2465.
(36) Su, C.; Hong, B. Y.; Tseng, C. M. Sol–Gel Preparation and Photocatalysis of Titanium Dioxide. *Catal. Today* **2004**, *96*, 119–126.
(37) Ohno, T.; Sarukawa, K.; Matsumura, M. Photocatalytic Activities of Pure Rutile Particles Isolated From TiO_2 Powder by Dissolving the Anatase Component in HF Solution. *J. Phys. Chem. B* **2001**, *105*, 2417–2420.
(38) Andersson, M.; Österlund, L.; Ljungström, S.; Palmqvist, A. Preparation of Nanosize Anatase and Rutile TiO_2 By Hydrothermal Treatment of Microemulsions and Their Activity for Photocatalytic Wet Oxidation of Phenol. *J. Phys. Chem. B* **2002**, *106*, 10674–10679.
(39) Kim, S.-J.; Lee, H.-G.; Kim, S.-J.; Lee, J.-K.; Lee, E. G. Photoredox Properties of Ultrafine Rutile TiO_2 Acicular Powder in Aqueous 4-Chlorophenol, Cu–EDTA and Pb–EDTA Solutions. *Appl. Catal., A* **2003**, *242*, 89–99.
(40) Xu, M.; Gao, Y.; Moreno, E. M.; Kunst, M.; Muhler, M. Photocatalytic Activity of Bulk TiO_2 Anatase and Rutile Single Crystals Using Infrared Absorption Spectroscopy. *Phys. Rev. Lett.* **2011**, *106*, 138302–138304.
(41) Gaskov, A. M.; Rumyantseva, M. N. Nature of Gas Sensitivity in Nanocrystalline Metal Oxides. *Eniv. Prob. Chem. Technol.* **2001**, *74*, 439–444.

(42) Hurum, D. C.; Agrios, A. G.; Gray, K. A.; Rajh, T.; Thurnauer, M. C. Explaining the Enhanced Photocatalytic Activity of Degussa P25 Mixed-Phase TiO_2 Using EPR. *J. Phys. Chem. C* **2003**, *107*, 4545–4549.

(43) Shen, Q.; Katayama, K.; Sawada, T.; Yamaguchi, M.; Kumagai, Y.; Toyoda, T. Photoexcited Hole Dynamics in TiO_2 Nanocrystalline Films Characterized Using a Lens-Free Heterodyne Detection Transient Grating Technique. *Chem. Phys. Lett.* **2006**, *419*, 464–468.

(44) Wilson, J. N.; Idriss, H. Structure Sensitivity and Photocatalytic Reactions of Semiconductors. Effect of the Last Layer Atomic Arrangement. *J. Am. Chem. Soc.* **2002**, *124*, 11284–11285.

(45) Pan, J.; Liu, G.; Lu, G. Q. M.; Cheng, H.-M. On the True Photoreactivity Order of {001}, {010}, and {101} Facets of Anatase TiO_2 Crystals. *Angew. Chem. Int. Ed.* **2011**, *50*, 2133–2137.

(46) Luttrell, T.; Halpegamage, S.; Tao, J.; Kramer, A.; Sutter, E.; Batzill, M. Why Is Anatase a Better Photocatalyst Than Rutile? - Model Studies on Epitaxial TiO_2 Films. *Sci. Rep.* **2014**, *4*, 1–8.

(47) Li, G.; Gray, K. A. The Solid–Solid Interface: Explaining the High and Unique Photocatalytic Reactivity of TiO_2-Based Nanocomposite Materials. *Chem. Phys.* **2007**, 173–187.

(48) Jung, K. Y.; Bin Park, S.; Jang, H. D. Phase Control and Photocatalytic Properties of Nano-Sized Titania Particles by Gas-Phase Pyrolysis of $TiCl_4$. *Catal. Comm.* **2004**, *5*, 491–497.

(49) Bakardjieva, S.; Subrt, J.; Stengl, V.; Dianez, M. J.; Sayagues, M. J. Photoactivity of Anatase–Rutile TiO_2 Nanocrystalline Mixtures Obtained by Heat Treatment of Homogeneously Precipitated Anatase. *App. Cata. B: Env.* **2005**, *58*, 193–202.

(50) Kolenko, Y. V.; Churagulov, B. R.; Kunst, M.; Mazerolles, L.; Colbeau-Justin, C. Photocatalytic Properties of Titania Powders Prepared by Hydrothermal Method. *App. Cata. B: Env.* **2004**, *54*, 51–58.

(51) Bickley, R. I.; Gonzalez-Carreno, T.; Lees, J. S.; Palmisano, L.; Tilley, R. J. D. A Structural Investigation of Titanium Dioxide Photocatalysts. *J. Solid State Chem.* **1991**, *92*, 178–190.

(52) Quesada-Cabrera, R.; Sotelo-Vazquez, C.; Bear, J. C.; Darr, J. A.; Parkin, I. P. Photocatalytic Evidence of the Rutile-to-Anatase Electron Transfer in Titania. *Adv. Mater. Interfaces* **2014**, *1*, 1400069–7.

(53) Sun, X.; Dai, W.; Wu, G.; Li, L.; Guan, N.; Hunger, M. Evidence of Rutile-to-Anatase Photo-Induced Electron Transfer in Mixed-Phase TiO_2 By Solid-State NMR Spectroscopy. *Chem. Comm.* **2015**, *51*, 13779–13782.

(54) Hurum, D. C.; Gray, K. A.; Rajh, T.; Thurnauer, M. C. Recombination Pathways in the Degussa P25 Formulation of TiO_2: Surface Versus Lattice Mechanisms. *J. Phys. Chem. B* **2005**, *109*, 977–980.

(55) Wang, W.-K.; Chen, J.-J.; Zhang, X.; Huang, Y.-X.; Li, W.-W.; Yu, H.-Q. Self-Induced Synthesis of Phase-Junction TiO_2 With a Tailored Rutile to Anatase Ratio Below Phase Transition Temperature. *Sci. Rep.* **2016**, *6*, 1–10.

(56) Kavan, L.; Grätzel, M.; Gilbert, S. E.; Klememz, C.; Scheel, H. J. Electrochemical and Photoelectrochemical Investigation of Single-Crystal Anatase. *J. Am. Chem. Soc.* **1996**, *118*, 6716–6723.

(57) A Patterned TiO_2(Anatase)/TiO_2(Rutile) Bilayer-Type Photocatalyst: Effect of the Anatase/Rutile Junction on the Photocatalytic Activity. *Angew. Chem. Int. Ed.* **2002**, *41*, 2811–2813.

(58) Shen, S.; Wang, X.; Chen, T.; Feng, Z.; Li, C. Transfer of Photoinduced Electrons in Anatase–Rutile TiO_2 Determined by Time-Resolved Mid-Infrared Spectroscopy. *J. Phys. Chem. C* **2014**, *118*, 12661–12668.

(59) Mi, Y.; Weng, Y. Band Alignment and Controllable Electron Migration Between Rutile and Anatase TiO_2. *Sci. Rep.* **2015**, *5*, 1–10.

(60) Bickley, R. I.; Gonzalez-Carreno, T.; Lees, J. S.; Palmisano, L.; Tilley, R. J. D. A Structural Investigation of Titanium Dioxide Photocatalysts. *J. Solid State Chem.* **1991**, *92*, 178–190.
(61) Kavan, L.; Grätzel, M.; Gilbert, S. E.; Klemenz, C.; Scheel, H. J. Electrochemical and Photoelectrochemical Investigation of Single-Crystal Anatase. *J. Am. Chem. Soc.* **1996**, *118*, 6716–6723.
(62) Scanlon, D. O.; Dunnill, C. W.; Buckeridge, J.; Shevlin, S. A.; Logsdail, A. J.; Woodley, S. M.; Catlow, C. R. A.; Powell, M. J.; Palgrave, R.; Parkin, I. P.; et al. Band Alignment of Rutile and Anatase TiO_2. *Nat. Mater.* **2013**, *12*, 798–801.
(63) Xiong, G.; Shao, R.; Droubay, T. C.; Joly, A. G.; Beck, K. M.; Chambers, S. A.; Hess, W. P. Photoemission Electron Microscopy of TiO_2 Anatase Films Embedded with Rutile Nanocrystals. *Adv. Funct. Mater.* **2007**, *17*, 2133–2138.
(64) Deák, P.; Aradi, B.; Frauenheim, T. Band Lineup and Charge Carrier Separation in Mixed Rutile-Anatase Systems. *J. Phys. Chem. C* **2011**, *115*, 3443–3446.
(65) Ohno, T.; Tokieda, K.; Higashida, S.; Matsumura, M. Synergism Between Rutile and Anatase TiO_2 Particles in Photocatalytic Oxidation of Naphthalene. *Appl. Catal., A* **2003**, *244*, 383–391.
(66) Zhang, J.; Xu, Q.; Feng, Z.; Li, M.; Li, C. Importance of the Relationship Between Surface Phases and Photocatalytic Activity of TiO_2. *Angew. Chem. Int. Ed.* **2008**, *47*, 1766–1769.
(67) Gao, Y.; Zhu, J.; An, H.; Yan, P.; Huang, B.; Chen, R.; Fan, F.; Li, C. Directly Probing Charge Separation at Interface of TiO_2 Phase Junction. *J. Phys. Chem. Lett.* **2017**, *8*, 1419–1423.
(68) Kullgren, J.; Huy, H. A.; Aradi, B. L.; Frauenheim, T.; De k, P. Theoretical Study of Charge Separation at the Rutile-Anatase Interface. *Phys. Status Solidi RRL* **2014**, *8*, 566–570.
(69) Kullgren, J.; Aradi, B.; Frauenheim, T.; Kavan, L.; Deák, P. Resolving the Controversy About the Band Alignment Between Rutile and Anatase: the Role of OH –/H +Adsorption. *J. Phys. Chem. C* **2015**, *119*, 21952–21958.
(70) Nosaka, Y.; Nosaka, A. Y. Reconsideration of Intrinsic Band Alignments Within Anatase and Rutile TiO_2. *J. Phys. Chem. Lett.* **2016**, *7*, 431–434.
(71) Shao, R.; Wang, C.; McCready, D. E.; Droubay, T. C.; Chambers, S. A. Growth and Structure of MBE Grown TiO_2 Anatase Films with Rutile Nano-Crystallites. *Surf. Sci.* **2007**, *601*, 1582–1589.
(72) Atrei, A.; Cortigiani, B.; Ferrari, A. M. Epitaxial Growth of TiO_2 Films with the Rutile (110) Structure on Ag (100). *Rep. Prog. Phys.* **2012**, *24*.
(73) Deskins, N. A.; Kerisit, S.; Rosso, K. M.; Dupuis, M. Molecular Dynamics Characterization of Rutile-Anatase Interfaces. *J. Phys. Chem. C* **2007**, *111*, 9290–9298.
(74) Nolan, M.; Deskins, N. A.; Schwartzenberg, K. C.; Gray, K. A. Local Interfacial Structure Influences Charge Localization in Titania Composites: Beyond the Band Alignment Paradigm. *J. Phys. Chem. C* **2016**, *120*, 1808–1815.
(75) Hosono, E.; Fujihara, S.; Imai, H.; Honma, I.; Masaki, I.; Zhou, H. One-Step Synthesis of Nano–Micro Chestnut TiO_2 With Rutile Nanopins on the Microanatase Octahedron. *ACS Nano* **2007**, *1*, 273–278.
(76) Penn, R. L.; Banfield, J. F. Imperfect Oriented Attachment: Dislocation Generation in Defect-Free Nanocrystals. *Science* **1998**, *281*, 969–971.
(77) Jovic, V.; Smith, K. E.; Idriss, H.; Waterhouse, G. I. N. Heterojunction Synergies in Titania-Supported Gold Photocatalysts: Implications for Solar Hydrogen Production. *ChemSusChem* **2015**, *8*, 2551–2559.
(78) Le Chen; Grapham, M. E.; Li, G.; Gray, K. A. Fabricating Highly Active Mixed Phase TiO_2 Photocatalysts by Reactive DC Magnetron Sputter Deposition. *Thin Solid Films* **2006**, *515*, 1176–1181.

CHAPTER 2

2.0 Theoretical Aspects of Instrumentation

This Chapter provides a theoretical overview of the experimental techniques used in this thesis. These include the principal technique of scanning tunneling microscopy (STM) used in all experimental Chapters (4-6) and low energy electron diffraction (LEED) employed in Chapter 5. In Chapter 6 X-ray Photoelectron Spectroscopy (XPS) is used to study adsorbed ethanol and photocatalytic surface intermediates. Quadrupole mass spectrometry (QMS) used in Chapter 6 is not discussed and a brief explanation of this technique is included in Chapter 3.

2.1 Electron Spectroscopy

In electron spectroscopy the energy and angular distribution of electrons emitted from surfaces after irradiation by either photons (utilising the photoelectron effect), electrons or other particles are measured.[1] Electron spectroscopy was used here to determine surface cleanliness via its chemical sensitivity. X-ray Photoelectron Spectroscopy (XPS) was used to study the adsorption of ethanol on anatase TiO_2(101) and to determine the identity of species adsorbed on the surface after UV light exposure in the presence of oxygen.

The surface sensitivity of XPS, Auger and Low energy electron diffraction (LEED) are determined by the inelastic mean free path (IMFP) of electrons (how far an electron travels before losing energy). The IMFP is sensitive to the electron's energy and relatively insensitive to the identity of the solid (metal oxide, metal, semiconductor). The IMFP, λ_M, as a function of energy is defined by a universal curve which is a function fitted to empirical data, expressed by Seah and Dench[2] as:

$$\lambda_M = c_0 E^{-2} + c_1 (lE)^{1/2}, \qquad \text{Eqs. 2.1}$$

where E is the kinetic energy of the electron in eV. For metal oxides (inorganic compounds), the material parameters are c_0 = 2170 and c_1 = 0.72. In this equation, l is the monolayer thickness in nm. As shown in **Figure 2.1** (grey shaded box), the IMFP has a value of ~1 nm between 10-500 eV. This electron energy range encompasses Auger electrons, photoelectrons emitted in XPS and elastically scattered electrons in LEED and therefore these techniques are surface sensitive.

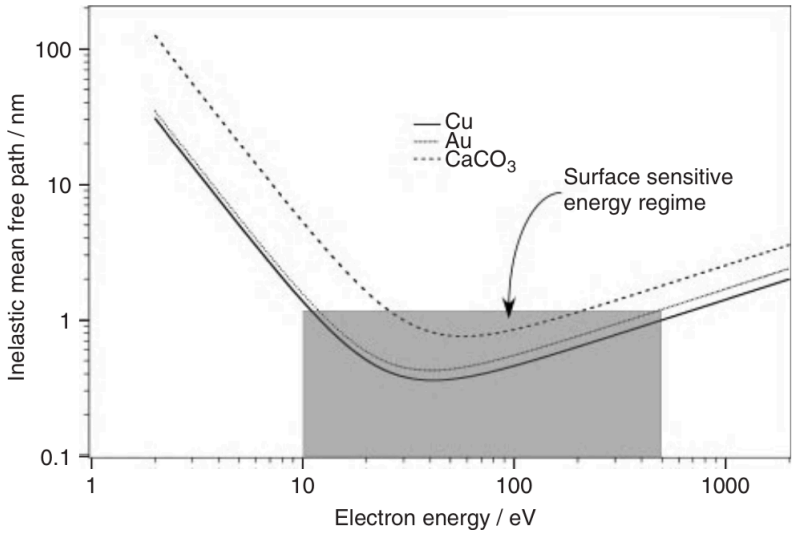

Figure 2.1: The universal curve of the inelastic mean free path (IMFP) (nm) of electrons as a function of energy (eV). Displayed are functions for Cu (black line), Au (grey dashed line) and $CaCO_3$ (black dashed line). The filled grey box indicates the surface sensitive 1 nm IMFP region (10-500 eV). Adapted from reference.[1]

2.2 X-Ray Photoelectron Spectroscopy (XPS)

In XPS, the energy of the photoelectrons emitted through the interaction of X-rays with the atoms core electrons are studied. The X-ray photon energy must be greater than the binding energy of the electron. The photon is absorbed with the remaining energy minus a work function term, transferred to the photoelectron, which then reaches the vacuum level and is detected. This leads to the inference of the electrons core level energy by the measurement of the electrons kinetic energy.[1] The photon energy of the core level can be expressed as: [3]

$$h\nu = E_B + E_{K,XPS} + \phi, \qquad \text{Eqs. 2.2}$$

where $h\nu$ (planck's constant × frequency) is the photon energy, E_B the electron binding energy referenced to the surface Fermi level E_F, $E_{K,XPS}$ the photon-electron's kinetic energy and ϕ is a work function term, whose precise value depends on the spectrometer and sample.[3] The electron binding energy is sensitive to the atom's environment, resulting in a 'chemical shift' in energy where E_B is modulated by the changes in the positive charge on the atom. An increase of positive charge (decrease in electron density) leads to an increase in binding energy. The binding energy of all core levels changes by the approximately same amount.[3] Within this thesis the C1s orbital of carbon of CH_3CH_2OH(a) on anatase TiO_2(101) is studied, where the two carbon environments (-CH_3, -CH_2) can be resolved and the formation of a third -COOH is detected.

An XPS peak is a convolution of a Lorentian and Gaussian functions.[3] These take into account the inherent XPS peak width (Lorentian) and aspects of the instrumentation (Gaussian) in obtaining the XPS spectrum. The latter includes: photon source, thermal broadening and the analyser. The inherent peak width of a core level, Γ, is defined by the Heisenberg uncertainty principle as: [4]

$$\Gamma \approx \frac{\hbar}{\tau}, \qquad \text{Eqs. 2.3}$$

where $\hbar = h/2\pi$, and τ is the core hole lifetime.

The first few layers (10-20 Å) of the surface are sampled in XPS due to the photoelectron IMFP/escape depth, as defined in **Figure 2.1**; where photoelectrons emitted at a greater depth are lost through interaction with the material. Using knowledge of the materials escape depth, the thickness of a film deposited on a surface can be determined.

Atomic electronic state energies are determined by the principal quantum number *n* and angular momentum contributions. The Russell-Saunders scheme for coupling of spin and orbital angular momentum involves a vector sum $j = l + s$, where l is the orbital angular momentum term and *s* the spin term. If the core orbital $l > 0$ such as p, d, f orbitals, there will be two initial states corresponding to $l \pm ½$. The shells are labelled by *n*: (1, 2, 3, 4): K, L, M, N and the angular momentum *j* is defined by the subscript. The 1st shell is K_1 (1s) the second shell is L_1 (2s) L_2 ($2p_{1/2}$) and L_3($2p_{3/2}$). This fine structure is apparent by the presence of doublets in the photoelectron spectrum.[1]

2.3 Auger Electron Spectroscopy (AES)

The secondary electrons emitted from atoms, after ionisation of a core electron by irradiation (ions, electrons, X-rays), are known as Auger electrons. The technique bears the name of Pierre Auger who first described the process in 1925[5]; although it was independently discovered by Lise Meitner.[6] In Auger electron spectroscopy (AES), peaks within the secondary electron distribution emitted from a surface as a function of energy are studied.

In the AES conducted in this thesis the exciting source was an electron beam, which was also shared by the LEED optics. In this measurement, the energy region of ~ 30-1000 eV was analysed, where Auger peaks are present. The energy of an Auger electron after removal of the K_1 level electron can be expressed for a $K_1L_1L_{2,3}$ transition as:

$$E_{K_1L_1L_{2,3}} = E_{K_1} - E_{L1} - E_{L_{2,3}} - \phi, \qquad \text{Eqs. 2.4}$$

where $E_{K_1L_1L_{2,3}}$ is the energy of Auger electron, E_{K_1} is the K_1 energy level, E_{L1} is the L_1 energy level, $E_{L_{2,3}}$ the $L_{2,3}$ energy level and ϕ the work function.

After the intra-electron transfer and emission of an electron, a doubly charged atom results. In fact, a cascade effect involving multiple further Auger processes can lead to highly

charged atoms. In Eqs. 2.4, the energies are with respect to the surface E_F and a surface work function term is included. A more precise form includes terms to represent the relaxation of electrons resulting from the presence of core level holes.[3] **Figure 2.2** displays a $K_1L_1L_{2,3}$ Auger transition, where after removal of a K_1 electron, a photon (red arrow) or Auger electron (green arrow) can be emitted, the emission of a photon is referred to as X-ray fluorescence.

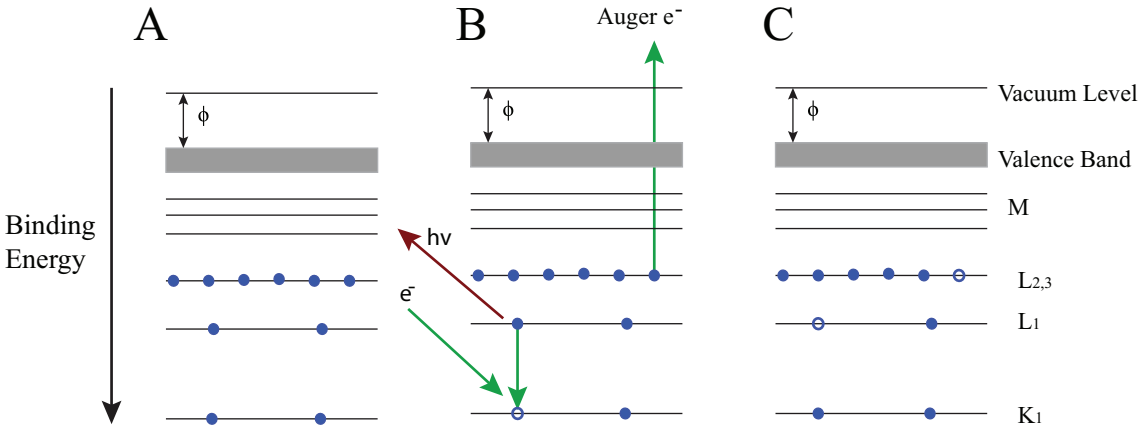

Figure 2.2 A detailed schematic of the Auger process involving three core levels (K_1, L_1, $L_{2,3}$). An electron removes the K_1 electron. (**A**) The filled electron levels of the atom (**B**) The atom after removal of a core K electron with emission of a photon or Auger electron indicated. (**C**) The atom following the emission of the $L_{2,3}$ electron. Adapted from reference.[1]

The energy of the Auger electron, as indicated by Eqs. 2.4, is independent of the energy of the exciting source. However, the ionisation cross-section for a core level is dependent on the energy, typically at a maximum at 4-5 times the core level binding energy.[3] The AES employed in this study used a 3 kV electron source. As the atomic number of the element increases, the possible energy of Auger electrons increases. This complexity is mitigated by the probability of photon fluorescence increasing with binding energy, reducing the observed Auger peaks.[3]

In addition, a large broad intensity towards 0 eV is present on the secondary electron spectrum. This broad peak results from excitations resulting from secondary electrons; removing other electrons within the inelastic mean free path escape depth. Additionally, there are ionization loss, plasmon loss and diffraction features present in the electron energy spectrum.[3]

2.4 Low Energy Electron Diffraction (LEED)

Low energy electron diffraction (LEED) is arguably the first technique of surface science. It was discovered by Davisson and Germer in the 1920s; who by accident formed multiple large crystalline nickel domains on a nickel target, which provided a diffraction pattern by electron bombardment.[7] This was before the discovery of the wave nature of the electron and thus its first demonstration. Davisson and Thomson received the 1937 Nobel Prize in physics for their work on LEED. This technique was employed in this thesis for experimental work conducted with the *Omicron* AFM/STM chamber, for; i) single crystal sample preparation; ii) surface structural analysis of thin titania films grown on single crystal tungsten W(100).

In LEED, a monochromatic electron beam (30-150 eV) is directed to the sample and the elastic peak within the secondary electron spectrum from the sample is filtered and analysed. At these energies the electrons wavelength is comparable to the atom spacing in the surface lattice and periodic diffraction occurs.[8] This relationship is demonstrated by the de-Broglie wavelength of an electron, defined by:

$$\lambda(\text{Å}) = \left(\frac{150.4(\text{Å}^2\text{eV})}{E(\text{eV})}\right)^{0.5} \quad , \qquad \text{Eqs. 2.5}$$

where E is the beam energy in eV and λ is the electron wavelength in Å. For energies of 30-150 eV, λ is 3-1 Å. In LEED, surface sensitivity results from the IMFP of the electrons (**Figure 2.1**).[1] This reduces the depth that scattered electrons can return elastically to the detector (fluorescent screen). At an energy of 100 eV, the IMFP is ~5 Å, approximately one to two stepped layers of the anatase TiO_2(101) and W(100) surfaces studied in this thesis.[9]

Surface diffraction can be explained using a one-dimensional (1D) periodic arrangement of atoms of separation *a* (**Figure 2.3**). For two parallel electron paths at an incident angle θ_i, and the diffraction angle θ_d, separated by *a*, the total path difference between two parallel diffracted outgoing electrons θ_d can be determined by two $a.\sin(\theta)$ products which is: [8]

$$|\Delta P| = |\Delta P_1 - \Delta P_2| = |a(\sin(\theta_i) - \sin(\theta_d))| \quad , \qquad \text{Eqs. 2.6}$$

where ΔP is the total path difference and the component path differences ΔP_1 and ΔP_2 are expressed as a function of sine function of incidence θ_i and diffracted angle θ_d and lattice spacing a. ΔP_1 and ΔP_2 are defined by the bold arrows in **Figure 2.3**. For constructive interference the path difference must be equal to an nλ, where n is an integer to fulfil the Bragg condition,[10] which is:

$$\left|a\left(\frac{\sin(\theta_i)}{\lambda} - \frac{\sin(\theta_d)}{\lambda}\right)\right| = |n| \quad , \qquad \text{Eqs. 2.7}$$

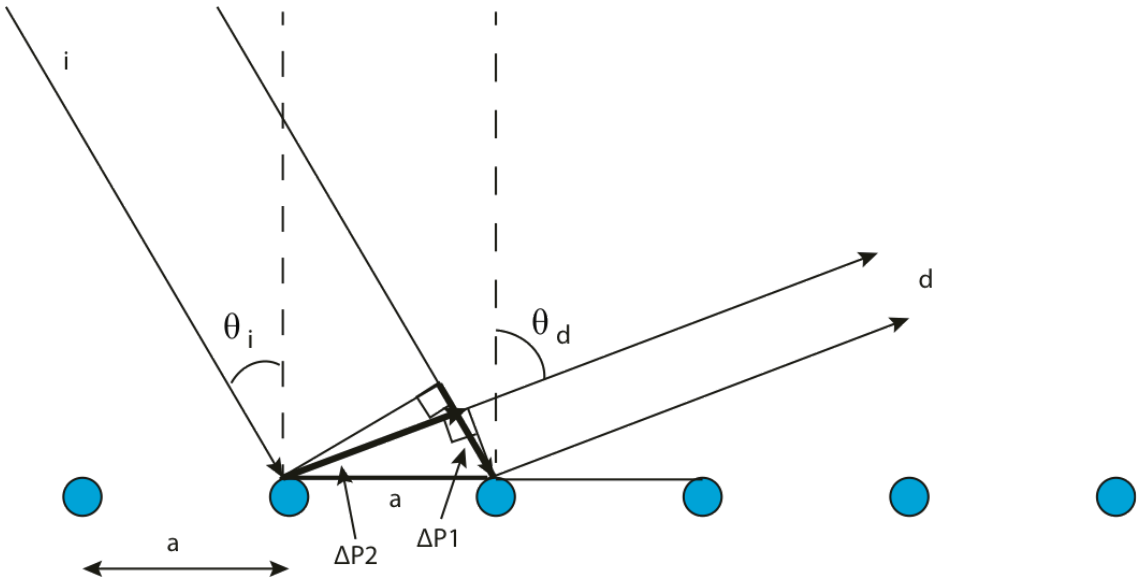

Figure 2.3: A one-dimensional (1D) arrangement of atoms (blue filled circles) separated by *a*, from which interference between two incident electrons occurs. The path difference is determined by the difference between *a* sin(θ_i) and *a* sin(θ_d) (bold black lines).

The components parallel to the surface for the incident and diffracted waves can also be expressed in wave vector form with direction and magnitude as:[8]

$$k\|_i = \frac{2\pi}{\lambda}\sin(\theta_i) \text{ and } k\|_d = \frac{2\pi}{\lambda}\sin(\theta_d) \quad , \qquad \text{Eqs. 2.8}$$

where the two waves undergoing interference are parallel and the incident and diffracted angles are defined. Therefore the Bragg condition (Eqs. 2.7) can be expressed as:

$$2\pi\left(\frac{\sin(\theta_i)}{\lambda} - \frac{sin(\theta_d)}{\lambda}\right) = \frac{2\pi n}{a} \quad , \qquad \text{Eqs. 2.9}$$

Or after substitution as:

$$k_{\|i} - k_{\|d} = \left(\frac{2\pi}{a}\right) n \quad , \qquad \text{Eqs. 2.10}$$

This results in a difference in the wave vectors equal to $\left(\frac{2\pi}{a}\right) n$, where $\frac{2\pi}{a} = a^*$is identified as the reciprocal lattice vector.

For the situation where the θ_i=0, Eqs. 2.9 reduces to the familiar Bragg expression:[10]

$$asin\theta_d = n\,\lambda \quad , \qquad \text{Eqs. 2.11}$$

This analysis can be demonstrated to also show the Bragg reflection condition in the orthogonal surface direction and the resulting spots result in the inference of the $\frac{2\pi}{b} = b^*$.

Up to now we have only considered a 1D surface. The incident wave vector has a component perpendicular and parallel to the surface plane, expressed as:

$$k_i = k_{i_\perp} + k_{i_\|} \quad , \qquad \text{Eqs. 2.12}$$

where $k_{i_\perp}$is the component perpendicular to the surface and $k_{i_\|}$ is the component parallel to the surface. The magnitude of the elastically scattered LEED electron wave vector is conserved,

where $k_i{}^2 = k_d^2$. In addition the conservation of momentum for diffraction from a 2D lattice results in:

$$k_{i_\parallel} = k_{d_\parallel} + g_{hk} \quad , \qquad \text{Eqs. 2.13}$$

where $k_{d_\parallel}$ is the diffracted component parallel to the surface and g_{hk} the surface lattice vector. This is an equivalent statement to the Bragg law. The 2D surface reciprocal lattice vector, g_{hk}, neglecting the partial order in the l (g_{hkl}) crystallographic direction is expressed as:[11]

$$g_{hk} = \mathrm{ha}^* + \mathrm{kb}^* \quad , \qquad \text{Eqs. 2.14}$$

where the reciprocal lattice vectors a^* and b^* are defined in terms of real lattice vectors as:[11]

$$a^* = 2\pi \frac{b \times n}{|a \times b|} \quad , \quad b^* = 2\pi \frac{n \times a}{|a \times b|} \quad , \qquad \text{Eqs. 2.15, Eqs. 2.16}$$

where n is a unit vector perpendicular to the surface. It follows from the mathematical relationships that $a^*$and b^* must be in the sample plane and a^* is perpendicular to b and b^* perpendicular to a. Evaluation of Eqs 2.15 and 2.16 leads to an expression for the reciprocal lengths as:

$$|a^*| = \frac{2\pi}{a \sin\theta} \quad , \qquad \text{Eqs. 2.17}$$

where θ is the angle between a and b.

Therefore the real space (a, b) representation of crystal surface can be obtained from the reciprocal space (a^*, b^*) LEED diffraction pattern. A simulation of the intensity of the diffraction spots in LEED with a model surface selvedge of a few atomic layers thick as a function of electron beam energy can be used model the surface structures. This is known as I-V LEED such a method is not employed for the work conducted in this thesis.[8]

2.5 Scanning Tunneling Microscopy

2.5.1 Introduction

Scanning Tunneling Microscopy (STM) is the principal experimental technique in this work, forming a core component of Chapters 4-6. The STM was invented in 1981 by Binnig and Rohrer;[12,13] for which they received the Nobel prize in Physics in 1986. They applied the existing technologies of the piezoelectric effect in certain materials and feedback control electronics, utilizing electron tunneling to create an atomically resolving microscope.

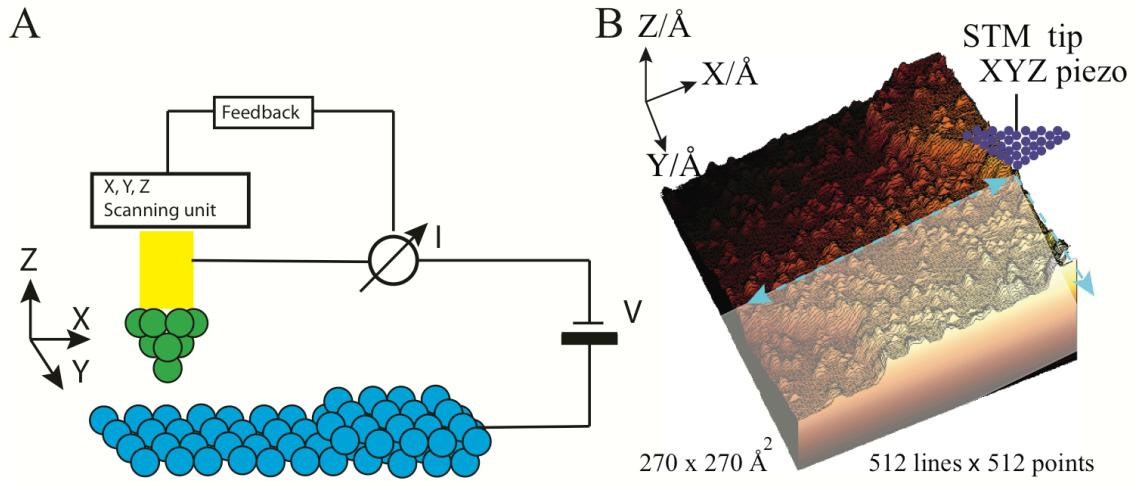

Figure 2.4: **(A)** A schematic of the STM. A tip (green spheres) with an atomically sharp apex is in tunneling contact with the surface (blue spheres). The tip height (Z) is controlled by a feedback loop, controlling the voltage applied to the z-piezoelectric. A bias voltage (v) is applied and a current flows. Lateral motion (X, Y) results in a measurement to the surface topology. Adapted from reference.[14] (**B**) A 3D 270 × 270 Å^2 STM image (+2 V sample bias, 0.08 nA) of EtOH / anatase TiO_2(101) (512 points × 512 lines). The purple triangle of circles represents the positions of the tip. The dashed blue arrows indicate the path the tip takes. The slightly opaque area is yet to be imaged. The Z, X, Y (Å) directions are identified by the blue dashed arrows.

In brief, in STM a sharp metallic tip is brought to within 5-10 Å of a surface, at which point a small tunneling current (1 nA) can flow if a bias voltage is applied between a conducting sample and the metallic tip, dependent on the conductance at that point.[14] The tip's *z*-axis position is controlled by the voltage applied to the piezoelectric drive. A simplified diagram of the STM is shown in **Figure 2.4A**. An example STM image of anatase TiO_2(101) is shown in **Figure 2.4B** of an area 270 × 270 Å^2. The scanning unit is rastered laterally on the surface

(**Figure 2.4B**) and a *z-x* trace of topographical height, converted by calibration from the piezo-voltage, is obtained. The tip is moved an incremental distance in the *y* direction and another line is recorded. An image is formed from the collection of lines. An identical path is retraced forward and back with the image formed only of forward (or back) lines to prevent image distortion from creep and hysteresis.[14]

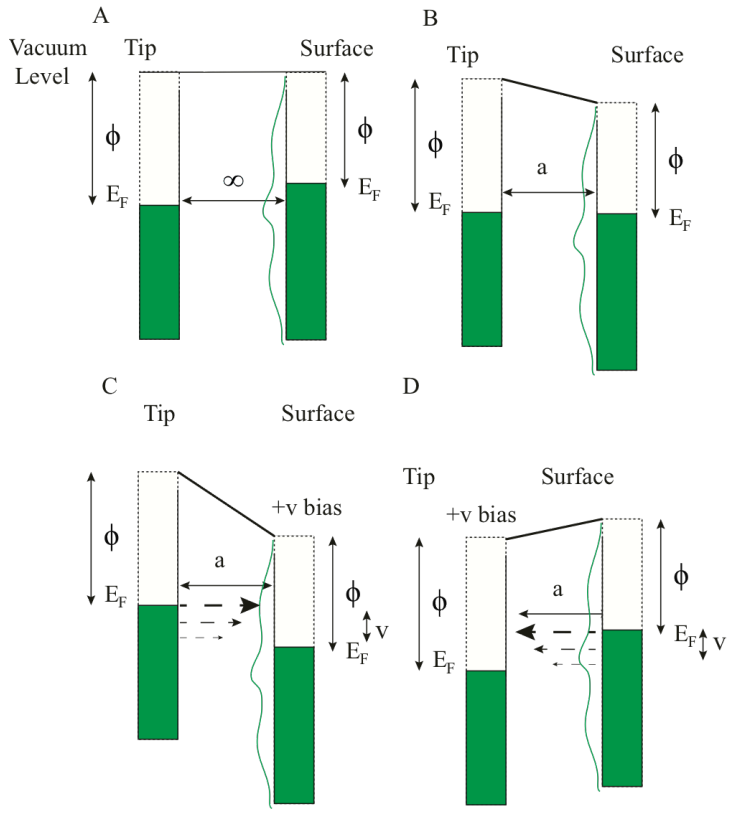

Figure 2.5: A simple model displaying the band structure of a metallic tip and surface with non-identical work functions ϕ (Vacuum level – E_F). (**A**) At infinite separation. (**B**) In contact at separation of *a*. (**C**) With a small positive bias V applied to the sample at separation *a*. (**D**) In contact with a small positive bias V applied to the tip. The direction of electron tunneling though the potential barrier is indicated by the black dashed arrows, greatest at the Fermi level (E_F) and decreasing in magnitude (smaller dashed arrows). Green filled square indicate the filled electron states and white squares are empty states. The green line indicates the population of surface states.

Shown in **Figure 2.5** is a simple band structure model of a metallic tip and surface with non-identical work functions. These are shown at an infinite separation (**Figure 2.5A**) where the vacuum level is shared. After electrical contact at separation *a* the Fermi levels E_F are aligned (**Figure 2.5B**). When a positive voltage bias V is applied to the surface (**Figure 2.5C**), filled states of the tip become aligned with empty surface states and vice versa for the negative

surface bias (**Figure 2.5D**). In the STM model, there is a potential barrier V between the tip and sample. Classically, this region cannot be crossed since the energy of the particle E is less than V. However electrons can tunnel elastically into the opposing state without being excited above the barrier. Due to the Pauli exclusion principle,[4] electrons can only travel from filled to empty states between the two electrodes.

Considering a one dimensional electron wavefunction in the z-direction crossing a square potential barrier V(z); where V(z) = V_0 inside the barrier (0 < z < a). The time independent solution to the Schrödinger equation within the barrier region has the decaying form of:[4]

$$\psi(z) \propto e^{i\kappa z} \quad , \qquad \text{Eqs. 2.18}$$

where $\kappa = \{2m(V_0 - E)/\hbar^2\}^{1/2}$, is a decay constant and m is the electron mass. The tunneling current is proportional to the magnitude of the wavefunction at the right hand side of the barrier. A transmission probability T can be expressed as the ratio of the square at boundaries, 0 and a, which has the form:

$$T = \frac{|\psi(a|^2}{|\psi(0)|^2} \propto e^{-2\kappa a} \quad , \qquad \text{Eqs. 2.19}$$

where a is the separation between the surface and tip. As V_0 can be considered as the vacuum level, for electrons at the Fermi level, $V_0 - E$ is interpreted as the surface work function, ϕ. The transmission probability, for a metal with a ϕ of a few eV (4.5 eV) results in κa having a value of 2 Å^{-1}. Therefore a change in a of 1 Å leads to an order of magnitude change in T.[14] This leads to a huge sensitivity in tunneling current with separation between the tip and sample resulting in the tunneling current occurring mainly through the single atom at the tip apex and explains ultimately how atomic resolution can be achieved. This simple model can be used to explain the behaviour over large features on the 10-20 Å scale. However, in order to understand STM, a more complex theory is required.

2.5.2 Tersoff and Hamman Theory of STM

Bardeen perturbation theory when applied to tunneling in STM considers the tip barrier region and sample barrier region as separate electronic systems.[15] This theory pre-dates STM. Here a tunneling junction is formed of planar electrodes in a metal-insulator-metal junction. The electronic states for the tip (μ) and surface (ν) are solved independently with the time independent Schrödinger equation and the tunneling of electrons between the tip and sample is represented by time dependent quantum mechanical perturbation theory.[4] An expression for the tunneling current from first order perturbation theory is:[16]

$$I = \frac{2\pi|e|}{\hbar} f(E_\mu) - f(E_\nu)\left|M_{\mu,\nu}\right|^2 \delta(E_\nu + |e|V - E_\mu), \qquad \text{Eqs. 2.20}$$

where $M_{\mu,\nu}$ is a matrix element between the surface ψ_ν and tip ψ_μ, E_ν is the energy of the surface electronic state relative to the sample Fermi level ($E_{\text{F, sample}}$) and E_μ is the tip energy relative to the tip Fermi level ($E_{\text{F, tip}}$), $\delta(E_\nu + eV - E_u)$ is a Dirac delta function which is zero if $E_\mu \neq E_\nu$ + |e|V and unity if $E_\mu = E_\nu$ + |e|V. The Fermi function $f(E_u)$ accounts for temperatures above 0 K, where the Fermi-Dirac distribution of states, relative to the Fermi level is applied, $f(E - E_F) = \frac{1}{1+\exp\left[\frac{E-E_F}{K_B T}\right]}$. At the Fermi level $f(E - E_F) = 0.5$ and tails off exponentially as E increases. In the zero temperature limit the electronic states are filled up to the Fermi level and empty above.

At low bias voltage, Eqs. 2.20 can be reduced to:

$$I = \frac{2\pi|e|^2 V}{\hbar} \sum_{\mu,\nu}\left|M_{\mu,\nu}\right|^2 \delta(E_\nu - E_F)\delta(E_\mu - E_F), \qquad \text{Eqs. 2.21}$$

. where the summation of the delta function $\sum_{\mu,\upsilon} \delta(E_{\mu,\upsilon} - E_F) = \rho(E)_{\mu,\upsilon}$ is equivalent to the density of states (DOS) of the sample or tip; distribution functions which describe the number of states in an energy range between E and $E + dE$. The sample Fermi level ($E_{F,sample}$) is the

reference point for both.[14] $M_{\mu,v}$ is an integral equation performed over a separation surface S entirely within the barrier region and separating the two halves of the electrodes (tip and sample) wavefunction ψ_μ and ψ_v and defined by Bardeen[17] as:

$$M_{\mu,v} = \frac{\hbar}{2m}\int dS \ .(\psi_\mu^* \nabla\psi_v - \ \psi_v \nabla\psi_\mu^*), \qquad \text{Eqs. 2.22}$$

where ∇ indicates the partial differentiation of the wavefunction.

Tersoff and Hamann adapted the Bardeen model to represent a three dimensional real surface and tip tunneling phenomenon, not simply planar electrodes.[18] This is achieved by neglecting the energy dependence in the matrix element. The tip is modeled as a mathematical point source at r_t from the surface, (**Figure 2.6**). Evaluation of the matrix element results in the current (Eqs. 2.21) being approximated as:

$$I \ \propto \ \sum_v |\psi_v(r_t)|^2 \delta(E_v - E_F) \equiv \rho_{sample}(E_F, r_t) \qquad , \qquad \text{Eqs. 2.23}$$

where $|\psi_v(r_t)|^2 \delta(E_v - E_F)$ describes the surface density of states at the position of the tip at a distance r_t from the surface restricted to the Fermi level E_F. The wave function of the surface is therefore determined at a plane above the surface at r_t. The tip itself is defined as an spherically symmetric s-wave tip. This defines the local density of states (LDOS), $\rho_{sample}(E_F, r_t)$ at the Fermi level of the tip E_F. Therefore the geometric structure or charge density are not directly measured, but the DOS at energy E_F.

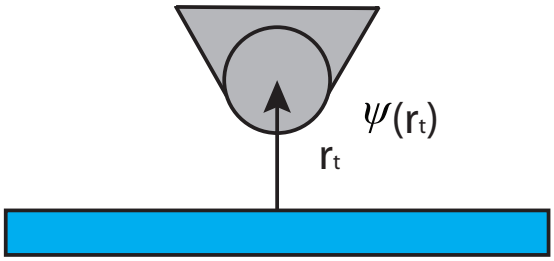

Figure 2.6: Schematic of the Tersoff-Hamann approximation: the STM tip (grey sphere) is modeled as a locally spherical potential, radius of curvature *R* centered at distance r_t above the surface (blue rectangle) with wavefunction $\psi(r_t)$. Adapted from reference.[18]

This theory neglects the tip-sample interaction, evaluating the surface electronic structure in the absence of the tip. It also assumes a low bias voltage with the tip required to be an spherically symmetric wave function with the probability of the surface function evaluated at the centre (r_t). At higher bias, tunneling from states below the Fermi level cannot be neglected. This theory is valid for large tip-sample distances (~6 Å) and can explain resolution of large features but fails to explain observed atomic resolution on metal and semiconductor surfaces.

In the range of 1-3 V bias as used in STM performed in this thesis Eqs. 2.23 can be extended beyond the sample E_F and an expression of the form results:

$$I \approx \int_{E_F}^{E_F+|e|V} \rho_{sample}(E_F, r_t)dE \quad , \qquad \text{Eqs. 2.24}$$

where the integration of LDOS is performed in the region E_F to E_F + eV. This is acceptable as long as the bias voltage is still less than the work function of the surface. Problems arise due to the energy dependence of matrix element and tip density of states. To determine the current at higher bias is the simper Wentzel-Kramers-Brillouin (WKB) model can also be used.[19] This approximates the two electrodes as being planar surfaces. An expression is:

$$I = \int_0^{eV} \rho_{sample}(r, E)\rho_{tip}(r, +eV - E)T(E, eV, r)dE \quad , \qquad \text{Eqs. 2.25}$$

where $\rho_{sample}(r, E)$ and $\rho_{tip}(r, +eV - E)$ are the density of states of sample and tip

respectively with respect to their own Fermi level for a positive sample bias. The bias is eV and energy E is measured from the sample Fermi level. The energy dependent transmission probability $T(E, eV, r)$ is included, derived from the matrix element and it is of the form:

$$T(E, eV, r) = exp\left(\frac{-2z\sqrt{2m}}{\hbar}\sqrt{\frac{\phi_s+\phi_t}{2}+\frac{eV}{2}}-E\right), \quad \text{Eqs. 2.26}$$

where here z is the separation between the tip and surface, m is the electron mass, $\frac{\phi_s+\phi_t}{2}$ is the average work function to approximate the trapezoidal barrier, and eV and E the bias and energy of an elastic tunneling electron. Under positive sample bias (eV > 0), for the images presented in this thesis, a maximum in $T(E, eV, r)$ occurs at E = 0, corresponding to tunneling from the Fermi level of the tip.

2.5.3 Lang's Model and STM of Surface Adsorbates

Adsorbates typically appear as some deviation in the topographic height compared to the bare surface centred at their location on the surface. The interpretation of the height and lateral location is problematic; when appearing as a protrusion the apparent height is often lower than the real adsorbate height. Also, in general adsorbates can display an STM contrast dependent on their orientation, surface density and on the tunneling condition of bias voltage as well as the tip apex. Several good reviews of theoretical approaches on metal and semiconducting surface exist.[20,21] Lang developed a theory to explain the STM's response to single adsorbed atoms on a metal surface as imaged by a metallic tip.[22,23] In his theory the Bardeen approach is used to model the tunneling current density across the surface of the two planar electrodes in a small bias voltage range; with the Jellium model used for the metal surfaces.[24] The current density J(r) (r = separation between electrodes) is a function of the time independent wave function $\Psi_{\mu,v}(r, t)$ in the vacuum region for tip and sample. Lang modelled a

Na atom on one electrode as it traversed adsorbate atoms on the other electrode (Na, S, He) (**Figure 2.7**); the J(r) demonstrated a strong dependence with a negative depression in the He case. An evaluation of the density of states at the Fermi level (metal + adsorbate) indicated that the He closed shell polarises states away from the Fermi level. Additionally, the apparent height in STM reflects the LDOS at the Fermi level and is not directly reflective of the periodic geometrical structure. For example, the TiO_2(110) surface provides a relevant example where the Ti_{5c} and bridging O_{2c} rows appear normally opposite in height to the actual structure.[25] In Chapter 6 images are presented of an organic molecule (ethanol) adsorbed on anatase TiO_2(101). The frontier orbitals of adsorbed ethanol are energetically far above the surface Fermi energy level, [26] and therefore in empty state imaging it is the tail extending to the Fermi level, which contributes to the LDOS.[20]

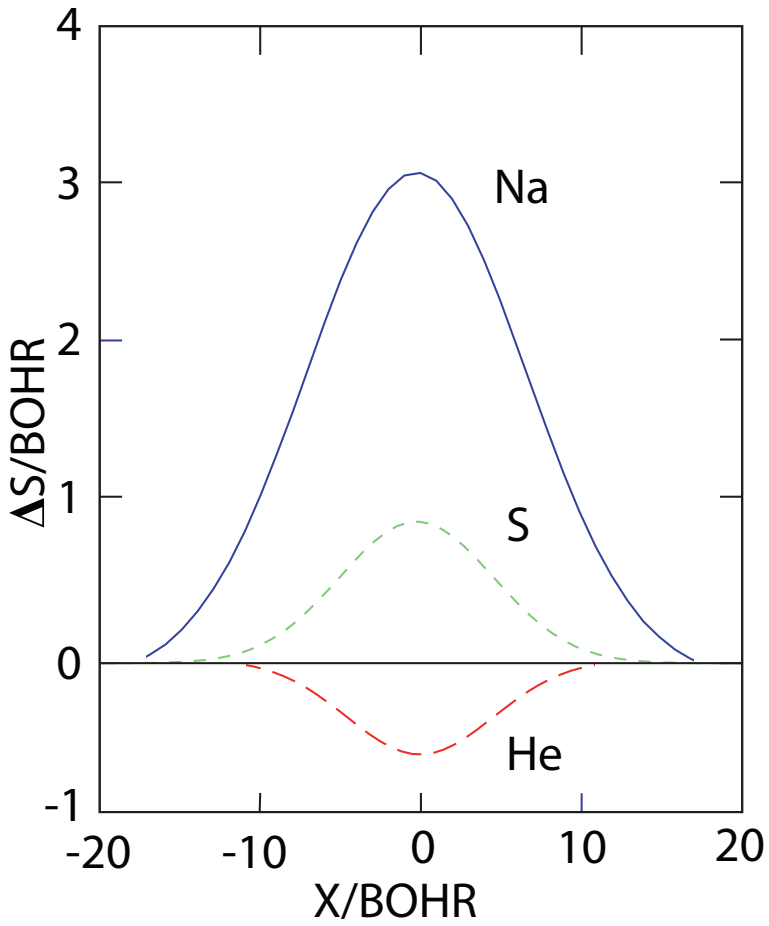

Figure 2.7: Change in tip distance ΔS with respect to lateral separation X as the Na atom at the tip apex is traversed over the adsorbates (Na, S, He), where at 0 the two atoms are coincident. Both the tip and surface φ use the Jellium model (1 Bohr = 0.529 Å). This figure was adapted from reference.[23]

2.5.4 Chen's Model

Tersoff-Hamman theory is insufficient to explain some experimental observations of STM. For example the ~ 2.5-3 Å resolution reported on metal surfaces such as Au(111)[27] was less than the predicted ~ 6 Å.[28] This is in accord with Lang who predicted that features of 10 Å diameter were resolvable.[22]

A theory of STM was developed by Chen to include a better description of the surface and tip atom wave functions, which are evaluated in the transmission matrix elements.[28] The sample wavefunctions are expanded with spherical harmonic and radial components and evaluated at the tip apex atom.[28] The form of the spherical harmonic component is dependent on the orbital considered the *l* and *m* quantum numbers e.g. orbitals: s, p_z, p_x, p_y, d_{z2}. The tunneling matrix element can therefore be evaluated with these as a linear combination of derivatives of the sample wavefunction at the tip apex.

To model the surface electronic structure of a hexagonal close packed metal surface with *p6mm* symmetry, the electronic charge density $\rho(r) = \sum_{E<Ef}|\psi(r)|^2$ structure of the surface is considered. Here *r* is the sample-tip distance parameter. In the leading Bloch waves method, $\rho(r)$ is evaluated in surface Bloch waves, which share the symmetry of the top layer atoms.[16] The charge density is evaluated and the ratio of the electron density at the corresponding location in reciprocal space can be used to define the corrugation amplitude height Δz observed in STM. For the theory to obtain the STM measured corrugation amplitude in atomically resolved images of metal surfaces, a tip sample separation of 3-6 Å and tip apex dz^2 orbital wavefunction are required. This is representative of tungsten metal tips, used in this thesis, which at the Fermi level contain 85% d-states.[28] This orbital can be positioned either on the tip or the sample atoms due to the reciprocity principle.[28] This latter principal states that if the tip and sample states are exchanged the STM image remains the same. A simplified picture is shown in **Figure 2.8**.

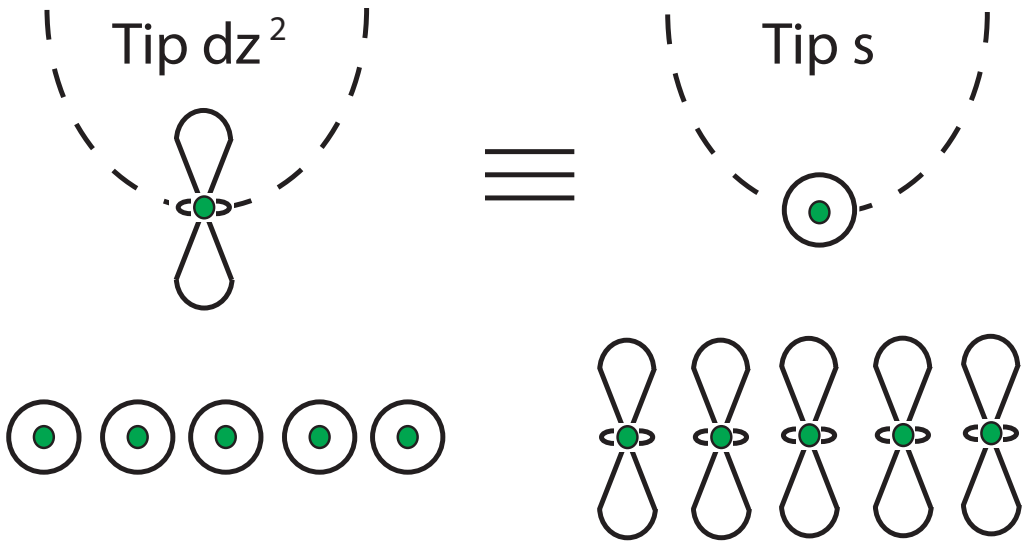

Figure 2.8: A simplified picture of the STM imaging mechanism in terms of s and dz^2 orbital surface and tip states (left) with the reverse shown on the right. This is inferred from the principal of reciprocity. Adapted from reference.[28]

2.5.5 STM of Semi-Conductors

Obtaining useful STM images of semiconductor surfaces has unique challenges compared to metallic surfaces.[29,30] One challenge is surface structure complexity, the methods of surface preparation in UHV require annealing, often requiring extensive research using other techniques to define the periodic atomic positions.[25] A bulk-truncated (1 × 1) structure does not always occur after formation of a particular surface plane and some relaxation from the structure occurs e.g rutile TiO_2(110).[31] Resolution under particular preparation conditions is often feasible, eg. on Si and TiO_2 surfaces.

The Fermi-level, by definition, is located in the energy gap (2-4 eV) between the conduction band and valance band in a semi-conductor. This results in a requirement of a sample bias of ~ +2 V (- 2 V) to tunnel into empty sample states (filled sample states).[16]

The applied potential is not completely dropped within the vacuum separating the tip and sample. In low conductive samples this potential is dropped within a space charge or depletion region below the surface, under the tip. An expression for the radius *r* at 0 V bias of this region is defined as:[32]

$$r = \sqrt{\frac{2\varepsilon kT}{q^2 N}}, \qquad \text{Eqs. 2.27}$$

where ε is the sample permittivity, N is the number density of charge carriers, k the boltzman's constant, T is the temperature and q is the charge on an electron. Therefore the space charge region reduces with the number of charge carriers. The radius value (Eqs 2.27) varies between 2-200 Å. For example Si(111) surface has a radius of ~2 Å and ZnO up to 200 Å. The magnitude of the radius provides a further resolution limitation, where semiconductors of equivalent band gaps can have different lateral resolution, due to the charge depletion region smearing out electronic details.[32,33]

2.5.6 STM of Ultrathin Metal Oxide Films

Surface science investigations of metal oxide ultrathin films (~20 Å), provide a means to circumvent some of the problems encountered on their single crystal counterparts. These include availability e.g. Anatase TiO_2 single crystals,[33] conductivity such as CeO_2[34] and allow surface analysis using bulk techniques, such as paramagnetic electron spectroscopy.[35] Insight of the fundamental properties of the ultrathin films surface can be provided and the buried metal/metal oxide interface can be investigated. For instance, the commensurability between the surfaces can be probed by periodic Moiré patterns. Additionally under certain bias voltages, the underlying substrate can be imaged.[36] Some films e.g. Fe_3O_4 have a sufficient carrier density to allow tunnelling through even thick films. Direct tunneling through a non-conductive film is possible up to a maximum thickness of 10 Å,[37] where overlap of surface and tip states occurs.

STM of ultrathin metal-oxide films supported on metal surfaces can provide the surface morphology and under certain conditions atomic resolution can be achieved. In the presence of a non-conductive film e.g. NaCl, when the Fermi level of the tip is positioned in the middle of the thin film band gap at a low bias voltage then the tunneling current passes through. The tip to sample distance is then the sum of the film and gap region, modulations in the film lead to

variations in the tunneling barrier and therefore the STM tip height.[38] In addition, the tip can penetrate the film as the voltage bias is reduced and resolution of metal oxide films has been achieved in this way.[39] In the regime of higher bias, then the tip Fermi level can be aligned with the ultrathin film CB in empty sample state imaging or ultrathin film VB in filled sample state imaging. The electrons migrate from the thin film to the metal substrate and resolution of the film can be achieved. This has been demonstrated in ceria films supported on Pt(111). Subsequent conductivity between the film and metal substrate prevents surface charging.[37]

References

(1) Kolasinski, K. W. Surface Science; John Wiley & Sons, 2012.
(2) Seah, M. P.; Dench, W. A. Quantitative Electron Spectroscopy: a Standard Data Base for Electron Inelastic Mean Free Paths in Solids. *Surf. Interface Anal.* **1979**, *1*, 1–10.
(3) Briggs, D.; Seah, M. P. Practical Surface Analysis, Auger and X-Ray Photoelectron Spectroscopy; Wiley, 1990.
(4) Atkins, P. W.; Friedman, R. S. Molecular Quantum Mechanics; Oxford University Press, 2011.
(5) Auger, P. Sur L'effet Photoélectrique Composé. *Journal de Physique et le Radium* **1925**.
(6) Meitner, L. Über Die Entstehung Der B-Strahl-Spektren Radioaktiver Substanzen. *Z. Physik* **1922**, *9*, 131–144.
(7) Davisson, C.; Germer, L. H. Diffraction of Electrons by a Crystal of Nickel. *Phys. Rev.* **1927**, *30*, 705–740.
(8) Woodruff, D. P.; Delchar, T. A. Modern Techniques of Surface Science; Cambridge University Press, 1988.
(9) Venables, J. Introduction to Surface and Thin Film Processes; Cambridge University Press, 2000.
(10) Bragg, W. H.; Bragg, W. L. The Reflections of X-Rays by Crystals. *Proc. Royal Soc. A* **1913**, *17*, 1–11.
(11) Oura, K.; Lifshits, V. G.; Saranin, A. A.; Zotov, A. V.; Katayama, M. Surface Science: an Introduction; Springer, 2003; pp. 1–451.
(12) Binnig, G.; Rohrer, H.; Gerber, C.; Weibel, E. Surface Studies by Scanning Tunneling Microscopy. *Phys. Rev. Lett.* **1982**, *49*, 57–61.
(13) Binnig, G.; Smith, D. P. E. Single-Tube Three-Dimensional Scanner for Scanning Tunneling Microscopy. *Rev. Sci. Instrum.* **1986**, *57*, 1688–1689.
(14) Voigtlaender, B. Scanning Probe Microscopy; Springer: Berlin, Heidelberg, 2015.
(15) Hurum, D. C.; Agrios, A. G.; Gray, K. A.; Rajh, T.; Thurnauer, M. C. Explaining the Enhanced Photocatalytic Activity of Degussa P25 Mixed-Phase TiO_2 Using EPR. *J. Phys. Chem. C* **2003**, *107*, 4545–4549.
(16) Wiesendanger, R.; Güntherodt, H.-J. Scanning Tunneling Microscopy III; Wiesendanger, R.; Güntherodt, H.-J., Eds.; Springer Science & Business Media: Berlin, Heidelberg, 2013; Vol. 29.
(17) Bardeen, J. Tunneling From a Many-Particle Point of View. *Phys. Rev. Lett.* **1961**, *6*, 1–3.

(18) Tersoff, J.; Hamann, D. R. Theory of the Scanning Tunneling Microscope. *Phys. Rev. B* **1985**, *31*, 805–813.
(19) Bonnell, D. Scanning Probe Microscopy and Spectroscopy; Wiley-VCH, 2000.
(20) Sautet, P. Images of Adsorbates with the Scanning Tunneling Microscope: Theoretical Approaches to the Contrast Mechanism. *Chem. Rev.* **1997**, *97*, 1097–1116.
(21) Drakova, D. Theoretical Modelling of Scanning Tunnelling Microscopy, Scanning Tunnelling Spectroscopy and Atomic Force Microscopy. *Rep. Prog. Phys.* **2001**, *64*, 205–290.
(22) Lang, N. D. Vacuum Tunneling Current From an Adsorbed Atom. *Phys. Rev. Lett.* **1985**, *55*, 1–4.
(23) Lang, N. D. Theory of Single-Atom Imaging in the Scanning Tunneling Microscope. *Phys. Rev. Lett.* **1986**, *56*, 1–4.
(24) Zangwill, A. Physics at Surfaces; Cambridge University Press, 1988.
(25) Pang, C. L.; Lindsay, R.; Thornton, G. Structure of Clean and Adsorbate-Covered Single-Crystal Rutile TiO_2 Surfaces. *Chem. Rev.* **2013**, *113*, 3887–3948.
(26) Muir, J. N.; Choi, Y.; Idriss, H. Computational Study of Ethanol Adsorption and Reaction Over Rutile TiO_2(110) Surfaces. *Phys. Chem. Chem. Phys.* **2012**, *14*, 11910–11919.
(27) Hallmark, V. M.; Chiang, S.; Rabolt, J. F.; Swalen, J. D.; Wilson, R. J. Observation of Atomic Corrugation on Au(111) by Scanning Tunneling Microscopy. *Phys. Rev. Lett.* **1987**, *59*, 2879–2882.
(28) Chen, C. J. Origin of Atomic Resolution on Metal Surfaces in Scanning Tunneling Microscopy. *Phys. Rev. Lett.* **1990**, *65*, 448–451.
(29) Neddermeyer, H. Scanning Tunneling Microscopy of Semiconductor Surfaces; Neddermeyer, H., Ed.; Springer Science & Business Media: Dordrecht, 2012; Vol. 6.
(30) Kubby, J. A.; Boland, J. J. Scanning Tunneling Microscopy of Semiconductor Surfaces. *Surf. Sci. Rep.* **1996**, *26*, 61–204.
(31) Charlton, G.; Howes, P. B.; Nicklin, C. L.; Steadman, P.; Taylor, J. S. G.; Muryn, C. A.; Harte, S. P.; Mercer, J.; McGrath, R.; Norman, D.; et al. Relaxation of TiO_2(110)-(1 × 1) Using Surface X-Ray Diffraction. *Phys. Rev. Lett.* **1997**, *78*, 495–498.
(32) Bonnell, D. A. Scanning Tunneling Microscopy and Spectroscopy of Oxide Surfaces. *Prog. Surf. Sci.* **1998**, *57*, 187–252.
(33) Diebold, U. The Surface Science of Titanium Dioxide. *Surf. Sci. Rep.* **2003**, *48*, 53–229.
(34) Esch, F.; Fabris, S.; Zhou, L.; Montini, T. Electron Localization Determines Defect Formation on Ceria Substrates. *Science* **2005**, *309*, 749–752.
(35) Gonchar, A.; Risse, T.; Freund, H.-J.; Giordano, L.; Di Valentin, C.; Pacchioni, G. Activation of Oxygen on MgO: O_2.− Radical Ion Formation on Thin, Metal-Supported MgO(001) Films. *Angew. Chem. Int. Ed.* **2011**, *50*, 2635–2638.
(36) Degen, S.; Krupski, A.; Kralj, M.; Langner, A.; Becker, C.; Sokolowski, M.; Wandelt, K. Determination of the Coincidence Lattice of an Ultra Thin Al_2O_3 Film on Ni_3Al(111). *Surf. Sci.* **2005**, *576*, L57–L64.
(37) Pacchioni, G.; Valeri, S. Oxide Ultrathin Films; Pacchioni, G.; Valeri, S., Eds.; John Wiley & Sons: Weinheim, Germany, 2012.
(38) Kulawik, M.; Nilius, N.; Rust, H. P.; Freund, H. J. Atomic Structure of Antiphase Domain Boundaries of a Thin Al_2O_3Film on NiAl(110). *Phys. Rev. Lett.* **2003**, *91*, 256101–256104.
(39) Schmid, M.; Kresse, G.; Buchsbaum, A.; Napetschnig, E.; Gritschneder, S.; Reichling, M.; Varga, P. Nanotemplate with Holes: Ultrathin Alumina on Ni_3Al(111). *Phys. Rev. Lett.* **2007**, *99*, 196104–196104.

CHAPTER 3

3.0 Aspects of Instrumentation

This chapter details aspects of the instrumentation used in the experimental work presented in this thesis (Chapters 4-6). All work was conducted in UHV and therefore a discussion of the necessary theory and instrumentation is given. Three dedicated UHV instruments used are described: i) a X-ray Photoelectron Spectroscopy (XPS) chamber; ii) a scanning tunneling microscopy (STM) and photoreaction photon stimulated desorption (PSD) quadrupole mass spectrometry (QMS) chamber and iii) an Omicron STM/AFM chamber. The intrumental details of the auxiliary equipment (low energy electron diffraction (LEED), Auger electron spectroscopy (AES), residual gas analysis (RGA)) utilised in these chambers is also detailed. Also detailed are; the UHV sample preparation methods of the titanium dioxide and tungsten single crystals; the UV light irradiation methodology and set-up used for the study of surface photoreactions and the UHV electron bombardment and metal doser instrumentation in Chapter 4 and Chapter 5 respectively. The STM tip fabrication methodology and STM image analysis procedure are also included.

3.1 Instrumentation used in Achieving UHV

In this thesis the experimental investigations and final sample preparation has been conducted entirely in ultrahigh vacuum (UHV) (base pressure 2×10^{-10} mbar). This is necessary for the work conducted here on clean metal oxide and metal single crystal surfaces for both the surface preparation and subsequent study.[1,2] Gas phase molecules at higher pressures e.g. 1.3×10^{-6} mbar quickly (1 s) adsorb and saturate a surface. This surface contamination largely prohibits the study of atomically resolved STM. In addition, the study of ultrathin film growth, controlled electron bombardment, and photon stimulated desorption (PSD) mass spectrometry are not achievable if the surface is contaminated. An equation (Eqs. 3.1) governing the surface adsorption as a function of partial pressure is: [3]

$$R = \frac{n\bar{v}}{4}\text{per unit area} = p/(2\pi mkT)^{1/2} \quad , \qquad \text{Eqs. 3.1}$$

where n is the molecular density, $\bar{v}$ is the mean speed of molecules and m is the molecular mass ($n \times 1.6605\times10^{-27}$ kg), k/ JK^{-1} is the Boltzmann constant and T/K the temperature. The arrival rate R is defined here in units of molecules.$m^{-2}s^{-1}$ where ρ is in Pascal (1 mbar = 100 Pa). The monolayer arrival time τ is dependent on the definition of the monolayer, where N_0 = 1 ML and $R.\tau = N_0$. For example, for the ideal planar anatase TiO_2(101)-(1 × 1) (Chapters 4 and 6), the ML is defined in this thesis with respect to the surface density of Ti_{5c} in the first atomic layer; which has a density of $\sim5.17\times10^{18}$ Ti m^{-2}.[1] For the example molecule CO, present in the residual vacuum, if a sticking coefficient of ~1 is assumed; the monolayer arrival time at a pressure of $\sim10^{-10}$ mbar is 17980 s (~5 hours). This indicates the necessity of UHV for careful work on these systems.

In order to achieve $\sim10^{-10}$ mbar (UHV) the instruments are constructed of custom made welded stainless steel (low carbon 304) chambers with borosilicate pyrex glass windows. These

contain flange ports to attach system components, sealed by the compression of standard conFlat copper flanges, used only once after tightening.[4] The three UHV instrumental system designs are shown in section 3.2. Materials entered into the UHV, such as Ta and Mo were chosen carefully based on their known outgassing rate under UHV to ensure a pressure of ~10^{-10} mbar.[5]

The chamber gas volume was evacuated by a series of vacuum pumps. These consisted of first roughing displacement (oiled and dry) pumps, which achieve a pressure of ~2.10^{-2} mbar.[5] Rotary vane pumps and dry pumps also provided a sufficient pressure differential behind the turbo molecular pumps. The pressure (down to 10^{-2} mbar) of the rotary behind the turbo pump was monitored with pirani pressure gauges.[5] Turbo molecular pumps (kinetic) were then used to reduce the pressure before and during bake-out, and to reduce the fast-entry load-lock (FEL) to an acceptable pressure.[4] An ion getter pump ran continuously in the systems maintaining a UHV pressure of ~10^{-10} mbar.[4] Ti sublimation pumps (TSP) were used to maintain an improved constant UHV pressure (10^{-10} mbar), than achievable by the ion pump alone.[4] The limiting chamber pressure 10^{-6}-10^{7} mbar resulting from the outgassing desorption of molecular species from internal surface areas such as water from the chamber walls necessitated a 'bake-out'; where the system was heated for 24 hours at ~410 K to desorb and evacuate the chamber to achieve 10^{-10} mbar. Components that would be subsequently elevated in temperature were heated close to the working temperature to fully outgas.

The system was vented with dry nitrogen gas during opening and samples were entered into the system using a fast entry loadlock (FEL), which was vented to atmospheric pressure with nitrogen gas. RGA quadropole mass spectrometers (QMS) analysed the residual gas composition. Pressure measurements in the UHV systems used standard Bayard-Alpert pressure gauges.[6] The measurement is proportional to the sensitivity factors of the molecules as well as the partial pressure and emission current, calibrated by the manufacturer to N_2 gas. Values are reported here with a 10%-30% error bar.[4,5]

3.2 Instrumental UHV Chambers used in this Thesis

The instruments used in this thesis are shown in **Figure 3.1,3.2**. Top down view diagrams of the chambers are shown in **Figure 3.1** and photographs in **Figure 3.2**.

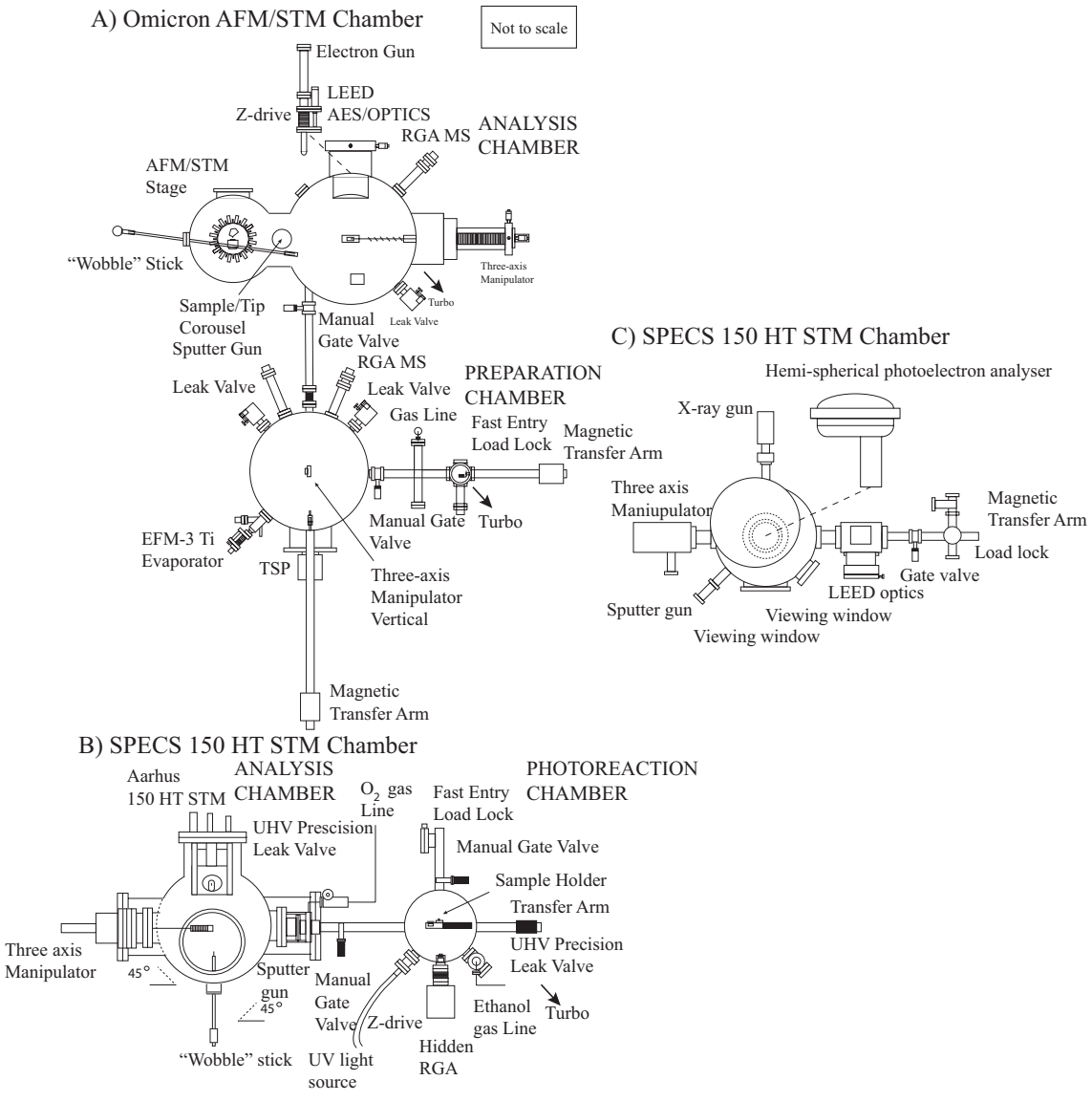

Figure 3.1: Schematic top down view drawings of: (**A**) the UHV preparation chamber and analysis chamber of the *Omicron* AFM/STM system; (**B**) the UHV *SPECS* HT-150 Aarhus STM analysis/preparation chamber and photoreaction chamber. (**C**) Schematic top down view of the *Scienta* XPS chamber. All system devices used in this thesis are represented here.

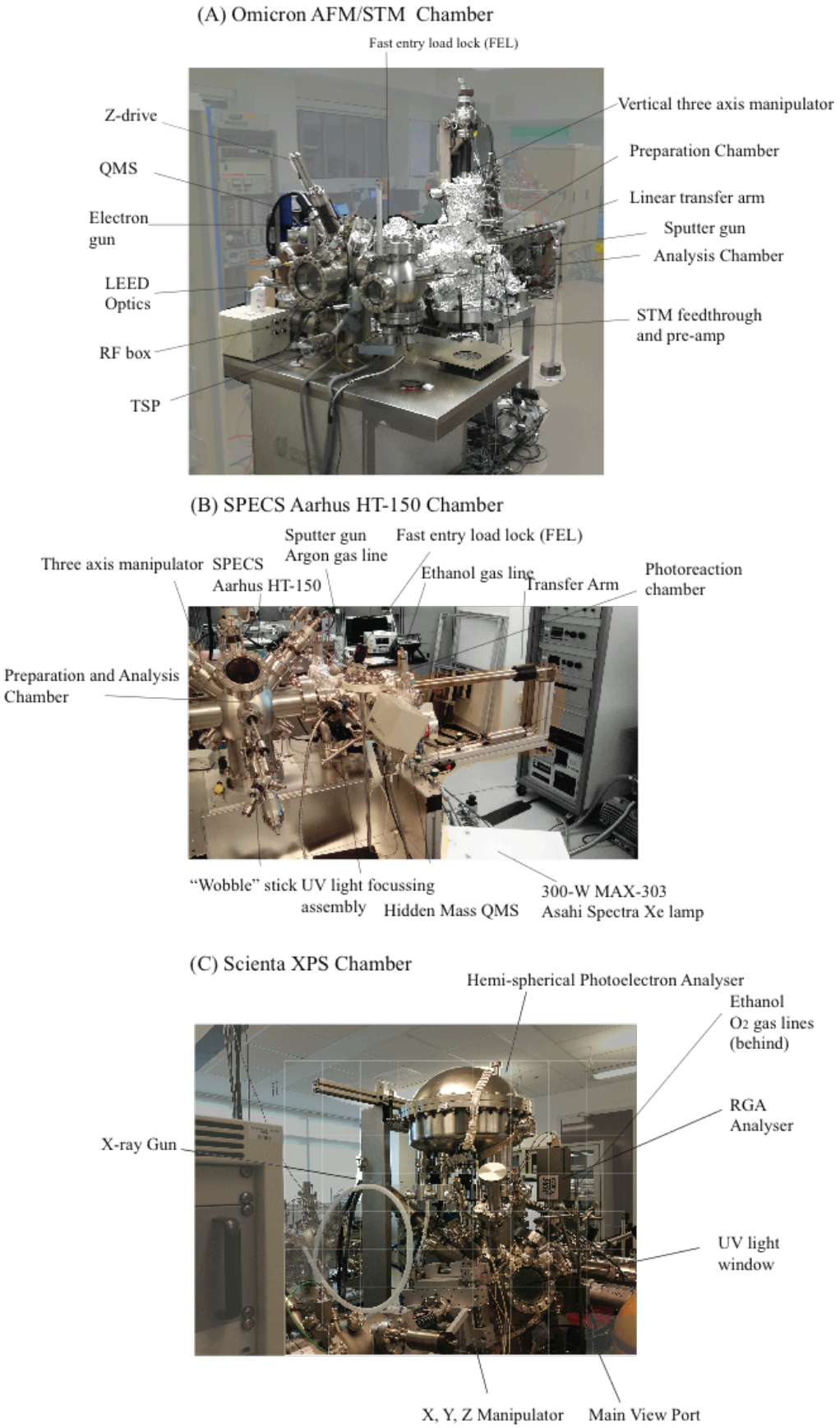

Figure 3.2: Photographs of the UHV systems: **(A)** Photograph of the UHV *Omicron* AFM/STM chamber. **(B)** Photograph of the *SPECS* STM HT-150 Aarhus Chamber. **(C)** Photograph of the *Scienta* XPS chamber.

3.3 Sample Preparation and Treatment and Motion in UHV

Single crystal samples studied in this thesis: W(100) and a natural anatase TiO_2(101) were cut and polished by the manufacturers to obtain a surface plane with a tolerance of 1-2°. In a UHV clean environment they were spot welded with Ta strips onto standard *Omicron* or *SPECS* sample plates. Prior to entry into the UHV the samples were sonicated in water and then isopropronol. The samples were introduced into the system using a FEL under a positive pressure of N_2(g). Samples were transferred between the FEL to the preparation and analysis chambers via z-motion and rotating magnetic manipulators. Manipulators controlling Z, X, Y movement and 360° rotation were used to precisely position the sample for sputtering, annealing, Ti dosing, as well as for LEED, electron bombardment and online mass spectroscopy. In order to transfer samples between the sample storage and STM stage for analysis a pincer or rotating SPECS "wobble stick" was used.

In this thesis, sample preparation was achieved *in-situ* using cycles of sample heating and Ar^+ surface sputtering.[7,8] After many cycles of sputtering followed by sample heating the sample surface and sub-surface region was apparently depleted of impurities, with residual argon detected by AES. On the *Omicron* AFM/STM, sputtering was carried out at a grazing 45° angle,[9] and in the *SPECS* preparation chamber a normal angle was used with no observable difference.

Heating in the AFM/STM *Omicron* system (470-1670 K) and *SPECS* Aarhus 150-HT STM chamber was conducted using electron bombardment (1 kV, ~30 mA). The sample temperature (±~40 K) was measured using an infrared pyrometer (emissivity of ~0.25 ε). In the Scienta XPS system the sample was heated by an e-beam heater (HEAT3-PS by *PREVAC*). In the *SPECS* STM and Scienta XPS systems a K-type thermocouple attached to the sample plate mounting was used to monitor the temperature, which was calibrated with a pyrometer (*Sirius*).

To expose surfaces to gases (O_2, EtOH, CH_3COOH) and achieve Ar^+ sputtering, the UHV pressure was increased using UHV precision leak valves which connected the UHV chamber to dedicated 5 mm Swagelok gas lines at slightly above atmospheric pressure (1.5

Bar). Upon installation, these lines were heated to ~370 °C and the inner surface was passivated with the respective gas by exposure for several hours before use.[5] The monolayer arrival time (Eqs. 3.1) can be used for coverage calculations, using the exposure to adsorbing gas phase molecules, as the pressure remained in the molecular flow regime.[5]

Physical evaporation of Ti (99.9%) was achieved using a commercial EFM-3 UHV *Omicron* electron bombardment evaporator at 2×10^{-10} mbar. A schematic is shown in **Figure 3.3**. The EFM-3 employed a solid Mo crucible containing a Ti metal rod heated to 1600 K.[5] An integrated internal flux monitor measured the metal cations passing with an ion collector. This current is directly proportional to the beam flux. The quantification of the dosed Ti was judged directly by the titania films prepared in STM after oxidation with a similar methodology as employed by Mathru previously using the same device.[10]

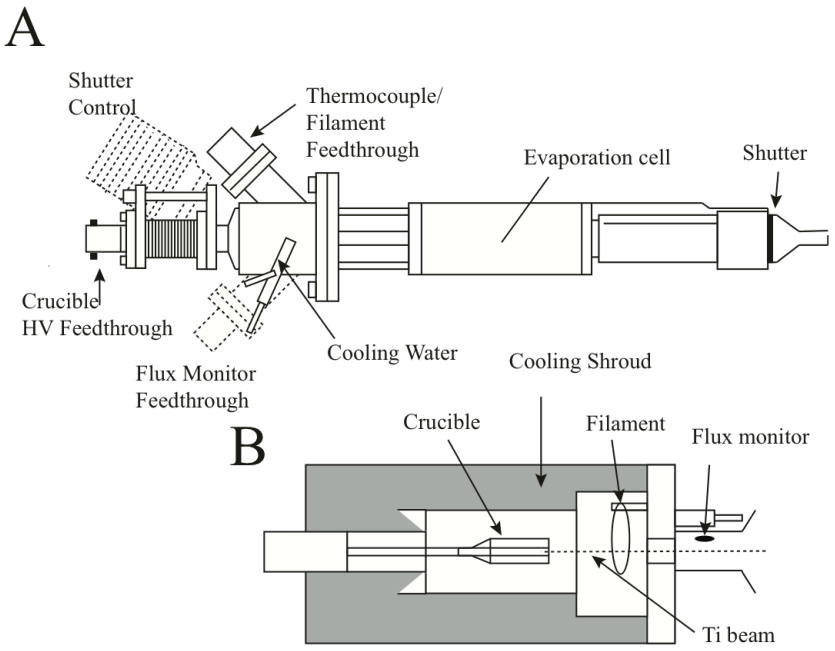

Figure 3.3: Schematic of the EFM-3 UHV Omicron evaporator. A) EFM-3 B) Evaporation cell Adapted from reference.[11]

The UV light used in Chapter 6 for surface irradiation was produced from a *Xenon Arc 300-W MAX-303 Asahi Spectra Xe* lamp located outside of the UHV system. Light of UV-IR (250-1000 nm) range was emitted by pressurised Xenon within a glass vial when an electrical discharge occurred across a cathode and anode. The majority of the IR component of the light of 760-1000 nm is removed by a series of mirror modules; the remaining light is then passed

through a final neutral density (ND) filter, which did not affect the light wavelength (**Figure 3.4A**). During the measurements this was set to 50% (Chapter 6) transmission. The light was passed though a quartz fibre optic of 5 mm diameter, 0.5 m length; and then a lens system was used to reduce the beam size to 2 cm at a distance of 10 cm. The light was incident on the sample at an angle of 45° through a standard UHV glass window.

The UHV glass window reduces the power intensity of the light by approximately 10-20% and eliminated the remaining IR component. A spectrum of the emitted light is displayed in **Figure 3.4B**, where the blue dashed box is the filtered light remaining.

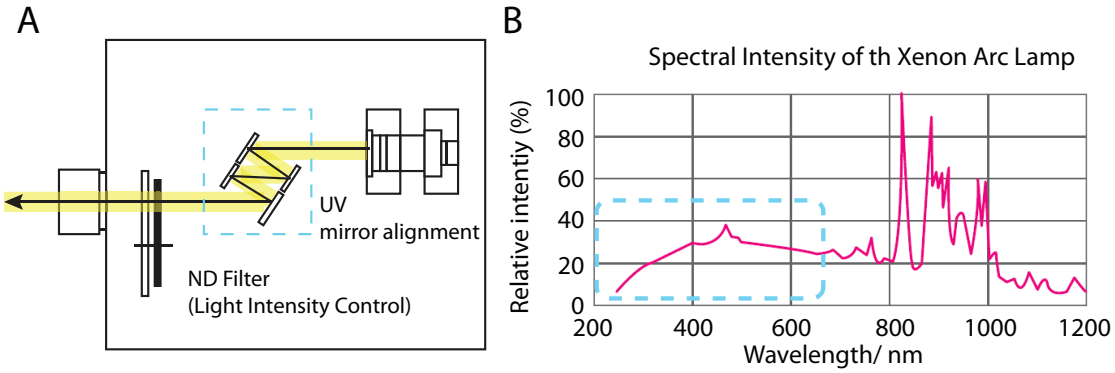

Figure 3.4: (A) Schematic of the Xenon UV lamp, the set of mirrors (blue dashed box) are configured to retain light of 300-650 nm λ. A filter is applied to reduce the intensity. **(B)** Spectrum of the original Xenon arc lamp light. Adapted from reference.[12]

The photon flux was determined with a handheld photo-diode UV light meter. (*Radiometer UVP*). The measurement was taken with a setup outside of UHV similar to the light path used in the experimental measurements. A calculation [1] of the approximate photon flux in units photons $s^{-1}cm^{-2}$, incident on the sample for 5 $mWcm^{-2}$ UV light using the equations: i) $c = v\lambda$ ii) $E = h\nu$ was made. This determined a flux of ~8.8×10^{15} photons $s^{-1}cm^{-2}$.

Electron bombardment (e-beaming) was conducted with a commercial UHV electron gun (*Thermo LEG62*). This provided a high energy and electron flux with fine control of electron dose. Electrons emitted by a thoria coated tungsten filament were processed by two

[1] Range of hν 310-390 nm (4-2.4 eV); 6.4×10^{15} J/ hν – 3.98×10^{15} J/ hν ; Power of UV = 5×10^{-3} $Js^{-1}cm^{-2}$, Flux = $7.8 \times 10^{15} – 9.8 \times 10^{15}$ photons s^{-1} cm^2. Mean Avg. Flux = 8.8×10^{15} photons s^{-1} cm^{-2}

electrostatic lenses (condenser and focus) and a quadrupole electrostatic lens at the opening to further manipulate the spot position. A schematic of the electron gun is shown in **Figure 3.5**. During operation the electron gun aperture was positioned 12 mm from the face of the sample and perpendicular to the surface plane. At the desired beam energy (3 kV for use in Chapter 4) the filament current was increased to achieve the desired emission current of 1 mA, then the condenser and focus were systematically varied to maximise the sample drain current (~60 μA). The beam was subsequently defocussed to increase the size of the electron beam blue spot to 3 mm.

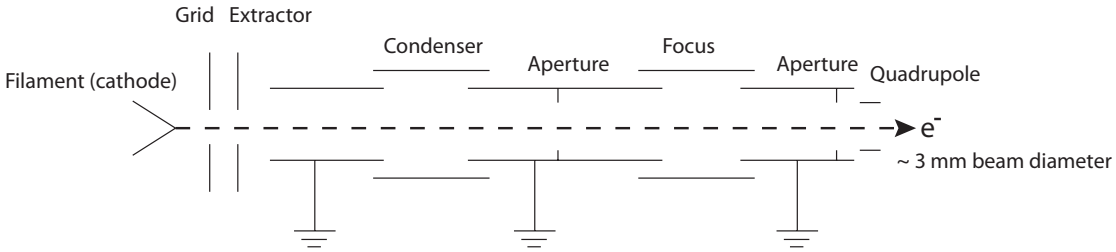

Figure 3.5: A schematic of the electron gun. A filament (cathode) emits electrons, which are processed by an electrostatic extractor condenser to form an electron beam.

3.4 Experimental Techniques

3.4.1 Quadrupole Mass spectrometry (QMS)

Quadrupole Mass Spectrometry (QMS) resolves ionised molecules and molecular fragments by their mass/charge (*m/e*) ratio and a detailed account is provided by de Hoffmann.[13] This was employed for routine analysis of the residual vacuum. It was used to determine if the UHV had a leak to air or contamination. In addition, QMS was employed in He leak testing and to assess the purity of gases leaked into the chamber. Mass spectrometry scans performed (*Hidden*) indicated a typical resolution across the mass range of *m/e* 0.4, indicated by fitting a Gaussian function to the peak to determine the full width half maximum (FWHM). Therefore masses separated by ~*m/e* 1 can be easily resolved.

Shown in **Figure 3.6** is the setup used for the photochemical oxidation of ethanol on anatase TiO_2(101) in Chapter 6, further details are provided therein. A detailed diagram of the sample and glass shroud placed on the QMS head is shown in **Figure 3.6A** and a top down photograph in **Figure 3.6B.** A transparent glass shroud was placed on the head with a small aperture (1 cm diameter) positioned ~1 mm front of the sample. This was to maximise the desorbing surface species entering the ionisation region of the mass spectrometer, improving the signal/noise ratio. This had been demonstrated necessary in previous photon stimulated desorption experiments by Idriss and co-workers.[14] The UV light is directed at a 45° angle to the sample and is of an insufficient flux to affect the products in the gas phase or quadrupole filter.

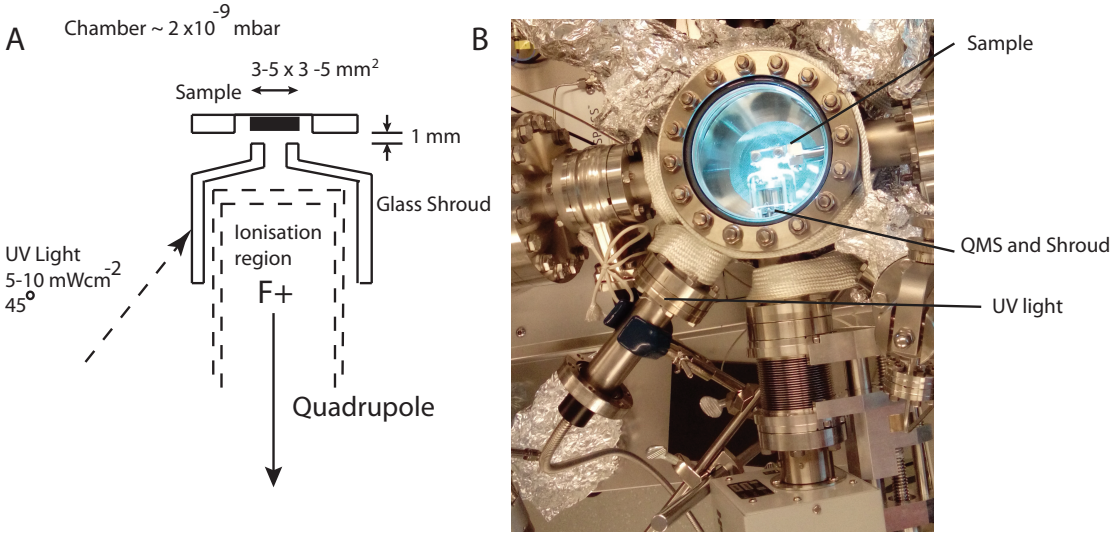

Figure 3.6: (A) A schematic of the shroud and QMS used in the photochemical experiments conducted on the anatase TiO_2(110) surface. (**B**) A photograph of the photoreaction chamber with QMS and pyrex glass shroud in position under UV light irradiation.

During the experiments four masses were scanned simultaneously, with the correct individual QMS modulating electric field (V/V) and constant electric field (U/V) U/V ratio, to record the four masses (eg. *m/e* 31, 29, 44, 15) within a time period of 1 second.[13] A secondary electron multiplier (SEM) detector (after conversion of m^+ fragments to e^-) was used with a description provided by de Hoffmann.[13] The mass trace signal recorded is proportional to the rate of ionisation of mass fragments with increments of a second.[15] Integration of the signal with

time results in a value proportional to the number of molecules. A baseline linear function was placed connecting the flat region before opening the UV light shutter and the flat region after closing, this was deducted from the signal. This integration of the area was computed simply in Igor Pro using the Trapezoidal rule approximation with a similar procedure used by Idriss and co-workers.[16]

In Chapter 6, rate constants and photoreaction cross-sections of desorbing acetaldehyde (CH_3CHO) under photon irradiation were extracted using the following procedure;

i) the initial height of the peak in mbar was determined. This was found to take between 1-3 seconds after opening the UV light shutter;

ii) a calibration with respect to 1×10^{-7} mbar ethanol (*m/e* 31, *m/e* 29) was made. The ethanol (*m/e* 31, m/e 29) peaks in mbar were then multiplied by fragment correction factors (CF)[2] and compared to the calibrated ion gauge in the photoreaction chamber. A correction of $(\frac{1\times10^{-7}}{9\times10^{-7}}) = 0.11$ was then applied;

iii) a CF for the *m/e* 29 mass fragment of 1.21 was subsequently applied to this value;

iv) this determined pressure value in mbar was converted into a molecular density $\frac{n}{cm^3}$ by applying Eqs. 3.2.[3] Hence:

$$\frac{n}{cm^3} = Ap \text{ where } A = (100)/kT\times10^6 \qquad \text{Eqs. 3.2}$$

where *p* is in mbar and *k* Boltzmann's constant JK^{-1}.

A photoreaction chamber volume of 3600 cm^3 was determined and used to extract the molecular number *n*. This molecule number was divided by 3 seconds, the average time for the trace to reach the peak. The molecule number *n* could be converted to MLs^{-1} by dividing by the crystal surface area 0.09 cm^2, taking into account that an ideal planar anatase $TiO_2(101)$ surface contains 5.2×10^{14} Ti_{5c} atoms cm^{-2} in the first atomic layer.

[2] This CF was determined using a procedure detailed in reference.[16]

Further analysis is detailed in Chapter 6 in connection with the use of the method in the quantitative treatment of acetaldehyde desorbing from the anatase TiO_2(101) surface under photon irradiation.

3.4.2 X-Ray Photoelectron Spectroscopy (XPS)

X-rays for XPS are typically generated by the bombardment of an Mg or Al anode by electrons, leading to the removal of core electrons and subsequent atomic relaxation of an electron with emission of X-ray radiation. The X-ray energy is dependent on the orbital from which the core electron is removed, with an intrinsic line width. The cross-section for removal is a function of the bombarding electron's energy.[4] MgK_α (1253.6 eV) and AlK_α (1486.6) (electron removed from the K_1 orbital) were used in this thesis. The single K_α X-ray line is seen with minor satellites on a background of Bremsstrahlung irradiation, which contributes to the background observed in XPS spectra.[4]

The XPS measurements described in this thesis were performed in a dedicated UHV system with a base pressure of 1×10^{-9} mbar. This was equipped with a non-monochromatised *SPECS* XR50 dual anode X-ray source (Al Kα and Mg Kα). The Mg Kα X-ray source was used at a energy of 10 kV and power of 285 W. A Scienta R3000 hemispherical electrostatic energy electron analyser was used. A description of the hemispherical analyser is provided in this reference.[4] The X-ray source and electron analyser were positioned close (3 cm) to the sample to maximise the X-ray flux reaching the sample and collection of photoelectrons.

The resolution ΔE FWHM is defined as a convolution of the natural line width, ΔE_i, the resolution of the X-ray source, ΔE_x, and the analyser resolution, ΔE_a. That is:

$$\Delta E = (\Delta E_i^{\,2} + \Delta E_x^{\,2} + \Delta E_a^{\,2})^{1/2} \qquad \text{Eqs. 3.3}$$

Therefore to maintain a good resolution of ~0.5 eV, all resolution components must be maintained at a low value.[4]

3.4.3 Auger Electron Spectroscopy

The Auger electron energy analyser employed in this study is the retarding field analyser (RFA), due to convenience, where the instrumentation is also used as LEED optics in the *Omicron* AFM/STM. A schematic is shown in **Figure 3.7** adapted from Taylor.[17] The RFA was first adopted for the study of Auger by Weber and Peria.[18] In the instrument used in this thesis the electron beam is directed normal to the surface and the scattered and emitted electrons travel back to the optics.

The instrument optics consists of four concentric grids. The first (closest to sample) is grounded, which results in a field free region, so the electrons travel radially. A retarding negative potential –V is applied to the next two grids, which prevents electrons of lower energy from passing, functioning as a high pass filter. The fourth grid is grounded and the electrons are collected by the screen resulting in a measurable current, which has a biased voltage several hundred V.[17] The electrons collected as a function of the sweep -V would therefore be the integral I(V*)* of the energy spectrum $N(E)$,[19] where E is defined by the high pass filter and E_{max} the specular reflection:

$$I(V) = \int_{E}^{Emax} N(E)dE \quad , \qquad \text{Eqs. 3.4}$$

The N(E) spectrum is obtained by differentiation of I(V). This is accomplished by applying a small sinusoidal modulation of V, then employing a phase sensitive lock-in amplifier tuned to the second harmonic (2ω) of the modulation, proportional to I(V)'', and therefore $\frac{dN(E)}{dE}$, the derivative of the spectrum. Small peaks can be identified easily and the large sloping secondary electron background is reduced. A Taylor expansion of the current as a function of voltage V and additional modulating voltage $\Delta V = k\sin \omega t$, after collecting terms first (ω) and second harmonic (2ω) terms, is defined below:[9]

$$I(V + \Delta V) = (V) + \left[I'(V)k + \frac{I''(V)}{8}k^3 \ldots\right]\sin\omega t - \left[\frac{I''(V)k^2}{4} + \frac{I^{IV}(V)k^4}{48} + \right]\cos 2\omega, \quad \text{Eqs. 3.5}$$

where k is the peak-peak modulation voltage.

As the lock-in amplifier is tuned to the second harmonic (2ω), with a small enough k this is proportional to the second order derivative $I''(V)$, $k^4 \cong 0$.

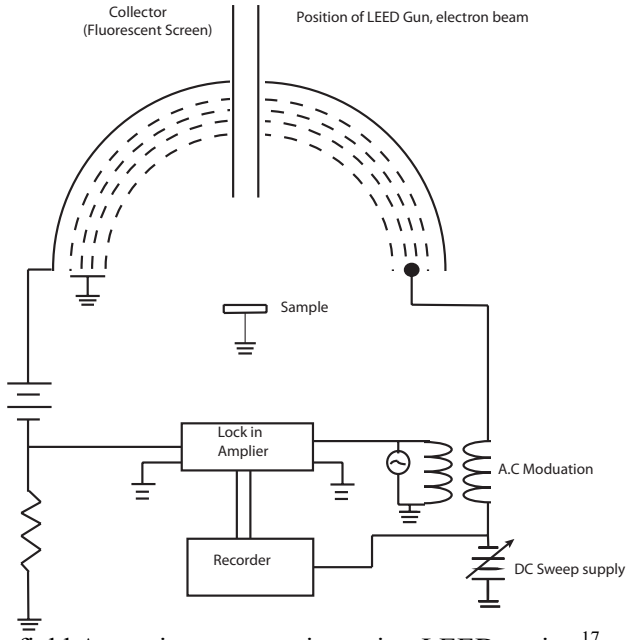

Figure 3.7: Retarding field Auger instrumentation using LEED optics.[17]

The RFA is relatively insensitive compared to other electron energy analysers. This is broadly because the RFA is a high pass filter, allowing all electrons to pass of energy above the biased voltage |-V|. A rough calculation can determine the sensitivity in ML, where a maximum value of signal peak voltage corresponds to roughly 10^{15} surface atoms cm^{-2}.[19] As the tolerable S/N at ~1 (0.1 μV) (measured current is converted to a voltage) is equivalent to $1\times10^{15}/(5\times10^{3})$ = 1×10^{12} atomscm^{-2}. This value of 0.1 % ML (1 ML ≈ 1×10^{15}) is then the upper limit of the sensitivity. The S/N can be improved by increasing current as the noise has a square root dependence. In this thesis Auger spectroscopy is mainly used qualitatively for assessing sample cleanliness.

3.4.4 Low Energy Electron Diffraction (LEED)

Here we employed a reverse view LEED, where the diffracted electrons are filtered by the RFA, as described for AES. The instrumentation diagram is shown in **Figure 3.8**. The electron beam of energy +Ve is directed towards the sample. The diffracted electrons are scattered radially in a field free region. After passing though the first grid, the next two grids have an –Ve + ΔV applied to filter out any inelastically scattered electrons. The resulting diffraction spots are recorded on a fluorescent screen. In general, when comparing LEED results all focusing and beam parameters and sample positioning were maintained constant.

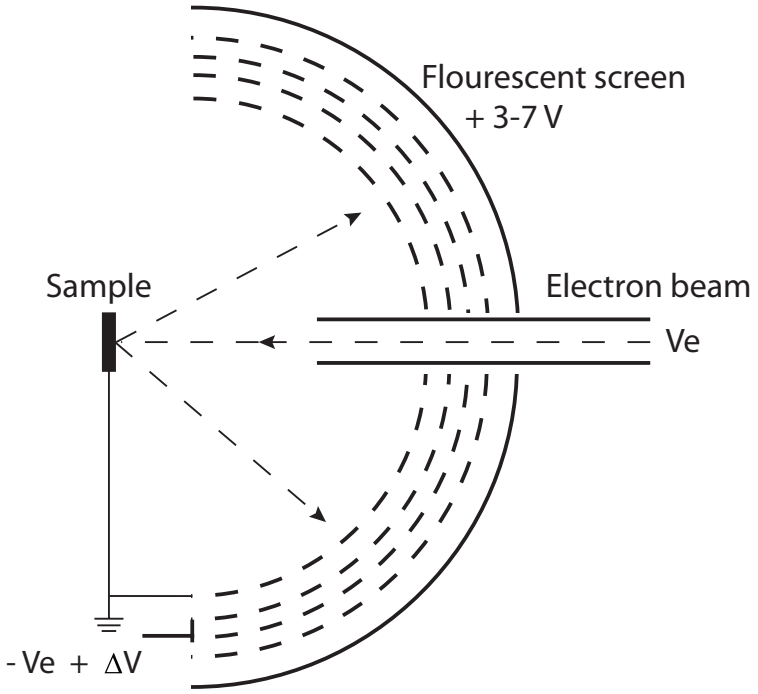

Figure 3.8: A schematic of the LEED optics employed. An electron beam +Ve is incident normal to the sample surface, which is grounded, the electrons are scattered back radially in a field free region and are filtered by the middle two grids, -Ve +ΔV. The 4th grid is grounded. The electrons are accelerated towards the fluorescent screen ~3-7 kV and a LEED pattern is recorded.

3.4.5 STM Instrumentation and Operation

The STM microscopes employed in this work were two commercial UHV models: the *Omicron* UHV AFM/STM and the *SPECS* Aarhus 150 *HT* UHV STM.

The STM instruments employ piezo-actuators to adjust the tip (or sample) relative to the sample (or tip) for fine motion; with a sensitivity of position of 0.1 Å in X, Y (in-plane) and Z directions (out of plane). These are typically lead titanate ceramics (PZT, $Pb[ZrxTi1-x]O_3$).[20] These materials will deform, extending and compressing in an applied electric field (~400-800 V).[21] The piezoactuators employed in this study for fine STM tip control are the tube type; which is compact with a high natural vibrational frequencies.[20] A bias ΔV_z is applied between the inner and outer electrodes to extend and compress for Z-motion of the tip and applied across to flex for in plane X-Y motion of the tip.

The *Omicron* UHV AFM/STM was utilised to produced the images presented in Chapters 4 and 5. In fact, it was only used in STM mode so the AFM functionality will be neglected here. Imaging was undertaken at room temperature and Scala 5.0 software was used. This STM has the advantage that the macroscopic position of the sample with respect to the tip could be moved laterally (and forward) with a coarse piezoactuator (inertia slider) in steps of 100 nm and STM tips could be readily exchanged. An automated approach procedure was used to advance the sample towards the tip after careful positioning of the tip (5 mm) with the aid of a camera. This approach was terminated when a tunneling current of ~0.3-4 nA at +1.6-2 V was achieved. Mechanical contact often occurred, evidenced by a typical surface disturbance in the first image. Presented in **Figure 3.9** are top down and side view labeled photographs of the STM stage.

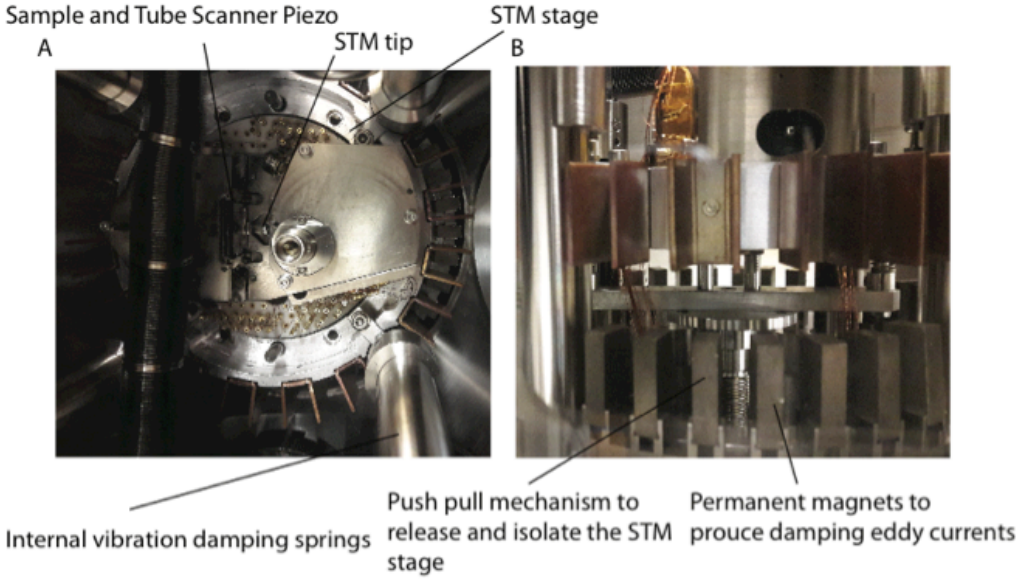

Figure 3.9: Photographs of the *Omicron* AFM/STM. **(A)** Top down view of the STM where the stage with STM tip (right) and sample (left) are visible. **(B)** Side view of the STM where the interlocking damping mechanism is visible, prior to stage suspension.

The *SPECS* Aarhus STM was utilised to produce the images presented in Chapter 6. A photograph of the internal STM stage is shown in **Figure 3.10A** and a cross-sectional view of the STM sample mount and tip is shown in **Figure 3.10B.** It is a variable temperature (90-400 K) microscope with a temperature stability of ± 2 K; however during the study it was only used at room temperature. The piezodrive was located behind the tip with a linear drive inchworm mechanism used to advance the tip in the mm range. The tip could not be moved laterally and thus for a certain sample position was limited by the fine piezoactuator with only a region of 15000 × 15000 $Å^2$ available to investigate, without repositioning the sample. During all measurements a single tungsten etched STM tip was used.

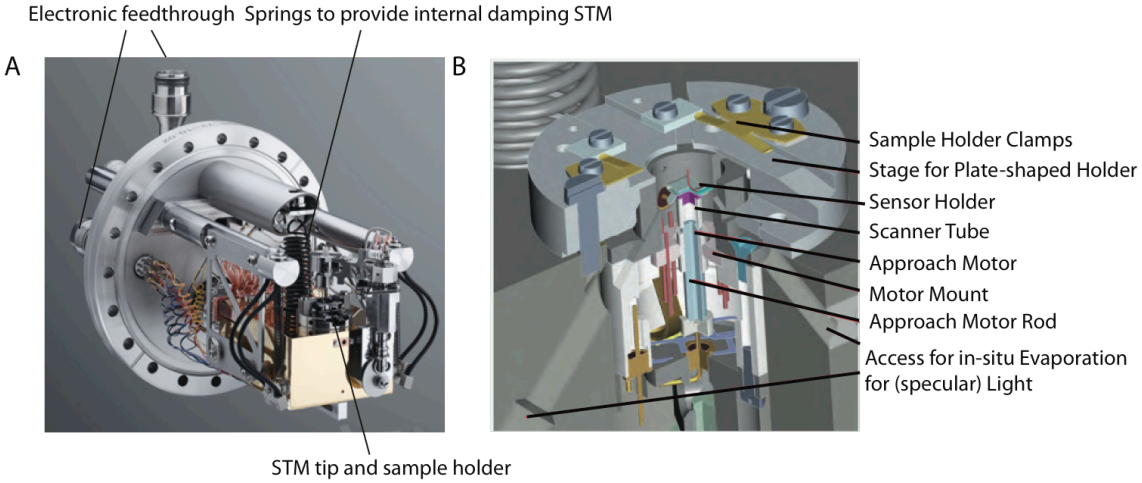

Figure 3.10: (A) A photograph of the *SPECS* Aarhus HT-150 STM stage **(B)** A 3D internal cross-sectional view of the scanner mount and coarse approach mechanism. (SPM Aarhus Series brochure)[22]

Two types of STM tip were employed for use in the *Omicron* AFM/STM. The first was commercial PtIr machined to have a sharp apex. The second type was electrochemically etched from tungsten wire (0.25-0.4 mm diameter). A photograph of the apparatus and schematic used to conduct the tip etching is shown in **Figure 3.11**.

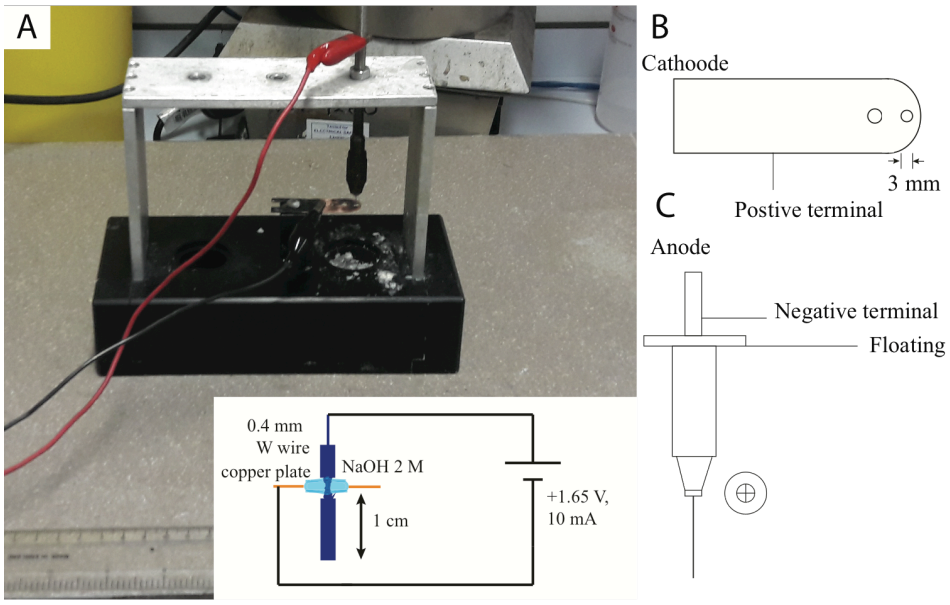

Figure 3.11: Apparatus for fabrication of tungsten etched tips. **(A)** A photograph of the support and base. Wires travel to the DC power supply. **(B)** The copper cathode with a hole punched. **(C)** The anode which had the W wire inserted. Inset: electrochemical circuit: a +1.65 DC bias was applied between the copper and W electrodes with a meniscus of NaOH (aq) 2 M until electrochemical etching resulted in a section of wire breaking contact and dropping off onto shaving foam.

The tungsten wire (anode) was straightened and abraded by emery paper then was placed in a hole in a copper plate (cathode) and supported in a vertical orientation. A meniscus of 4 mm diameter, 2 mm depth of 2 M NaOH(aq) solution was created. A DC voltage bias of +1.65 V was placed between the terminals, which resulted in (WO_3 reduction potential -1.43 V with respect to H_2/H^+)[23] a flow of current of ~10 mA and maintained by keeping a constant meniscus volume. The immersed tungsten wire dissolved with evolution of gas and after ~30 minutes the section below the meniscus fell under its own weight (1 cm length) onto a collection of shaving foam. This 'dropped off' section was collected and used as the STM tip.

The balanced equation for the electrochemical etching of the tungsten tip is shown below; Eqs. 3.6, Eqs 3.7, indicating the overall reaction in Esq. 3.8: [23]

$$6H_2O + 6e^- \rightarrow 3H_2 + 6\,OH^- \text{ Cathode} \qquad \text{Eqs. 3.6}$$

$$W(s) + 8OH^- \rightarrow WO_4^{2-} + 4H_2O + 6e^- \text{ Anode} \qquad \text{Eqs. 3.7}$$

$$W(s) + 2OH^- + 2H_2O \longrightarrow WO_4^{2-} + 3H_2(g) \qquad \text{Eqs. 3.8}$$

Tips were rinsed (water and iso-propanol) then spot-welded onto an AFM/STM *Omicron* tip holder and further sonicated in water. Inspection using an optical microscope was used to detect damaged tips. In UHV, the tips were heated to 370-470 K for 12 hours, by a filament placed behind, (2.0A, 1.4 V) to remove residual contamination and WO_3. The majority of tips formed proved usable as adjudged by the ability to obtain atomic resolution on the surface of rutile TiO_2(110) in STM. A single STM tip used for all imaging on the *SPECS* was prepared in a similar way. The wire thickness was 0.2 mm. Further treatment was achieved with high sample bias (+10 V) scans and tip pulses.

To achieve a resolution ~ 0.1 Å in the z-direction or ~2-3 Å in x-y-direction, the vibrational oscillation amplitude which is transferred to the STM must be ≤ 0.01 Å. As typical building vibrations have an amplitude of 10^4 Å,[20] without damping the periodic motion of the tip would be drowned out in the background.

As the STM scanning unit behaves as harmonic oscillator,[24] the natural resonant frequency $\omega_0 = \sqrt{k/m}$, is required to be outside the range of high external amplitude vibrations to prevent resonance (0.5-1 Hz). In addition, a window (1 Hz to 10 kHz) of low transfer coefficient (10^{-6} to 10^{-8}) between external vibrations and those experienced by the tip is required, achieved by vibrational instrumental damping.[20]

The two UHV STM systems used different strategies to achieve vibrational isolation. In the AFM/STM, measurements were performed in the basement of the building (dep. chem. UCL), which had reduced vibrational amplitude. Devices such as rotary pumps, which resulted in mechanical sources of noise were located in a different laboratory room. The analysis AFM/STM UHV chamber was mounted on active damping elements (*Halcynoics)*. The remaining part of the system chamber was connected by flexible bellow component in the long connecting cylinder. Further more, the STM stage was suspended by thin vertical springs to vibrationally isolate the STM. A concentric ring of interlocking permanent magnets provided additional damping by the induction of eddy currents. In the *SPECS* Aarhus HT-150 STM, the internal vibrational isolation proved sufficient to provide extremely stable, fast and well resolved high-resolution imaging.

The heart of the STM is the feedback controller. Shown in **Figure 3.12** is a generalised block diagram of the electronic feedback loop tip control applicable to the STMs used in this thesis.[20] The STM tunneling current ~0.1-1 nA measured during incremental movement of the tip across the surface is electronically converted into a voltage signal and then amplified. This analogue voltage response is converted to a digital signal. The voltage is compared to a pre-set voltage to determine an error signal. Furthermore, a controller processes this error signal, where the factor k determines the responsiveness. The voltage is amplified and applied to the z-piezo to adjust the tip height. The tunneling current is measured and the cycle repeats. [20] The feedback control in the instruments employed here, was handled digitally by the computer software for the *Omicron* AFM/STM and *SPECS* Aarhus HT-150 STM.

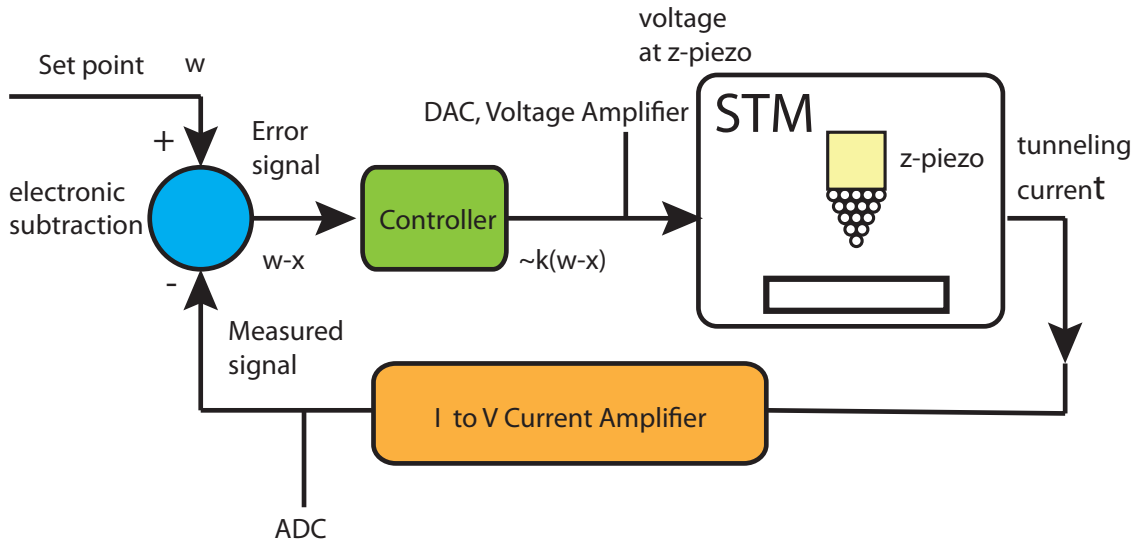

Figure 3.12: A generalised electronic block diagram of the STM system under feedback control. This was adapted from reference.[20]

In the ideal limit when the tunneling set point is maintained, so called constant current (CC) imaging results. All surface topographic and electronic information is encoded in the changing applied z-piezo voltage. An example CC STM topographic height image is presented in **Figure 3.13A**. In this thesis all images are CC. If a region of the surface is flat enough the feedback can be disabled, then assuming the sample is oriented normal to the tip raster direction and flat, constant height (CH) mode is obtained. The CC imaging is an ideal situation and the tunneling current varies due to inefficiency of feedback. The tunneling current variation (~0.7 nA) in **Figure 3.13B** is sufficient to reproduce the surface features. A height line profile (green) is depicted in **Figure 3.13C.** In **Figure 3.13D** the tunneling line profile (green) is shown where the periodic rows and spikes in tunneling current as a step edge is traversed are observed. The latter is accompanied by a smearing of the step edge in the height profile. Analysis of the forward and backward scan images and many images was used to identify tip (e.g multiple apex) and instrumental (peizo drift, thermal drift) related artifacts

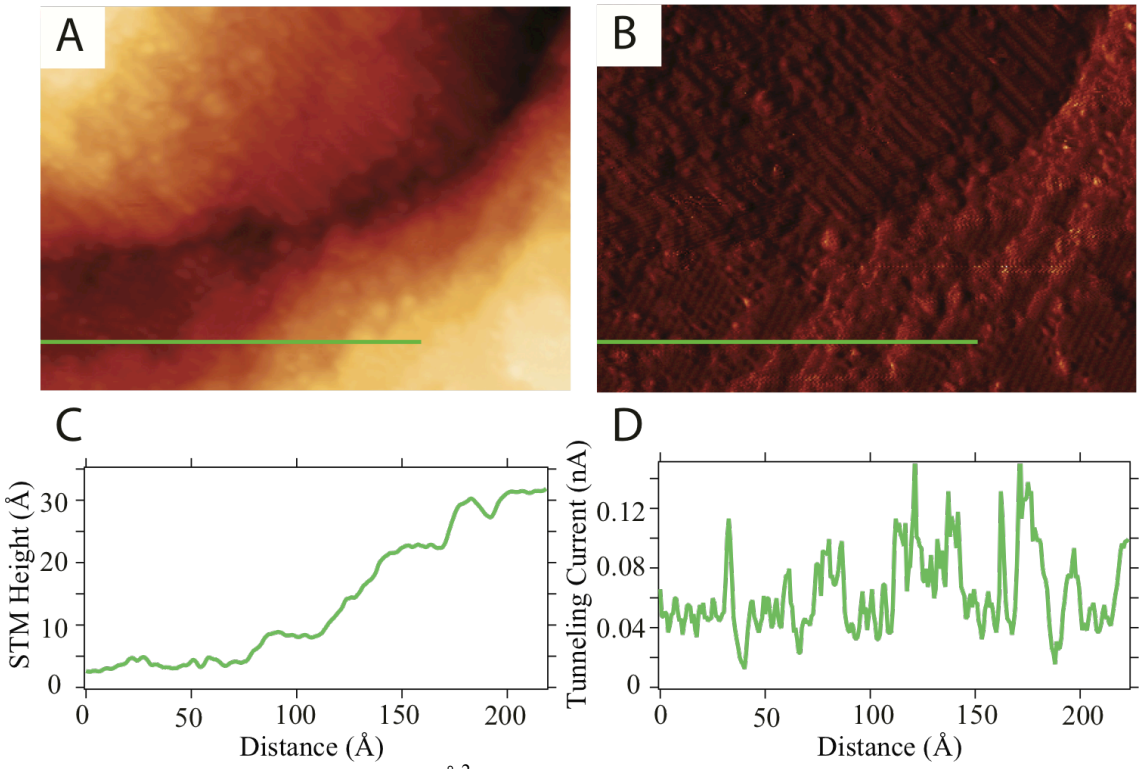

Figure 3.13: An example 310 × 220 Å^2 STM image (+1.6 V sample bias and constant tunneling ~0.1 nA) from Chapter 4 of a tip modified anatase TiO_2(101) surface. **(A)** The topographic height STM image, which is derived from the voltage applied to the z-piezo. **(B)** The simultaneously recorded tunneling current STM image which has a variation of ~0.7 nA.

3.4.6 Image Preparation and Treatment

A minimal amount of treatment was administered to the STM images. The images were processed in Gwyddion® and Image SXM® packages. As the sample is not aligned completely normal to the tip direction (or vice versa), or drift occurs; the images were adjusted until the three points were in a plane by deducting the plane defined by the three points from the image.[25] An example image processing in Gwyddion® for an STM image (**Figure 3.14A**) of anatase TiO_2(101) is shown in **Figure 3.14**. The adjusted image (**Figure 3.14B**) can be used to extract a step height (**Figure 3.14C**) used for calibration of the z-piezo height with reference to the known step height 3.8 Å.[1] For some of the images, to present a large corrugated area, polynomial functions (order = 1-11) were fitted to the data in vertical and horizontal directions and deducted.

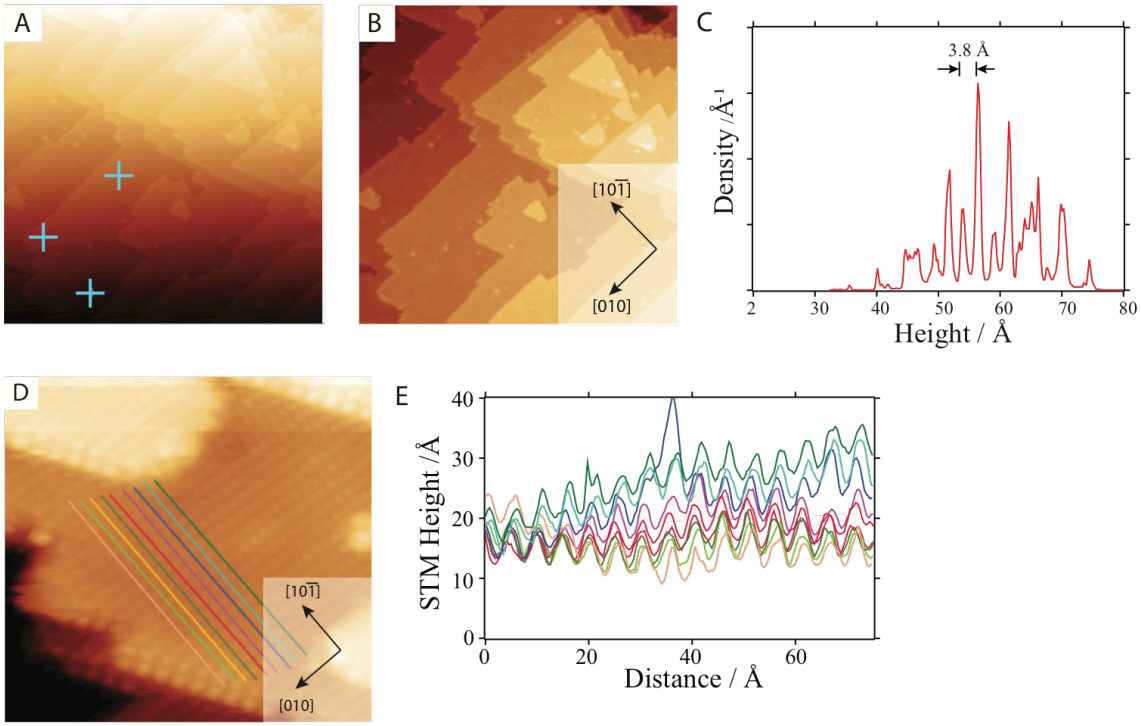

Figure 3.14: An example data treatment. (**A**) A tilting of an image of anatase TiO_2(101), in the 1000 × 1000 Å2 image (+1.6 V, 0.1 nA), the blue crosses indicate points chosen to tilt the entire image until they are in one plane. (**B**) A 1000 × 1000 Å^2 image after the tilting. (**C**) The height histogram of image (**B**) the step edge height can be determined from the distance between peaks and is used for height calibration. (**D**) STM image 109 × 103 Å^2 (**E**) Line profiles from image used from calibration (**D**).

The calibration of the in plane dimensions was achieved by measuring many line profiles of the [10$\bar{1}$] (**Figure 3.14D**) and [010] surface directions on atomically resolved images of anatase TiO_2(101); this was used for Chapters 4 and 6 and rutile TiO_2(110) was used in Chapter 5. The mean average determined unit cell was used to calibrate the x-y dimensions taking into account the angle with respect to the vertical and horizontal image direction. The determined calibration factors were used to adjust images before measurements on the STM images were taken.

Noise in present in images was filtered by determining the Fast Fourier Transform (FFT) of the image, then subtracting high frequency noise from the FFT and carrying out the inverse function to obtain the clean STM image.

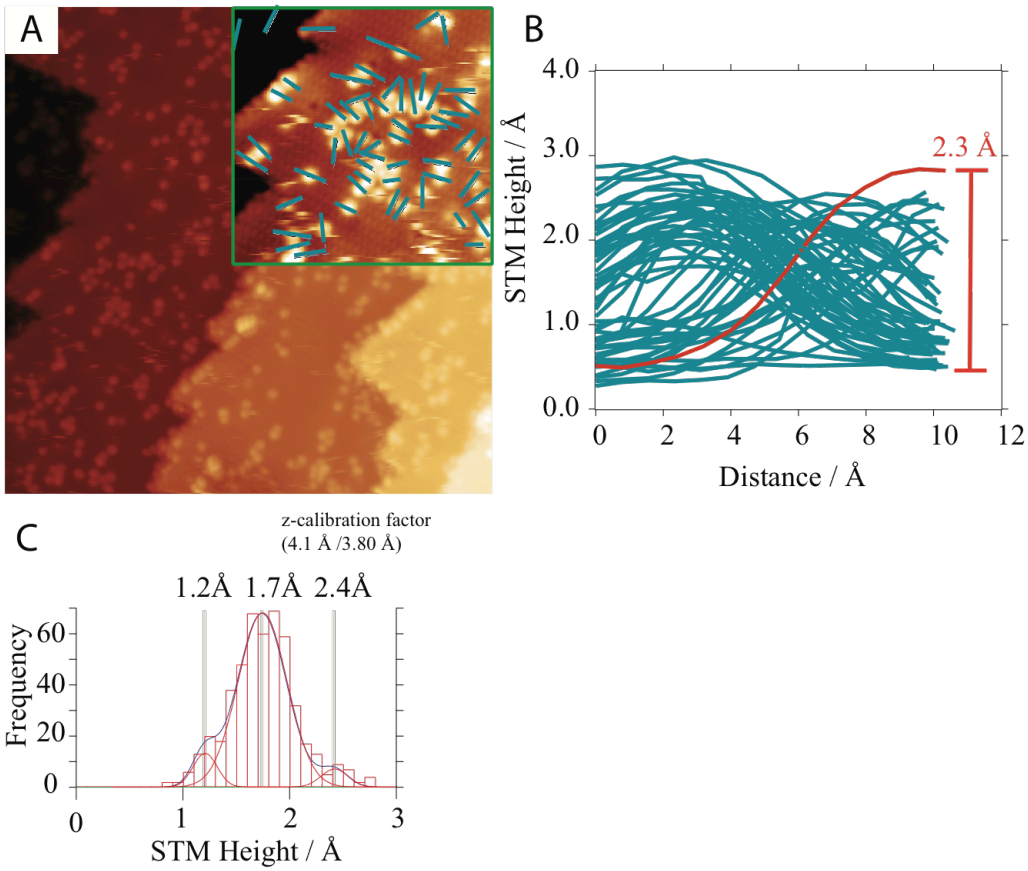

Figure 3.15: An example processing procedure used to obtain height histograms of surface adsorbates for ethanol/anatase TiO_2(101) (Chapter 6). (**A**) 350 × 350 $Å^2$ STM image (+2 V tunneling current, 0.420 nA) Inset: zoom 140 × 140 $Å^2$ with blue height line profiles overlaid. (**B**) Uncalibrated height line profiles indentified in (**A**). (**C**) Calibrated particle histogram with a bin width of 0.1 Å, peaks of 1.2 Å,1.7 Å and 2.4 Å are identified.

In order to determine an apparent height histogram of surface adsorbates as presented in the Chapters 6 studying ethanol on anatase TiO_2(101), the following procedure was used and an illustration is provided by **Figure 3.15**: The image to be analysed was adjusted so the terraces were in plane as described. Height line profiles were extracted from the image (**Figure 3.15A** inset), the minimum and maximum was determined from the individual profiles (**Figure 3.15B**) and a z-calibration factor applied determined from the step height. A histogram was compiled in Igor Pro® from this, to determine the resolvable peaks in the STM height distribution function, as shown in **Figure 3.15C**.

References

(1) Diebold, U. The Surface Science of Titanium Dioxide. *Surf. Sci. Rep.* **2003**, *48*, 53–

229.
(2) Henrich, V. E.; Cox, P. A. The Surface Science of Metal Oxides; Cambridge University Press: Cambridge, 1996.
(3) Venables, J. Introduction to Surface and Thin Film Processes; Cambridge University Press: Cambridge, 2000.
(4) Briggs, D.; Seah, M. P. Practical Surface Analysis, Auger and X-Ray Photoelectron Spectroscopy; 2nd ed.; Wiley: Chichester, 1990.
(5) O'Hanlon, J. F. A User's Guide to Vacuum Technology; 3rd ed.; John Wiley & Sons: Hoboken, NJ, USA, 2005.
(6) Alpert, D. New Developments in the Production and Measurement of Ultra High Vacuum. *J. Appl. Phys.* **1953**, *24*, 860–876.
(7) Instruction Manual Sputter Ion Gun; 04-161/04-162 2 kV; Perkin Elmer: Edne Prairie, Minnesota, 1980; pp. 1–31.
(8) Woodruff, D. P.; Delchar, T. A. Modern Techniques of Surface Science; 2nd ed.; Cambridge University Press: Cambridge, 1988.
(9) Oechsner, H. Untersuchungen Zur Festkörperzerstäubung Bei Schiefwinkligem Ionenbeschuß Polykristalliner Metalloberflächen Im Energiebereich Um 1 keV. *Z. Physik* **1973**, *261*, 37–58.
(10) Matharu, J. Surface Science of Ultrathin Metal Oxide Films, (Doctoral thesis), University College London, London, UK, 2011, pp. 1–177.
(11) Freund, H.-J.; Pacchioni, G. Oxide Ultra-Thin Films on Metals: New Materials for the Design of Supported Metal Catalysts. *Chem. Soc. Rev.* **2008**, *37*, 2224–2242.
(12) Xenon Light Source 300W Monochromatic Light Source with Filters (MAX-303) Manual; 1st ed.; Asahi Spectra: Tokyo, Japan, 2014.
(13) de Hoffmann, E.; Stroobant, V. Mass Spectrometry; 3rd ed.; John Wiley & Sons: Chichester, 2013.
(14) Nadeem, A. M.; Muir, J.; Connelly, K. A. Ethanol Photo-Oxidation on a Rutile TiO_2(110) Single Crystal Surface. *Phys. Chem. Chem. Phys.* **2011**, *13*, 7637–7637.
(15) Thompson, T. L.; Yates, J. T. Control of a Surface Photochemical Process by Fractal Electron Transport Across the Surface: O_2 Photodesorption From TiO_2(110). *J. Phys. Chem. B* **2006**, *110*, 7431–7435.
(16) Nadeem, M. A.; Majeed, I.; Waterhouse, G. I. N.; Idriss, H. Study of Ethanol Reactions on H_2 Reduced Au/TiO_2 Anatase and Rutile: Effect of Metal Loading on Reaction Selectivity. *Catal. Struct. React.* **2015**, *1*, 61–70.
(17) Taylor, N. J. The Role of Auger Electron Spectroscopy in Surface Elemental Analysis. *Vacuum* **1969**, *19*, 575–578.
(18) Weber, R. E.; Peria, W. T. Use of LEED Apparatus for the Detection and Identification of Surface Contaminants. *J. Appl. Phys.* **1967**, *38*, 4355–4358.
(19) Chattarji, D. The Theory of Auger Transitions; Elsevier: London, 2012.
(20) Voigtlaender, B. Scanning Probe Microscopy; Springer: Berlin, Heidelberg, 2015.
(21) Binnig, G.; Smith, D. P. E. Single-Tube Three-Dimensional Scanner for Scanning Tunneling Microscopy. *Rev. Sci. Instrum.* **1986**, *57*, 1688–1689.
(22) SPM Aarhus Series, 2017, 1–24.
(23) Ibe, J. P.; Bey, P. P., Jr.; Brandow, S. L.; Brizzolara, R. A.; Burnham, N. A.; DiLella, D. P.; Lee, K. P.; Marrian, C. R. K.; Colton, R. J. On the Electrochemical Etching of Tips for Scanning Tunneling Microscopy. *J. Vac. Sci. Technol. A* **1990**, *8*, 3570–3575.
(24) Hofer, W. A.; Foster, A. S.; Shluger, A. L. Theories of Scanning Probe Microscopes at the Atomic Scale. *Rev. Mod. Phys.* **2003**, *75*, 1287–1331.
(25) Klapetek, P.; Necas, D.; Anderson, C. Gwyddion User Guide; 2nd ed.; 2016; pp. 1–192.

CHAPTER 4

4.0 Synthesis and Reactivity of a Novel Rutile/Anatase Interface: An Electron Beam Damage and Tip Modification Study of Anatase TiO_2(101)

An STM characterisation of an e-beamed anatase TiO_2(101) surface under different electron fluxes, at the outer edge and centre of the beam has been undertaken. Single row, 5 Å, half unit cell (unit cell = 10.24 × 3.78 $Å^2$) width and double row 10 Å, unit cell width depressions elongated in the [010] direction are formed; a model is proposed formed by the removal of TiO_2 units. Further electron irradiation results in the formation of a surface composed of small rectangular (101)-(1 × 1) terminated islands, predominately elongated in the [010] direction. In line with existing studies, the mechanism of formation is attributed to a Knotek-Feibelman radiolysis mechanism.[1,2] *The e-beaming does not lead to severe surface disordering as evidenced by the large domains of (101)-(1 × 1) surface that are retained, corroborated by a LEED diffraction pattern.*

STM tip-pulse modification at a sample bias of +10 V on the e-beamed anatase TiO_2(101) resulted in a modified surface structure consisting of a large protrusion (~ 400 Å diameter, 30 Å height) in a surface hole surrounded by a pristine outer area of anatase TiO_2(101)-(1 × 1). A crystalline ordered structure was formed on the e-beamed surface (embedded in the large protrusion) and characterised in-situ by STM. High-resolution images indicated one region had an atomically resolved unit mesh of (3.1 ± 0.2 Å × 14.2 ± 0.5 Å) and corrugation along the long spacing of ~2 Å. This is consistent with the surface structure of rutile TiO_2(100)-(1 × 3). In-situ exposure and surface adsorption of acetic acid resulted in a monolayer coverage of adsorbates resulting in a (6.1 ± 0.3 Å × 14.7 ± 0.6 Å) unit mesh. Analysis of the STM images allowed the assignment of the reduced rutile TiO_2(100)-(1 × 3)-β surface structure and by implication a well characterised rutile surface and interface formed on an anatase single crystal. Plausible epitaxial relationships of the ultrathin film on the anatase

(101) surface are proposed. The formed rutile/anatase interface was sharp with a maximum distance of ~ 30 Å between the top of the resolved anatase and rutile surfaces.

4.1 Introduction

The study of the interaction of electrons with surfaces encompasses a core component of surface science and the foundation for numerous techniques such as LEED and AES already described in the Chapters 2 and 3. The electron-surface interaction has also been used in the manipulation of atomic and molecular species[3] and the creation of point defects and new nanoscale structures.[4] Electron damage to materials is often an undesirable side effect of a measurement employing electrons such as in electron microscopy.[5] The ability to fine-tune the surfaces of materials at the nano-scale with electrons has emerged as a large field and is hugely relevant for current and future applications in electronics. In addition, the ability to tailor metal oxide surfaces presents a useful tool for the fundamental study of photo-catalytic systems such as TiO_2.[6] The STM tip in tunneling mode presents a very localized source of electrons or holes, which can be applied to modify a surface with precise control and a means of high-resolution direct space characterisation. The high local field electric field ~ 0.2 $VÅ^{-1}$ and injection of electrons is shown here to lead to surface transformations not yet observed with other techniques.

4.2 Literature Review

4.2.1 Electron Beam Modification of Surfaces

Electron beams are used extensively in nanotechnology to modify the structure of surfaces.[7,4] One example modification is electron beam surface deposition,[8,9] where gas phase species are adsorbed at the surface and decomposed by the electron beam or the adsorption behaviour is modified by the electron exposure. Additionally, in many cases the action of the electron beam can lead to the sputtering of surface layers, resulting from elastic knock-on

collisions requiring energies of the order of 100 kV[5] to remove light atoms from surfaces. This sputtering can be used in lithography to etch or disorder surface layers.[7] In the lower energy regime below 100 kV, the ejection of surface atoms through processes such as radiolysis are important.[1,2] Specific examples include the Si(111)[10] and TiO_2 surfaces.[11]

However, the interaction of an electron beam with a surface does not always result in more disorder or etching. The electron beam has also been observed to create local ordered structures. For instance, the beam/surface interaction has been shown to separate cationic and anionic components under the action of an induced electric field by electron bombardment (e-beam) within a certain depth.[5] The electron beam can also result in the synthesis of new phases, of zero (nanoparticles), one (nanowires) and two dimensions on the surface.[4] Some of those ordered products have been evidenced by the observation of crystalline structure which could be determined by electron micrographs and selected area electron diffraction.[12] Schirmer et al. have for example realised the synthesis of reduced transition metal oxide TiO_x nanostructures (<1000 Å) successfully on Si(100) by the deposition of titanium tetraisoproxide and decomposition in UHV induced by a highly focused electron beam.[8]

4.2.2 Electron Beam Modification of Titanium Dioxide TiO_2

Electron beams have been used to induce structural and chemical changes to metal oxides. Vergara et al.[13] studied the effect of a 3 keV electron beam on TiO_2 during AES measurement and in this investigation observed an increase of Ti^{3+} ions induced by the beam. Smith et al. demonstrated that a highly energetic electron beam of 400 keV on a TiO_2 sample could lead to its reduction and the formation of a TiO_x phase on the surface.[12] These products were characterised by electron microscopy, and the process was later shown to be a general phenomenon occurring on maximally valent transition metal oxides. An epitaxial relationship was eventually demonstrated by McCartney et al.[14] The dominant mechanism was proposed to be a radiolytic O^+ removal from TiO_2, proposed by Knotek and Feibelman to involve an Auger decay.[1,2] Recent work on radiolysis of TiO_2 has been completed by Lee et al..[15]

Electron bombardment (e-beaming) has been demonstrated to produce oxygen vacancies on rutile TiO_2(110) without affecting the Ti interstial defect density in an STM and XPS study by Yim et al.[16] and STM and TPD by Petrik et al.[17] Numerous other studies have shown that low energy electrons can produce oxygen vacancies on TiO_2 surfaces.[18-21] Pang et al. used low energy electron beams of 75 eV to modify rutile TiO_2(110); the electron beam was used to increase the concentration of bridging oxygen row vacancies ($O_b$vacs), in addition to electron stimulated desorption of the capping OH_b. In the presence of water, the $O_b$vacs are converted to OH_b.[16]

Electron bombardment has been studied on the surface of rutile TiO_2(110). Features of 'pitting' on rutile TiO_2(110), where an area of the surface is considered to be removed, have been indicated by SPM data.[19] A greater flux of electrons at 300 eV results in the loss of oxygen from the rutile TiO_2(110) selvedge. This results in the formation of sub-stoichiometric reconstructions, with STM indicating the presence of 1 × 2, 1 × 3, 1 × 4 and 1 × 5 reconstructions.[19] When e-beaming at 3 kV, Humphrey et al. evidenced another way that the surface can react to a loss of oxygen, namely an ordered 'nano-crack' zig-zag arrangements, as observed by STM.[22] Under a greater electron flux, a partially disordered surface with (1 × 2) symmetry was found.[22] At 720 K Mentes et al. formed a low temperature (LT) 1 × 2 reconstruction using 60 eV electrons. A missing row model was proposed, invoking the lateral diffusion of oxygen vacancies at 720 K.[11]

4.2.3 STM Surface Modification

The scanning tunnelling microscope (STM) and other scanning probe techniques were used to modify the structure of surfaces very soon after its development.[3] The STM can inject electrons (holes) into empty (filled) states of the surface to result in structural change. Structural modification can also result from the surface-tip force interaction, and even mechanical contact.[3] The STM has been shown to be an ideal tool for nano-modification and *in-situ* STM characterisation. Much early work was undertaken on silicon surfaces: Avouris and co-workers[23] created protrusions and holes on the Si(111) surface with ±3 V sample bias pulses;

Lagally et al. carried out similar modifications of the Si(001) surface.[24] In both studies at RT, field evaporation of ions was the implicated mechanism. Evidence was also presented of a bridge-like structure forming between tip and surface. The STM tip has been used in a wide range of precise atomic modification, including those involving Si surface dangling bonds such as on hydrogenated surfaces.[3]

Ordered nanoscale architectures have been formed using STM. On GaAs(110), Cs 2D structures were formed by field induced effects at RT (+3 V for 0.1 s).[25] At RT using a high sample bias of +6, +10 V at a low tunneling current, silicon islands were formed on Si(111) by Shyklyaev et al.[26] The mechanism proposed was field-induced evaporation involving the transfer of atoms from the sample to the tip and from the tip to the sample.

The STM at higher temperature ~770-870 K, where lateral or bulk diffusion of material is promoted has been explored; Iwatsuki et al. (1992) formed facetted pyramid like structures on Si(111) and quadrangular structures on Si(100).[27] Using a sample tunneling bias of -0.3 to -0.8 V and tunneling current of 30-50 nA at high temperature, craters could be formed with an activation energy of 1-2 eV.[27] The mechanism at low bias and close contact was mostly identified as field evaporation of material towards the tip centre. Whether a pyramid or crater like structure is formed depends on the bias polarity. These structures were often found to be epitaxial to the substrate.

Field emission has been shown to be a mechanism involved in etching the surface by the STM tip. On oxidised Si(100) at 970 K, Li showed that the oxide layer was removed by the STM tip.[27] A linear relationship was found between the duration and the size of the quadrilateral nanoscale pits formed on Si(111) at 870 K.[28] Clean flat Si(111) and Si(001) regions could be produced on the oxidised surfaces. These were formed at large tip-sample distances ~100 nm and high bias 30-160 eV, where the electric field does not have as great an effect.[29] The mechanism of SiO_2 removal was found to be due to a Knotek-Fieldemen mechanism, where $O_2(g)$ and SiO are formed. At high temperature the SiO is volatile and desorbs.[30]

4.2.4 STM Modification of TiO_2 Surfaces

The STM has been used to modify the surface structure of TiO_2 surfaces.[6] Most work has been conducted on rutile TiO_2(110). Scans at +3 V were able to desorb the capping OH_b point defects.[19] Other adsorbates have also been desorbed by the action of the STM tip.[31] Pang et al. were able to form regions of a (1 × 2) surface by pulsing at +10 V; these could be transformed back to the (1 × 1) structure by further tip pulses.[19] Humphrey et al. carried out a similar investigation on an electron bombarded (e-beamed) surface; the action of the tip pulse resulted in a reformation of the (1 × 1) surface.[22] Klusek used repeated line scans above +4 V sample bias on the rutile TiO_2(110) to convert the surface to a modified granular (20 Å diameter) surface, and STS indicated the modified region had a reduced Ti_2O_3 structure.[32] Diebold and co-workers also used repeated ~+4-5 V STM scans to manipulate sub-surface vacancies. Under the action of the electric field on anatase TiO_2(101) these were pulled to the surface. A quantitative analysis indicated the involvement of "hot" non-thermalised surface electrons.[33]

4.2.5 Anatase TiO_2(101)

Anatase is the thermodynamically less stable form of TiO_2 with respect to rutile under all temperatures and pressures. Anatase's presence in nanomaterials[34,35] is due to the interplay between bulk and surface considerations at the nanoscale.[36] When anatase is heated a phase conversion to rutile can occur. The absolute temperature of this conversion (670-1470 K) to rutile is dependent on the impurities, crystallite size and other factors.[36] There are relatively few studies on single crystal anatase TiO_2 due to the limited availability of high quality single crystals, with the majority of work completed on thin anatase films grown on $SrTiO_3$ and $LaAlO_3$ substrates. The anatase (101) surface and can be prepared in UHV by annealing below the anatase to rutile conversion temperature to form a pristine (1 × 1) surface.[37] There are numerous DFT studies of the surface; [38,39] STM studies routinely obtain atomic resolution of the (1 × 1) surface. The surface at RT does not from stable oxygen vacancies,[40] resulting in its near

pristine appearance. E-beaming (300-500 eV) of the surface has been used to create surface oxygen vacancies at 107 K, imaged by STM.[18,41] After heating the surface to 230 K, the surface oxygen vacancies start to migrate into the bulk and are not present at 300 K.[18]

4.2.6 Rutile TiO_2(100)-(1 × 3)

Single crystal rutile TiO_2(100) can be prepared at 1000 K, resulting in a (1 × 1) surface evidenced by LEED; further annealing (1200 K) results in the formation of a (1 × 3) reconstruction.[42] SPM has identified three clear types of (100)-(1 × 3) reconstruction,[42] as well as a (100)-(1 × 7) termination.[43] A grazing incidence x-ray diffraction (GIXRD) study determined the 'microfacet' (100)-(1 × 3) structure formed of TiO_2(110) facets.[44] This polyhedral structure is shown in **Figure 4.1A**. This surface structure has no centre of inversion (*i)* ([010] and $[0\bar{1}0]$ inequivalent) and therefore the Ti_{5c} are not symmetrically placed in the (1 × 3) unit cell, explaining the asymmetry observed in STM. **Figure 4.1B** presents an STM image of a highly corrugated (5 Å) structure where the rows A and B are correspond to the unsaturated surface Ti positions in the model in **Figure 4.1C,** other Ti atom positions are identified by the black unit cell. The systematic absence of a bridging oxygen on the upper A site is deduced from STS and photoemission measurements.[45,46]

In addition, a recent structure determination of the TiO_2(1 × 3) was made by Landree et al.[47] using direct methods GIXRD. A reduced reconstruction of edge-sharing octahedra was determined as the structure, with a single Ti_{5c} per unit cell. This is analogous to the reduced Magnéli phases of TiO_{2-x}. This is referred to here as the Landree model and shown in **Figure 4.1D**, **4.1E** and **4.1F**, where Ti_{5c} and Ti_{6c} sites are indicated.

Figure 4.1G depicts an STM image of a mixture of (100)-(1 × 1) and what was assigned as the (100)-(1 × 3)-α microfacet.[42] The (100)-(1 × 3)-α was modeled as three bulk terminated rows, where two are separated by one unit cell (4.59 Å) in the [010] direction and the third row is shifted slightly (breaking Ti-O bond) towards the second.[42] **Figure 4.1H** presents the reduced (100)-(1 × 3)-β structure formed after annealing the (100)-(1 × 3)-α surface. The

defining features of the (100)-(1 × 3)-β structure, which contains three rows; *a*, *b* and *c,* is the low corrugation of ~2 Å and the appearance of rows *b* and *c* (rows of the lower Ti-O (1 × 1) surface) separated by one unit cell in the [010] direction, with *b* separated by half a unit cell from *a*.[42]

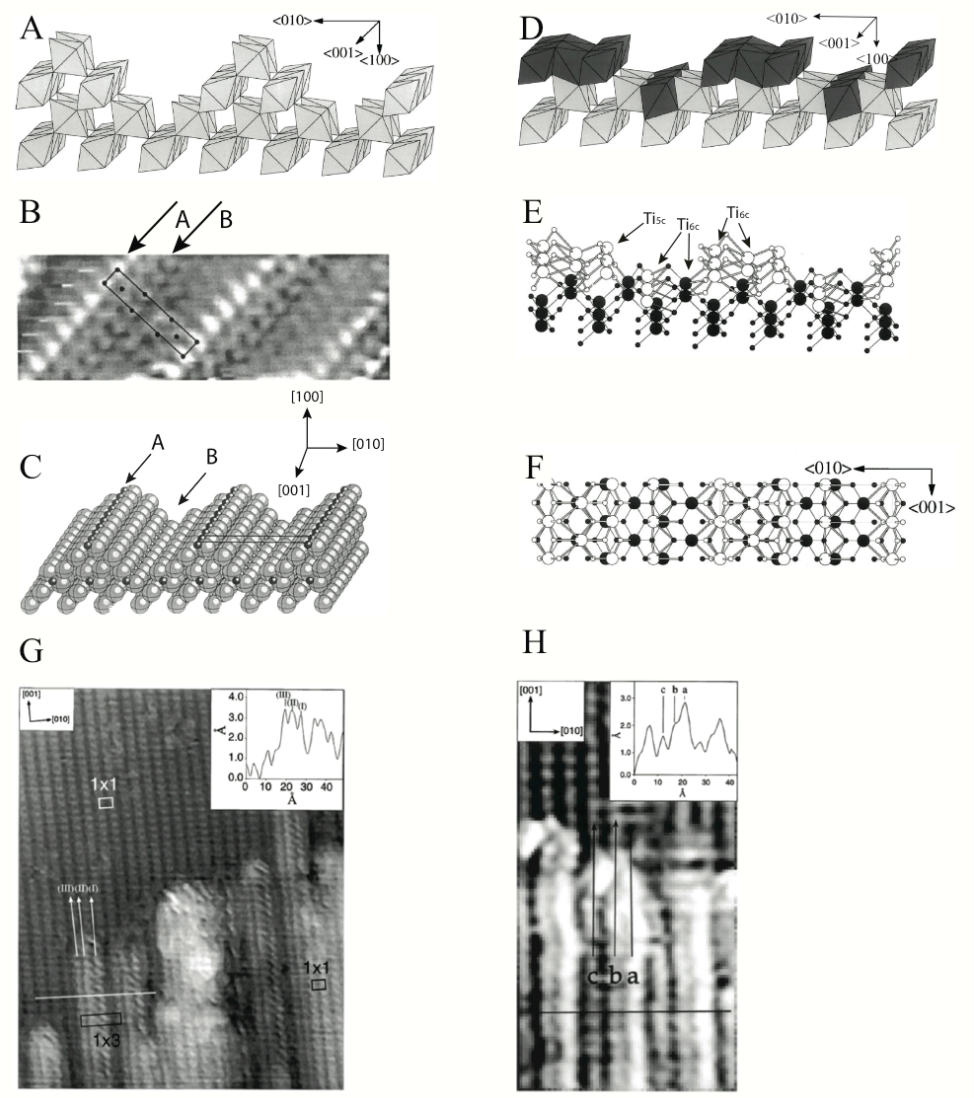

Figure 4.1: (A) An octahedron model of the proposed TiO_2(100) micro-facet (1 × 3). Adapted from reference.[44] (**B**) A constant current image (+2 V sample bias, 0.3 nA). A unit cell of the TiO_2(100)-(1 × 3) microfacet is overlaid on top of the image, rows A and B are labeled by arrows, identified in model (**C**). Adapted from reference.[48] (**C**) Filled ball model where rows A and B are identified. Azimuths are defined with respect to rutile. Adapted from reference.[48] **(D)** A more recent proposed octahedron model of the of the TiO_2(100)-(1 × 3) structure. Adapted from reference.[47] **(E)** A ball and stick proposed model of the more recent TiO_2(100)-(1 × 3) structure, where Ti_{5c} and Ti_{6c} sites are labeled in one unit cell. Adapted from reference.[47] The azimuth with respect to the TiO_2(100) surface are presented. (**F**) Top view of the structure displayed in **(E).** Adapted from reference.[47] **(G)** A 125 × 155 $Å^2$ STM image (+1 V sample bias, 0.8 nA) of the TiO_2(100)-(1 × 1) and (1 × 3)-α structure. Adapted from reference.[42] (**H**) A 50 × 70 $Å^2$ STM image (+1 V sample bias, 0.8 nA) of the TiO_2(100)-(1 × 3)-β structure. Adapted from reference.[42]

4.2.7 Nucleation of Rutile from Anatase

The rutile to anatase phase transition has been studied in depth;[36] in particular the structural characteristics in relation to photocatalytic activity. As discussed in Chapter 1, Shao et al. observed the rutile phase incorporated in an anatase (001) polycrystalline film. Of particular relevance to this Chapter, high resolution STM images (**Figure 4.2**) and diffraction spots measured in transmission electron microscopy (TEM) indicated the presence of epitaxial rutile TiO_2(100)-(1 × 3) domains.[49]

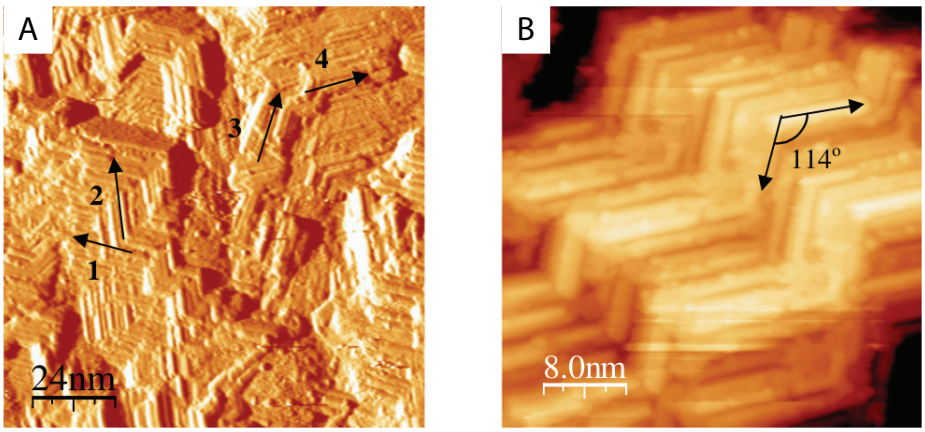

Figure 4.2: (A) A differentiated STM image of four rutile domains embedded in an anatase TiO_2(001) film of 50 nm thickness supported on a $LaAlO_3$(001) surface. **(B)** High resolution STM image showing rutile TiO_2(100)-(1×3) domains 3 and 4 that form a 114° angle. Adapted from reference.[49]

Modelling work has addressed the nucleation of rutile from anatase particles, finding that the (112) surface (ridge connecting {101} planes in particles) can support the TiO_2-II phase (α-PbO structure), which is kinetically favorable.[50] This is considered to be a pre-cursor to rutile growth and phase conversion. A junction of TiO_2-II sandwiched between two (112) anatase planes with a rutile phase attached at the interface was studied and shown to be structurally favorable.[51] Experimental evidence for such a system has been provided by Hosono et al. using SEM electron microscopy.[52]

Deskins et al. applied molecular dynamics (MD) simulations to determine favorable matches between planar surfaces of anatase and rutile; relevant to this study the arrangement of

anatase (101) to rutile (100) has a slightly lower negative adhesion energy (less stable) and mismatch % relative to the rutile TiO_2(110) surface of a large super cell, although both were relatively stable.[53] This former interface is presented in **Figure 4.3** due to its relevance to this work presented in this Chapter. The interfacial region between anatase and rutile was shown in this study to display disorder of 4 Å depth. A more recent study of a simulated rutile / anatase interface using DFT methodology, has indicated the presence of tetrahedral Ti_{4c} and oxygen vacancies (VO) at the interface as well as disordering.[54]

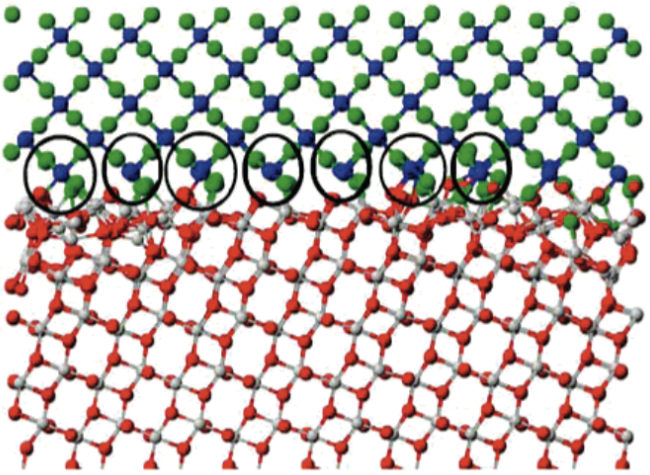

Figure 4.3: The interface formed by MD simulated annealing from anatase TiO_2(101) and rutile TiO_2(100) in the orientation where rutile-[010] and anatase-[$\bar{1}$01] are parallel. In the lower anatase layer Ti atoms are silver balls, O atoms are red balls. In the upper rutile layer, Ti atoms are blue balls, O atoms are green balls. The black ovals identify completed Ti octahedron at the rutile interface. Adapted from reference.[53]

4.3 Outline of Work

To study the technically important TiO_2 rutile/anatase interface with STM, the suitability of e-beam and tip pulsing methodology to synthesise a model system has been investigated. These two methods rely on the ability to drive the anatase (101) surface to the thermodynamically stable rutile phase.

Direct modification of TiO_2(101) with a defocussed electron gun (3 kV) was assessed. This resulted in a modified anatase (101) surface composed of many small non-equilibrium terraces, eventually forming a surface containing more amorphous features.

STM tip pulses were performed on this e-beamed surface. A new rutile crystalline surface phase was formed on the surface of the anatase TiO_2(101) (others are presented in the Appendix **A.4, A.5**), where a periodic lattice structure could be resolved by STM and evidenced to be distinct from the anatase TiO_2(101) surface. An epitaxial relationship to the anatase (101) is proposed and the mechanisms of surface structural change induced by the STM tip are discussed.

In an effort to further characterise the rutile TiO_2(100)-(1 × 3) phase identified on TiO_2(101) and resolve possible structural candidates, acetic acid was dosed *in-situ* onto the surface at RT and the adsorbed surface monolayer on the new surface phase was imaged by STM.

4.4 Experimental Details

All measurements were performed in a single UHV system, composed of a preparation chamber, to carry out cycles of sputtering and annealing, and an analysis chamber with an *Omicron* AFM/STM and LEED/AES optics. This system is described fully in Chapter 3.

The experiments were conducted at a pressure of 1×10^{-10} mbar. Argon and acetic acid were leaked into the chamber by backfilling UHV precision leak valves. The acetic acid was of 99% purity, purchased from Sigma Aldrich. All gases leaked into the chamber were checked for purity using a quadrupole mass spectrometer (QMS).

A natural anatase TiO_2 single crystal (*Pi-kem)* was used in this study with a (101) surface area of 3 × 3 mm^2 and a thickness of 2 mm. The crystal was attached to an *Omicron* Tantalum plate with spot welded strips of tantalum.

The anatase TiO_2(101) was cleaned in UHV by cycles of 20 minute 1 kV sputtering and 10-15 minutes annealing to 970 K; the temperature was measured (on the tantalum plate) by a pyrometer set to an ε emissivity of 0.25. This preparation was repeated until the AES signal of

carbon and other impurities were reduced to near the noise level, and a flat terraced surface was obtained in STM, with atomic resolution possible.

Electron beam (e-beam) irradiation was performed using an electron gun (*Thermo-Electron*) at RT. The source was thoroughly degassed prior to electron irradiation. The electron gun was positioned normal to the grounded anatase TiO_2(101) crystal at a distance of 12 mm. The focusing parameters were tuned so that at 3 kV a maximum 60 μA drain current was measured with an ammeter placed between the sample and ground. During e-beaming the total pressure was below 5×10^{-9} mbar.

Figure 4.4A is a photograph of the sample evidencing a blue florescent beam spot observed during electron irradiation. This was focussed to a diameter (2.8 mm) (**Figure 4.4B**) equivalent to the exposed face of anatase TiO_2(101) crystal. A beam spot of 0.19 cm^2 and a current density of 0.2 $mAcm^{-2}$ resulted in an average flux of electrons (1.602×10^{-19}C/e) of 1.5×10^{15} electrons $s^{-1}cm^{-2}$, with energy 0.7 $Js^{-1}cm^{-2}$. This is close to the $3.8\text{-}4.4 \times 10^{15}$ electrons $s^{-1}cm^{-2}$ flux used by Humphrey et al..[22] The e-beam profile was not determined, but is assumed, as previously done,[22] to be a Gaussian. Therefore a flux with a factor of $2\text{-}3 \times 10^{15}$ electrons $s^{-1}cm^{-2}$ and energy of 1.4 $Js^{-1}cm^{-2}$ at the centre of the beam is expected. This region is where the majority of STM measurements presented were taken and all atomic scale modifications with tip pulsing were realised. The temperature of the sample during the irradiation was measured using a thermocouple (K-type) connected to the sample plate housing. The temperature rise was ~15 K after 5-10 minutes of irradiation. STM measurements were performed on the irradiated sample after durations of 5-10 minutes. A maximum single duration of irradiation (35 minutes) was shown to result in a completely disordered surface. Possibly an interplay of temperature and electron intensity, although the temperature rise is computed (see 4.5.3) to be small.

LEED was performed on the surface at a beam energy of 67 eV. The LEED electron beam spot was ~1.4 mm in diameter judged by the blue fluorescent sample spot and positioned in the centre of the e-beamed area. All LEED photographs were identically filtered in photo-shop, inverted and made black/white.

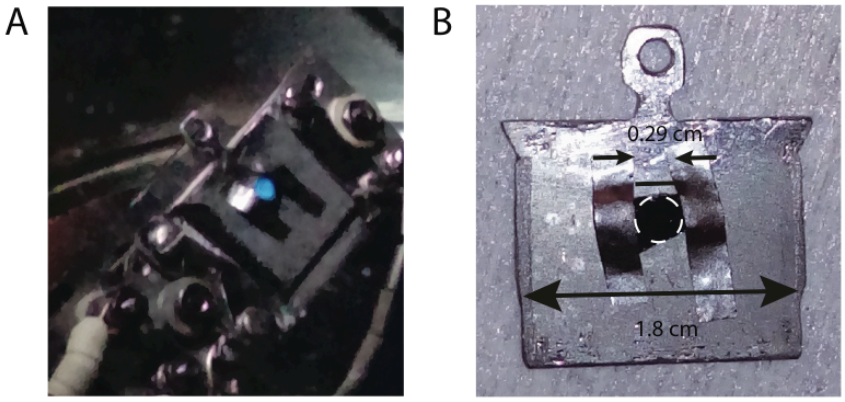

Figure 4.4: (**A**) Photograph of the anatase TiO_2(101) sample *in-situ* during electron irradiation. The blue fluorescence of the electron beam spot is evident. (**B**) The anatase TiO_2(101) sample mounted on the tantalum plate. The exposed width of the crystal is 2.9 mm; a dashed white circle indicates the position of the electron beam with a diameter of ~2.8 mm.

All STM measurements were performed with the same tungsten (0.4 mm diameter) electrochemically etched tip. The tip was inserted into UHV and degassed by heating with a filament at 370-470 K and conditioned by high sample bias +10 V scans at 1-5 nA. During experiments, the STM imaging was stable for ~12 hours.

All STM images were processed in the SPM image package Gwyddion®. Images were made level with respect to one terrace by deducting from the image the plane formed by three chosen points on a single terrace. Calibration was achieved for the *z*-direction by comparison to the anatase step height ~3.8 Å, and in-plane using the row spacing in the $[10\bar{1}]$ direction and resolution in [010] direction. An example of the way the calibration was performed is presented in the Appendix **A.3**. Polynomial functions were deducted from some images to flatten the entire image so a larger height range can be viewed more easily.

Tip pulsing was performed either on a clean sample prepared as described or on the surface after a total (5 + 3×10 minutes) 35 minutes exposure to electron irradiation at 3 kV. STM was performed on the e-beamed surface 1-5 weeks after formation, with the same surface in a background pressure of 10^{-10} mbar. The tip pulses were performed with the *Omicron* Spectroscopy function. Shown in **Figure 4.5** is a schematic of the pulsing process. The protocol was as follows; during a line scan in the formation of an STM image, the tip was halted in position and held at +1.6 V, 0.1 nA for 1 second. The feedback loop was disabled and the

voltage was ramped in increments of +0.2 V/100 μ seconds. After achieving the voltage set point of between +3-10 V sample bias, this was held for between 100-500 ms. During the tip pulse the current and distance were monitored and the former was measured to often be in excess of 50 nA, the limit of the STM current measurement. After an area was found to be of interest, standard STM experiments were typically run for 24-48 hours to best characterise the surface morphology. Images were recorded without moving the tip more than ~500-1000 nm from the pulsed region, during measurement (<100 hours), with the tip maintained in tunneling condition (+1.6V, 0.1 nA).

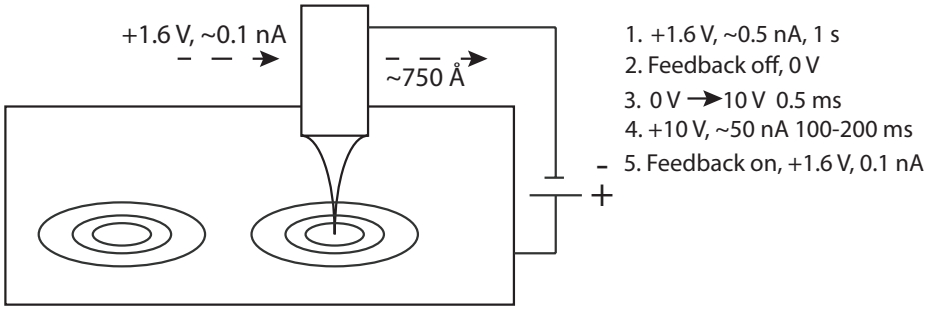

Figure 4.5: Schematic of the 'tip pulsing' procedure. The tip traverses the surface according to the protocol (1-5). During the tip pulse the STM feedback is disabled and the sample bias voltage is set to the pulse bias voltage (+4-+10 V). The concentric rings indicate the modified surface.

During STM, one of the pulsed regions was characterised by dosing acetic acid (CH_3COOH) *in-situ*. The acetic acid was leaked into the chamber through a precision leak valve. The acetic acid in the glass-to-metal sealed vial was purified by two cycles of: freezing (liquid nitrogen), evacuation by using turbo-molecular pump and warming to RT. The acetic acid purity was verified by using the RGA. The surface was imaged (+2 V, 0.1 nA,) *in-situ* during acetic acid exposure at RT, with a maximum pressure of 1×10^{-8} mbar (initial system pressure 2×10^{-10} mbar), while pumping the system using a turbo pump. A total time of 3000 s, equivalent to 22 Langmuir exposure resulted in a saturation coverage on all surface regions.

4.5 Results and Discussion:

4.5.1 Preparation of Clean Anatase TiO_2(101) Surface

As described in the experimental section, a natural single crystal of anatase TiO_2 was used. STM measurements have been performed on this crystal within the Thornton group, in the work of Grinter et al.[55,56] It has had approximately ~40 sputter and anneal cycles. The resulting reduced TiO_{2-x} was coloured black (see **Figure 4.4B)**.

Cycles of argon sputtering and annealing at 870 K resulted in a LEED pattern with a high background and diffuse (1 × 1) LEED pattern; STM evidenced a surface covered in amorphous (oxide) material. The temperature was increased to 970 K and the LEED pattern reduced in background and a sharp (1 × 1) pattern was obtained, (**Figure 4.6A**) with a characteristic surface formed.

Figure 4.6A presents an (inverted) photograph of a LEED diffraction pattern recorded at 67 eV after exposure for < 1 hour at 2×10^{-10} mbar in the analysis chamber. A single set of sharp spots is obtained, identifiable with the unreconstructed unit cell of anatase TiO_2(101)-(1 × 1).[56] These are the reciprocal representations of the real space primitive (green) unit cell or the centred unit cell 10.24 × 3.78 $Å^2$ (black). The corresponding real space unit cells are identified in the surface model of anatase TiO_2(101) (**Figure 4.6B**). The relationship between the real space vectors (**a1**, **a2**) and (**b1**, **b2**) and reciprocal space vectors (**a1'**, **a2'**) and (**b1'**, **b2'**) are shown in **Figure 4.6C**). The reciprocal mathematical relationship is described in Chapter 2.

The AES spectrum in **Figure 4.6D** displays a single scan from 180-580 eV at 100 μA and 1.4 kV. Minor peaks are evident at 220 eV and 280 eV, corresponding to argon embedded in the surface during the sputtering procedure and a very small residual quantity of carbon, respectively. The main prominent peaks can be identified with Ti LMM (385 eV) and O KLL (515 eV) of the TiO_2 single crystal. The AES indicates a line shape and ratio of Ti/O comparable to previous work on anatase TiO_2(101), including work undertaken with the same

crystal.[56] A top down view of the (101) surface is shown in **Figure 4.6B** with the unit cells identified and azimuths labelled.

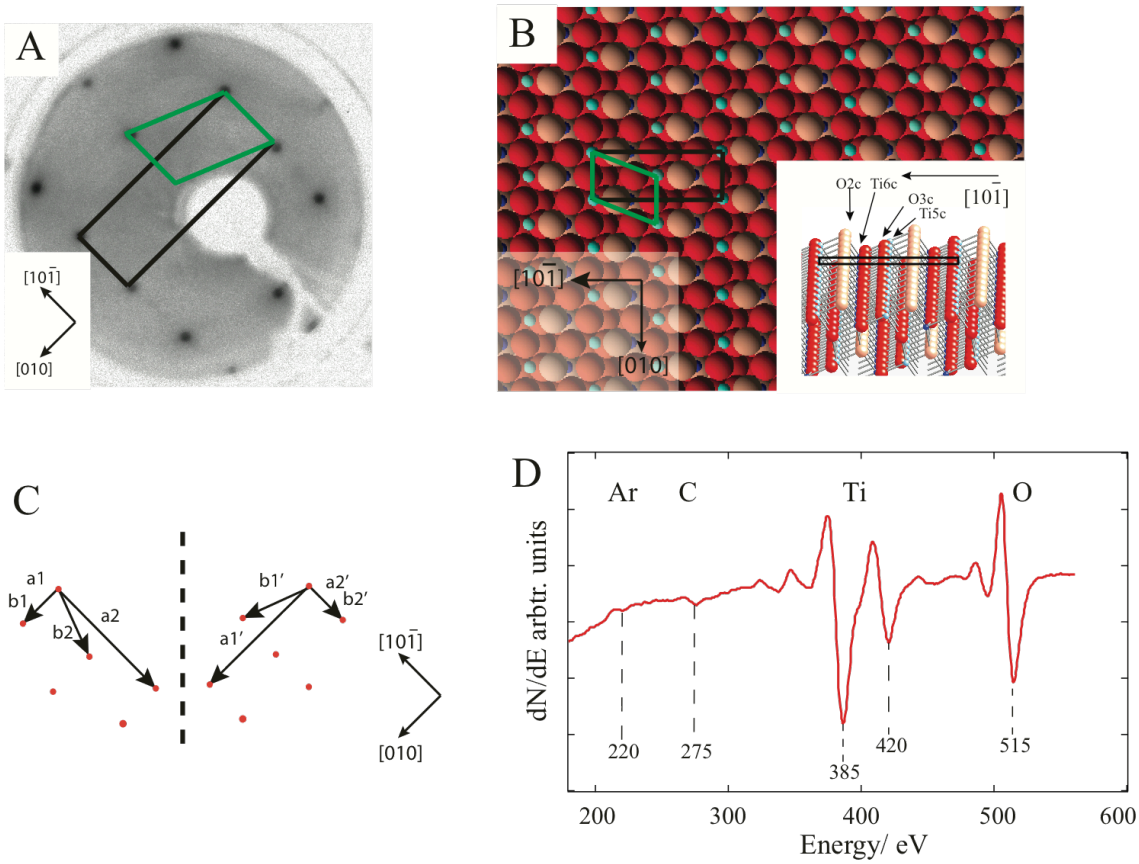

Figure 4.6: (**A**) LEED obtained at an electron beam energy of 67 eV. The primitive (green) and centred (black) unit cells are identified. The (101) azimuths are displayed. **(B)** Ball model of the top view of the anatase (101) surface; the black (3.78 × 10.24 Å^2) and green primitive cells are indicated. Inset: tilted view ball and stick model of the anatase TiO_2(101) surface. The light blue spheres are titanium atoms (5c), the dark blue spheres are the titanium atoms (6c), the red and beige spheres are the (3c) and (2c) oxygen atoms respectively. The (101) azimuths are displayed. **(C**) The real (left) and reciprocal (right) (101)-(1 × 1) LEED pattern. (**D)** AES 1.4 keV spectra recorded with LEED optics.

STM indicated that some damage was occurring on the surface after exposure to the AES for 30-45 minutes at 1.4 kV, with similar phenomena to the e-beamed surface presented here. Therefore, LEED and AES were used sparingly in subsequent preparations of the clean and e-beamed surface.

Figure 4.7 presents empty states STM images of the surface after preparation at 970 K. The large-scale STM image (**Figure 4.7A**) depicts a surface composed of large terraces of

3000-5000 Å × 100-500 Å width. This surface roughness was acceptable for the tip and electron beam modification and gas dosing experiments, with routine imaging possible.

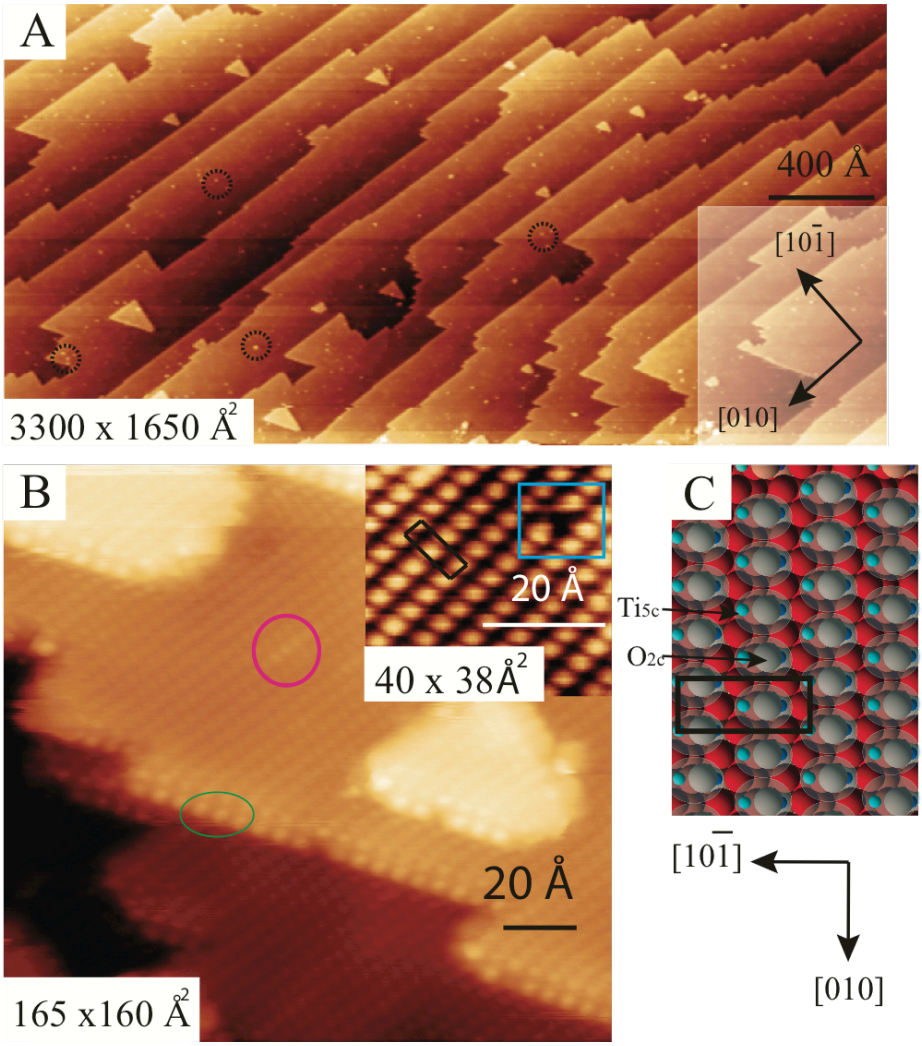

Figure 4.7: (A) 300 K 3300×1650 Å^2 empty states STM image (+1.6 V, 0.1 nA) of the anatase TiO_2(101) surface after preparation. Inset: the (101) azimuth is shown. Impurities attributable to carbon are identified by the dashed black circles. **(B)** 300 K A representative high resolution 165×160 Å^2 image; tunneling conditions +1.6 V, 0.4 nA, displaying an atomically resolved step edge (green oval) and a point defect (pink circle) extended in the [010] direction. Inset: zoom of the (1 × 1) surface. Bright oval protrusions are Ti_{5c}-O_{2c} pairs, a blue square identifies a point defect (water), the non-primitive unit cell is identified (black rectangle). Theses images share the azimuth orientations in (**A**). **(C)** On-top view of a model of the (101) surface. Ti_{5c}-O_{2c} pairs are identified by translucent grey ovals. The unit cell (black rectangle) and O_{2c} and Ti_{5c} sites are identified. The red balls are O_{3c} atoms and the light blue balls Ti_{5c} atoms. The O_{2c} are beige (grey because of the grey translucent oval). The azimuths with respect to the (101) surface are shown.

Diebold and co-workers investigated the thermodynamic preference of step edges on anatase TiO_2(101),[57] where the theoretical prediction of the stability of the [$\bar{1}$11] and [11$\bar{1}$] step edges leads to triangular/trapezoidal terrace features ([10$\bar{1}$] direction directed to the large base).

Our images (**Figure 4.7A**) evidence strips of terrace running in the [010] direction and the triangular terrace structures, which allows the direction of the $[10\bar{1}]$ to be determined. There is some contamination present at this scale, which is assumed to be the carbon identified in AES. High-resolution STM images are presented in **Figure 4.7B,** which display atomic resolution. Bright ovals with a repeating 5.1 × 3.7 $Å^2$ arrangement are identified; the centred 10.24 × 3.78 $Å^2$ unit cell is shown by the black box in **Figure 4.7B** inset. A blue box indicates a point defect, with a depression centred at a $Ti_{5c} – O_{2c}$ site,[58] is characteristic of adsorbed water.[59] A step edge with a resolved Ti features is observed (green oval). In addition a pink circle identifies is a feature attributable to impurities in the mineral sample. These latter features have also been reported previously.[41,57,60] Recent evidence has demonstrated that in empty state images recorded at positive sample bias the Ti d-orbital states contribute most to the bright oval (**Figure 4.7B**) where geometrically, the region extends over the Ti_{5c}-O_{2c} site.[58] The top view ionic ball model of the anatase TiO_2(101) surface is shown in **Figure 4.7C**. The translucent ovals correspond to the ovals in atomically resolved anatase TiO_2(101) images.

4.5.2 Preparation and Study of the 3 kV E-beamed Anatase TiO_2(101) Surface

E-beaming of the anatase TiO_2(101) surface was undertaken for two principal reasons. First, to assess whether any surface phase transition could be effected on the anatase surface as had previously been demonstrated on TiO_2, albeit with a much higher energy.[12] The second was to assess the efficacy of STM tip pulsing on an e-beamed (3 kV) disordered anatase surface in order to form a patch of rutile. A parallel study has been conducted on rutile TiO_2(110) by Humphrey et al.[22] It should be noted that a preliminary tip pulse experiment on as-prepared anatase TiO_2(101) proved to be unsuccessful, resulting in amorphous structures, with no lattice structure resolvable by STM.

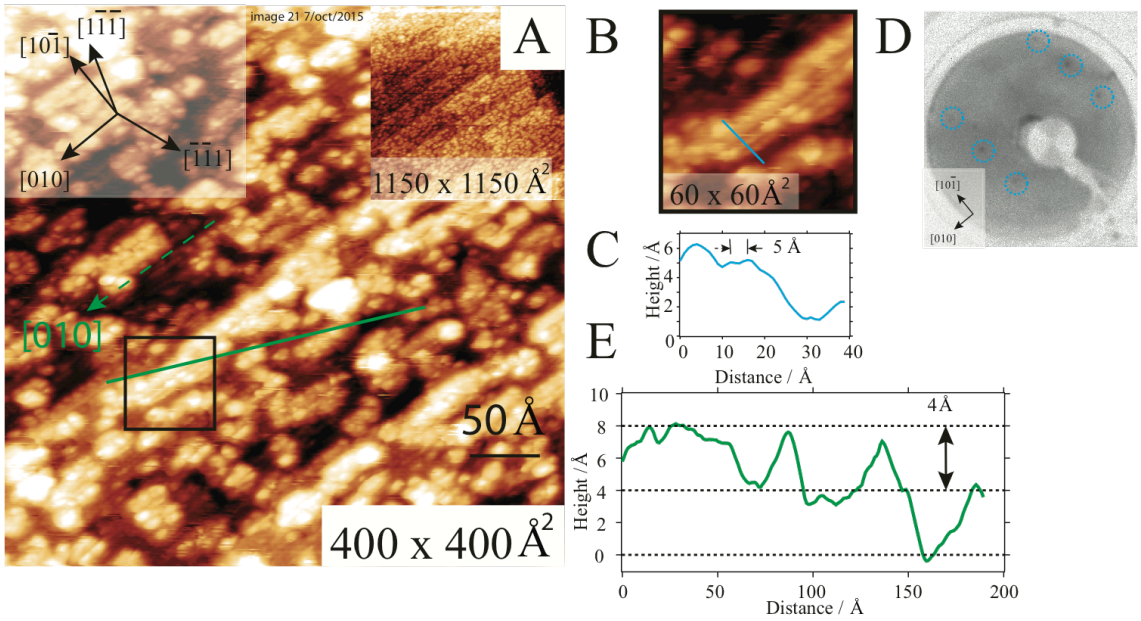

Figure 4.8: Centre of the anatase TiO_2(101) sample after 15 (5 + 10) minutes total time of e-beaming (2-3 × 10^{15} electrons $s^{-1}cm^{-2}$ electron flux). **(A)** 300 K STM image 400×400 Å^2 (+1.6 V sample bias, 0.1 nA) after 15 minutes (5+10) e-beaming. A green line profile is overlaid along one terrace. A dotted green arrow depicts the [010] surface direction. Top left inset: azimuths of the principal directions of (101) surface are shown. Top right inset: 1150 × 1150 Å^2 zoom-out of the surface. **(B)** An enlarged STM image 60 × 60 Å^2 displaying rows in the [010] direction. A blue line profile is overlaid across one island. (**C**) Line profile indicating the distance of the rows in the [10$\bar{1}$] direction. **(D)** Photograph of a LEED diffraction pattern (101)-(1 × 1) of the surface at 67 eV (1.5 mm beam d), the reciprocal space reflexes of the real space unit cell (10.24 × 3.78 Å^2) are identified (blue circles). **(E)** STM height line profile from the green line in (**A**), the double arrow indicates the apparent step height of ~4 Å, with three (top, middle, bottom) step height layers identified by the horizontal black dashed lines.

The STM image **Figure 4.8A** depicts the centre of the anatase TiO_2(101) surface after a 15 min. total irradiation time (5+10) minutes of e-beaming (3 kV, 60 μA). The centre of the surface after 5 minutes is presented in the Appendix (**A.1**). The surface retains the characteristic trapezoidal anatase (101) terrace morphology (**Figure 4.8A** inset) and is now formed of small rectangular-like islands of length 40-80 Å and width 20-40 Å, in registry with the (101) surface. The presence of (101)-(1 × 1) terminated (~5.1 Å width) rows and amorphous features (see **Figure 4.8B** zoom and line profile **Figure 4.8C**) is apparent and corroborated by the faint (1 × 1) LEED diffraction pattern recorded at 67 eV (**Figure 4.8D)**; blue dashed circles outline the **a1'** and **a2'** reciprocal reflexes, as defined in **Figure 4.6C**. A height profile (green line) along the terrace (**Figure 4.8E**) demonstrates a single step height layer (~4 Å) of the islands and three anatase TiO_2(101) layers of ~3.8 Å height existing simultaneously on what were (on the clean

surface) single layer terraces. The area percentages of the three layers as determined from a 16000 $Å^2$ area STM image are; top layer (44%); middle layer (52%) and bottom layer (4%).

The islands are of quasi-equilibrium geometry;[57] irregular curved edges are present with prominent thermodynamically stable step edges identified by the green dashed arrow in the [010] direction in **Figure 4.8A**.[57] The rectangular islands are extended parallel to the [010] direction. This observation indicates an electron beam formation process not controlled purely by the thermodynamic stability of the resulting surface, where apparent preferential removal/bulk migration of TiO_2 layers in the [010] direction occurs, driven by a lower activation energy in forming [010] orientated step edges.

There exist no SPM studies of anatase TiO_2(101) reconstructions or reports of e-beaming at high exposure, as described here. This contrasts with the situation for rutile TiO_2(110), for which Pang et al.[19] at RT and by Mentes et al.[11] at 720 K have reported thermally driven reconstructions.

The intermediate stage of electron beam surface damage was investigated in this thesis as previously Humphrey et al. observed an electron flux dependent behaviour at the centre and outer edge of an e-beamed (3 kV) rutile TiO_2(110);[22] with the outer edge studied by STM. **Figure 4.9** depicts STM images recorded at the edge of the e-beamed anatase (15 minutes total irradiation time). An approximate electron flux of $5\text{-}7\times10^{14}$ electrons $s^{-1}cm^{-2}$ is expected at the edge, which is 25% of that at the centre. In **Figure 4.9A** the anatase TiO_2(101)-(1 × 1) atomically resolved surface is apparent in the STM image, with depressions of dimensions (5.12n × 3.78m), where (n, m) are integers. The mean width is 10 Å (n), and length is 14 Å (m), determined from a 500×500 $Å^2$ image, equivalent to ~ n = 2, m = 4. The aspect ratio (m/n) of ~1.3 indicates an extension of these features in the [010] direction. Two-row width (black dashed box) and single row width (green dashed box) dark features of lower height are identified. In addition, bright protrusions in close proximity appear that are absent from the as-prepared surface.

STM images from e-beamed surfaces were recorded with bias voltages ranging from +1.6 V to - 1 V and images are presented in the Appendix (**A.2**). No significant variation in

STM height was evidenced in the features, signifying a likely structural origin and not a feature of the local density of states (LDOS) resulting from the (101) subsurface.[41,61] Line profiles in **Figure 4.9B** indicate an apparent depth of ~2 Å (half a TiO_2 layer). These features are similar to the 'nano-cracks' unit cell width structures observed by Humphrey et al., after exposing a rutile TiO_2(110) to a low flux of 3 kV e-beam; there an auto-compensated surface formed by the removal of TiO_2 units was proposed.[22]

In recent studies[33] Setvin et al.[61] and Scheiber et al.[18] identified depressions after annealing (450 K) an e-beamed (500 eV, 8 μA cm^{-2}) anatase TiO_2(101) surface at 105 K. The depressions were identified as clusters of sub-surface O_{vacs}. These O_{vac} are formed by e-beaming, which then form clusters if the local temperature is sufficient to activate the process. We suggest that our features result from the same O_{vac} mediated process and are notably similar to a 'pitting' layer formed on rutile TiO_2(110) after e-beaming at 75 eV.[19] The bright protrusions are suggestive of adsorbates or unsaturated Ti and Ti_{4c}/Ti_{5c} sites produced at the edges of removed surface layers. These could be carbon, which would be in line with the formation of Ti-C demonstrated by Vergara et al. for electron irradiation of rutile TiO_2(110) after e-beaming (3 kV and 30 $mAcm^{-2}$).[13]

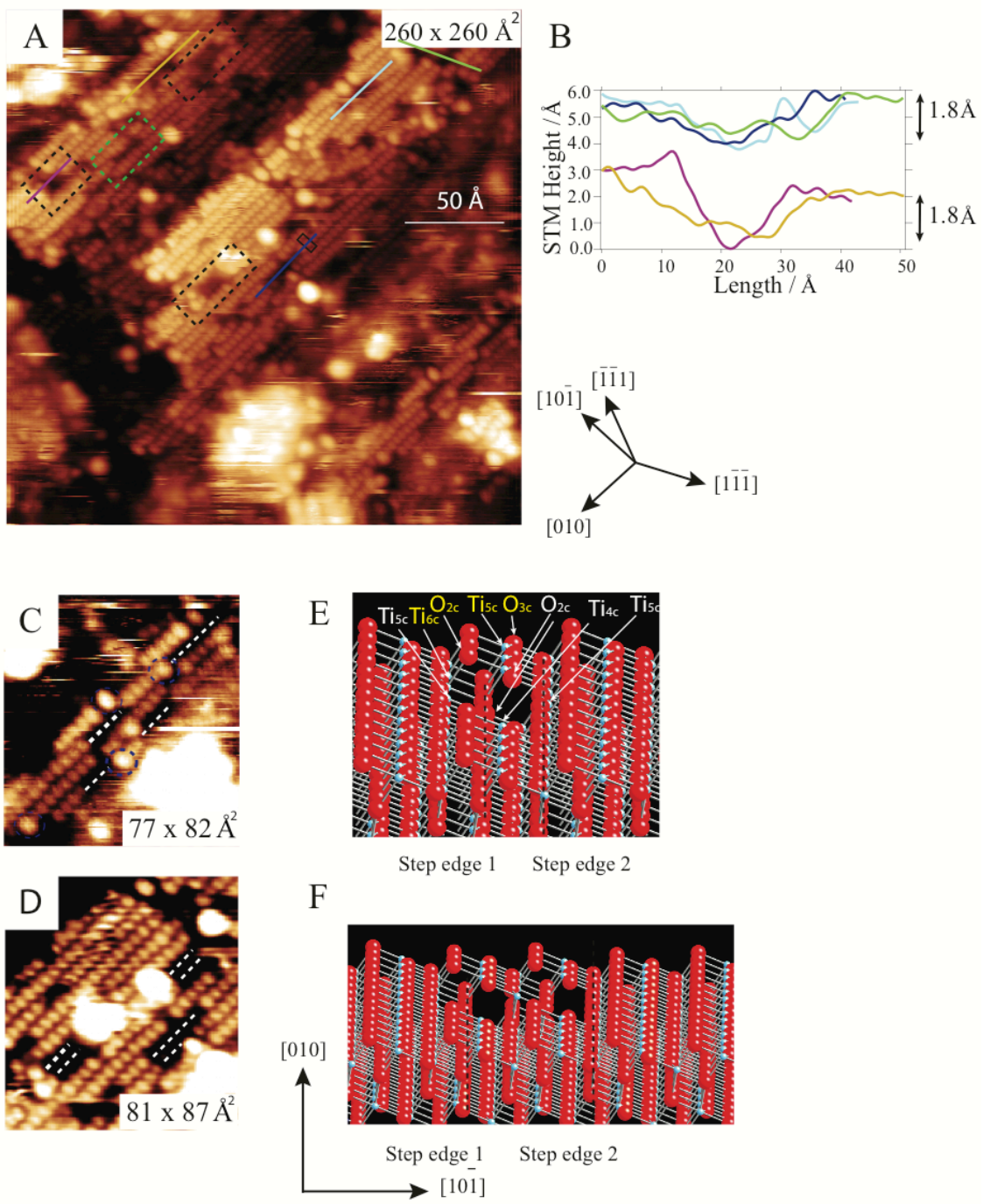

Figure 4.9: 300 K STM image (+1.6 V sample bias, 0.1 nA) at the outer edge of the e-beamed (5 +10 minutes) (5-7×10^{14} electrons $s^{-1}cm^{-2}$) anatase TiO_2(101) surface. **(A)** A STM image 260 × 260 Å^2. The black dashed box identifies 10 Å width depression; the green dashed box identifies a 5 Å width depression. The (101) surface azimuths are identified. (**B**) STM line profiles corresponding to the coloured lines in (**A**). **(C)** Zoomed-in 77×82 Å^2 image, where single row width (white dashed lines) are indicated. **(D)** Zoomed-in 81×87 Å^2, where double row width (white dashed line) are indicated. **(E)(F)** Anatase TiO_2(101) ball and stick models with a single missing TiO_2(101) row (**E**) ~5 Å width and double missing TiO_2(101) row ~10 Å (**F**). Two step edges (1 and 2), parallel to the [010] direction are indicated by the dashed black lines. The (101) azimuths are shown for the models.

Shown in **Figure 4.9C and 4.9D** are zoomed in images of the anatase TiO_2(101) surface containing rectangular depression features of 5 Å width (single row) and width 10 Å width (double row), extended in the [010] surface direction and identified by white dashed lines. Tentative anatase TiO_2(101) stoichiometric surface structural models to explain the STM data are presented in **Figure 4.9E** and **4.9F**. The structural models are formed by the removal of neutral TiO_2 units, 2 O_{2c} (1 Ti), Ti_{5c} (3 O) and O_{3c} (2 Ti) unit, where the parentheses indicate the number of bonds broken. These plausible structural models are presented on the basis of; i) the structures are formed by removing an integer number of neutral TiO_2 units, hence preserving the surface stoichiometry and fulfilling Tasker's rule of auto-compensation;[62] ii) the structure results in the formation of thermodynamically stable non-identical step edges calculated by Gong et al.[57] These previously modelled [010] direction steps have energies of 0.10 (step edge 1) and 0.13 eV $Å^{-1}$ (step edge 2) and the former forms the base of the observed trapezoidal terraces;[57] iii) the models proposed are consistent with observations at low and high electron flux.

Double row width (~10 Å) depressions would result from the removal of adjacent rows by the loss of TiO_2 units. In our model the central separating TiO_2 unit is removed, on the basis that the Ti site would be four coordinate and unstable.[37] To fully determine the structure, further SPM and theoretical modelling studies are clearly required.

To further disorder the surfaces; two additional 10 minute e-beam doses were completed without surface re-preparation. STM images (centre of the e-beam) are shown in **Figure 4.10**. **Figure 4.10A** is a 350 × 350 $Å^2$ STM image; where the (101)-(1 × 1) surface is still present as indicated by the atomically resolved zoomed-in inset. An increase in amorphous patches (black dashed circle) to ~0.2 ML coverage is observed and removed sections of terrace (green dashed box) are identified. The ratio of the 1st, 2nd and 3rd areas of terraces defined previously indicates that the 1st makes up 21% surface area, the 2nd layer makes up 67% surface area and the 3rd layer below makes up 12%. Therefore, the protruding islands of TiO_2 have been preferentially removed. After a further 10 minutes (**Figure 4.10 B**), the amorphous patches still occupy ~0.2 ML in which the 1st layer is 15%, the 2nd layer 43 %, and the 3rd layer 42 %. After a

total aggregate time of 35 minutes e-beam, the (101)-(1 × 1) surface is still present and corroborated by the (101)-(1 × 1) LEED diffraction pattern (**Figure 4.10B** lower inset), noticeably sharper than the intermediate stage after 15 minutes.

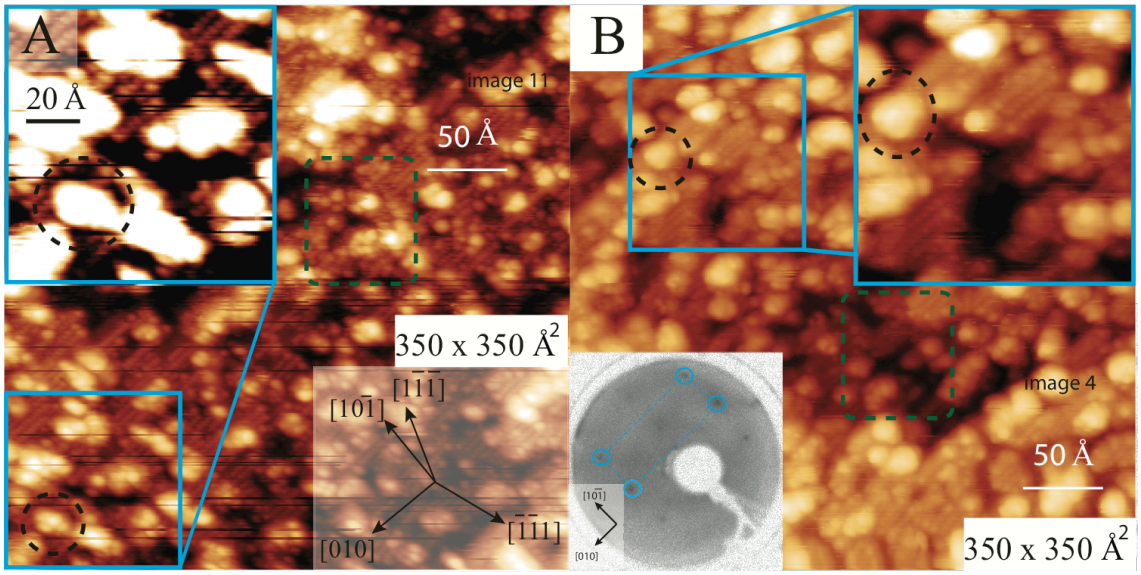

Figure 4.10: (A) 300 K 350×350 Å^2 STM images (+1.6 V, 0.1 nA) images of the anatase TiO_2(101) surface after a further 10 minutes e-beaming (10+10+5 = 25 minutes). Upper inset: zoom at 110×100 Å^2. Lower inset: the azimuths with respect to the (101) surface. **(B)** 300 K 350×350 Å^2 image (+1.6 V, 0.1 nA) of the surface after a further 10 minutes e-beaming (total: 5+10+10+10 = 35 minutes). The green dashed boxes identify the areas where the third lower layer is visible, black dashed circles identify amorphous regions. Upper inset: a 90 × 90 Å^2 zoomed-in image of the surface. Lower inset: LEED patterns obtained at 67 eV beam energy where blue circles identify reflexes of the TiO_2(101)-(101) centred unit cell (10.24 × 3.78 Å^2).

4.5.3 Discussion of E-beam Mechanism

An annealing process induced by the e-beam could be considered. Pittaway developed heat transport equations to describe the surface heating effect of an electron beam.[63] This model assumes that the electrons impart all energy, the beam spot is a vanishingly thin disc with a Gaussian distribution and heat exchange with the surroundings can be neglected; the surface temperature rise at time t_2 at the beam centre for a semi-infinite solid is defined as:

$$T\ /\mathrm{K} = \frac{I_P E_p}{\pi^{\frac{3}{2}} K d} tan^{-1} 2\left(\frac{K t_2}{\rho c d^2}\right)^{1/2} \quad . \qquad \text{Eqs. 4.1}$$

Here I_P (C s^{-1}) is the current, E_p the beam energy (Cal C^{-1}), K (Cal.$cm^{-1}K^{-1}$) the thermal conductivity, d (cm) is the std. deviation of the e-beam spot (~ radius), ρ (g cm^{-3}) is the density, c (Cal g^{-1}) the specific heat and t_2 is the final time where $t_1 = 0$. For bulk anatase TiO_2 K is 0.02 Cal.$cm^{-1}K^{-1}$.[64] This results in a steady state ($t_2 \sim \infty$, $\tan^{-1}2(\frac{Kt_2}{\rho c d^2})^{1/2} \rightarrow \pi/2$), $T_\infty/K = \frac{I_P E_p}{\frac{1}{2\pi^2}Kd}$ temperature rise. For our parameters of: I_P = 60 μC s^{-1}, E_p= 720 Cal.C^{-1}, d = 1.44×10^{-1} cm the maximum computed rise is ~4 K. This is in line with the temperature rise we measure on the sample holder of 15 K and insufficient to explain the STM observations.

The energy of e-beaming of 3 kV is also far below the 100 kV required to cause 'knock on' sputtering of surface atoms with electrons. The transferred energy through collision is 0.5 eV (two body), 1-5% of a reasonable atom desorption energy 10-50 eV.[4] Therefore this explanation is neglected.

A radiolysis mechanism involving an Auger process through the initial removal of a Ti core electron in our energy range, is the most likely explanation. This would involve the ejection of O^+ from the surface. Subsequent bulk migration of Ti would lead to the half step height features (**Figure 4.9**) and full step height islands ~ 4 Å (**Figure 4.8**). The O_{vac} migration and formation of sub-surface clusters at RT feature by Setvin et al.[33] are also consistent with our results.

The e-beaming of rutile TiO_2(110) (3 kV, 30 mA cm^{-2}) by Vergara et al. resulted in the formation of surface Ti_2O_3 and TiC; this is in accord with observations by Pang of (n × 2) reconstructions,[19] and the demonstration of increased Ti^{3+} in XPS by Wang et al..[65] The expectation is that our anatase surface is reduced in comparison to the as-prepared surface.

Overall, our data indicate a cyclic process where small rectangular islands are formed, which are then preferentially removed. This process is repeated, with the generation of amorphous material. Here less amorphous disordering of the surface occurs in comparison to work on TiO_2(110) with a focused electron beam (15 kV and 3 nm diameter).[66] Work on rutile TiO_2(110) also demonstrated patches of amorphous oxide under similar conditions.[22]

During the e-beam procedure, LEED (67 eV) diffraction patterns were recorded at the sample centre, co-incident with e-beam spot centre. The (101)-(1 × 1) LEED pattern remains throughout the procedure, with an oscillation in spot brightness observed: brighter after 5 and 35 minutes than the intermediate 15 minute stage. The surface at this intermediate stage, has a minimum terrace size, formed of small islands (ca. 50% area coverage) resulting in a diminished coherent diffraction. In addition, no apparent spot splitting due to periodic reconstructions or formation of new phases are evidenced by LEED.

4.5.4 Tip Pulsing on the E-beamed Modified Anatase TiO_2(101) Surface

Here the intention is to use the STM tip to modify the surface of anatase TiO_2(101) to produce a region of the rutile phase, providing a suitable system to investigate the rutile/anatase interface with STM/STS. There are some constraints:

i) The anatase-rutile interface region is required to be of a sufficient size for adequate STM photochemical studies with adsorbed photo-reactive molecules;

ii) characterisation can only be achieved *in-situ* by STM, therefore a sufficient domain size is required ~1000 $Å^2$, where the periodic and/or lattice defect structure can be reliably identified.

iii) A short interface with the underlying anatase (101) is desirable.

There are limited reports of the effect of the STM tip electrical field to modify the anatase TiO_2(101) surface,[61] particularly under high tip-sample bias and current.[33] It is clearly beneficial to investigate the fundamentals of this process and acquire mechanistic understanding to improve control. A large effort was made to form ordered structures (rutile or otherwise) by the effect of the tip pulse on the clean anatase TiO_2(101) surface. The tip formed only amorphous surface morphology.

STM tip modification was performed in the centre of the e-beamed anatase TiO_2(101) surface (**Figure 4.10B**). The disordered surface where a large step edge density is present, is

likely to be conducive to the formation of a new crystalline surface. Principally, this is because; i) the step edge density results in a higher surface energy and therefore is more amenable to transformation; (ii) the additional step density could favourably influence the epitaxial nucleation and growth of new poorly-matched (compared to regrowth of anatase (101)) crystalline surfaces, allowing relaxation, as demonstrated in ultrathin films on metal substrates.[67]

In line with the clean surface, structural modification was observed only above a +4 V sample bias. A +4 V sample bias was also the threshold to cause structural modification to TiO_2(110) in an STM report by Klusek et al.[32] Our value is also coincident with the +4.3 V threshold observed by Setvin et al. required to pull sub-surface oxygen vacancies to the surface on anatase TiO_2(101).[61]

Figure 4.11 displays STM images (3130 × 3130 Å^2) of arrays of tip-induced modified (+4 V- +10 V sample bias, 100 ms, 3.5-50 nA) areas of surface. One such array (+4 V) is shown in **Figure 11A**. Some events resulted in no change, likely due to a change in the STM tip apex. Horizontal streaks in the image recorded during the tip pulses (not shown) indicated some tip surface interaction. The zoomed-in image **Figure 4.11B** (720 × 720 Å^2) depicts the characteristic modification of the anatase (101); a poorly resolved mound (pink dashed circle) within a hole of displaced surface (green dashed circle). Crystalline features were detected at the outer edge of this mound. The outer area (dark blue dashed circle) is cleared of amorphous small features and composed of small 30 Å terrace, where the (101)-(1 × 1) (10.24 × 3.78 Å^2) surface of resolved Ti_{5c}-O_{2c} rows are present as shown in the zoomed 65 × 65 Å^2 **Figure 4.11B** inset. These rows are aligned with the LEED and STM determined principal crystallographic [010] surface direction. The diameter of the hole, mound, outer region and mound height monotonically increased with tip bias voltage as shown in the +6 V (**Figure 4.11D,E**) and +10 V (**Figure 4.11G,H**) images. Red line profiles across the modified regions are displayed in **Figure 4.11C, F, I.** Here the typical mound heights (20-46 Å) and mound hole diameters (250-700 Å) are indicated. A typical 'volcano-like' indentation at the centre of the pulse is indicated in **Figure 4.11F,** with further examples shown in the Appendix (**A.4** , **A.5**).

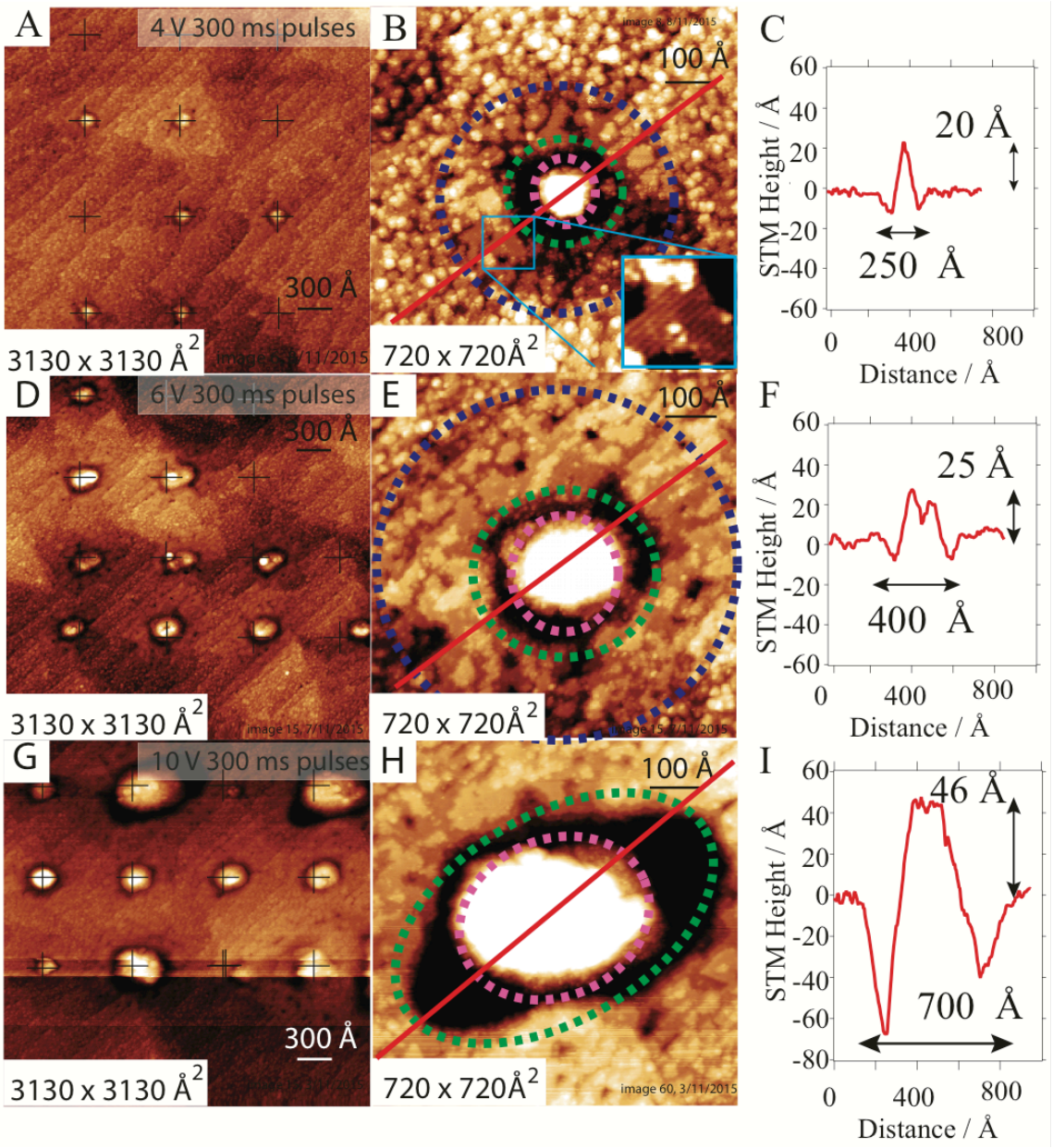

Figure 4.11: 300 K STM images (+1.6 V, 0.1 nA) of tip-modified anatase TiO_2(101) after e-beaming (35 minutes, 3 kV, 0.2 $mAcm^{-2}$). **(A)** 3130 × 3130 $Å^2$ STM image of a surface modified by +4 V, 100 ms, ~3.5 nA, tip pulses **(B)** A high magnification 720 × 720 $Å^2$ STM image of one modified region. Three pulsed regions are identified; the healed outer area (blue dashed circle); the inner hole (green dashed circle) and mound (pink dashed circle). A red line profile is overlaid. Inset: a 65 × 65 $Å^2$ zoom-in image (blue box) of the healed region. **(C)** Height line profile from the red line in (**B**), where the height of the mound (20 Å) and diameter of the hole (250 Å) are indicated. **(D)** A 3130 × 3130 $Å^2$ STM image of a surface modified by +6 V, 100 ms tip pulses, 50 nA. **(E)** A high magnification 720 × 720 $Å^2$ STM image of one modified region with identical features identified as in (**B**). (**F**) Height line profile from the red line in (**E**) where the height of the mound (25 Å) and diameter of the hole (400 Å) are indicated. **(G)** A 3130 × 3130 $Å^2$ STM image of a surface modified by +10 V, 100 ms pulses, 50 nA tip pulses. **(H)** A high magnification 720 × 720 $Å^2$ STM image of one modified region, with identical features identified as in (**B**). (**I**) Height line profile form the red line in (**H**), where the height of the mound (46 Å) and diameter of the hole (700 Å) are indicated. Black-crosses identify the pulse centre in all images.

[3] 50 nA was the maximum measured current in the *Omicron* spectroscopy measurements

The formation mechanism is uncertain, although field evaporation towards the highest electric field strength point, directly under the tip, is likely. This has been proposed in similar studies, where the surface dipole and tip-field attractive interaction were invoked to explain similar structures, such as Avouris et al's report on Si(111).[23] A localised heating resulting from field-emitted electrons no doubt has some effect; however, the central depressions in the mound structures would suggest that tip-surface mechanical contact occurs during the pulsing event. A flow of current upon mechanical contact is likely to lead to localised heating, explaining the annealed appearance of the outer anatase TiO_2(101)-(1 × 1) and the formation of the mound. Under these conditions deposition of some tip tungsten oxide is conceivable.

Figure 4.12 is a correlation between the mean diameter of the modified outer area (red), inner hole (blue) and mounds (green) (identified in image **Figure 4.11** by the blue dashed circle, green dashed circle and pink dashed circles respectively) as a function of sample bias voltage pulse set point. The diameter data points in **Figure 4.12** are mean averages of 10-30 pulsing event measurements, with the error bar determined from one standard deviation. For the oval pulsed areas an averaged diameter was used. The three diameter measurements are apparently closely correlated with bias voltage, indicating; i) all are sensitive to the electric field ($VÅ^{-1}$) and power density ($W.Å^{-2}$) of the pulses; ii) the correlation in hole/mound diameter suggests that the mound results from accretion of surface material and not deposition from the tip, as dropping of tip material would not be expected to require the removal of surface layers.

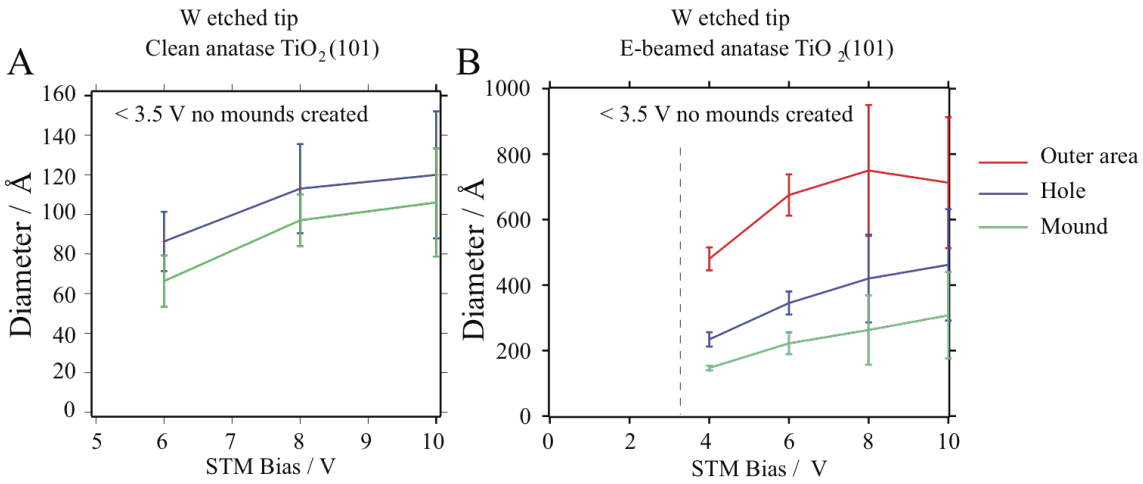

Figure 4.12: A correlation of the mean average diameters of holes (blue) and mounds (green) and outer area (red) of modified regions of the anatase TiO_2(101) surface produced by tip pulses (sample bias +6 to +10 V, 100 ms, 3.5-50 nA) with bias V. The error bars were determined from the standard deviation. **(A)** As prepared clean TiO_2(101) surface. **(B)** The total time 35 minute e-beamed TiO_2(101) surface.

A comparison of the results of pulsing the as-prepared and e-beamed anatase TiO_2(101) surfaces indicates that the diameter of the mounds/holes for the latter are around twice as large, this surface structure sensitivity indicates that the material is unlikely to be simply deposited from the tip. This difference, likely arises from a reduction in terrace size (increase step edge density) leading to a reduced energy difference between the depressions created by pulsing and the initial surface. Mechanical contact between the tip and surface would be promoted by field evaporation of less strongly bound amorphous surface (assumed to be TiO_x) towards the tip forming a tip-surface junction.

In comparison to a similar study on rutile TiO_2(110) by Humphrey et al.[22] of tip modification on an e-beamed surface of rutile TiO_2(110), where a multi-stepped cross-linked (110)-(1 × 2) surface was created, no obvious reconstruction is observed here on anatase TiO_2(101).

Where oval outer regions were observed, these were typically directed with the longest axis in the [010] azimuth (two events in **Figure 11C, Figure 11E).** A measurement of 43 events resulted in an aspect ratio [010]/[$10\bar{1}$] of 1.2 ± 0.1. Previous work studying the desorption of capping hydroxyls on rutile TiO_2(110) by pulsing of the tip demonstrated an oval shaped area of

effect, attributed to anisotropic surface electrical conductivity in the [001] direction. No previous measurements examining possible anisotropic surface electrical conductivity have been performed on anatase TiO_2(101).

The tip is initially located approximately within ~5 Å of the surface in tunneling contact and heights of mound exceeded ~50 Å. It is therefore highly probable that as the tip is not under z-position control a mechanical tip/surface junction is formed by the accretion of surface material under the tip. This proposal is supported by indentations observed in the mounds at the original location of the tip. The supplied current is dependent on this junction. Assuming this to be TiO_2; the bulk resistivity of TiO_2 ranges from 2000 to 10 Ωcm^{-1}.[37] If the junction connecting the tip and surface is assumed to be a cylinder of amorphous TiO_2 (~10 Å thickness, 100 Å radius) a resistance of 10^8 –10^6 Ω results. If the anatase sample-TiO_2-tip junction forms a resister series, where the 10 V potential drop occurs entirely in the junction region; the energy dissipated (Joule heating P ≈ IV) per second is therefore: 10 V × (0.04-10 μ A) = ~10^{-7}-10^{-5} Js^{-1}. STM evidence presented here suggests this energy is dissipated in a region of anatase surface which can be modelled by ~ 400 Å diameter × 50 Å height cylinder, of anatase containing 2×10^5 TiO_2 bulk unit cells. For a 200 ms tip pulse, this results in 10^9-10^6 eV per TiO_2[4], orders of magnitude above the cohesive energy of TiO_2 ~20 eV, sufficient to cause the re-crystallisation.[19] Such a mechanism would be highly dependent on the junction dimensions leading to the wide-ranging effects observed. As shown later, the crystalline phases created are in-line with the thermodynamic stability and the relatively low surface energies of TiO_2(101) (Appendix **A.4**) and rutile TiO_2(100)-(1 × 3).

[4] This calculation uses the resistivity $\Omega\,cm^{-1}$ (ρ) equation: $\rho = R\frac{A}{l}$ (A = area cm^2, l = length cm) to determine resistance R/Ω. The current is determined by ohms law: I = V/R (I = current A, V = volts /V) assuming it can be applied. The unit cell (3.7845 × 9.5143 × 4 $Å^3$ of anatase is considered which contains 4 TiO_2 units.

4.5.5 Example of an Ordered Crystalline Modified surface: Rutile TiO_2(100)-(1 × 3)

Some tip modified surface mounds displayed regions of crystallinity. This ranged from grain like features analogous to the work of Klusek et al.,[32] to single crystalline regions of 7000-10000 $Å^2$, evidenced by repeating rows. This structural order was obtained relatively sporadically, it being difficult to obtain reproducible structures (morphology and surface type). The probability of forming an ordered crystalline structure is estimated at ~1/100 tip pulse events on the e-beamed surface. In practice 5 sets of ~20 pulses were required. This is heavily influenced by the quality of the STM tip apex with atomic resolution images usually coinciding with reproducible pulse features. Similar conditions were used throughout to produce different surfaces, indicting a subtle energetic kinetic growth dependence. Characterisation was achieved *in-situ* by STM and one structure, a rutile TiO_2(100)-(1 × 3) surface is presented and analysed here. The characterisation of other phases: a TiO_2 anatase (101)-(1 × 1) surface rotated by 64° in-plane (**A.4)** with respect to the underlying (101) surface and a second undefined surface are included in the Appendix (**A.5).**

As a general rule, the ordered crystalline regions were found mainly at the perimeter of large (>400 Å diameter) mounds. This suggests a preference for formation at an intermediate distance from greatest electric field strength $VÅ^{-1}$ and field emission current directly under tip apex. It is probable that the highly stepped surface is crucial in the nucleation and growth of the rutile crystallised regions. Similar studies have shown this effect on NiO/Ni(100), where growth of the film on steps relieved strain from a mismatch of unit cells.[67]

STM images of a tip-pulse modified surface structure (+10 V sample bias, 200 ms, 50 nA) are shown in **Figure 4.13**, recorded 1-18 hours after formation (background pressure was 2×10^{-10} mbar). A 690 × 690 $Å^2$ image (**Figure 4.13A**) depicts the full modified mound region, within a displaced region (max. depth ~24 Å) and surrounding region of apparently healed (101)-(1 × 1) anatase TiO_2(101). A crystalline region (indicated by green oval) at the bottom

edge of the mound adjacent to the anatase surface is evidenced by the presence of rows, running directly away from the pulse centre (black cross), at 65° with respect to the [010] anatase substrate surface direction.

Figure 4.13B is a zoomed in 380 × 390 $Å^2$ representative image (the corner edge of a green box in the right hand corner of **Figure 4.13A** displays the position of the zoom in) which displays the modified structure, and surrounding region of formed pristine (101)-(1 × 1) anatase TiO_2(101), the latter is orientated in the original (101) surface crystallographic orientation indicated previously by LEED and STM. Decorating the (101)-(1 × 1) region are features (0.035 ML) with a bright-dark-bright motif, consistent with the STM appearance of water.[59] Water would result from desorption from the W tip apex during the pulse event or derives from the residual vacuum, (18 hours ~ 2×10^{11} mbar P_{water} ~1 Langmuir exposure). The stable adsorption of water on anatase TiO_2(101) at 300 K is considered to rely on sub-surface oxygen vacancies or other defects, as discussed by Diebold and co-workers.[59,68] These sub-surface oxygen vacancies are most likely created by the electrons of the tip during the pulse. The blue dashed lines outline a well-resolved terrace, which provides much of the subsequent detailed analysis.

Line profiles[5] are overlaid on image **Figure 4.13B** running in the row directions (green) and across (dark blue) to determine the modified surfaces angle with respect to the anatase (101) substrate plane (light blue). Angles of 10° ± 1 (along rows), 3.5° (across rows) and 0° (anatase (101) terrace) were determined (shown in **Figure 4.13C**) (average and standard deviation determined from 10 measurements placed 5 Å apart on the terrace feature situated at the intersection of the blue and green line). Therefore the observed region of new structure (blue dashed outline) is not co-planar with the (101) surface, in line with the other modified surface structures characterised (included in the Appendix (**A.4**)).

High-resolution, drift free images of the modified surface are presented in **Figure 4.13D** (220 × 120 $Å^2$) and **Figure 4.13E (**125 × 125 $Å^2$). A lattice parameter after calibration was extracted from those examples. An example lattice determination and error is shown in the

[5] These were extracted from an identical image where the image was tilted until three points on one terrace formed a plane.

Appendix (**A.3**). The line profile **Figure 4.13F** displays the repeating saw-tooth structure with an average row separation of 14.2 ± 0.5 Å[6] between the high rows and an apparent maximum corrugation of ~1.5-2 Å. In **Figure 12D** a rare tip contrast mode is obtained at +1.6 V, 0.1 nA depicting resolution along the prominent higher rows. The line profile overlaid on such row shown in **Figure 4.13G**, indicates a small corrugation of ~0.3-0.4 Å with a separation of 3.1 ± 0.2 Å. Therefore the unit cell lattice of this domain within the new surface is apparently 3.1 ± 0.2 Å × 14.2 ± 0.5 Å. The dark blue dashed lines overlaid on the prominent ridges of **Figure 4.13E** identify similar rows above and below the step edge (height 1.7-4 Å), a slight offset between the upper and lower terrace by approximately 4.3 ± 0.5 Å length from an average of 5 measurements was determined and is indicated by the white lines and arrows in **Figure 4.13E**.

In summary, the structural parameters of the small exposed terrace domain (blue dashed line outline in **Figure 4.13B**) in the STM height image are: i) lattice constants of (3.1 ± 0.2 Å × 14.2 ± 0.5 Å); ii) offset of the lower and upper terrace (white lines and arrows in **Figure 4.13E** (4.3 ± 0.5 Å); iii) a maximum corrugation across the rows of ~1.5-2 Å in **Figure 4.13E**.

[6] Calibrated with respect to the resolved anatase TiO_2(101)-(1 × 1) unit lattice within the same image.

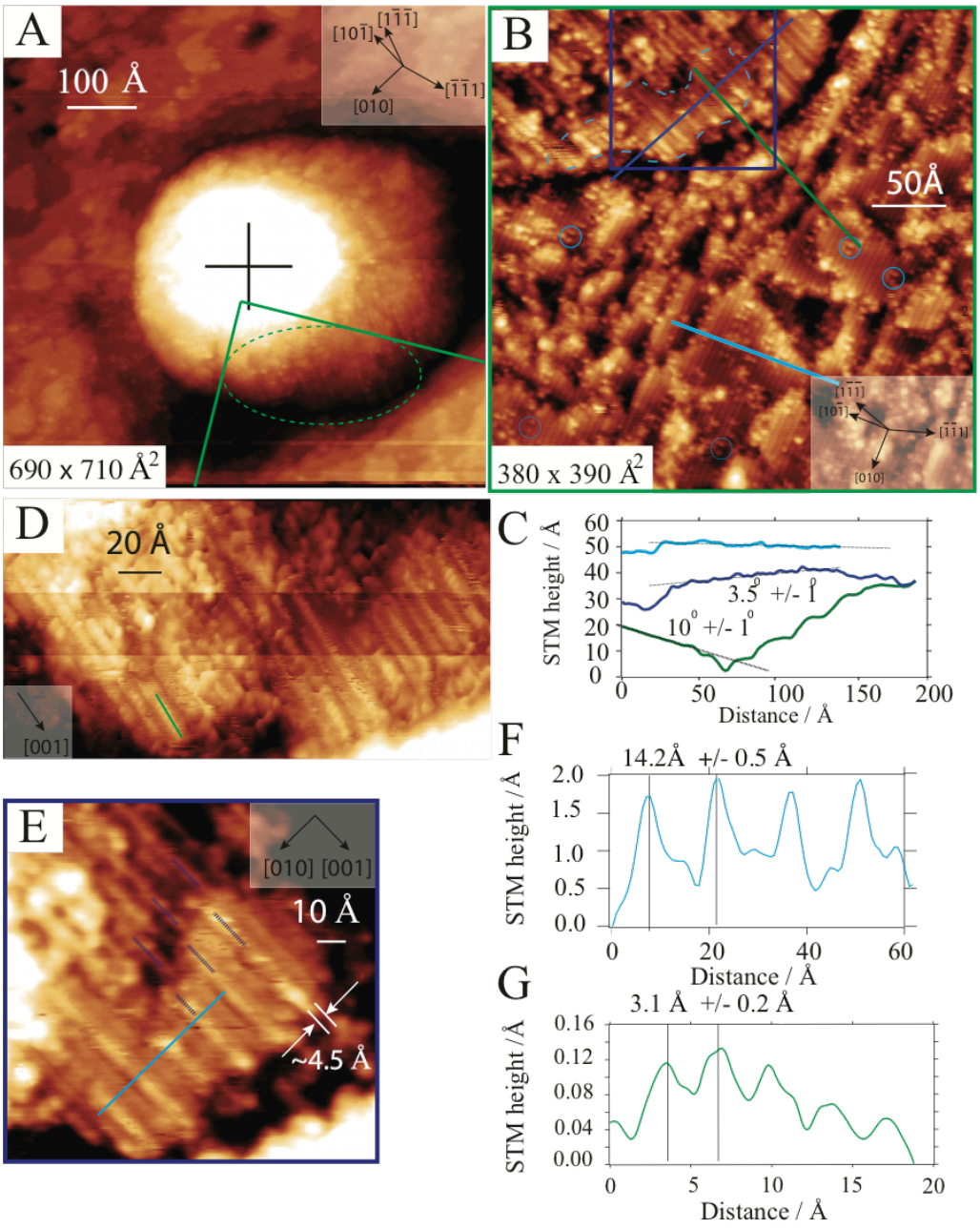

Figure 4.13: 300 K STM images (+1.6 V sample bias, 0.1 nA) of a +10 V, 200 ms, 50 nA tip pulse modified e-beamed (35 minutes, 3 kV, 0.2 $mAs^{-1}cm^{-2}$) anatase TiO_2(101) surface. (**A**) A 690 × 710 $Å^2$ image of the tip-modified anatase TiO_2(101). Identified; pulse centre (black cross); green lines and oval identify the corresponding top left hand corner of zoomed in region in and crystalline region respectively in (**B**). Top inset: the principal (101) azimuths. **(B)** A 380 × 390 $Å^2$ image (polynomial subtracted) of the healed anatase TiO_2(101)-(1 × 1) adjacent to a tip modified region of the mound. Identified; bright-dark-bright defects (blue circles); a terrace of a crystalline modified region (blue dashed lines); height line profile from the unfiltered topographic image (green, light blue, dark blue). Bottom inset: the principal (101) azimuths. (**C**) Height line profiles as indicated in (**B**). (**D**) A high resolution 220 × 120 $Å^2$ image with resolution along the rows, green height line profile. The principal rutile TiO_2(100) azimuths are shown. (**E**) A zoomed-in of 125 × 125 $Å^2$ of a region of terrace as indicated by the blue square in (**B**), black dashed lines indicate ridges, a light blue height profile is drawn across the rows. The white lines indicate the off-set between the upper and lower terrace. The principal rutile TiO_2(100) azimuths are shown. (**F**) Line profiles perpendicular to the row direction in (**E**). (**G**) A green line profile along the row in (**D**).

Considering possible candidates for the modified structure based on TiO_2, no obvious known or integer multiples of anatase unit cell sizes are consistent; the (1 × 1) unit cell dimensions are (100)-(9.51 × 3.78 $Å^2$), (101)-(10.24 × 3.78 $Å^2$). The ~3 Å lattice separation suggests the rutile surface (1n0) plane orientation such as an (110) surface. A previous modelling study of stable rutile surfaces on the anatase (101) surface leads to similar favourable adhesion energies (ca. -1.7 Jm^{-2}) of the rutile (110) and (100) surfaces.[53] The 4.3 Å offset is consistent with a surface structure formed from the rutile TiO_2(100) plane, where 4.3 Å is close to the lateral rutile unit cell parameter 4.59 Å.[37]

Early STM evidence provided by Thornton and co-workers of the TiO_2(100)-(1 × 3) reconstruction measured a unit cell of (3.3 × 15.3 $Å^2$).[45] In a separate study, the long spacing of ~14 Å and step edge heights and adjacent step edge off-sets of one rutile unit cell of ~4.59 Å were measured.[48] This STM data was consistent with GIXRD, which determined the atomic position within the (1 × 3) unit cell to consist of facets of {110}.[44] STM evidence demonstrated apparent resolution of features consistent with the positions of the unsaturated (T_{5c}) and six coordinated Ti atoms (see **Figure 4.1B**).[48] Rows of oxygen vacancies, modifying the structure, are suggested to be present on upper ridge by inference of STS measurements[45] and supported by photoemission.[46] This structure is referred to as the (1 × 3) microfacet and is shown in **Figure 4.14A and 4.14B**. Klusek et. al. carried out an STM study of the system and measured an early stage (100)-(1 × 3) reconstruction with a 14.8 Å long spacing which after longer annealing decreased to 13.4 Å (100)-(1 × 3).[43] Pang et al. used STM and non-contact atomic force microscopy (NC-AFM) to study the (100)-(1 × 3) reconstruction, obtaining a (3 × 14 $Å^2$) unit cell.[42] Here two further intermediate (100)-(1 × 3) reconstructions were determined with proposed models for (100)-(1 × 3)-α and (100)-(1 × 3)-β. A more recent GIXRD study of (100)-(1 × 3) surface resulted in the unit cell of 2.96 × 13.77 $Å^2$ structure which contains edge and face sharing octahedral. This structure is shown in **Figure 4.1D** and referred to as the Landree model.[47]

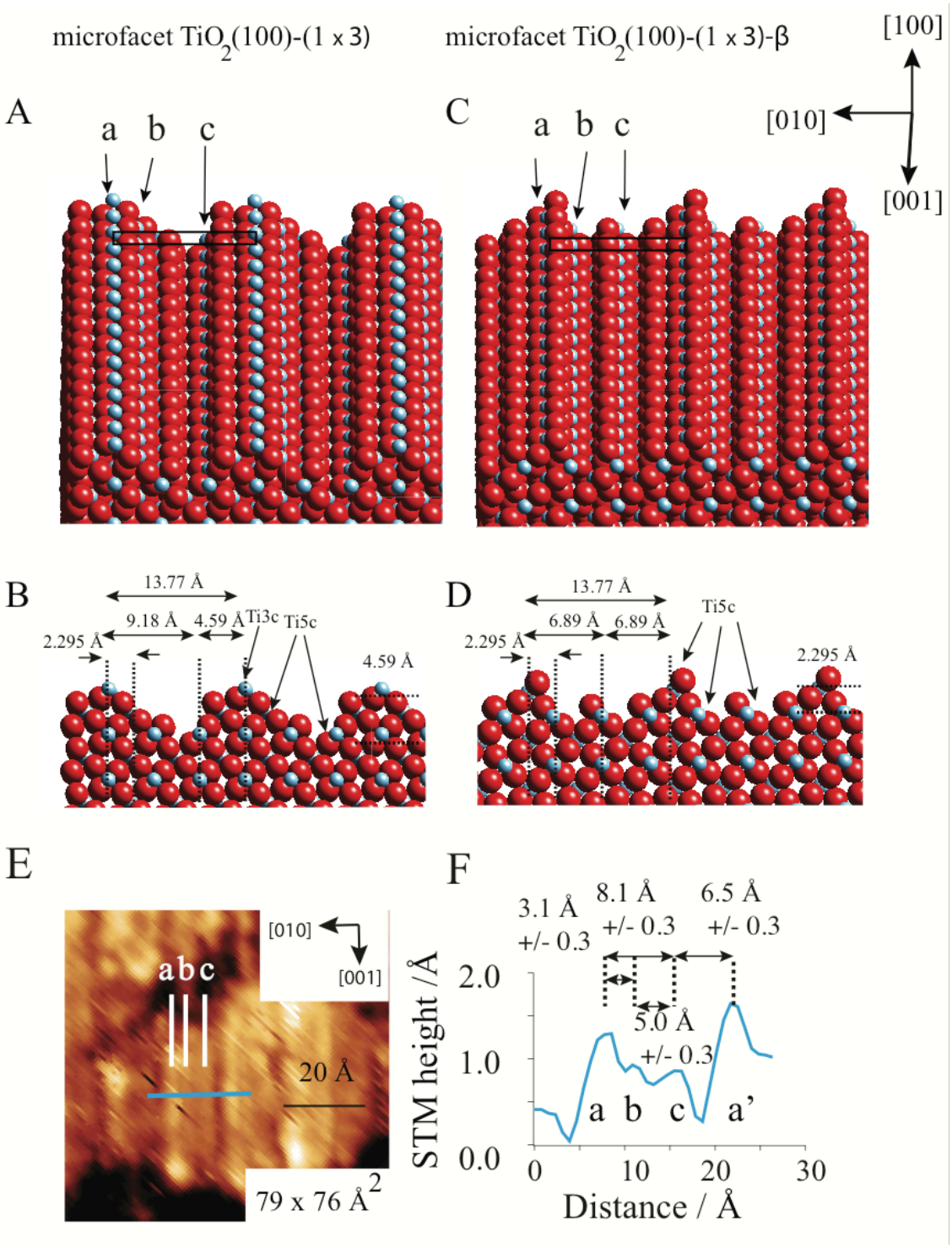

Figure 4.14: Structural filled ball models of two rutile $TiO_2(100)$-(1 × 3) models from reference.[42] (**A**) The tilted view rutile $TiO_2(100)$-(1 × 3) microfacet model. (**B**) The side view model of (**A**). (**C**) The tilted view rutile $TiO_2(100)$-(1 × 3)-β microfacet model. (**D**) The side view model of (**C**). Indicated by the black arrows are the rows *a* , *b* and *c* of Ti_{5c}/Ti_{3c}. The (2.96 × 13.77 Å) unit cell is indicated by the black rectangle. The Ti_{3c}/Ti_{5c} rows are identified by the black arrows. The inter-row separation of Ti_{5c}/Ti_{3c} (dotted lines) for both models are shown. (**E**) A 300 K STM image (79 × 76 $Å^2$) (+1.6 V, 0.1 nA). Indicated are the three repeating rows *a*, *b* and *c* by the white lines. A blue line profile is drawn across the repeating structure. (**F**) A blue line height profile indicates a maximum corrugation of 1.5 Å. The distances between, |*b*-*a*|, |*c*-*a'*|, |*c*-*b*| and |*a*-*c*| are indicated. The $TiO_2(100)$ principal azimuths are shown for both the STM image and model.

The area outlined by the blue dashed lines in **Figure 4.13B** indicates the (100)-(1 × 3) region, where the lattice parameters ~ 3 × 14.2 Å^2 are reasonably close to the reported values. At this point the (100)-(1 × 3)-α can be neglected as a candidate for the structure from the evidence presented here, based on the absence of its characteristic STM motif (see **Figure 4.1G).**[42] The (100)-(1 × 3) microfacet, (100)-(1 × 3)-β model and (100)-(1 × 3) Landree model[47] are consistent with the unit cell dimensions measured and broadly the qualitative appearance in this study.

Models of the ideal auto-compensated microfacet rutile (100)-(1 × 3) and (100)-(1 × 3)-β are presented in **Figure 4.14A, 4.14B** and **Figure 4.14C, 4.14D** respectively. The unit cell dimensions are indicated (2.96 × 13.77 Å^2) (black rectangle) in the models. An STM image (same region as **Figure 4.13E**) is presented in **Figure 4.14E** where a blue horizontal line profile is depicted, this highlights the presence of an asymmetrical three row repeating structure [7], these are labeled by the white lines as *a*, *b* and *c*. It is tentatively assumed at this point given previous work on the rutile TiO_2(110) surface[69] that the unsaturated Ti_{3c}/Ti_{5c} rows (black arrows indicate position), would form the prominent *a*, *b* and *c* rows in the empty surface state, positive sample bias images, due to the Ti d orbitals main contribution to the conduction band. Therefore the image is inline with the structural models, in which the Ti_{5c} are asymmetrically (no centre of symmetry) disposed within the (1 × 3) unit cell.

From the structural models (**Figure 4.14A** and **Figure 4.14B)** row *c* is positioned with an |*a*-*c*| (|*c*-*a'*|) distance of 9.18 Å (4.59 Å) and 6.18 Å (6.18 Å) between rows *a* to *c* and the next lateral a row, a', for the micro-facet and reduced β-micro facet respectively, as indicated by **Figure 4.14B and 4.14D**. The three row, saw tooth motif observed in our STM images display a relationship of |*a*-*c*| (|*c*-*a'*|) of 8.1 Å (6.2 Å) in between the location of the two models. The rows *a* and *c* have been resolved in STM images of both the (100)-(1 × 3) and the (100)-(1 × 3)-β micofacet[42] (see **Figure 4.1B**), in the latter an asymmetry in distance of |*a*-*c*| (|*c*-*a'*|) of 8.9 Å (6.0 Å) is present. The discrepancy to the (100)-(1 × 3)-β structural model and STM image was

[7] The forward and backward scans performed simultaneously demonstrated an identical structure, therefore eliminating the asymmetry in the image resulting from the tip structure.

previously attributed to a lateral relaxation from the bulk truncated structure and/or a feature of the *c* row Ti atoms position on the {110} facet and a similar argument would apply here.[42] Our measured position of |*b*-*c*| of 5 Å is also close to the (100)-(1 × 3)-β structure. The maximum corrugation of ~1.5 Å is in line with the (100)-(1 × 3)-β structural model which is structurally 2.3 Å, and corroborated by the STM image presented (see **Figure 4.1H**) by Raza et al. ~2 Å, where as images of (100)-(1 × 3) have tended to indicate a 3-5 Å corrugation. On this basis together with similar STM motif we can tentatively assign the exposed region of surface created in the tip pulse to rutile TiO_2(100)-(1 × 3)-β.[42]

4.5.6 *In-situ* Acetic Acid Adsorption and Reactivity of the Tip Modified Rutile TiO_2(100)-(1 × 3) Surface

In order to probe the reactivity of the modified structure and provide an additional probe of the modified surface structure, the modified anatase (101) surface was exposed to acetic acid (CH_3COOH). The surface was exposed (22 L) at RT, *in-situ,* during imaging (tip continuously scanned the region **Figure 4.13A**). The adsorption of acetic acid on TiO_2 surfaces is well studied,[70] and is one of the few organic molecules studied on anatase TiO_2(101).[55] The molecule spontaneously dissociates and strongly adsorbs on TiO_2(101), with bi-dentate coordination to the Ti_{5c} along the [010] direction. There are limited adsorption studies of acetic acid on rutile TiO_2(100),[70] and no STM studies. As the (100)-(1 × 3) Landree and microfacet models contain unsaturated Ti_{5c} sites, separated by 3.0 Å along the [001] direction, dissociative bi-dentate adsorption to these sites forming a (2 × 1) monolayer is expected. This is on the basis of studies of acetate on the (110) surface, where bi-dentate bonding to adjacent Ti_{5c} is observed [71], which are separated by 2.95 Å. Furthermore the (1 × 3) microfacet models have a close structural similarity to the rutile TiO_2(110), since the microfacets are (110) terminated (**see Figure 4.14**).[69]

Figure 4.15 presents STM images recorded after exposure (22 L) to acetic acid at 300 K. In **Figure 4.15A** the modified mound region and healed outer ca. pristine (101) areas are now decorated with bright protrusion. The coverage on the tip modified mound region varies from a complete to partial monolayer. On the healed outer area: densely packed regions ~0.25 ML and less densely packed regions ~0.05 ML are present. In the latter, upper step edge sites are occupied by adsorbate chains with patches of bare anatase TiO_2(101)-(1 × 1) surface visible (black dashed oval). These have an appearance consistent with acetate imaged previously,[55] of ~1.5-2 Å apparent height (+1.6 V, 0.1 nA) and 6 Å diameter. The reduced coverage most likely results from the tip being positioned in this region during acetic acid exposure, although a possible effect from the modified surface requires further investigation. The modified crystalline domain depicts rows of protrusions, where the rutile (100) [001] rows are orientated at 65° with respect to the substrate [010] (as shown in **Figure 4.15F**), co-incident with the rows analysed in **Figure 4.13**. The alignment of the anatase (101) and rutile (100) unit cells are shown in **Figure 4.15F**. A single direction of the rows on the modified surface suggests that it is a single crystalline domain. Other regions of the modified surface mound display the appearance of disordered protrusions, consistent with the amorphous region observed in STM prior to exposure.

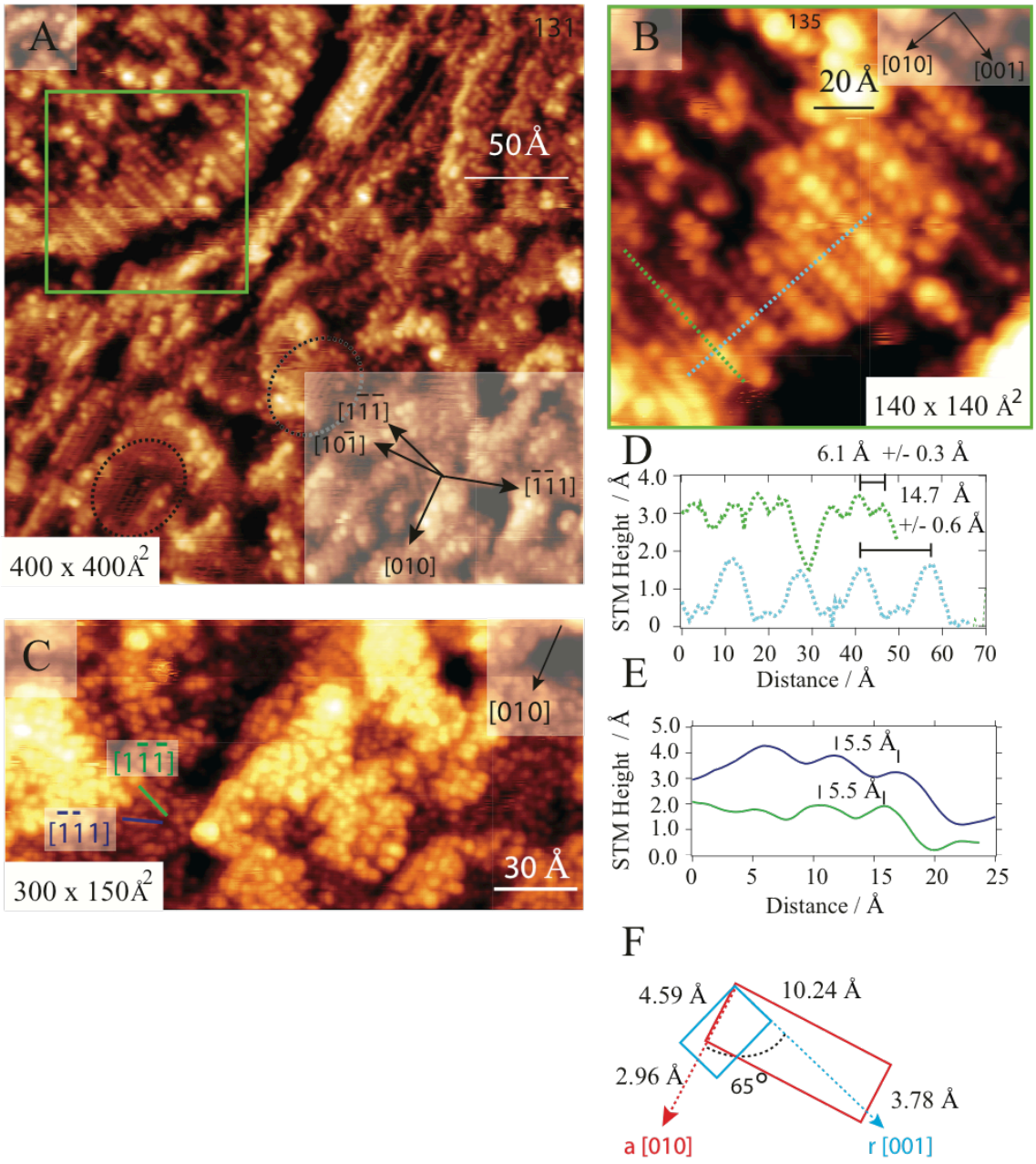

Figure 4.15: 300 K STM images (+1.6 V, 0.1 nA) of the same area of the surface-modified anatase TiO_2(101) surface imaged in **Figure 4.13** after exposure of acetic acid (22 L) at 300 K. **(A)** Large-area image (400 × 400 Å^2) of the region, where black dashed ovals indicate pristine TiO_2(101). Lower inset: the principal (101) azimuths are indicated. (**B**) Zoomed-in (140 × 140 Å^2) of the terrace identified by the green box in (**A**)**.** Blue and green dashed lines correspond to the line profiles in (**D**) along and across the rows. The distances between rows and bright features are indicated. **(C)** 300 × 150 Å^2 region of densely packed acetic acid 0.25 ML. Overlaid are a green line profile in the [$1\bar{1}\bar{1}$] direction and a blue line profile in the [$\bar{1}\bar{1}1$] direction. **(D)** STM height line profiles across (blue dashed) and along (green dashed) the rows of protrusions in **B**. The distances representative of a rutile (100)-(2 × 3) are indicated. (**E**) STM height line profile along the rows of adsorbates from the lines in (**C**). (**F**) The alignment of the rutile TiO_2(100) (4.59 Å × 2.96 Å) (blue) and the anatase TiO_2(101) (10.24 × 3.78 Å) (red) unit cells. An angle of 65° is between rutile [001] and anatase [010] directions.

A zoomed-in image shown in **Figure 4.15B** depicts the same ~900 Å^2 terrace imaged in **Figure 4.13** displaying the same structural motif, where prominent and lower rows of bright protrusions are present. Line profiles along (green dotted) and across (blue dotted) the rows show the adsorbate separation and the profiles are shown in **Figure 4.15D**. The protrusions are separated by 6.1 ± 0.3 Å along the rows, twice the separation observed prior to acetic acid exposure (~3 Å). The prominent rows are separated by 14.7 ± 0.6 Å, with a deep 2 Å corrugation. The lower row of protrusions is slightly asymmetrically located (~ 0.76 Å/0.71 Å) in between. The above observations are consistent with acetate adsorbed on two neighbouring Ti_{5c}-Ti_{5c} pair sites, in line with studies of acetate on rutile TiO_2(110).[72]

The presence of an upper and lower row of identical adsorbate chains, indicates that the unit cell contains at least two unsaturated reactive Ti_{5c} sites per (1 × 3) unit cell, which would suggest the structure is not the Landree (1 × 3) structure, which has one Ti_{5c} site per (1× 3) unit cell. Our evidence is, however, consistent with the microfacet derived models (see **Figure 4.14A** and **4.14C**) containing three unsaturated Ti_{5c} sites per (1 × 3) unit cell. Overall a unit cell of (6.1 ± 0.2 Å × 14.7 ± 0.6 Å) is observed. This is a (2 × 1) arrangement with respect to the modified region imaged before or (2 × 3) to the rutile (100) surface.

Figure 4.15C is a zoom of a region of densely packed acetate adsorbed on pristine healed surface (see **Figure 4.13**) of 0.25 ML, qualitatively similar to a previous study of acetate/TiO_2(101) by Grinter et al.[55] The features are of a single apparent height (~ 2 Å) and of limited order. Rows of protrusions are evident in the (101) $[1\bar{1}\bar{1}]$ and $[\bar{1}\bar{1}1]$ surface vector directions and line profiles are overlaid in green and blue for these, respectively. The height line profiles in **Figure 4.15E** display a separations of ~5.5 Å in both directions. This indicates a slight ordering, where previously[55] small domains of (2 × 1) were present after the surface was exposed at 420 K with an arrangement of bi-dentate co-ordinated acetate are also aligned in $[1\bar{1}\bar{1}]$ and $[\bar{1}\bar{1}1]$.

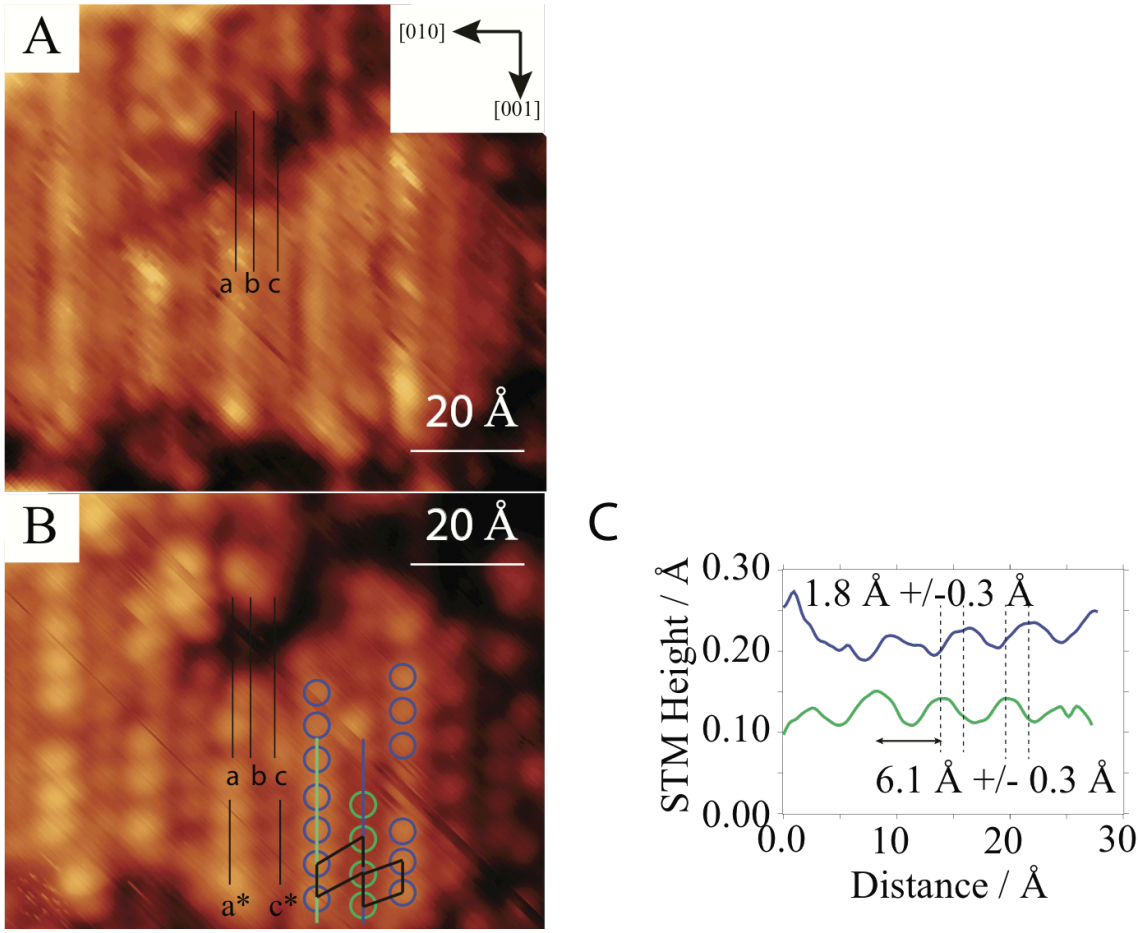

Figure 4.16: STM images (+1.6V, 0.1 nA) of the modified region of anatase TiO_2(101) before and after exposure to acetic acid. (**A**) 91 × 83 $Å^2$ image of the modified 100-(1 × 3)-β region. Identified: three rows *a*, *b* and *c* (black parallel line). Top inset: the (100) azimuths. (**B**) A 91 × 73 $Å^2$ image of the modified 100-(1 × 3)-β-acetate region. Identified: three rows *a*, *b* and *c* by black parallel lines; the adsorbate rows (black parallel lines) assigned as *a** and *c**; circles overlaid on top of the upper (blue) and lower rows (green); parallel line profiles on the upper (green) and lower (blue) rows; black rhomboids overlaid on four nearest neighbours. (**C**) Line profiles displaying the phase difference of 1.8 Å ± 0.3 Å between the parallel rows of adsorbates.

Figure 4.16 provides a direct comparison of the STM images of the *tentatively* assigned TiO_2(100)-(1 × 3)-β modified anatase TiO_2(101) (**Figure 4.14**) and TiO_2(100)-(1 × 3)-β-acetate surface after exposure to acetic acid **Figure 4.15**. In **Figure 4.16A** the repeating three rows *a*, *b* and *c*, as defined in **Figure 4.14**, are identified by the black lines. The STM image of TiO_2(100)-(1 × 3)-acetate (**Figure 4.16.B**), horizontally aligned with **Figure 4.16A** indicates the location of the bright protrusion with respect to the underlying rows: *a*, *b* and *c*. It is apparent that the upper and lower rows of bright protrusion are approximately (± 0.5 Å) aligned with rows a and *c*: defined as *a** and *c**. The rows of protrusions on the upper and lower row

(identified by green and blue circles respectively) can be examined by parallel line profiles (green and blue) and these line profiles are displayed in **Figure 4.16C**. An analysis of the line profiles in **Figure 4.16C** indicates that the upper and lower adsorbate rows are out of phase by 1.8 Å ± 0.3 Å (ca. half unit cell [001] direction), as indicated by the black dashed lines. This explains the non-hexagonal surface arrangement indicated by the overlaid black rhomboids on **Figure 4.16B**.

Tilted and top view structural models of the rutile microfacet TiO_2(100)-(1 × 3)-acetate and mircrofacet TiO_2(100)-(1 × 3)-β-acetate surfaces are shown in **Figure 4.17** in the crystallographic (100) surface orientation as indicated by the azimuths;[42] here acetate species are positioned in a bi-dentate coordination mode on the Ti_{3c}/Ti_{5c} rows *a*, *b* and *c* assigned as rows *a**, *b** and *c**, with STM only indicating the presence of *a** and *c**. Studies conducted on rutile TiO_2(110) would suggest the acetates are coordinated perpendicular to the plane of the {110} microfacets with a Ti-$O_{acetate}$ distance of ~2 Å[69] (see **Figure 4.17A**). In the case of the microfacet TiO_2(100)-(1 × 3) the exact orientation of the acetate, on the Ti_{3c} site at the top of the microfacet is not clear, one orientation is shown and an alternative is shown in the inset in **Figure 4.17A**.

The STM image represents a top view and it is not obvious where the maxima in the empty surface LDOS of the adsorbates would be aligned ($Ti_{5c,}$ -COO-, -CH_3). In **Figure 4.17C and 4.17D** top view structural models display blue and yellow circles overlaid on the acetates, centred halfway between the Ti_{5c} and coordinating oxygen. If the adsorbate row on *b** is present, the tip apparently cannot resolve this row; which would be expected from the short distance (2.3 Å) between *a* and *b*.

Based on the analysis of the image, only the TiO_2(100)-(1 × 3)-β structure can be consistent with the STM data, where the rhomboids in the model (**Figure 4.17D**) are reasonably reproduced with measured separations on adjacent rows in the [001] direction of ~1.8 Å ± 0.3 Å (and ~4.2 Å ± 0.3 Å) between adjacent adsorbates. This latter evidence would indicate that row *c* is structurally positioned half a unit cell lower in depth as the TiO_2(100)-(1 × 3)-β model indicates. The TiO_2(100)-(1 × 3) is ruled out on the basis that it would have a ~3 Å separation

between the adjacent rows of adsorbates (see **Figure 4.17A**) resulting from and a full unit cell lower height of *c* compared to *a*.

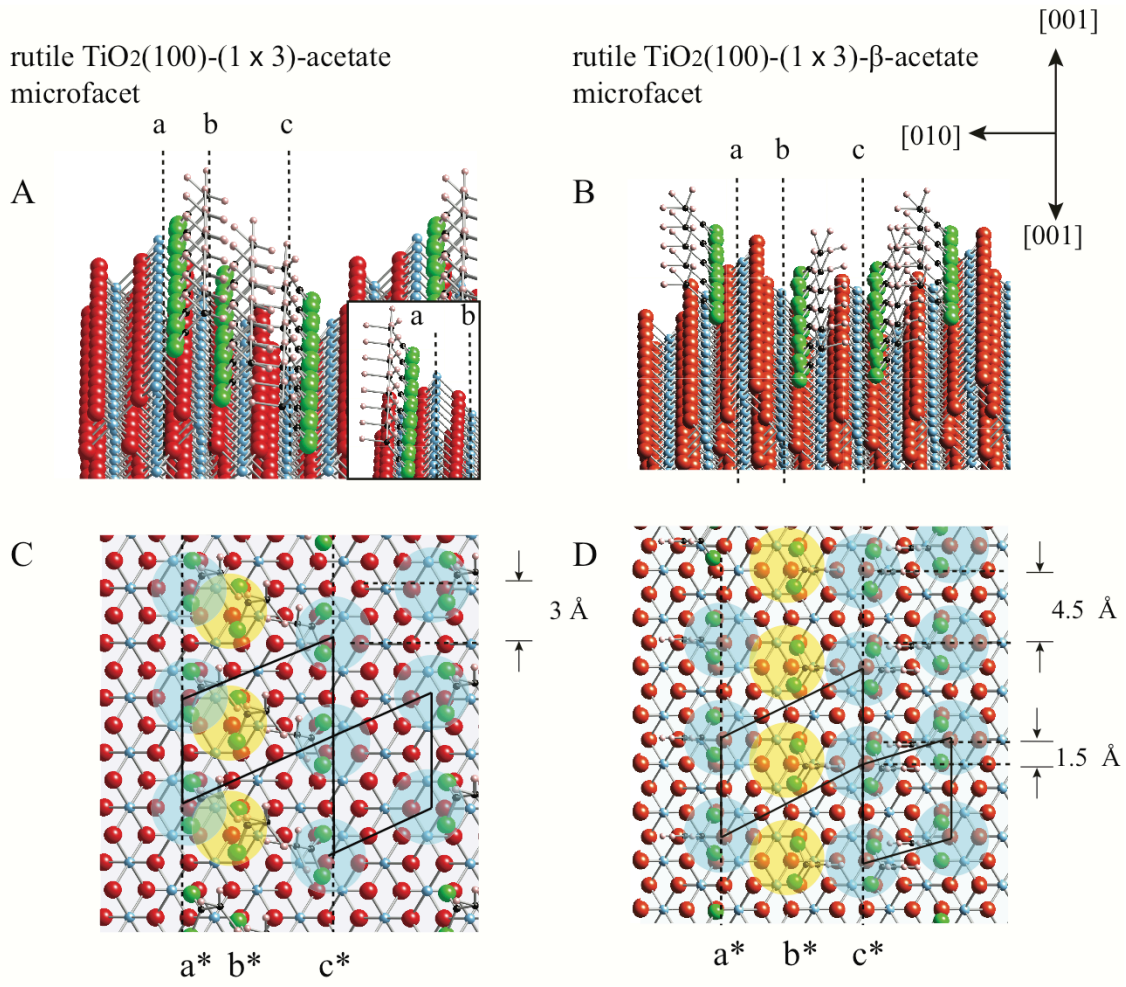

Figure 4.17: (A)(B) Tilted structural ball and stick models of the rutile $TiO_2(100)$-(1 × 3)-β and rutile $TiO_2(100)$-(1 × 3) with acetate molecules binding in a bi-dentate mode along the [001] direction to the Ti_{5c}. Inset (**A**): acetate in a second possible co-ordination postion. Lattice is represented by red spheres (oxygen atoms) and blue spheres (titanium atoms). The carboxylic acid are represented by green spheres (oxygen atoms) the black spheres (carbon) and white spheres (hydrogen. Rows of Ti_{5c} labelled *a*, *b* and *c* are identified. **(C) (D)** Top view of the upper respective structural models. Blue circles are overlaid on top of rows *a** and *c** and yellow on *b** co-incident halfway between the –COO-Ti atoms. Black rhomboids identify geometry of four nearest neighbours and separation along is shown. The distances between the acetates across adjacent rows are identified. The principal azimuths of the rutile $TiO_2(100)$ surface are indicated.

A large region of the modified mound surface appears to be single crystalline, identified by parallel rows. The total (lower estimate) of the domain size can be determined from the ordered rows after acetic acid adsorption of 6000 $Å^2$ (35% of mound surface). This remaining area likely consists of rutile $TiO_2(100)$ or other rutile facets.

The TiO_2(100)-(1 × 3)-β domain studied is tilted by 10° with respect to the underlying anatase TiO_2(101) substrate. Moreover, the rutile (100) [001] azimuth is rotated in-plane by 65° with respect to the anatase (101) [010] azimuth. It seems likely that this arises from the formation of the interface under extreme conditions. It is also conceivable that there is an intermediate surface phase between the underlying (101) and rutile TiO_2(100). Three phase systems with a buffer layer such as TiO_2-II or a relatively disordered layer have been predicted to be stable at anatase/rutile interfaces.[50,53,54] In addition, a study of the attachment of rutile and anatase nanoparticles of TiO_2 indicated that rough stepped surfaces create a mixture of dislocations.[73]

Figure 4.18 presents the simplest picture of the arrangement with an epitaxial relationship between planar anatase (101) and rutile (100) surfaces at the in-plane orientation angle. The anatase (101)-(1 × 1) (red) surface and the rutile (100)-(1 × 1) (black) surface unit meshes are overlaid in **Figure 4.18A**. The super cell coincident mesh $\begin{pmatrix} \boldsymbol{b1} \\ \boldsymbol{b2} \end{pmatrix}$ is outlined in blue and the matrix relationship between the substrate **a1** and **a2** vectors is as defined is: $\begin{pmatrix} \boldsymbol{b1} \\ \boldsymbol{b2} \end{pmatrix} = \begin{pmatrix} -5 & 3 \\ -3 & -1 \end{pmatrix} \begin{pmatrix} \boldsymbol{a1} \\ \boldsymbol{a2} \end{pmatrix}$. The percentage mismatches between the overlayer and the substrate are 2.43% in the ***b*1** direction and 3.02% in the ***b*2** direction. A pictorial representation is shown in **Figure 4.18C**, where an angle of 10° is indicated. The discontinuity between the upper and lower surfaces of unknown origin leading to the STM observed 10° angle is represented by the blue dashed line.

It is possible that the angle of 10° in the orientation indicated by STM with respect to the (100) results directly from the plane in epitaxial contact with rutile. The 10° angle is best represented by the theoretical (901) rutile miller plane slice of ~10.23°. This structure of the facet adhering to Tasker's rules results in a vicinal surface formed of TiO_2(100) facets, with a unit mesh of (2.96 Å × 13.51 Å). If this is overlaid on the anatase (101) it has a 1.35% mismatch in the ***b*1** direction and 3.02% in the ***b*2** direction. A pictorial representation is shown in **Figure 4.18D**.

The percentage mismatches determined for contact of the (901) and (101) surfaces are reasonable based on previous molecular dynamic modelling of the rutile anatase interface, where a 3-0.5% was reported.[53] In this previous study a rutile (100)/anatase (101) interface was considered where the rutile [010] direction was aligned parallel and perpendicular to the anatase [$\bar{1}$01] direction.[53] Favourable adhesion energies of ~-1.7 Jm^{-2} and percentage mismatches of ~1% were determined. Further work is required to determine the effect of the rotation by 25° of the two lattices.

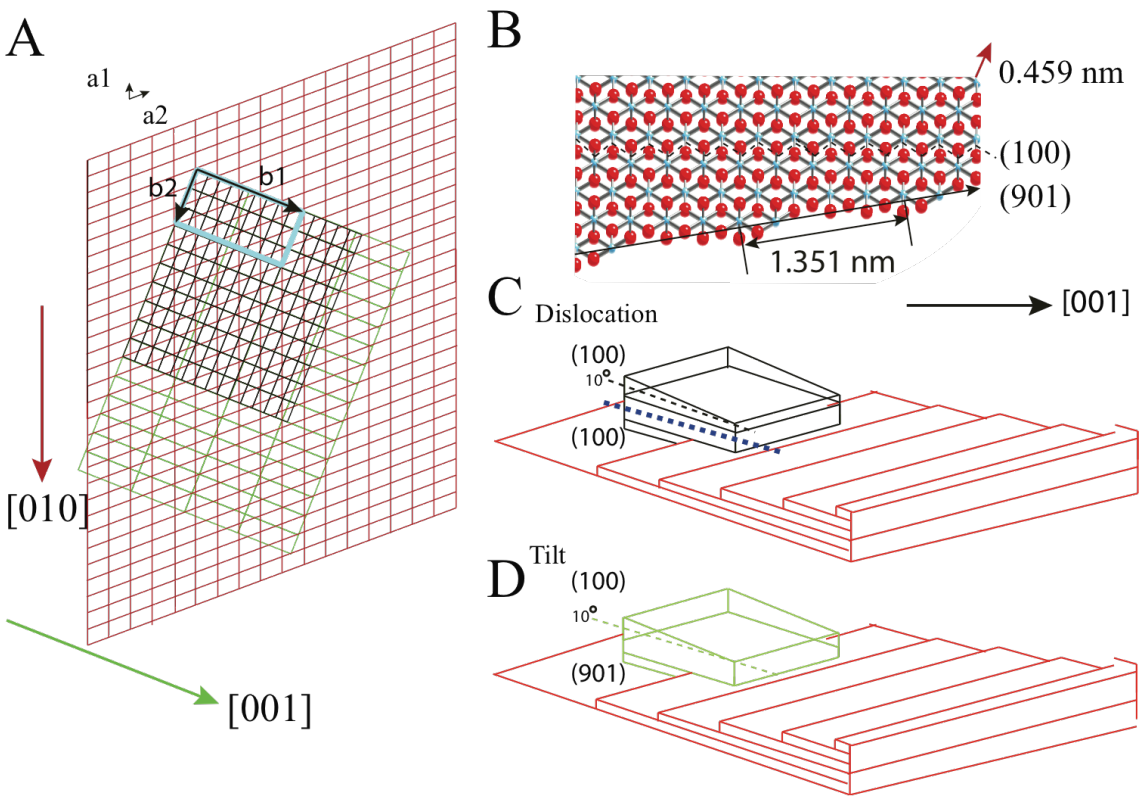

Figure 4.18: (A) The unit cells of the rutile (100) (black) and rutile (901) (green) unit cells overlaid on the anatase (101) unit cells (red). The rutile [001] direction (green arrow) is at 65° with respect to the red anatase [010] direction (red arrow). The super cell is indicated by the blue rectangle. **(B)** The (901) (13.51 × 4.59 $Å^2$) vicinal surface. The zig-zag dashed line indicates the auto-compensated (100) surface. The rutile [001] direction is indicated. **(C)** Model of a thin rutile layer supported on the anatase (101) surface, where (100) and (100) surfaces are present at the bottom and on the surface, with a dislocation indicated (blue dashed line). **(D)** Model of thin rutile layer where (100) and (901) surfaces are present at the surface and bottom respectively resulting in the 10° angle.

It is clear that further modelling work is required to present conclusive results about the nature of the rutile/anatase interface investigated here, as both discussed scenarios are plausible. STM observation of a thinner layer where a Moiré pattern or epitaxial surface registry is more apparent is required.

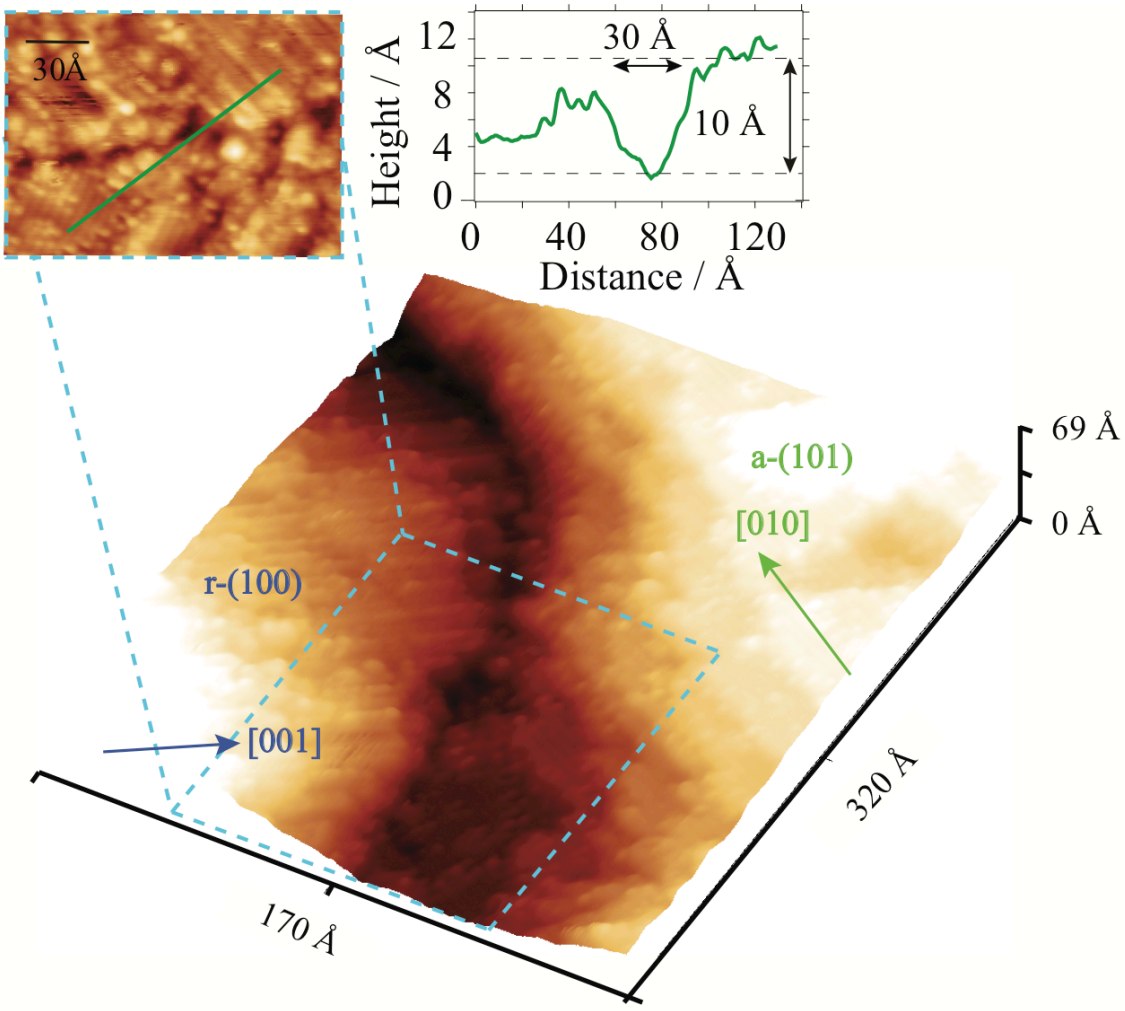

Figure 4.19: 3D view of the topographic STM image (+1.6 V, 0.1 nA) of 170 × 320 Å^2 of the rutile TiO_2 / anatase TiO_2(101) heterojunction. Identified are the two regions of interest the rutile rutile-(100) (blue) and anatase (green) a-(101) surfaces; the azimuths of rutile-(100) [001] (blue) and anatase-(100) [001] (green). A 2D STM image of the interfacial region defined by the blue dashed box is shown, where the green height profile is overlaid and displayed.

The modified anatase TiO_2(101) presents an apparently well defined rutile (100) / anatase (101) heterojunction and a three dimensional view is presented in **Figure 4.19.** This heterojunction consists of buried vertical interface of rutile/anatase or rutile/ unknown phase /anatase inaccessible by STM and a sharp lateral interface between rutile (100) and anatase (101). The STM indicates that the there is no more than ~10 Å vertically and ~30 Å laterally

between the flat resolved top surfaces of single crystalline rutile and anatase (see inset zoomed in STM image in **Figure 4.19** and line profile). This would indicate the two phases are in close enough (below the TiO_2 electrical screening length ~100 Å)[74] contact to explore electronic phenomenon such a band bending and electron exchange.

4.6 Conclusion:

We have demonstrated the preparation of a well STM characterised e-beamed anatase TiO_2(101) surface. STM analysis under different electron fluxes in UHV, at the outer edge and centre of beam allows a phenomenological process unique to the anatase TiO_2(101) surface to be established. Single row width (5.12 Å) and double row width (10.24 Å) depressions are formed; under further electron irradiation these result in the formation of rectangular (101)-(1 × 1) islands, predominately orientated in the [010] direction. The mechanism of formation is hypothesised to involve the Knotek-Feibelman radiolysis mechanism.[1,2] Large domains of (101)-(1 × 1) surface are retained even after an accumulated total time of 35 minutes of e-beaming at 3 kV (2-3×10^{15} electrons $s^{-1}cm^{-2}$) as corroborated by LEED. The e-beaming study presents a useful methodology for forming an anatase surface with a high density of step edges.

STM tip modification at above +4 V on the e-beamed surface resulted in a reproducible characteristic modified structure: mound, hole, and healed outer area. This had a larger modified area than formed on the clean surface and contained crystalline ordered structures. Some mounds contained crystalline regions. One surface was formed and characterised in real space by STM and a single area (embedded at the edge of a mound) demonstrated an atomically resolved unit mesh of (3.1 ± 0.2 Å × 14.2 ± 0.5 Å) and corrugation along the long spacing of ~1.5 Å. This was found to be consistent with the surface structure of the micro-facet rutile TiO_2(100)-(1 × 3)-β model. *In-situ* adsorption of acetic acid resulted in a monolayer coverage of adsorbates resulting in a (6.1 ± 0.3 Å × 14.7 ± 0.6 Å) unit mesh. The acetate coordination allows the position of unsaturated Ti_{5c} to be determined. Analysis of the STM images of the acetate

adsorbed modified surface allows the precise assignment of the rutile TiO_2(100)-(1 × 3)-β surface. The boundary between the rutile and anatase phases is sharp and well defined. This discovery opens a new avenue in the experimental study of rutile and anatase TiO_2 heterojunctions for photocatalytic investigation and the study of the nucleation of rutile on anatase. Here titania rutile/anatase TiO_2 nanoparticles in photocatalytic systems (P25) are modelled by a planar rutile/anatase TiO_{2-x} single crystalline junction.

4.7 Perspectives

To further support the assignment of a modified rutile surface in this Chapter a study of acetic acid adsorption on a single crystal surface of rutile TiO_2(100)-(1 × 3) is required. A computational simulation of both the interface and tip pulsing process would also be of value.

The formation of the rutile/anatase interface is of great interest. This system provides a model surface to study holes/electron pairs formed by UV light absorption. Such a study would require *in-situ* STM of photo-active adsorbed molecules such as ethanol or trimethylacetic acid (TMA),[75] where reactivity as a function of UV light fluxes (~1 $mWcm^{-2}$) can be studied. At low UV light flux a difference in the photo desorption of adsorbed molecules both on the exposed anatase (101) surface and formed rutile as a function of exposure and distance to the opposite phase might exist. This would provide a means to extract the photoreaction cross-section as a function of distance from the heterojunction, by knowing the initial and final surface adsorbate population. Whether the rutile or anatase surface provides the most reactive surface would also be of interest. The interfacial region in itself might likely also be identified as a photoreaction 'hotspot'.

Additionally, characterisation of the rutile and anatase surfaces by scanning tunneling spectroscopy (STS) will demonstrate the reduction state, aid characterisation and directly provide the electronic structure, from which band-bending and band alignment at the interface of the two phases can be examined. This information would greatly support photochemical measurements by indicating the likely movement direction of photo-excited holes and electrons

between the rutile and anatase phase. Also it would further the understanding of the rutile/anatase VB and CB band alignment and perhaps determine the microscopic details, which control its nature (type I-V).

References

(1) Knotek, M. L.; Feibelman, P. J. Ion Desorption by Core-Hole Auger Decay. *Phys. Rev. Lett.* **1978**, *40*, 964–967.

(2) Feibelman, P. J.; Knotek, M. L. Reinterpretation of Electron-Stimulated Desorption Data From Chemisorption Systems. *Phys. Rev. B* **1978**, 6531–6531.

(3) Dujardin, G.; Mayne, A. J. Atomic and Molecular Manipulation; Elsevier, 2011.

(4) Gonzalez-Martinez, I. G.; Bachmatiuk, A.; Bezugly, V.; Kunstmann, J.; Gemming, T.; Liu, Z.; Cuniberti, G.; Rümmeli, M. H. Electron-Beam Induced Synthesis of Nanostructures: a Review. *Nanoscale* **2016**, *8*, 11340–11362.

(5) Jiang, N. Electron Beam Damage in Oxides: a Review. *Rep. Prog. Phys.* **2016**, *79*, 016501.

(6) Pang, C. L.; Thornton, G. Manipulation of Oxide Surfaces. *Surf. Sci.* **2009**, *603*, 3255–3261.

(7) Tennant, D. M. Progress and Issues in E-Beam and Other Top Down Nanolithography. *J. Vac. Sci. Technol., A* **2013**, 050813–050819.

(8) Schirmer, M.; Walz, M.-M.; Vollnhals, F.; Lukasczyk, T.; Sandmann, A.; Chen, C.; Steinrück, H.-P.; Marbach, H. Electron-Beam-Induced Deposition and Post-Treatment Processes to Locally Generate Clean Titanium Oxide Nanostructures on Si(100). *Nanotechnology* **2011**, *22*, 085301–085311.

(9) Botman, A.; Mulders, J. J. L.; Hagen, C. W. Creating Pure Nanostructures From Electron-Beam-Induced Deposition Using Purification Techniques: a Technology Perspective. *Nanotechnology* **2009**, *20*, 372001–372018.

(10) Nakayama, K.; Weaver, J. H. Electron-Stimulated Modification of Si Surfaces. *Phys. Rev. Lett.* **1999**, *82*, 980–983.

(11) Menteş, T. O.; Locatelli, A.; Aballe, L.; Pavlovska, A.; Bauer, E.; Pabisiak, T.; Kiejna, A. Surface Modification of Oxides by Electron-Stimulated Desorption for Growth-Mode Control of Metal Films: Experiment and Density-Functional Calculations. *Phys. Rev. B* **2007**, *76*, 155413–155414.

(12) Smith, D. J.; McCartney, M. R.; Bursill, L. A. The Electron-Beam-Induced Reduction of Transition Metal Oxide Surfaces to Metallic Lower Oxides. *Ultramicroscopy* **1987**, *23*, 299–303.

(13) Vergara, L. I.; Passeggi, M. C. G., Jr.; Ferrón, J. Chemical Changes Induced on a TiO_2 Surface by Electron Bombardment. *Thin Solid Films* **2007**, *515*, 8365–8370.

(14) McCartney, M. R.; Smith, D. J. Epitaxial Relationships in Electron-Stimulated Desorption Processes at Transition Metal Oxide Surfaces. *Surf. Sci.* **1989**, *221*, 214–232.

(15) Lee, J.; Zhang, Z.; Yates, J. T. Electron-Stimulated Positive-Ion Desorption Caused by Charge Transfer From Adsorbate to Substrate: Oxygen Adsorbed on TiO_2(110). *Phys. Rev. B* **2009**, *79*, 081408–4.

(16) Yim, C. M.; Pang, C. L.; Thornton, G. Oxygen Vacancy Origin of the Surface Band-Gap State of TiO_2(110). *Phys. Rev. Lett.* **2010**, *104*, 036806.

(17) Petrik, N. G.; Zhang, Z.; Du, Y.; Dohnálek, Z. Chemical Reactivity of Reduced TiO_2(110): the Dominant Role of Surface Defects in Oxygen Chemisorption. *J. Phys. Chem. Lett.* **2009**, *113*, 12407–12411.

(18) Scheiber, P.; Fidler, M.; Dulub, O.; Schmid, M.; Diebold, U.; Hou, W.; Aschauer, U.;

Selloni, A. (Sub)Surface Mobility of Oxygen Vacancies at the TiO_2 Anatase (101) Surface. *Phys. Rev. Lett.* **2012**, *109*, 136103–136105.
(19) Pang, C. L.; Bikondoa, O.; Humphrey, D. S.; Cabailh, G.; Ithnin, R.; Chen, Q.; Muryn, C. A.; Onishi, H.; Thornton, G. Tailored TiO_2(110) Surfaces and Their Reactivity. *Nanotechnology* **2006**, *17*, 5397–5405.
(20) Dulub, O.; Batzilln, M.; Solovev, S.; Loginova, E. Electron-Induced Oxygen Desorption From the TiO_2 (011)-2×1 Surface Leads to Self-Organized Vacancies. *J. Phys. Chem. Lett.* **2007**, *317*, 1052–1056.
(21) Onda, K.; Li, B.; Petek, H. Two-Photon Photoemission Spectroscopy of TiO_2(110) Surfaces Modified by Defects and O_2 Or H_2O Adsorbates. *Phys. Rev. B* **2004**, *70*, 045415–045411.
(22) Humphrey, D. S.; Pang, C. L.; Chen, Q.; Thornton, G. Electron Beam and Scanning Tunnelling Microscope Tip Induced Modification of TiO_2 Surfaces. *in preparation*.
(23) Lyo, I. W.; Avouris, P. Field-Induced Nanometer-to Atomic-Scale Manipulation of Silicon Surfaces with the STM. *Science* **1991**, *253*, 173–176.
(24) Salling, C. T.; Lagally, M. G. Fabrication of Atomic-Scale Structures on Si(001) Surfaces. *Science* **1994**, *265*, 502–506.
(25) Stroscio, J. A.; Eigler, D. M. Atomic and Molecular Manipulation with the Scanning Tunneling Microscope. *Science* **1991**, *254*, 1319–1326.
(26) Shklyaev, A. A.; Shibata, M.; Ichikawa, M. Kinetics of Tip-Induced Island Growth on Si(111) with a Scanning Tunneling Microscope. *J. Vac. Sci. Technol. B* **2000**, *18*, 2339–2343.
(27) Li, N.; Yoshinobu, T.; Iwasaki, H. Nanofabrication on Si Oxide with Scanning Tunneling Microscope: Mechanism of the Low-Energy Electron-Stimulated Reaction. *Appl. Phys. Lett.* **1999**, *74*, 1621–1623.
(28) Ueda, N.; Sudoh, K.; Li, N.; Yoshinobu, T.; Iwasaki, H. Controllable Nanopit Formation on Si(001) with a Scanning Tunneling Microscope. *Jpn. J. Appl. Phys.* **1999**, *38*, 5236–5238.
(29) Fujita, K.; Watanabe, H.; Ichikawa, M. Nanometer-Scale Si Selective Epitaxial Growth on Si Surface Windows in Ultrathin Oxide Films Fabricated Using Scanning Tunneling Microscopy. *Appl. Phys. Lett.* **1998**, *73*.
(30) Iwasaki, H.; Yoshinobu, T.; Sudoh, K. Nanolithography on SiO_2/Si with a Scanning Tunnelling Microscope. *Nanotechnology* **2003**, *14*, R55–R62.
(31) Onishi, H.; Fukui, K.; Iwasawa, Y. Molecularly Resolved Observation of Anisotropic Intermolecular Force in a Formate-Ion Monolayer on a TiO_2(110) Surface by Scanning Tunneling Microscopy. *Colloids Surfaces A Physicochem. Eng. Aspects* **1996**, *109*, 335–343.
(32) Klusek, Z.; Busiakiewicz, A.; Datta, P. K.; Schmidt, R.; Kozlowski, W.; Kowalczyk, P.; Dabrowski, P.; Olejniczak, W. Room and High-Temperature Scanning Tunnelling Microscopy and Spectroscopy (HT-STM/STS) Investigations of Surface Nanomodifications Created on the TiO_2(110) Surface. *Surf. Sci.* **2007**, *601*, 1513–1520.
(33) Setvin, M.; Schmid, M.; Diebold, U. Aggregation and Electronically Induced Migration of Oxygen Vacancies in TiO_2 Anatase. *Phys. Rev. B* **2015**, *91*, 195403–195409.
(34) Zhang, H.; Banfield, J. F. Structural Characteristics and Mechanical and Thermodynamic Properties of Nanocrystalline TiO_2. *Chem. Rev.* **2014**, *114*, 9613–9644.
(35) Ohtani, B.; Prieto-Mahaney, O. O.; Li, D.; Abe, R. What Is Degussa (Evonik) P25? Crystalline Composition Analysis, Reconstruction From Isolated Pure Particles and Photocatalytic Activity Test. *J. Photochem. Photobiol. B* **2010**, *216*, 179–182.
(36) Hanaor, D. A. H.; Sorrell, C. C. Review of the Anatase to Rutile Phase Transformation. *J. Mater. Sci.* **2011**, *46*, 855–874.
(37) Diebold, U. The Surface Science of Titanium Dioxide. *Surf. Sci. Rep.* **2003**, *48*, 53–

229.
(38) Zhang, R.; Liu, Z.; Ling, L.; Wang, B. The Effect of Anatase TiO_2 Surface Structure on the Behavior of Ethanol Adsorption and Its Initial Dissociation Step: a DFT Study. *Appli. Surf. Sci.* **2015**, *353*, 150–157.
(39) Li, Y. F.; Aschauer, U.; Chen, J.; Selloni, A. Adsorption and Reactions of O_2 On Anatase TiO_2. *Acc. Chem. Res.* **2014**, *47*, 3361–3368.
(40) Hebenstreit, W.; Ruzycki, N.; Herman, G. S.; Gao, Y.; Diebold, U. Scanning Tunneling Microscopy Investigation of the TiO_2 Anatase (101) Surface. *Phys. Rev. B* **2000**, *62*, 1–3.
(41) He, Y.; Dulub, O.; Cheng, H.; Selloni, A.; Diebold, U. Evidence for the Predominance of Subsurface Defects on Reduced Anatase TiO_2(101). *Phys. Rev. Lett.* **2009**, *102*, 106105–106109.
(42) Raza, H.; Pang, C. L.; Haycock, S. A.; Thornton, G. Evidence of Discrete Bond Breaking Steps in the 1 × 1 to 1 × 3 Phase Transition of TiO_2(100). *Phys. Rev. Lett.* **1999**, *82*, 5265–5268.
(43) Klusek, Z.; Busiakiewicz, A.; Datta, P. K. Scanning Tunnelling Microscopy and Spectroscopy of the Reduced TiO_2(100) Surface. *Surf. Sci.* **2006**, *600*, 1619–1623.
(44) Zschack, P.; Cohen, J. B.; Chung, Y. W. Structure of the TiO_2(100)(1× 3) Surface Determined by Glancing Angle X-Ray Diffraction and Low Energy Electron Diffraction. *Surf. Sci.* **1992**, *262*, 395–408.
(45) Murray, P. W.; Leibsle, F. M.; Fisher, H. J.; Flipse, C.; Muryn, C. A.; Thornton, G. Observation of Ordered Oxygen Vacancies on TiO_2(100)1×3 Using Scanning Tunneling Microscopy and Spectroscopy. *Phys. Rev. B* **1992**, *46*, 12877–12879.
(46) Hardman, P. J.; Prakash, N. S.; Muryn, C. A.; Raikar, G. N.; Thomas, A. G.; Prime, A. F.; Thornton, G.; Blake, R. J. Oxygen-Vacancy Sites on TiO_2(100)(1 X 3) Using Surface Core-Level-Shift Photoelectron Diffraction. *Phys. Rev. B* **1993**, *47*, 16056–16059.
(47) Landree, E.; Marks, L. D.; Zschack, P.; Gilmore, C. J. Structure of the TiO_{2-X} (100)-1× 3 Surface by Direct Methods. *Surf. Sci.* **1998**, *408*, 300–309.
(48) Murray, P. W.; Leibsle, F. M.; Muryn, C. A.; Fisher, H. J.; Flipse, C. F. J.; Thornton, G. Interrelationship of Structural Elements on TiO_2(100)-(1 × 3). *Phys. Rev.* **1994**, *72*, 689–692.
(49) Shao, R.; Wang, C.; McCready, D. E.; Droubay, T. C.; Chambers, S. A. Growth and Structure of MBE Grown TiO_2 Anatase Films with Rutile Nano-Crystallites. *Surf. Sci.* **2007**, *601*, 1582–1589.
(50) Zhu, S.-C.; Xie, S.-H.; Liu, Z.-P. Nature of Rutile Nuclei in Anatase-to-Rutile Phase Transition. *J. Am. Chem. Soc.* **2015**, *137*, 11532–11539.
(51) Zhao, W.-N.; Zhu, S.-C.; Li, Y.-F.; Liu, Z.-P. Three-Phase Junction for Modulating Electron–Hole Migration in Anatase–Rutile Photocatalysts. *Chem. Sci.* **2015**, *6*, 3483–3494.
(52) Hosono, E.; Fujihara, S.; Imai, H.; Honma, I.; Masaki, I.; Zhou, H. One-Step Synthesis of Nano–Micro Chestnut TiO_2 With Rutile Nanopins on the Microanatase Octahedron. *ACS Nano* **2007**, *1*, 273–278.
(53) Deskins, N. A.; Kerisit, S.; Rosso, K. M.; Dupuis, M. Molecular Dynamics Characterization of Rutile-Anatase Interfaces. *J. Phys. Chem. C* **2007**, *111*, 9290–9298.
(54) Nolan, M.; Deskins, N. A.; Schwartzenberg, K. C.; Gray, K. A. Local Interfacial Structure Influences Charge Localization in Titania Composites: Beyond the Band Alignment Paradigm. *J. Phys. Chem. C* **2016**, *120*, 1808–1815.
(55) Grinter, D. C.; Nicotra, M.; Thornton, G. Acetic Acid Adsorption on Anatase TiO_2(101). *J. Phys. Chem. C* **2012**, *116*, 11643–11651.
(56) Grinter, D. C. Surface Studies of Metal Oxide Catalysts and Ultrathin Films, UCL, (doctoral thesis), University College London, London, 2011, pp. 1–227.
(57) Gong, X. Q.; Selloni, A.; Batzill, M.; Diebold, U. Steps on Anatase TiO_2(101). *Nat.*

Mater. **2006**, *5*, 665–670.
(58) Stetsovych, O.; Todorović, M.; Shimizu, T. K.; Moreno, C.; Ryan, J. W.; León, C. P.; Sagisaka, K.; Palomares, E.; Matolin, V.; Fujita, D.; et al. Atomic Species Identification at the (101) Anatase Surface by Simultaneous Scanning Tunnelling and Atomic Force Microscopy. *Nature* **2015**, *6*, 1–9.
(59) He, Y.; Tilocca, A.; Dulub, O.; Selloni, A.; Diebold, U. Local Ordering and Electronic Signatures of Submonolayer Water on Anatase TiO_2(101). *Nat. Mater.* **2009**, *8*, 585–589.
(60) Hebenstreit, W.; Ruzycki, N.; Herman, G. S.; Gao, Y.; Diebold, U. Scanning Tunneling Microscopy Investigation of the TiO_2 Anatase (101) Surface. *Phys. Rev. B* **2000**, *62*, 334–337.
(61) Setvin, M.; Schmid, M.; Diebold, U. Aggregation and Electronically Induced Migration of Oxygen Vacancies in TiO_2 Anatase. *Phys. Rev. B* **2015**, *91*, 195403–195409.
(62) Tasker, P. W.; Nakamura, K. The Stability of Ionic Crystal Surfaces. *J. Phys. C: Solid State Phys.* **1979**, *12*, 1183–1193.
(63) Pittaway, L.G, The temperature distributions in thin foils and semi-infinite targets bombarded by an electron beam. *Brit. J. Appl. Phys.* **1964**, 15, 967-982
(64) Lin, H.; Xu, S.; Wang, X.; Mei, N. Thermal Conductivity and Secondary Porosity of Single Anatase TiO_2 Nanowire. *Nanotechnology* **2013**, *24*, 415706–415713.
(65) Wang, L.-Q.; Baer, D. R.; Engelhard, M. H. Creation of Variable Concentrations of Defects on TiO_2(110) Using Low-Density Electron Beams. *Surf. Sci.* **1994**, *320*, 295–306.
(66) Vollnhals, F.; Woolcot, T.; Walz, M.-M.; Seiler, S.; Steinrück, H.-P.; Thornton, G.; Marbach, H. Electron Beam-Induced Writing of Nanoscale Iron Wires on a Functional Metal Oxide. *J. Phys. Chem. C* **2013**, *117*, 17674–17679.
(67) Baumer, M.; Cappus, D.; Kuhlenbeck, H.; Freund, H. J.; Wilhelmi, G.; Brodde, A.; Neddermeyer, H. The Structure of Thin NiO(100) Films Grown on Ni(100) as Determined by Low-Energy-Electron Diffraction and Scanning Tunneling Microscopy. *Surf. Sci.* **1991**, *253*, 116–128.
(68) Herman, G. S.; Dohnálek, Z.; Ruzycki, N. Experimental Investigation of the Interaction of Water and Methanol with Anatase-TiO_2(101). *J. Phys. Chem. B* **2003**, *107*, 2788–2795.
(69) Pang, C. L.; Lindsay, R.; Thornton, G. Structure of Clean and Adsorbate-Covered Single-Crystal Rutile TiO_2 Surfaces. *Chem. Rev.* **2013**, *113*, 3887–3948.
(70) Thomas, A. G.; Syres, K. L. Adsorption of Organic Molecules on Rutile TiO_2 And Anatase TiO_2 Single Crystal Surfaces. *Chem. Soc. Rev.* **2012**, *41*, 4207–4211.
(71) Tao, J.; Luttrell, T.; Bylsma, J.; Batzill, M. Adsorption of Acetic Acid on Rutile TiO_2(110) vs (011)-2 × 1 Surfaces. *J. Phys. Chem. C* **2011**, *115*, 3434–3442.
(72) Guo, Q.; Cocks, I.; Williams, E. M. The Orientation of Acetate on a TiO_2(110) Surface. *J. Chem. Phys.* **1997**, *106*, 2924–2931.
(73) Penn, R. L.; Banfield, J. F. Imperfect Oriented Attachment: Dislocation Generation in Defect-Free Nanocrystals. *Science* **1998**, *281*, 969–971.
(74) Zhang, Z.; Yates, J. T., Jr. Band Bending in Semiconductors: Chemical and Physical Consequences at Surfaces and Interfaces. *Chem. Rev.* **2012**, *112*, 5520–5551.
(75) White, J. M.; Henderson, M. A. Trimethyl Acetate on TiO_2(110): Preparation and Anaerobic Photolysis. *J. Phys. Chem. B* **2005**, *109*, 12317–12430.

CHAPTER 5

5.0: Lepidocrocite-like TiO_2 and TiO_2(110)–(1 × 2) supported on W(100)

Ultrathin films of TiO_2 were grown on a W(100)-O-(2 × 1) substrate and characterised using a combination of scanning tunneling microscopy (STM) and low energy electron diffraction (LEED). In addition to islands of rutile TiO_2(110) with (1 × 1) termination that were reported previously, we also observed rutile TiO_2(110) islands with a (1 × 2) film termination. A lepidocrocite-like TiO_2 nanosheet, closely related structurally to an anatase (001) bi-layer, was also observed on the W(100) surface simultaneously with rutile TiO_2(110) terminated (1 × 1) islands. High-resolution STM images show that the nanosheet grows in the principal orthogonal directions of the W(100) substrate and forms a commensurate (1 × 7) coincident cell. This two phase titania ultrathin film of rutile TiO_2(110)/ lepidocrocite-like TiO_2/W(100)-O-(2 × 1) provides a model system to study the electronic properties of an interface between two titania phases and affect on photochemical reactivity.

5.1 Introduction

As discussed in Chapter 1 there is great interest in the study of oxide surfaces;[1] due to their use in a multitude of applications, including catalysis and electronics.[2-5] In many of these studies, thin oxide films are used.[2,6] Thin film alternatives to bulk oxides supported on conducting substrates are typically employed to make insulating oxides sufficiently conductive to allow charged-particle techniques, such as scanning tunneling microscopy (STM) to be used on otherwise insulating oxides.[7,8] In some cases, such as for anatase TiO_2, high quality crystals are difficult to grow and ultrathin and thin films provide an alternative to natural crystals.[9-12]

Structures with no bulk-counterparts are of great interest as new material properties may be discovered and exploited.[3,4]

As the most thermodynamically stable face of rutile TiO_2, the (110) face has been studied extensively.[13] **Figure 5.1** presents filled ball models of the bulk terminated (1 × 1) and reconstructed (1 × 2) terminated (added row Ti_2O_3),[14] where the unit cells are indicated by black rectangles of 6.49 × 2.96 $Å^2$ and 12.98 × 2.96 $Å^2$ size respectively.[15] Ultrathin rutile TiO_2(110) islands have been grown on various substrates and are usually terminated by the (3.0 Å × 6.5 Å) (1 × 1) surface (**Figure 5.1A**),[8,16-24] but if the deposited Ti is not completely oxidised, the reduced (3.0 Å × 13.0 Å) (1 × 2) (**Figure 5.1B**) reconstruction can also be observed, where the unit cell mesh is doubled in the [$\bar{1}$10] direction.[18] As mentioned above, ultrathin films of anatase TiO_2 have also been grown. The (001) surface generally displays a (1 × 4) reconstruction,[9-12] consistent with measurements of the single crystal.[25,26]

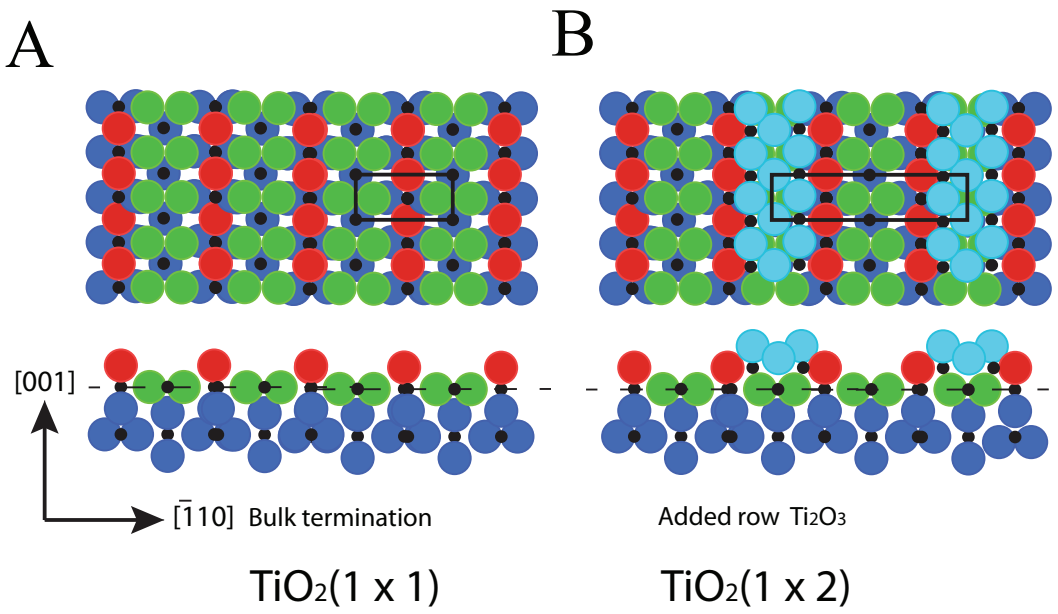

Figure 5.1: (**A**) Top down and side view of the filled ball ionic model of the bulk terminated TiO_2(110)-(1 × 1) surface. The unit cell of 6.49 × 2.96 $Å^2$ is indicated by the black rectangle. Blue spheres, bottom layer O atoms. Red spheres, bridging O atoms. Green spheres, O atoms top layer. Black spheres, Ti atoms. (**B**) Top down and side view filled ball ionic model of the 'Added row Ti_2O_3' TiO_2(110)-(1 × 2) mode with the unit cell of 2.96 × 12.98 $Å^2$ indicated by the black rectangle. The light blue spheres are O atoms of the added row Ti_2O_3 unit. The black dashed line is co-incident with top (1 × 1) Ti layer. Adapted from reference.[15]

TiO_x films have also been reported that have no bulk counterpart, such as a quasi-hexagonal TiO_x phase on $Ni_{94}Ti_6(110)$[27] or Ni(110)[17,24] and TiO_x nanodots on Ni(110).[24] A series of TiO_x phases have also been grown on Pt(111),[28,29] several of which are related to encapsulation layers observed on TiO_2(110)-supported nanoparticles.[30,31] Of particular relevance to this Chapter are the family of lepidocrocite-like films that have been observed on Pt(110)-(1 × 2), Ni(110), Ag(100), and $Pt_3Ti(111)$.[17,19,28,32,33] This film is so-named due its structural similarity to the FeO(OH) lepidocrocite bilayer.[34] In calculations, the lepidocrocite-like structure forms spontaneously from a (001) anatase bilayer,[19,32 35,36] the top layer displacing by half a unit cell. The substrate-free bilayer has surface lattice parameters of ~3.75 Å × 3.00 Å. [17,19,28,32,37,38] **Figure 5.2** presents a structural model of the substrate free anatase bi-layer and lepidocrocite-like bi-layer. The anatase [100] bi-layer unit cell is shown from the top (**Figure 5.1A)** and side (**Figure 5.2B**). The oxygen atoms (red circles) are either 2-coordinated (2c) or 3-coordinated (3c) and the titanium atoms (blue circles are 5-coordinated (5c). A unit cell of (a = b = 3.78 Å) is indicated by the black rectangle. The lepidocrocite-like bilayer is shown from the top (**Figure 5.2C** and side (**Figure 5.2D).** An imaginary intermediate side view indicating the forming bonds (black dashed lines) is shown in **Figure 5.2E**. The described structural change results in a more stable bi-layer formed of 6-coordinated Ti ions.

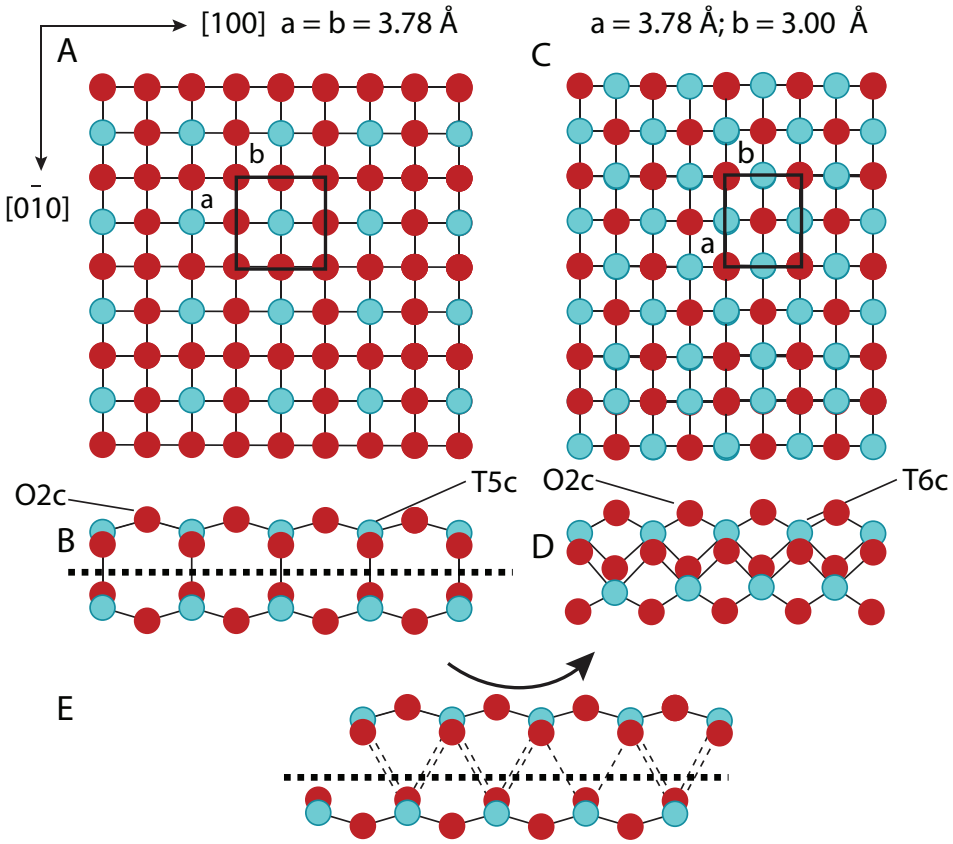

Figure 5.2: (**A**) Top view of a ball and stick model of an substrate free anatase TiO_2(001) bi-layer. Unit cells identified by the black box **(B)** Side view of the anatase TiO_2(001) bi-layer, the O_{2c} and Ti_{5c} atoms are labelled. (**C**) Top view of a ball and stick model of a substrate free lepidocrocite–like bi-layer. Unit cell identified by the black box. (**D**) Side view ([010] into page) of the anatase TiO_2(001) bi-layer, the O_{2c} and Ti_{6c} atoms are labelled. (**E**) Side view of a notional intermediate stage, black dotted line the mid point in the bi-layer. Black arrow direction of transformation. In all models the red spheres are oxygen atoms and blue spheres titanium atoms. Azimuths are shown with respect to the anatase (001) surface. Adapted from this reference with the authors DFT derived lattice paramters.[32]

Here, we have studied ultrathin TiO_2 films grown on W(100)-O-(2 × 1) surfaces using STM and low energy electron diffraction (LEED). The W(100)-O-(2 × 1) reconstruction is formed by removing (or adding) alternate rows of W along [001] or [010] to create {110} microfacets that contain O in the 3-fold hollow sites.[39] This gives a primitive surface unit cell of 6.3 Å × 3.2 Å that is nearly lattice matched with rutile TiO_2(110). Apart from the (1 × 1) phase which was previously observed,[20] we observed a TiO_2 lepidocrocite-like structure as well as the TiO_2(110)-(1 × 2) reconstruction for the first time on W(100).

The anatase derived lepidocrocite-like supported films on W(100), which can also support rutile TiO_2(110), provides a model system to study the electronic properties of the interface between two defined single crystalline titania polymorphs with both bulk sensitive and

macroscopic averaging techniques and microscopy to reveal mixed polymorph electronic and photo-chemical characteristics which could be generalised.[40] The presence of the W(100) substrate provides a 3rd metallic component, integral to current photocatalytic model systems studied. These act as electron sinks and sites for reduction such as H_2 formation.[40] This would be an 'inverse' catalytic system.[41] Mixed metal oxide photocatalysts of TiO_2 and WO_3 have been studied, where excited CB electrons are spatially separated from holes by transfer to the WO_3 component. This lepidocrocite-like TiO_2/ rutile TiO_2(110) / W(100) system provides scope to examine the three components with potentially enhanced photo-reactivity reactivity at the interfacial regions of the three components.[42]

5.2 Experimental Details

The experiments were conducted in an ultrahigh vacuum (UHV) system comprising a preparation and analysis chamber with base pressures in the 10^{-10} mbar range, equipped with quadrupole mass spectrometers for residual gas analysis (RGA). The analysis chamber housed an *Omicron* UHV AFM/STM, calibrated with a rutile TiO_2(110) single crystal, and rear-view LEED optics that were also employed for retarding field Auger electron spectroscopy (AES). The rutile TiO_2(110) single crystal was prepared by cycles of argon sputtering and annealing 1100 K. The films were grown in the preparation chamber, which was equipped with an ion sputter gun, an electron bombardment sample heater, and metal evaporators. Prior to the growth of the films, the W(100) sample (*Surface Preparation Laboratory*) was prepared by cycles of argon sputtering and annealing to ~1173 K in 2×10^{-8} mbar O_2 and UHV, followed by flashing to 1500-1600 K, until a well-ordered W(100)-O-(2×1) was identified in LEED and STM and any contamination was below the detection limit of AES.[20]

STM images were recorded at room temperature using positive sample bias (tunneling into empty sample electronic states) and either etched tungsten or mechanically formed PtIr tips. Estimates of coverage are given in monolayer equivalents (MLE) where 1 MLE is defined as

complete coverage of the surface by a single layer of TiO_2 that has a thickness of 3.25 Å. Likewise for the TiO_2 lepidocrocite-like phase, 1 MLE is defined as the complete coverage of the surface by a bilayer, the thickness being estimated at 5 Å.

The first step of the film preparation was the deposition of 2-3 monolayers (ML) of Ti (determined retrospectively from the film coverages) onto the W(100)-O-(2 × 1) surface at room temperature from the vapour of a metal wire (*Goodfellow*) using a commercial evaporator (*Omicron* EFM) with a deposition rate of 10^{-2} MLs^{-1}, an identical procedure was used as by Mathru.[43] The second step consisted of annealing under 2-7 × 10^{-7} mbar O_2 at 800-850 K between 1-1.5 hours, followed by cooling to room temperature in UHV. The final step was a UHV anneal to 920-980 K for 10 minutes. Sample temperatures were measured with an optical pyrometer (*Minolta*). Three TiO_2 films were studied, each grown under slightly different conditions: (1) A TiO_2(110)-(1 × 1) ultrathin film was formed by annealing to 840 K under 2-7 × 10^{-7} mbar O_2 for 1 hour and annealing in UHV at 970-990 K. (2) A TiO_2(110)-(1 × 2) ultrathin film was formed by annealing in 2-7 × 10^{-7} mbar O_2 for 1.5 hours at 840 K and annealing to 920 K in UHV. (3) A TiO_2(110)-(1 × 1)/lepidocrocite-TiO_2 ultrathin film was annealed at 840 K at 2-7 × 10^{-7} mbar O_2 for 1 hour, then annealing to 920 K in UHV.

5.3 Results and Discussion

5.3.1 Preparation of W(100)-O-(2 × 1)

The procedure employed by Pang et al.[20] to prepare the same W(100)-O-(2 × 1) was used. After a final flash anneal for 3 minutes at 1500-1600 K, a LEED diffraction pattern was recorded; this is presented in **Figure 5.3.** Two orthogonal sets of sharp (1 × 2) patterns are apparent in the LEED (50 eV) photograph; this is line with previous LEED of the surface by Matharu.[43] The discussed the (1 × 2) reconstruction which occurs on the W(100) surface during preparation in the presence of gas phase O_2 results in an 'apparent' (2 × 2) LEED pattern due to the four-fold surface symmetry.[39,44,45] This (2 × 2) pattern is deconstructed by the composite of

the simulated LEED pattern formed of two rotational domains of the W(100)-O-(2 × 1). Grids of black and red circles in **Figure 5.3A** and **5.3B** in reciprocal space (a^*, b^*) are presented with the corresponding real space (a) distances, related by the equation, $a^* = \frac{2\pi}{a}$, as defined in Chapter 2 and combined in **Figure 5.3C** which compares favourably with the photograph of the LEED in **Figure 5.3D.** This LEED pattern was examined over a range of electron beam energies (40-100 eV) and demonstrated only the (1 × 2) pattern.

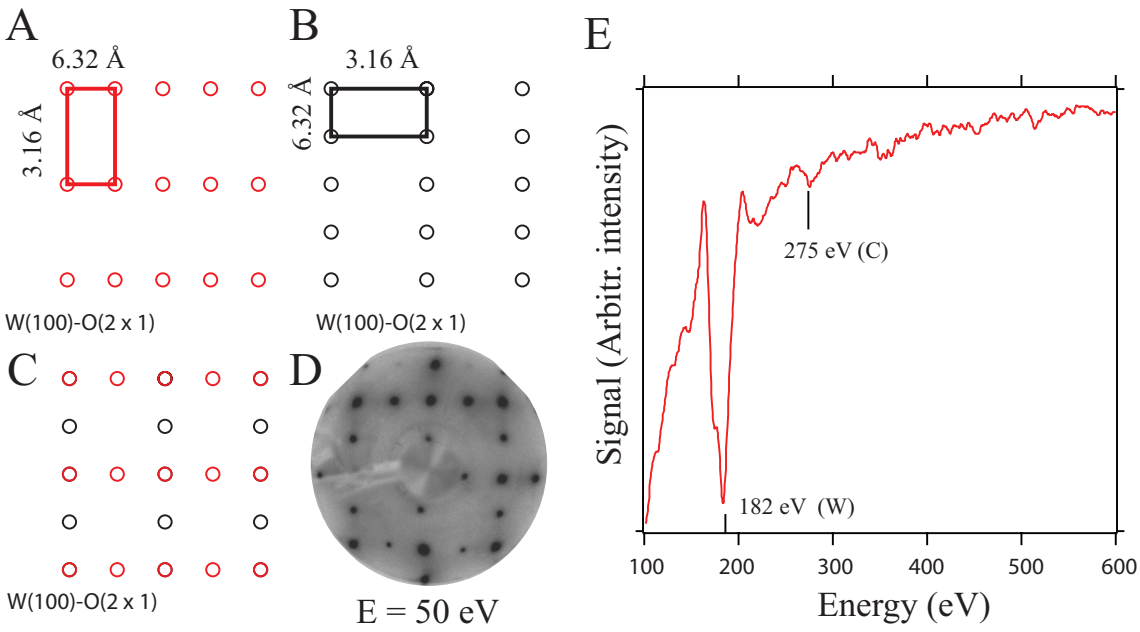

Figure 5.3: Simulated LEED reciprocal patterns for two rotational domains (**A, B**) of W(100)-O-(2 × 1) unit cell (red and black circles). The respective real space W(100)-O-(2 × 1) unit cell distances are shown.(**C**)The composite pattern formed of (**A**) and (**B**). (**D**) LEED pattern recorded at 50 eV. Processed in Adobe Photoshop: colour inverted and converted to grey scale. (**E**) AES (100-600 eV) recorded with a 3 kV electron beam. Identified are Auger peaks at 182 eV (W) and 275 eV (C).

AES was recorded to determine the cleanliness of the sample after the preparation, (**Figure 5.3E**) apart from the strong tungsten ($N_5O_3O_3$) 182 eV peak there is a weak peak at 275 eV attributed to carbon impurity. This carbon feature originates as a bulk metal impurity.

The W(100)-O-(2 × 1) surface was examined in UHV by STM to verify that an *ca.* identical surface, as formed in by Pang[20] was indeed prepared and images are presented in **Figure 5.4**. The 290 × 290 $Å^2$ empty sample state image in **Figure 5.4A** depicts terraces of 200 Å width and 500-1000 Å length. A blue line height profile indicates a terrace step height of 2 Å

± 0.5 Å which is in line with other studies of the surface.[20] The terraces are formed of discreet rectangular components of between 6-25 Å; terminated by domain boundary as also shown previously. This domain boundary is an apparent depression of lower ~1 Å height and ~3 Å length.

Seen in the zoom (**Figure 5.4B**) are resolved features of the W(100)-O-(2 × 1) reconstructed surface, similar to that achieved previously by early empty state STM by Meyer et al.[46] Black dashed black lines normal to the [001] direction indicate a 6.4 Å ± 0.3 Å separation, approximately 6.3 Å, twice the W(100)-(1 × 1) unit cell parameter and resolution along the row of oval features of ([001] direction in **Figure 5.4C**) of 3.1 Å ± 0.3 Å separation are indicated by blue dashed lines close to the W(100) unit cell length. The W(100)-O-(2 × 1) model presented in **Figure 5.4C**[44] has a unit cell of 6.32 × 3.16 $Å^2$ (black rectangle, containing two adsorbed oxygen atoms (green circle)); this can be overlaid exactly on repeating features of image **Figure 5.4B,** as shown by the black rectangle. As the oxygen atoms are considered by structural characterisation[44] to occupy three-point tungsten surface hollow sites and thus geometrically higher on the surface, each oval is likely representative of a pair of O atoms; simulated STM images would be required to prove this hypothesis.[47] The separation of two W(100)-O-(2 × 1) rows of *ca.* 12.5 Å (4 unit cells lengths), is identified by the green dashed lines, which indicates that a single unit cell of W(100)–O-(2 × 1) is absent or modified in the domain boundary. Shown in **Figure 5.4D** are green dashed lines overlaid along the W(100)-O-(2 × 1) [001] direction to analyse the domains. The rows of W(100)-O-(2 × 1) form small domains (defined here by length of row × no of adjacent rows) and are noticeably smaller than Mathru; who used a lower final anneal temperature (10 minutes at 1275 K).[43] The W(100)-O-(2 × 1) surface domain aspect ratio displayed a notable correspondence to the aspect ratio of the lepidocrocite islands in the titania films studied; where the lepidocrocite elongation surface directions are aligned with the elongated direction of the W(100)-O-(2 × 1) domains. This is in line with the epitaxial arrangement determined in that orientation. The blue circle identifies a feature of unknown identity; most probably the formation of the second layer of tungsten oxide, although AES indicates there is a small carbon surface contamination.

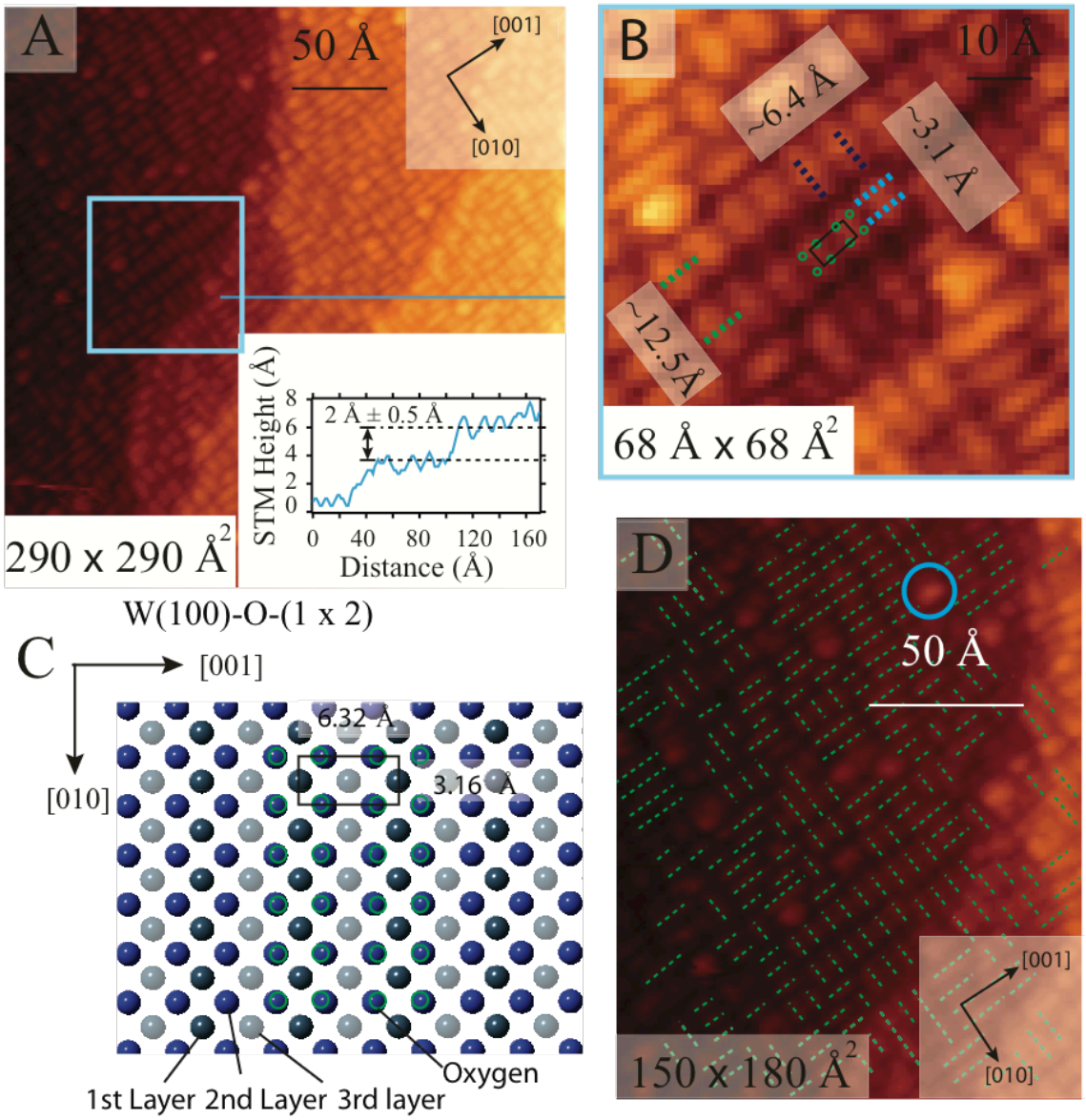

Figure 5.4: 300 K STM image (+1.2 V sample bias, 0.08 nA) of the W(100)-O-(2 × 1) surface prepared with a final UHV anneal 1500-1600 K. (**A**) 290 × 290 Å^2 image, blue horizontal line indicates position of height profile. Upper inset: azimuths with respect to the W(100) surface. Blue line profile is overlaid across three terraces. Lower inset: blue height line profile with a ~2 Å step height indicated. (**B**) 68 × 68 Å^2 zoomed-in image, identified are blue, black and green dashed lines identifying resolved features to the W(100)-O-(2 × 1) unit cell. The black box and green circles is the overlaid unit cell of W(100)-O-(2 × 1) (as shown in (**C**)) with scale determined from the unit cell parameters. (**C**) Structural model of the W(100)-O-(2 × 1) surface model: 1st top W layer green, 2nd middle W layer blue, 3rd W bottom layer light blue, oxygen atoms are identified by the green circles. (**D**) Zoomed-in 150 × 180 Å^2 image from (**A**), green dashed lines are overlaid along the W(100)-O-(2 × 1) reconstruction (parallel to the [010] for the reconstruction depicted in direction in (**C**)).

5.3.2 TiO_2(110)-(1 × 1) Ultrathin Film

STM images of a titania film grown on the W(100)-O-(1 × 2) are displayed in **Figure 5.5**. In the large area (1000 × 850 $Å^2$) image of **Figure 5.5A**, islands with mean heights of 20 Å, lengths of 150-200 Å, and widths of 70-100 Å can be seen, the coverage being ~2.4 MLE. The heights corresponds to six TiO_2(110) layers and the islands are elongated in the principal directions of the W(100) substrate. In the high resolution STM image (**Figure 5.5B**) taken from the top of one of the TiO_2(110) islands, the characteristic TiO_2(110) topography can be observed. Point defects resolved between bright rows (distance 6.5 Å) of Ti atoms are consistent with the observations of Pang et al.[20] Given that the film was left in a UHV chamber with a background water pressure of 2×10^{-11} mbar (estimated from RGA) for 76 hr after forming the film (~3 Langmuirs), we assume that the defects are bridging hydroxyl (OH_b), the coverage being 0.19 ML, where 1 ML is the density of Ti_{5c} sites. One OH_b is identified by the blue circle, of ca. 1 Å apparent height. A filled ball model of the rutile TiO_2(110) surface is shown in **Figure 5.5C**. The unit cell is identified by the yellow rectangle. **Figure 5.5D** is a 76 × 76 $Å^2$ STM image of a rutile TiO_2(110) single crystal prepared in UHV and exposed to a water (1 L). It displays a characteristic[13] surface with OH_b point defects after exposure to residual water in the chamber; one such feature (blue circle) of 0.8 Å is identified between the Ti_{5c} rows. A similar STM tunneling imaging mode between the rutile single crystal and titania film supported on W(100)-O-(2 × 1) is evidenced.

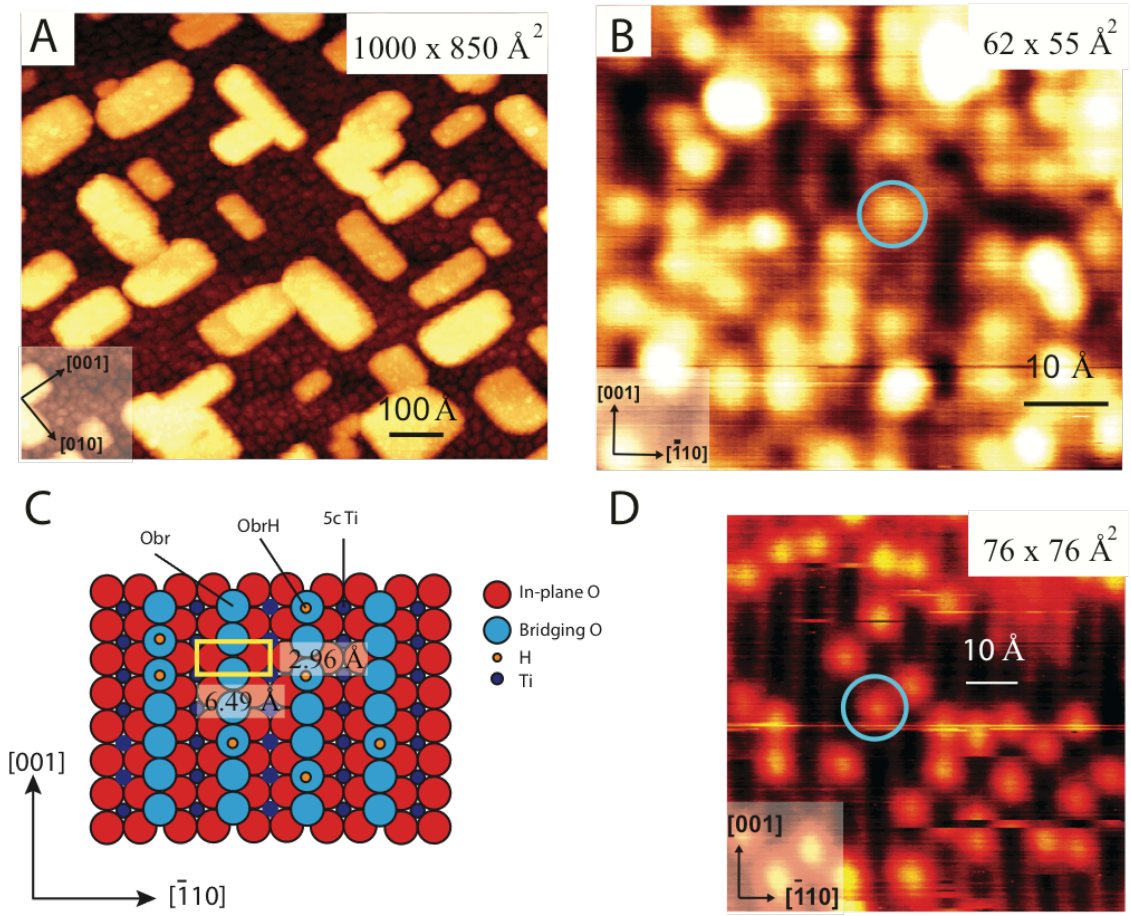

Figure 5.5: 300 K STM images (+1.6 V sample bias, 0.05 nA) of the TiO_2(110)-(1 × 1)/ W(100)-O-(2 × 1) film. (**A**) A large area (1000 Å × 850 Å) image, showing the rutile TiO_2(110) island morphology with a coverage of 2.4 MLE. The azimuths are defined with respect to the W(100) surface**. (B**) A high resolution (62 Å × 55 Å) image of the surface of a rutile island, six layers thick. The image is characteristic of the native TiO_2(110)-(1 × 1) surface: bright rows are Ti atoms, with point defects between on the bridging oxygen rows. The blue circle highlights a bridging hydroxyl (OH_b). (**C**) A filled ball model of the rutile TiO_2(110) surface. Identifed are; Obr, ObrH and 5c Ti. The atoms are labelled by the legend. (**D)** A 76 × 76 Å^2 STM image of a single crystal rutile TiO_2(110) surface, a blue circle identifies a bridging hydroxyl (OH_b). The azimuths are defined with respect to the rutile TiO_2(110) surface.

5.3.3 TiO_2(110)-(1 × 2) Ultrathin Film

The second film was prepared in a similar manner to the (1 × 1) film described in the previous paragraph except the final UHV anneal was at a reduced temperature of 920 K (as compared to 970-990 K). In some areas, islands of rutile TiO_2(110)-(1 × 1) were observed with the same characteristics as in **Figure 5.5**. In other regions the islands have a different structure. **Figure 5.6A** depicts a large area image of the film. As with the (1 × 1) islands, these are also elongated in the [001] and [010] directions of W(100). Within the islands, rows can be observed

and these run parallel to the direction of elongation, islands containing these rows are identified with green dashed boxes. In the high resolution image **Figure 5.6B**, it is apparent that the rows have a spacing of 12.5 Å ± 0.5 Å which is consistent with the rutile TiO_2(110)-(1 × 2) reconstruction.[13]

The coverage of the film is 3.1 MLE. In **Figure 5.6B,** the surface shown contains three different layers, all displaying the (1 × 2) reconstruction. The line profile in **Figure 5.6C** shows that the height of the step (3 Å ± 0.2 Å) is consistent with a step edge of TiO_2(110). This is the first time, to our knowledge, the (1 × 2) surface reconstruction has been observed on an ultrathin TiO_2 film on W(100). The (1 × 2) reconstruction is a reduced phase of TiO_2 and is thought to be composed of added rows of Ti_2O_3.[48]

Such a film containing a (1 × 2) reconstruction has been previously reported in connection with a Ni(110) substrate, where its appearance was attributed to incomplete oxidation of the as-deposited Ti.[17] The growth conditions for the (1 × 2) film involved a longer oxidation step than for the (1 × 1) film, and a final anneal step at a lower temperature. The lower temperature of the final anneal step may lead to incomplete oxidation of the Ti.

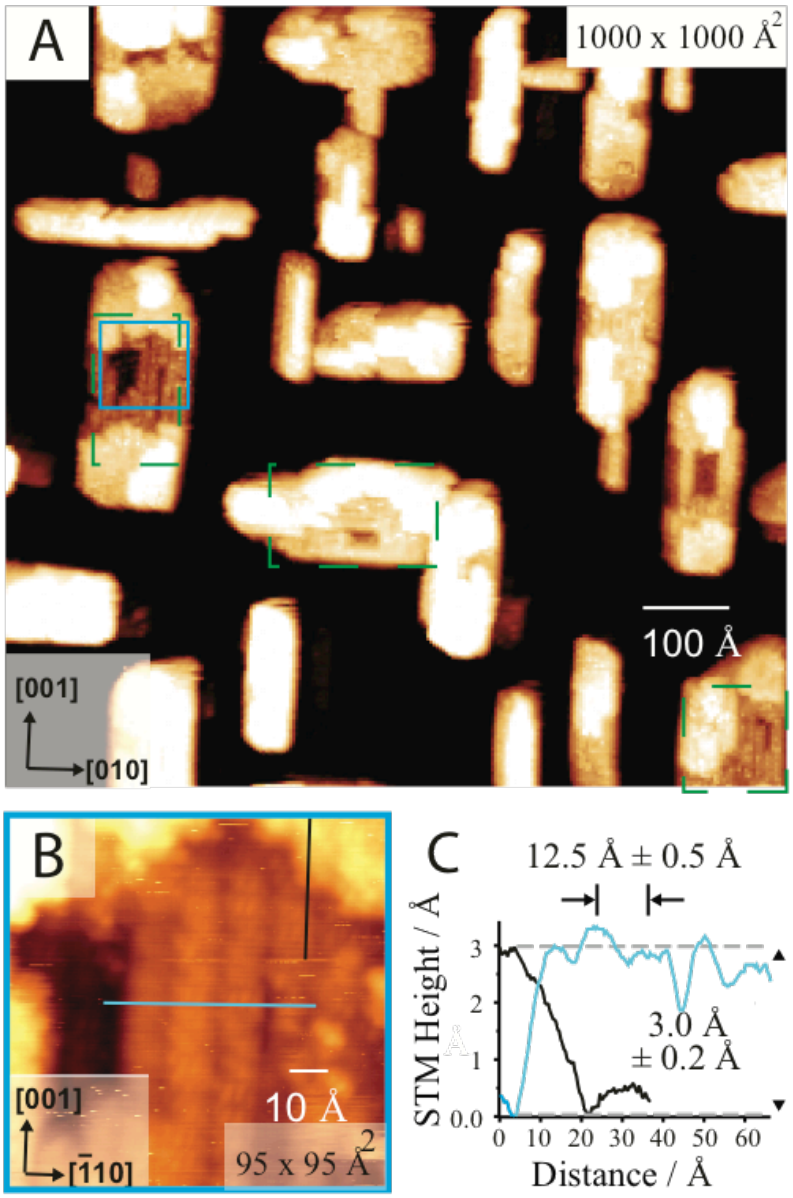

Figure 5.6: 300 K STM images (+1.6 V sample bias, 0.05 nA) of the TiO_2(110)-(1 × 2)/W(100)-O-(2 × 1) film. (**A**) A large area (1000 × 1000 Å^2) image of a 3.1 MLE titania film, displaying the TiO_2(110)-(1 × 2) surface reconstructed islands, identified by green dashed boxes. Azimuths are defined with respect to the W(100) surface (**B**) A 95 × 95 Å^2 image zoomed-in from the light-blue square in (**A**) displaying the (1 × 2) reconstruction. Azimuths are defined with respect to the rutile TiO_2 (110) surface. (**C**) Line profiles taken from the image in (**B**). The black profile displays the step edge on the island (3.0 Å ± 0.2 Å) and the light-blue profile shows the 12.5 Å ± 0.5 Å periodicity in the [$\bar{1}$10] direction, as well as another 3.0 Å ± 0.2 Å step edge.

5.3.4 TiO_2(110)-(1 × 1)/Lepidocrocite-like TiO_2 Ultrathin Film

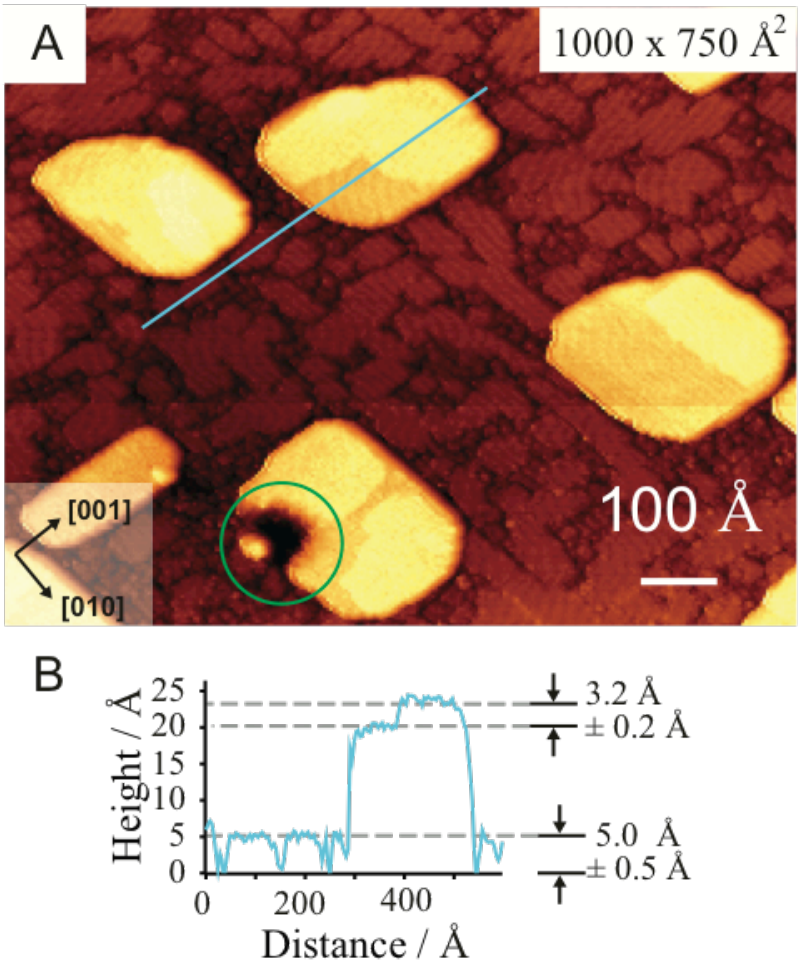

Figure 5.7: STM images (+1.6 V sample bias, 0.05 nA) of the TiO_2/W(100)-O-(2 × 1) film. (**A**) A large area 1000 × 750 Å^2 image of the titania film. TiO_2(110)-(1 × 1) islands are present together with the lepidocrocite-like TiO_2 nanosheet. A hole in one island is circled in green, and is presumably due to some interaction with the tip. The rutile TiO_2(110) islands and lepidocrocite-like film have coverages of 1.7 MLE and 0.42 MLE, respectively. (**B**) The blue line profile taken from the blue line indicated in (**A**), shows the heights of a rutile TiO_2(110)–(1 × 1) island and the lepidocrocite-like phase, which are 20-25 Å and 5 Å, respectively.

Figure 5.7A shows a large area STM image of the third film. Two distinct overlayers were observed with quite different mean heights. These are indicated by the blue line profile in **Figure 5.7B.** The taller of these overlayers corresponds to islands of rutile TiO_2(110). The islands have mean heights of 20-25 Å, a single step edge height inline with rutile TiO_2(110) is indicated. Co-existing with these islands is a pseudo-2D or 'nanosheet' overlayer that has a uniform height of ~5 Å. This nanosheet has a similar appearance and height to the lepidocrocite-like phases reported previously.[16] The rutile islands have an area coverage of 25%

and the nanosheet 42%. This corresponds to MLE coverages of 1.7 MLE and 0.42 MLE, respectively.

Higher resolution images of the nanosheet recorded from a different region of the sample are displayed in **Figure 5.8**. **Figure 5.8A** is a large area image and shows a long-range periodicity of ~20 Å along the [010] direction of the W(100) substrate. This periodicity is more apparent in the zoomed-in image of **Figure 5.8B**. The image in **Figure 5.8B** resembles a Moiré pattern with a short lattice and a superlattice that is periodic in the W(100) [010] direction. The short lattice has dimensions of 3.7 Å ± 0.2 Å in the W(100) [010] direction while being exactly matched with the substrate at 3.0 Å ± 0.2 Å in the W(100) [001] direction. The superlattice is 22.0 Å ± 0.2 Å (or six times the short lattice) in the W(100) [010] direction.

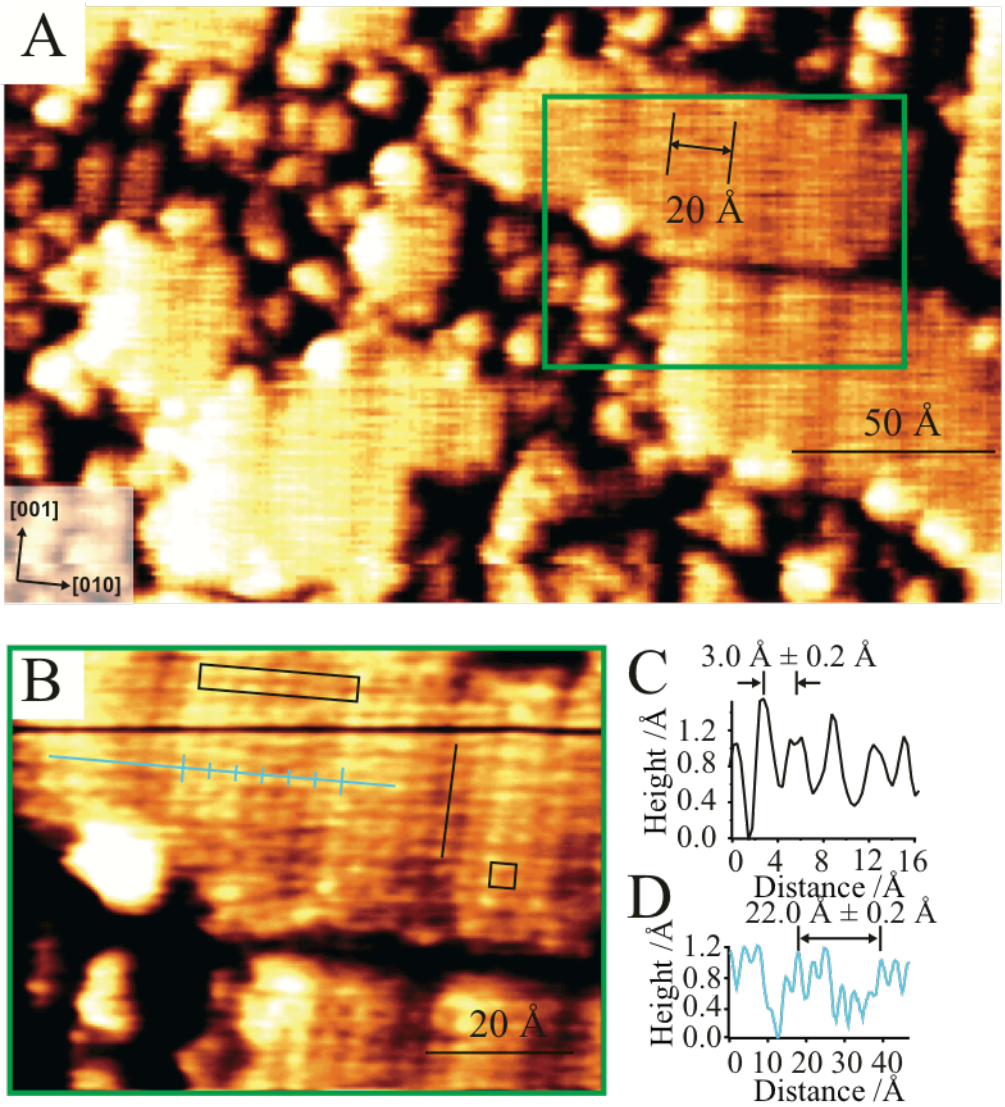

Figure 5.8: 300 K STM images (+1.6 V sample bias, 0.05 nA) of the W(100)-O-(2 × 1)-lepidocrocite-like film. Islands of 5 Å height, orientated in the principal directions of the W(100) crystal are observed, azimuths are defined with respect to the W(100) surface. (**A**) A large area (250 Å × 150 Å) STM image shows the islands have periodic stripes separated by ~20 Å, with the islands elongated perpendicular to these stripes. (**B**) A (80 Å × 60 Å) filtered image zoomed in from the green rectangle in a, where the primary unit cell and superlattice are visible (identified by black rectangles). The minor and major ticks on the blue line highlight this further. (**C**) Line profile taken from black line in (**B**) displaying the [001] direction unit cell spacing of the lepidocrocite-like phase (3.0 Å ± 0.2 Å). (**D**) Line profile taken from the light blue line in (**B**) depicting the periodicity of the superlattice (22.0 Å ± 0.2 Å) in the [010] direction.

Figure 5.9 shows LEED patterns simulated from the real-space lattice parameters together with a photograph of a LEED pattern recorded at 50 eV. **Figure 5.9A** and **5.9B** depict two orthogonal W(100)-O-(2 × 1) reflexes which are calculated from the lattice parameters of W(100)-O-(2 × 1). **Figure 5.9C** and **Figure 5.9D** show two orthogonal patterns with (1 × 7)

periodicity with respect to W(100). These are assigned to the superlattice of the nanosheet phase. **Figure 5.9E** is a superposition of all of these, which reproduces accurately the LEED pattern presented in **Figure 5.9F**. The {0 , ½} reflexes are consistent with either TiO_2(110) or W(100)-O-(2 × 1). According to our interpretation of the LEED pattern, the superlattice should be seven times the W(100) lattice (3.16 Å) which gives the periodicity of the superlattice as 22.1 Å, consistent with the STM measurement.

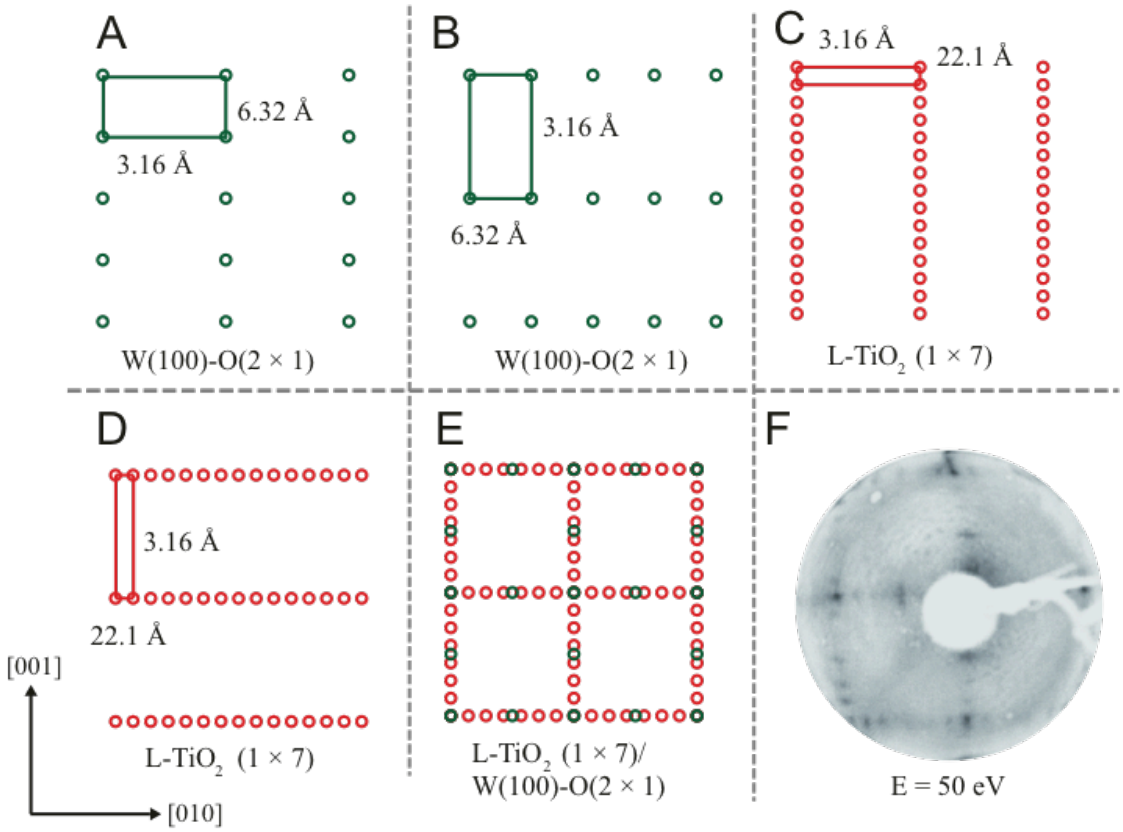

Figure 5.9: LEED patterns of the TiO_2 and lepidocrocite-like films on W(100)-O-(2 × 1).(**A**),(**B**) Schematics of the two orthogonal, calculated LEED patterns of W(100)-O-(2 × 1), with a real space unit cell of (3.16 Å × 6.32 Å).(**C**),(**D**) Schematics of the two orthogonal, calculated LEED patterns of a lepidocrocite-like film (L-TiO_2) that has (1 × 7) periodicity with respect to W(100) and a real space unit cell of (3.16 Å × 22.1 Å). (**E**) A superposition of schematics in a-d forming the predicted LEED pattern. (F) LEED pattern of the film at 50 eV, which compares favourably with (**E**). Azimuths are defined with respect to the W(100) surface.

A simple model derived from the LEED and STM data is shown in **Figure 5.10**. The substrate W(100)-(1 × 1) lattice is shown with black circles. Superimposed on this is the nanosheet layer. With respect to the azimuths of the W(100), in the [001] direction, the two are exactly matched, whereas in the [010] direction, the nanosheet layer does not coincide and has a

spacing of 3.69 Å. This leads to a commensurate (1 × 7) lattice that has a period of six times the lattice parameter of the nanosheet layer and seven times the W(100) lattice.

The theoretical lattice parameters for the substrate-free TiO_2 lepidocrocite-like phase is calculated at 3.73 Å × 3.02 Å by Vittadini et al.[35] and 3.766 Å × 3.007 Å by Atrei et al..[19] Thus the long side of our nanosheet unit cell would only represent a very modest contraction of 1.1-2.1% from the calculated values of the lepidocrocite-like phase. This compares to an expansion of 3.4-4.4% to 3.9 Å for the lepidocrocite-like phase on Pt(110)-(1 × 2)[36] and a contraction of 3.2-4.2% to 3.61 Å for the same film on Ag(100).

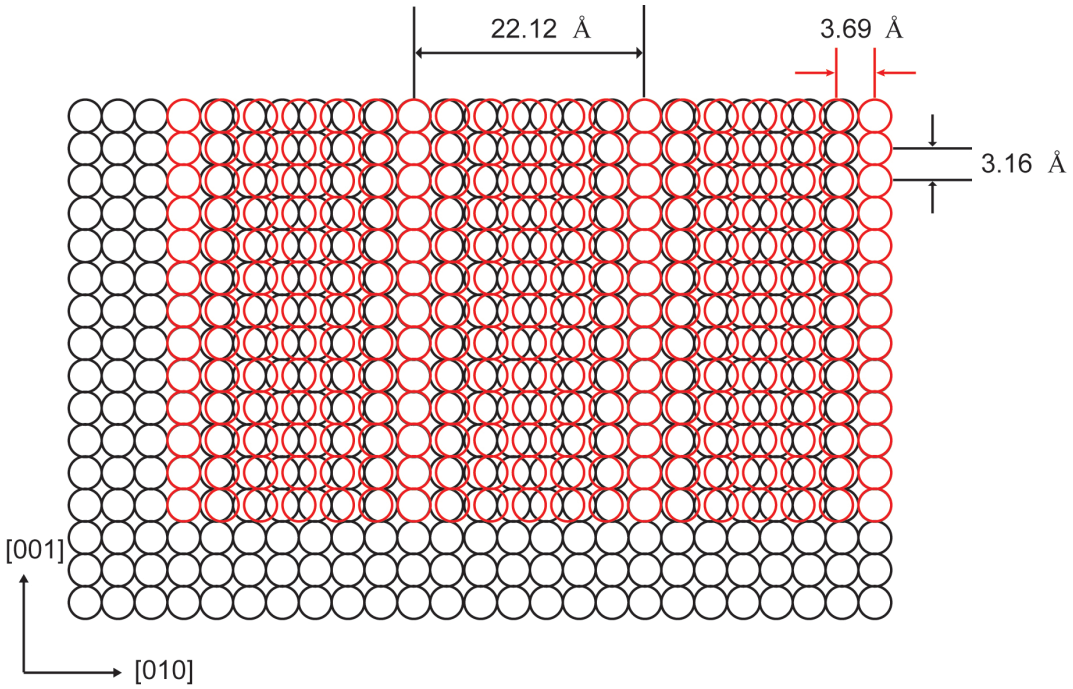

Figure 5.10: TiO_2 lepidocrocite overlayer schematic. A schematic representation of the TiO_2 lepidocrocite-like phase in red circles (3.69 Å × 3.16 Å) superimposed on top of the W(100)–(1 × 1) surface (3.16 Å × 3.16 Å) in black circles. These parameters were derived from the STM and LEED data. Azimuths are defined with respect to the W(100) surface.

The short side of our nanosheet unit cell (3.16 Å) also only represents a small expansion from the theoretical values of 4.3-5%. For comparison, the lepidocrocite-like phase on Ag(100) has a maximum contraction of 4-4.6% to 2.89 Å, making the short direction commensurate with the substrate. The short side of lepidocrocite-like phase unit cell on Pt(110)-(1 × 2), was measured in STM to have a length of 3.0 Å. This had an identifiable ×14 super cell with respect to the substrate in the [001] azimuth (2.77 Å).

As for the height of our nanosheet film, this was measured in STM to be 5 Å ± 0.5 Å. This is in agreement with the height of the lepidocrocite-like film on Ag(100) as determined by X-ray photoelectron spectroscopy and LEED intensity measurements.[19] On the other hand, Agnoli et al.[36] report an apparent height in STM of ~1.5 Å on Pt(110)-(1 × 2) but attribute this to electronic effects.

From this comparison, we conclude that our nanosheet phase is also a lepidocrocite-like phase. If the underlying substrate was W(100)-O-(2 × 1) this would imply a ×3.5 coincident lattice in the W(100) [010] direction. As such, we believe the oxygen from the W(100)-O-(2 × 1) is incorporated into the lepidocrocite-like phase which is then formed directly on the W(100) surface.

Poor stability of a delaminated titanate bilayer was observed previously by a transformation into anatase crystallites above 1070 K,[49] and we tested this on our film by annealing the sample to 1000 K. The (1 × 7) LEED spots were considerably weakened in intensity. Likewise, whereas before annealing the lepidocrocite-like overlayer had area coverage of 42 %, this was reduced to 3.3 % after annealing. A representative STM image after annealing is presented in the Appendix (**A.6**). The formation of the lepidocrocite-like phase may be related to the lower temperature of the final UHV step in comparison with the (1 × 1) film. In the two studies by Atrei et al.,[19,37] for the same growth conditions, the lepidocrocite-like phase was observed for up to one ML of Ti deposition, beyond which rutile TiO_2(110) islands co-exist on the surface. Thus another explanation for the appearance of the lepidocrocite-like phase in the current work could be related to a slightly lower coverage of Ti used to make this film in comparison to the two rutile TiO_2 films presented. A systematic study of Ti coverage is required to demonstrate this.

5.4 Conclusion

On a well STM characterised W(100)-O-(2 × 1) surface rutile TiO_2(110)-(1 × 2) terminated islands were grown. In addition, a TiO_2 lepidocrocite-like nanosheet was also shown to grow on W(100) and was characterised by STM and LEED. The unit cell of the film was 3.69

Å × 3.16 Å. The short side of the lattice was directly coincident with the W(100) substrate in one of the principal directions. A commensurate superstructure with respect to the substrate of 22.1 Å × 3.16 Å was observed. The modulation in height observed in STM had a period of 22.1 Å, six times the unit cell of the film and seven times the unit cell of the W(100) substrate. A mixed phase ultrathin film formed of rutile TiO_2(110) and lepidocrocite-like titania was prepared and characterised.

5.5 Perspectives

A systematic investigation of the ultrathin film growth with respect to the annealing temperature, O_2 pressure, Ti coverage and time of the oxidation is required to understand the growth mechanism of the (1 × 2) terminated (110) islands and lepidocrocite-like titania nanosheet.

The lepidocrocite-like TiO_2 phase is structurally related to the anatase (001) bi-layer. This rutile/ lepidocrocite-like TiO_2 model system could be used to investigate the properties of a titania mixed-phase interface and its influence on photo-reactive molecules when exposed to above band gap UV light, this is perhaps of general relevance to the specific rutile/anatase interface present in photocatalytic P25 titania powders.[40] The photo-oxidation of an organic molecule such as ethanol provides an excellent test molecule able to scavenge photogenerated holes. A study could use the methodology used in Chapter 6 for the single crystal anatase study. An analysis of the photoreaction cross-section by adsorbate desorption probed with STM might, on the TiO_2 film, be expected to reveal the role of the interface between the to phases on photo reactivity. This would be expected to result from intrinsic band bending effects[50] or electron migration favoured by any present differences of the conduction band minimum (CBM) and valence band minimum (VBM) band alignment.[51] The supporting W(100) surface's influence on photocatalysis could be probed by an examination of photo-activity of ethanol as a function of titania film thickness.

References

(1) Henrich, V. E.; Cox, P. A. The Surface Science of Metal Oxides; Cambridge University Press: Cambridge, 1996.

(2) Kuhlenbeck, H.; Shaikhutdinov, S.; Freund, H.-J. Well-Ordered Transition Metal Oxide Layers in Model Catalysis–a Series of Case Studies. *Chem. Rev.* **2013**, *113*, 3986–4034.

(3) Grinter, D. C.; Yim, C.-M.; Pang, C. L.; Santos, B.; Menteş, T. O.; Locatelli, A.; Thornton, G. Oxidation State Imaging of Ceria Island Growth on Re (0001). *Phys. Chem. C* **2013**, *117*, 16509–16514.

(4) Freund, H.-J.; Pacchioni, G. Oxide Ultra-Thin Films on Metals: New Materials for the Design of Supported Metal Catalysts. *Chem. Soc. Rev.* **2008**, *37*, 2224–2242.

(5) Luches, P.; Pagliuca, F.; Valeri, S. Morphology, Stoichiometry, and Interface Structure of CeO_2 Ultrathin Films on Pt(111). *J. Phys. Chem. C* **2011**, *115*, 10718–10726.

(6) Franchy, R. Growth of Thin, Crystalline Oxide, Nitride and Oxynitride Films on Metal and Metal Alloy Surfaces. *Surf. Sci. Rep.* **2000**, *38*, 195–294.

(7) Guo, Q.; Oh, W. S.; Goodman, D. W. Titanium Oxide Films Grown on Mo(110). *Surf. Sci.* **1999**, *437*, 49–60.

(8) Ashworth, T. V.; Thornton, G. Thin Film TiO_2 On Nickel(110): an STM Study. *Thin Solid Films* **2001**, *400*, 43–45.

(9) Xia, Y.; Zhu, K.; Kaspar, T. C.; Du, Y.; Birmingham, B.; Park, K. T.; Zhang, Z. Atomic Structure of the Anatase TiO_2(001) Surface. *J. Phys. Chem. Lett.* **2013**, *4*, 2958–2963.

(10) Silly, F.; Castell, M. R. Formation of Single-Domain Anatase TiO2(001)-(1×4) Islands on SrTiO3(001) After Thermal Annealing. *Appl. Phys. Lett.* **2004**, *85*, 3223–3225.

(11) Du, Y.; Kim, D. J.; Kaspar, T. C.; Chamberlin, S. E.; Lyubinetsky, I.; Chambers, S. A. In-Situ Imaging of the Nucleation and Growth of Epitaxial Anatase TiO_2(001) Films on $SrTiO_3$(001). *Surf. Sci.* **2012**, *606*, 1443–1449.

(12) Diebold, U.; Ruzycki, N.; Herman, G. S.; Selloni, A. One Step Towards Bridging the Materials Gap: Surface Studies of TiO_2 Anatase. *Catal. Today* **2003**, *85*, 93–100.

(13) Pang, C. L.; Lindsay, R.; Thornton, G. Structure of Clean and Adsorbate-Covered Single-Crystal Rutile TiO_2 Surfaces. *Chem. Rev.* **2013**, *113*, 3887–3948.

(14) Pang, C. L.; Haycock, S. A.; Raza, H.; Murray, P. W.; Thornton, G.; Gülseren, O.; James, R.; Bullett, D. W. Added Row Model of TiO_2(110)1× 2. *Phys. Rev. B* **1998**, *58*, 1586–1589.

(15) Bowker, M.; Bennett, R. A. The Role of Ti^{3+} Interstitials in TiO_2(110) Reduction and Oxidation. *J. Phys.: Condens. Matter* **2009**, *21*, 474224–474229.

(16) Diebold, U. The Surface Science of Titanium Dioxide. *Surf. Sci. Rep.* **2003**, *48*, 53–229.

(17) Papageorgiou, A. C.; Cabailh, G.; Chen, Q.; Resta, A.; Lundgren, E.; Anderson, J. N.; Thornton, G. Growth and Reactivity of Titanium Oxide Ultrathin Films on Ni(110). *J. Phys. Chem. C* **2007**, *111*, 7704–7710.

(18) Papageorigiou, A. C.; Pang, C. L.; Chen, Q.; Thornton, G. Low-Dimensional, Reduced Phases of Ultrathin TiO_2. *ACS Nano* **2007**, *1*, 409–414.

(19) Atrei, A.; Ferrari, A. M.; Szieberth, D.; Cortigiani, B.; Rovida, G. Lepidocrocite-Like Structure of the TiO_2 Monolayer Grown on Ag(100). *Phys. Chem. Chem. Phys.* **2010**, *12*, 11587–11595.

(20) Pang, C. L.; Grinter, D. C.; Matharu, J.; Thornton, G. A Scanning Tunneling Microscopy Study of Ultrathin Film Rutile TiO_2(110) Supported on W(100)-O(2 × 1). *J. Phys. Chem. C* **2013**, *117*, 25622–25627.

(21) Bennett, R. A.; Mulley, J. S.; Newton, M. A.; Surman, M. Spectroscopy of Ultrathin

Epitaxial Rutile TiO_2(110) Films Grown on W(100). *J. Chem. Phys.* **2007**, *127*, 084707.
(22) McCavish, N. D.; Bennett, R. A. Ultra-Thin Film Growth of Titanium Dioxide on W(100). *Surf. Sci.* **2003**, *546*, 47–56.
(23) Bennett, R. A.; McCavish, N. D. Non-Stoichiometric Oxide Surfaces and Ultra-Thin Films: Characterisation of TiO_2. *Top. Catal.* **2005**, *36*, 11–19.
(24) Ashworth, T. V.; Muryn, C. A.; Thornton, G. Nanodots and Other Low-Dimensional Structures of Titanium Oxides. *Nanotechnology* **2005**, *16*, 3041–3044.
(25) Hengerer, R.; Bolliger, B.; Erbudak, M.; Grätzel, M. Structure and Stability of the Anatase TiO_2(101) and (001) Surfaces. *Surf. Sci.* **2000**, *460*, 162–169.
(26) Thomas, A. G.; Flavell, W. R.; Kumarasinghe, A. R.; Mallick, A. K.; Tsoutsou, D.; Smith, G. C.; Stockbauer, R.; Patel, S.; Grätzel, M.; Hengerer, R. Resonant Photoemission of Anatase TiO_2(101) and (001) Single Crystals. *Phys. Rev. B* **2003**, *67*, 035110.
(27) Atrei, A.; Bardi, U.; Rovida, G. Structure and Composition of the Titanium Oxide Layers Formed by Low-Pressure Oxidation of the $Ni_{94}Ti_6$(110) Surface. *Surf. Sci.* **1997**, *391*, 216–225.
(28) Agnoli, S.; Mentes, T. O.; Niño, M. A.; Locatelli, A.; Granozzi, G. A LEEM/M-LEED Investigation of Phase Transformations in TiO_X/Pt(111) Ultrathin Films. *Phys. Chem. Chem. Phys.* **2009**, *11*, 3727–3732.
(29) Barcaro, G.; Agnoli, S.; Sedona, F.; Rizzi, G. A.; Fortunelli, A.; Granozzi, G. Structure of Reduced Ultrathin TiO_X Polar Films on Pt(111). *J. Phys. Chem. C* **2009**, *113*, 5721–5729.
(30) Dulub, O.; Hebenstreit, W.; Diebold, U. Imaging Cluster Surfaces with Atomic Resolution: the Strong Metal-Support Interaction State of Pt Supported on TiO_2(110). *Phys. Rev. Lett.* **2000**, *84*, 3646–3649.
(31) Bennett, R. A.; Pang, C. L.; Perkins, N.; Smith, R. D.; Morrall, P.; Kvon, R. I.; Bowker, M. Surface Structures in the SMSI State; Pd on (1 × 2) Reconstructed TiO_2(110). *J. Phys. Chem. C* **2002**, *106*, 4688–4696.
(32) Orzali, T.; Casarin, M.; Granozzi, G.; Sambi, M.; Vittadini, A. Bottom-Up Assembly of Single-Domain Titania Nanosheets on (1 × 2)-Pt(110). *Phys. Rev. Lett.* **2006**, *97*, 156101.
(33) Scanning Tunneling Microscopy Investigation of Ultrathin Titanium Oxide Films Grown on Pt_3Ti(111). *J. Phys. Chem. C* **2014**, *118*, 6186–6192.
(34) Zhukhlistov, A. P. Crystal Structure of Lepidocrocite FeO(OH) From the Electron-Diffractometry Data. *Crystallogr. Rep.* **2001**, *46*, 730–733.
(35) Vittadini, A.; Casarin, M. Ab Initio Modeling of TiO_2 Nanosheets. *Theor. Chem. Account* **2008**, *120*, 551–556.
(36) Agnoli, S.; Orzali, T.; Sambi, M.; Vittadini, A.; Casarin, M.; Granozzi, G. Ultrathin TiO_2 Films on (1 × 2)-Pt(110): a LEED, Photoemission, STM, and Theoretical Investigation. *J. Phys. Chem. C* **2008**, *112*, 20038–20049.
(37) Atrei, A.; Cortigiani, B.; Ferrari, A. M. Epitaxial Growth of TiO_2 Films with the Rutile (110) Structure on Ag (100). *Rep. Prog. Phys.* **2012**, *24*.
(38) Walle, L. E.; Agnoli, S.; Svenum, I. H.; Borg, A.; Artiglia, L.; Kruger, P.; Sandell, A.; Granozzi, G. High Resolution Photoemission and X-Ray Absorption Spectroscopy of a Lepidocrocite-Like TiO_2 Nanosheet on Pt(110) (1 × 2). *J. Chem. Phys.* **2011**, *135*, 054706.
(39) Yamazaki, H.; Kamisawa, T.; Kokubun, T.; Haga, T.; Kamimizu, S.; Sakamoto, K. Structure Analysis of Oxygen-Adsorbed Tungsten (001) Surface. *Surf. Sci.* **2001**, *477*, 174–178.
(40) Connelly, K. A.; Idriss, H. Photoreaction of Au/TiO_2 For Hydrogen Production From Renewables: a Review on the Synergistic Effect Between Anatase and Rutile Phases of TiO_2. *Mater. Renew. Sustain. Energy* **2012**, *1*, 1–12.

(41) Scanning Tunneling Microscopy in Surface Science, Nanoscience and Catalysis; Bowker, M.; Davies, P. R., Eds.; WILEY-VCH: Weinheim, 2009; pp. 1–261.
(42) Dozzi, M. V.; Marzorati, S.; Longhi, M.; Coduri, M.; Artiglia, L.; Selli, E. Photocatalytic Activity of TiO_2-Wo_3 Mixed Oxides in Relation to Electron Transfer Efficiency. *App. Cata. B: Env.* **2016**, *186*, 157–165.
(43) Matharu, J. Surface Science of Ultrathin Metal Oxide Films, (Doctoral thesis), University College London, London, UK, 2011, pp. 1–177.
(44) Yamazaki, H.; Kamimizu, S.; Hara, K.; Sakamoto, K. Structure Analysis of W(001)2×1–O Surface at Room and Liquid Nitrogen Temperatures. *Surf. Sci.* **2003**, *538*, L505–L510.
(45) Bauer, E.; Poppa, H.; Vuswanath, Y. Adsorption of Oxygen on W(100): Adsorption Kinetics and Structure. *Surf. Sci.* **1976**, *58*, 517–549.
(46) Meyer, J. A.; Kuk, Y.; Estrup, P. J.; Silverman, P. J. Atomic Structure of the High-Temperature O/W(001)-(2×1) Surface. *Phys. Rev. B* **1991**, *44*, 9104–9107.
(47) Hofer, W. A.; Foster, A. S.; Shluger, A. L. Theories of Scanning Probe Microscopes at the Atomic Scale. *Rev. Mod. Phys.* **2003**, *75*, 1287–1331.
(48) Pang, C. L.; Haycock, S. A.; Raza, H.; Murray, P. W.; Thornton, G.; Gülseren, O.; James, R.; Bullett, D. W. Added Row Model of TiO_2(110)1×2. *Phys. Rev. B* **1998**, *58*, 1586–1589.
(49) Fukuda, K.; Sasaki, T.; Watanabe, M.; Nakai, I.; Inaba, K.; Omote, K. Novel Crystal Growth From a Two-Dimensionally Bound Nanoscopic System. Formation of Oriented Anatase Nanocrystals From Titania Nanosheets. *Cryst. Growth Des.* **2003**, *3*, 281–283.
(50) Zhang, Z.; Yates, J. T., Jr. Band Bending in Semiconductors: Chemical and Physical Consequences at Surfaces and Interfaces. *Chem. Rev.* **2012**, *112*, 5520–5551.
(51) Deák, P.; Aradi, B.; Frauenheim, T. Band Lineup and Charge Carrier Separation in Mixed Rutile-Anatase Systems. *J. Phys. Chem. C* **2011**, *115*, 3443–3446.

CHAPTER 6

6.0 Mechanism of Ethanol Photooxidation on Single-Crystal Anatase TiO_2(101)

Despite the proven characteristics of the anatase phase of TiO_2 in photocatalysis, detailed mechanistic information regarding a photooxidation reaction has not yet been derived from single-crystal studies. Within this Chapter, we have studied the photooxidation of ethanol (as a prototype hole-scavenger organic molecule) adsorbed on the anatase TiO_2(101) surface by STM and online mass spectrometry to determine the adsorbate species in the dark and under UV illumination in the presence of O_2 and to extract kinetic reaction parameters under photoexcitation. This is a necessary preliminary study before the investigation of a photochemical reaction on the tip modified rutile / anatase TiO_2(101) surface. Here, the reaction rate for the photooxidation of ethanol to acetaldehyde was found to depend on the O_2 partial pressure and surface coverage. An order of the reaction with respect to O_2 was found to be close to 0.15. Carbon−carbon bond dissociation leading to the formation of CH_3 radicals in the gas phase was found to be a minor pathway, which is contrary, to the case of the rutile TiO_2(110) single-crystal. Our STM images distinguished two types of surface adsorbates upon ethanol exposure that can be attributed to its molecular and dissociative modes. A mixed adsorption is also supported by DFT calculations performed by Idriss et al. at SABIC, in which they determined similar energies of adsorption (E_{ads}) for the molecular (1.11 eV) and dissociative (0.93 eV) modes. Upon UV exposure at (and above) 3×10^{-8} mbar O_2, a third species was identified on the surface as a reaction product that can be tentatively attributed to acetate/formate species on the basis of C 1s XPS results. The kinetics of the initial oxidation steps were evaluated using the STM and mass spectrometry data.

6.1 Introduction

Fundamental studies of well-defined oxide surfaces have not yet received the required attention to construct reliable mechanistic pathways, this is despite oxide semiconductors important role in photocatalysis as discussed in Chapter 1. Among all metal oxide surfaces, TiO_2 is the most understood at the atomic level. The most relevant phase for photocatalysis, based on its dominance (80%) in existing used formulations (P25) is the anatase phase. Most photoreaction studies on well-defined single-crystal surfaces have been conducted on the rutile phase,[6-8] with very little work on anatase surfaces. Alcohol chemistry on metal[5,6,9] and oxide[10-13] surfaces can provide a wealth of fundamental information needed to understand catalytic reactions, particularly when conducted on model surfaces. Ethanol photochemical activity and its adsorption has been studied on powder polycrystalline TiO_2 samples for decades,[5,14-17] however no existing experimental studies of ethanol on the TiO_2 anatase (101) surface have been conducted (the most thermodynamically stable surface). There are reports of studies involving other molecules on the (101) surface. For example, methanol adsorption has been studied by temperature-programmed desorption (TPD),[18,19] where molecular adsorption/desorption was evidenced. The photo-oxidation of methanol was studied using 266-nm light at 100 K by TPD and time-of-flight (TOF) mass spectrometry. Infrared (IR) spectroscopy has also been used to determine the cross section for the photooxidation of CO to CO_2 in the presence of O_2 at 100 K, and this cross section was determined to be significantly greater than that for the rutile TiO_2(110) surface.[20] A recent study of acetaldehyde photoreaction at 100 K demonstrated the cross-coupled formation of 2-butanone.[21] Finally, a recent density functional theory (DFT) study of ethanol[22] on TiO_2(101) predicts that molecular adsorption is favored over dissociation.

The reactions of oxygenates on photoexcited TiO_2 are considered to proceed through a hole-scavenging mechanism.[23] Upon UV excitation, electrons are transferred from the valence

band (VB) to the conduction band (CB) of the semiconductor. In single-crystal studies of ethanol photooxidation, background O_2 has been shown to be required for activity. The mechanism inferred involves excited electrons in the conduction band being transferred to O_2 forming $O_2^{\cdot-}$ (oxygen anion radical), which leads to a decrease in the rate of electron−hole recombination.[24] Under ultrahigh vacuum (UHV) conditions, the first step in the photooxidation of ethoxides to acetaldehyde on rutile TiO_2(110) surfaces involves hydrogen atom removal from the hydroxyl carbon group. The amount of acetaldehyde detected in the gas phase was found to increase with an increasing dose of O_2. Some of the acetaldehyde undergoes a further oxidation step and is ultimately converted, through carboxylate species, to CO_2.[25,26] The formation of formate/acetate intermediates on the surface was revealed by X-ray photoelectron spectroscopy (XPS), where the development of a −COOH feature in the C 1s spectrum is observed after UV light exposure in the presence of O_2.[27] These results on single crystal rutile TiO_2(110) are similar to powder results where the photo-oxidation of primary and secondary alcohols and leads to the formation of carboxylate species as studied by *in-situ* IR spectroscopy.[14,17,28-31]

In this study, we have investigated the photocatalytic decomposition of ethanol on an anatase TiO_2(101) single-crystal to probe its reactivity and obtain accurate kinetic parameters (photoreaction cross section, reaction order, and rate constants) in a controlled environment. We used scanning tunneling microscopy (STM) and mass spectrometry to determine the reaction rates with complementary XPS measurements and DFT calculations. This provides an important initial study of photocatalysis of the hole scavenging ethanol molecule on the surface of anatase TiO_2(101) prior to a study on the rutile / anatase STM tip modified surface synthesised and characterised in Chapter 4. Ethanol has the advantage of containing a single functional group a C-C bond and its decomposition is industrially relevant.

6.2 Experimental and Computational Details

The mass spectrometry and STM measurements were performed in a single ultrahigh-vacuum (UHV) system operating at a base pressure of 1×10^{-10} mbar. The setup was equipped with an Aahrus 15 HT variable-temperature scanning tunneling microscope by *SPECS* and a HALO 301 residual gas analyser (RGA) by *Hiden* Analytical. All STM measurements were carried out at room temperature. The system was also equipped with a sputter gun and separate oxygen, argon, and ethanol gas lines that were fitted with precision UHV leak valves. For mass spectrometry measurements, the RGA was mounted inside a Pyrex shroud with a 5 mm aperture to enhance detection from the surface as shown in detail in Chapter 3. During the mass spectrometry measurements (with or without UV illumination), the sample was positioned ≤1 mm away from the aperture. A 300-W MAX-303 *Asahi* Spectra Xe lamp was used as a source of the UV light. The UV light produced by the Xe lamp was delivered to the sample using fiber optics and a focusing lens assembly. An illumination power close to 5 mW/cm^2 was measured for wavelengths ranging from 310 to 400 nm.

XPS was performed in a separate UHV system with a base pressure of 2×10^{-9} mbar equipped with SPECS XR50 dual- anode X-ray source (Mg Kα radiation was utilized) and a *Scienta* R3000 hemispherical electrostatic energy analyzer. Also, the system had a sputter gun and separate oxygen, argon, and ethanol gas lines fitted with precision UHV leak valves. A transparent standard UHV port window was positioned for UV illumination.

The anatase TiO_2(101) single crystal ($3 \times 3 \times 1$ mm^3) (same single crystal studied in the Chapter 4) was purchased from *Pi-Kem* and was mounted onto a Ta sample plate using Ta foil. The standard procedure used for preparing the anatase surface was to perform cycles of Ar^+ sputtering (1×10^{-5} mbar, 1 kV, 20 min, 6 μA drain current) and annealing at 700 °C for 15 min with the temperature of the sample being monitored using a Sirius pyrometer from *Process Sensors* and a calibrated K-type thermocouple.

The cleanliness of the sample surface was checked by STM. The clean anatase

TiO_2(101) surface displays a stepped sawtooth-like surface with unit-cell dimensions of 10.24 × 3.78 $Å^2$ and a step height of 3.8 Å. The unit-cell dimensions were used to calibrate the STM in-plane dimensions, and the step height was employed for out-of-plane calibration. In this study, a monolayer (ML) is defined with respect to the number of Ti_{5c}–O_{2c} pairs on an ideal planar anatase TiO_2(101) surface, namely, 5.17×10^{14} pairs of atoms per cm^2. A glass vial containing ethanol was connected to the UHV chamber through a high-precision leak valve located 10 cm away from the sample in the dosing configuration. The ethanol (99.85% purchased from VWR) line was cleaned using standard freeze− pump−thaw cycles. The dose of ethanol exposure is given in Langmuir (L, 1 L = 1.33×10^{-6}mbar s). Oxygen (99.9%) was introduced into the chamber using a high-precision leak valve. The anatase surface was exposed to O_2 for ~3 min at the designated pressure before the UV light shutter was opened. In the photoreactions conducted in the STM and photoreaction chamber, the time frame upon dosing and starting the measurements was 2 min, and each run was conducted for 2 min with monitoring of the gas-phase molecules [*m/e* 44 (CO_2, CH_3CHO), 31 (CH_2OH^+), 29 (CHO^+), and 15 (CH_3^+)] by the mass spectrometer.

Density functional theory (DFT) calculations were performed by Idriss and co-workers at SABIC.[32] They employed the Quantum Espresso code.[33] Calculations were performed using a generalized gradient approximation (GGA) for the ionic core description along with the Perdew−Burke−Ernzerhof (PBE) exchange correlation and GBRV ultrasoft pseudopotential.[34] All the atomic orbitals were considered filled and part of the core potential except for the titanium 3s, 3p, 3d, and 4s; the oxygen and carbon 2s and 2p; and the hydrogen 1s. For energy minimization, the specified total energy and total force convergence thresholds were 1×10^{-6} Ry and 1×10^{-4} Ry/ Bohr, respectively. The total kinetic energy cutoffs used for wave function and density were 50 and 200 Ry, respectively. A (3 × 3 × 1) Monkhorst−Pack k-point grid was used for all computations. To obtain smooth results, Gaussian smearing with 0.02 Ry (0.27 eV) spreading for Brillouin zone integration across the Fermi level was used. The convergence threshold employed for self-consistency was 1×10^{-6}. A 2 × 2 five-layer slab of anatase

TiO_2(101) was built from optimized parameters of the bulk TiO2 anatase unit cell. The optimized unit-cell parameters are a = 3.802 Å, c = 9.697 Å, and u = 0.2066, yielding a cohesive energy of 24.5 eV at a volume of 35.1 $Å^3$. The computed bulk modulus (B_0) is 185.2 GPa, and its derivative (B_0') is 4.47 GPa, calculated using the Murnaghan equation of state.[35] The vacuum distance on top of the slab was set to 15 Å. In this study, the bottom layer was fixed to simulate bulk properties, and the top four layers were allowed to relax. Isolated gas-phase molecules were simulated in a 15 × 15 × 15 Å periodic cell. The surface adsorption energy (E_{ads}) is defined by the Eqs 6.1:

$$E_{ads} = E_{ads+TiO_2} - (E_{bareTiO_2} + E_{EtOH}) \quad \text{Eqs. 6.1}$$

where $E_{ads+TiO2}$ is the energy of the adsorbed molecule on TiO_2, E_{EtOH} is the energy of isolated ethanol molecule, and $E_{bare\ TiO2}$ is the energy of the clean surface. In this study, the adsorbate coverage was set to 25%. Dispersion interaction forces were included through the use of the DFT-D2 method by Grimme to study the effects of weak interactions such as London forces in the adsorbate−semiconductor system.[36]

6.3 Results and Discussion

6.3.1 Scanning Tunneling Microscopy (STM) of CH_3CH_2OH−TiO_2(101) Anatase Single Crystal

The surface morphology of a clean freshly prepared anatase (101) crystal, studied by STM, showed wide terraces of 300 Å size (**Figure 6.1A**) with straight step edges oriented along the [010], $[\bar{1}11]$, and $[11\bar{1}]$ principal directions forming triangular terraces from which the orientation could be identified (i.e., $[10\bar{1}]$ directed towards the base[37]). The atomically resolved STM image of the pristine surface shown in **Figure 6.1B** allows the identification of the "non-primitive-centered" surface unit cell of 10.24 × 3.78 $Å^2$ (indicated by the black rectangle) and 1 × 1 periodicity. The bright round features observed on the surface are attributed to contaminants. These make up ca. 1% of surface coverage and are attributed to adventitious

carbon, consistent with the C 1s XPS data that also indicated the presence of carbon in trace amounts. The dark features indicated by the blue square in the same image are associated with more reduced TiO_{2-x} anatase surfaces, namely, subsurface oxygen vacancies that resulted from vacuum annealing.[24,38] These feature have been demonstrated in previous STM studies performed on anatase TiO_2(101) single-crystal surfaces.

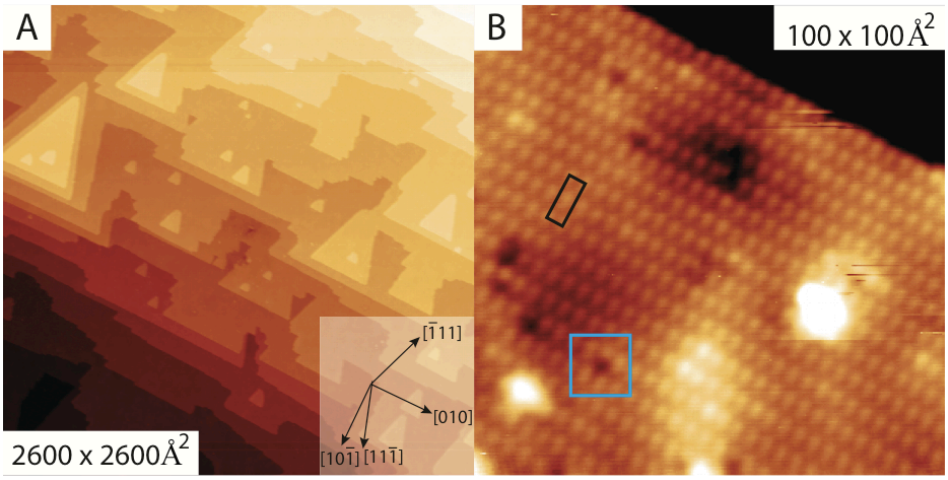

Figure 6.1: 300 K STM of a clean TiO_2 anatase single crystal. **(A)** A large scale image of a clean and prepared anatase TiO_2(101) (at 2700×2700 $Å^2$ resolution, 1.65 V, and 0.15 nA). **(B)** High-resolution image (at 100 × 100 $Å^2$, 1.65 V, and 0.2 nA). The blue box identifies a depression centered on Ti_{5c}–O_{2c} in the empty state image, most likely due to a subsurface O_{vac}. The black box identifies the surface unit cell, 10.24 × 3.78 $Å^2$.

The surface shown in **Figure 6.1** was then exposed to 18 L of ethanol at 300 K (**Figure 6.2A**). Round bright features representing a coverage of 8.5% ML of ethanol were observed on the surface as both clusters and isolated features. A mean sticking coefficient, S of 0.03 from 3 L exposure[8] was observed, and this value decreased to 0.007 after a 50 L exposure, indicating a relatively weak surface−adsorbate interaction. Images of the different ethanol coverage are presented in the Appendix (**A.8**). For comparison, using similar dosing conditions at a low exposure; Grinter et al.[39] determined a mean sticking coefficient of ~1 for a low coverage (0.1 L) of acetic acid adsorbed at room temperature. A high saturating acetic acid

[8]Flux $(z) = \frac{P\,(Pa)}{\sqrt{2\pi m(kg)k_b(m^2kgs^{-2}K^{-1})T(K)}}(\frac{1}{10{,}000})/\,molecules\,cm^{-2}s^{-1}$ at the pressure of 1.3x10^{-8} mbar ethanol 2×10^{12} molecules cm^{-2} s^{-1} (5.17×10^{14} Ti_{5c} cm^{-2})

coverage on anatase (101) is also shown in Chapter 4. The difference between the sticking coefficients of acetic acid and ethanol is related to the strong adsorption energy of the former compared to the latter.

Two distinct tunneling modes were observed, with ethanol appearing as bright features of ~6 Å diameter spread over the Ti_{5c}−O_{2c} positions (**Figure 6.2A**) or as bright−dark−bright features spanning three Ti_{5c}−O_{2c} pairs (see the **Figure 6.2A** inset, where a defect is circled, as well as the enlargement of the inset). These features were found to be equivalent in location by monitoring STM contrast changes. For example, several round surface species of ~1.6 Å apparent height in one mode could be unambiguously mapped directly to demonstrate this (see Appendix (**A.7**)). This discussed contrast behavior is found here to be independent of voltage bias for ethanol, as has been reported on anatase (101) for water, where it was attributed to the change in the metallic character of the tip, with coordination of H_2O to TiO_2 resulting in a redistribution and change in energy of the local density of states (LDOS) at the Ti−O site and observed as a depression in the empty state image.[40,41]

A higher density of ethanol molecules was observed at the bottom of step edges as opposed to upper step edges, as a result of ethanol diffusion at room temperature. This is in contrast to the behavior of acetic acid, as shown by Grinter et al., which undergoes stronger binding and shows no preference for terrace lower step edges.[39] Scanning tunneling spectroscopy (STS) measurements by Diebold and co-workers indicated that excess electrons can be trapped at the upper and lower step edges, leading to a preference for O_2 adsorption in these locations.[42]

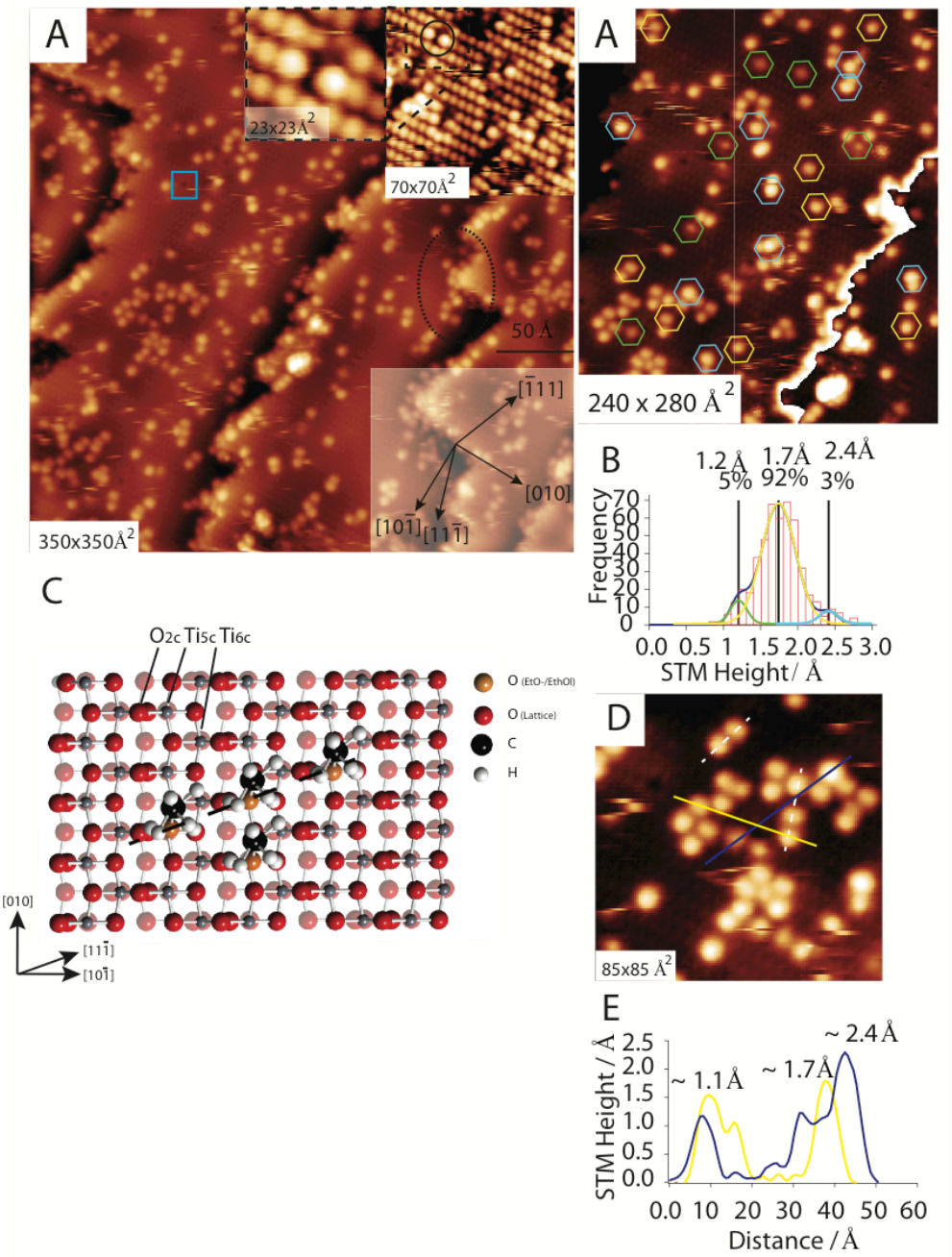

Figure 6.2: 300 K STM images of anatase TiO_2(101) after exposure to 18 L of ethanol at 300 K. **(A)** 350 × 350 Å^2 resolution, +2 V sample bias, 0.420 nA, with 0.085 ML EtOH/EtO$^-$ coverage. The blue square represents a feature associated with O_2. The black oval shows an example of ethanol clustering at the step edges. Upper inset: (70 × 70 Å^2) ethanol on anatase TiO_2(101) in "depression" contrast where the black circle indicates EtOH/EtO$^-$; a zoom of this feature is shown. Lower inset: the principal azimuths of anatase TiO_2(101). **(B)** Enlargement of panel **A** 240 × 280 Å^2 image, species of height ~1.2 Å (green hexagon), ~1.7 Å (yellow hexagon) and ~2.4 Å (blue hexagon) are identified. **(C)** Histogram of the measured heights of 495 particles from the 350 × 350 Å^2 image in image A with a bin width of 0.1 Å. **(D)** Model of the (101) surface with EtOH/EtO- molecules coordinated to the Ti_{5c}. **(E)** Enlargement of panel A: a (70 × 70 Å^2) Blue and yellow lines: line of the STM profile shown in image **A**. White dashed lines: arrangements of protrusions in the [11$\bar{1}$] and [$\bar{1}$11] and directions. (**F**) Line profile from panel (**E**), where ca. 1.2 Å and ca. 1.8 Å (1.7 Å in figure) height species can be identified.

Short chains of the adsorbed ethanol molecules with separations of ~5.5 Å were observed with preferential orientations along the $[\bar{1}11]$ and $[11\bar{1}]$ directions. This suggests coordination of ethanol in adjacent sites along the [010] direction, with the C−C moiety oriented perpendicular to the titanium rows. Similar arrangements of acetic acid and water on anatase TiO_2(101) have been demonstrated by STM.[39,63] A simple steric requirement can explain this arrangement: The short side of the surface unit cell (~3.7 Å) would prevent adsorption on two neighboring Ti cations. This is shown in the covalent radii ball-and-stick model of the (101) surface in **Figure 6.2D**, where ethanol molecules are coordinated to Ti_{5c}, forming a chain in the $[11\bar{1}]$ direction. In the model two molecules are shown positioned on Ti_{5c} nearest neighbors.

Ethanol imaged at positive sample bias in the protrusion mode on the surface at 300 K revealed three apparent heights, as shown in **Figure 6.2B,** where representative distinct height surface features are identified by the green, blue and yellow hexagons**.** These differing heights can be attributed to two adsorption modes of ethanol molecular and dissociated. A previous DFT study of ethanol adsorbed on anatase TiO_2(101) indicated a preference for molecular adsorption with coordination of the ethanol to the Ti_{5c} site.[22] The different heights could also be due to ethanol and water being co-adsorbed together, but the possibility of a significant population of water is discounted by the lack of a water signal in the mass spectrometry data (although there is no guarantee that the water would be desorbed by UV irradiation). The STM heights of 495 adsorbates in the image of **Figure 6.2A** were measured (total area of 135000 $Å^2$). The histogram in **Figure 6.2C**, with a bin width of 0.1 Å height, allows the determination of a major Gaussian peak at 1.8 Å (92%) and two minor Gaussian peaks at 1.2 Å (5%) and 2.4 Å (3%). Hansen et al.[43] reported a difference in STM height of 0.5 Å between two species attributed to EtOH (2.6 Å) and EtO− (2.0 Å) bound to Ti_{5c} on rutile TiO_2(110). On the basis that the two surfaces can be compared the majority species on anatase TiO_2(101) is assigned to EtO− 1.7 Å (yellow hexagons), with EtOH at 2.4 Å (blue hexagons) the minor contribution 1.2 Å (green hexagons) could not be reliably assigned. Further low temperature STM and TPD

study at low temperature is required for further validation. The high magnification image **Figure 6.2E** depicts the three different species, where blue and yellow height line profiles are overlaid. For example the species of 1.2 Å and 2.4 Å height are shown by the blue line and example species of height 1.1 Å and 1.7 Å by the yellow line (**Figure 6.2F**). A DFT study by Zhang et al.[22] indicated similar adsorption energies for the molecular and dissociative adsorptions of ethanol to Ti_{5c} on a perfect surface, with an activation barrier for dissociation of 0.95 eV (RT at 300 K = 0.0259 eV). In addition, the dark features that are associated with subsurface oxygen vacancies are apparently unreactive with ethanol (see **Figure 6.2A**, blue box). Features associated with surface hydroxyls such as Ti terminal OH identified recently by STM with distinctive dumb-bell motif,[44,45] were not observed.

6.3.2 Density Functional Theory of Ethanol and Acetaldehyde on TiO_2(101) Anatase Surface [Performed in collaboration by SABIC]

DFT calculations were performed at SABIC by Alghamdi and Idriss, to provide further theoretical under-standing of ethanol adsorbed on the surface of anatase (101).[32] A coverage of 0.25 ML was used, which is close to the upper saturation coverage observed by STM. A computational methodology similar to that used by Zhang et al.[22] was employed by Alghamdi, following a GGA and PBE approach. In addition, weak interactions such as London dispersion forces were modelled using the DFT-D2 method of Grimme et al.[36] Given the literature discussion, calculations were limited to coordination of ethanol to the Ti_{5c} site and scission of the O−H bond in ethanol. **Figure 6.3** depicts ball-and-stick models of the anatase TiO_2(101) surface with relaxed atomic positions for adsorbed ethanol and acetaldehyde (the latter is a reaction product that is discussed in the following sections). The atomic positions of the clean perfect surface were obtained, and they compare favorably to previous theoretical DFT work.[46,47] The DFT results indicate that the adsorption energies (E_{ads}) are very close for dissociated and molecular adsorptions: 1.11 eV for molecular ethanol on Ti_{5c} (**Figure 6.3A**) and 0.93 eV for dissociated ethanol on Ti_{5c} (**Figure 6.3B**). Additionally, acetaldehyde with a coordination identical to that of molecular ethanol (**Figure 6.3C**) was found to be less stable,

with an adsorption energy of 0.77 eV. The inclusion of the dispersion interaction between the adsorbates and the TiO_2 lattice leads to greater instability (~0.2 eV) of the dissociated form of ethanol when compared to the molecular form. **Table 6.1** presents some selected geometric parameters for ethanol, ethoxide, and acetaldehyde adsorptions. Among the computed modes, only the dissociated mode of ethanol induces major changes in the TiO_2 surface structure through the upward displacement of the Ti_{5c} site (0.42 Å), which, in turn, increases the Ti_{5c}–O_{3c} distance by 0.38 Å. Acetaldehyde does not show any structural differences when compared to molecular ethanol other than a 0.23 Å shorter O_{ads}–C1 bond.

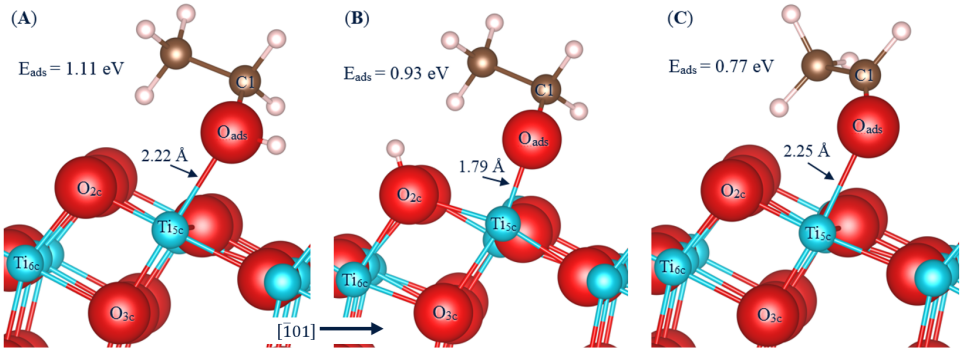

Figure 6.3: DFT GGA PBE + D computed parameters for the adsorption of ethanol on a relaxed anatase TiO_2(101) surface. (**A**) Molecular adsorption of ethanol on Ti_{5c}, E_{ads} = 1.11 eV. (**B**) Dissociative adsorption of ethanol on Ti_{5c} and coordination of H to the adjacent O_{2c}, E_{ads} = 0.93 eV. (**C**) Molecular adsorption of acetaldehyde on Ti_{5c}, E_{ads} = 0.77 eV. Color designations are as follows: red, oxygen; cyan, titanium; brown, carbon; and white, hydrogen. [This figure was kindly prepared by Idriss and Alghamdi.[32]]

Table 6.1: Adsorption energies of the bare slab, as well as molecular and dissociated ethanol and acetaldehyde on anatase TiO_2 (101) along with selected geometry parameters (all distances in Å). Atomic labels are shown in **Figure 3**.

Parameter	**Bare slab**	**EtOH-(a)**	**EtO-(a)**	**MeCHO-(a)**
Adsorption energy, eV	--	**1.11**	**0.93**	**0.77**
O_{ads} – Ti_{5c}	--	2.22	1.79	2.25
O_{ads} – C1	--	1.46	1.42	1.23
Ti_{5c} displacement in *z*-dir. w.r.t. relaxed slab	+0.08	+0.18	+0.42	+0.13
O_{plane} to C_{plane} (i.e. Ti_{5c} – C1)	--	3.28	3.02	3.21
Ti_{5c} – O_{3c}	1.78	1.87	2.16	1.84
Ti_{6c} – O_{2c}	1.85	1.86	2.04	1.85
O_{2c} – H_{ads}	--	--	0.98	--

[a]All distances in angstroms. [b]Atomic labels shown in **Figure 6.3**. [c]Ti displacement here is with respect to the unrelaxed slab. Ti_{5c} during relaxation moves downward with respect to the surface plane; yet, the top three layers slightly reconstruct during geometry optimization by moving upward in the z direction, making the absolute movement of Ti_{5c} positive (i.e., upward). [This table was kindly prepared by Idriss and Alghamdi. [32]]

6.3.3 STM of Ethanol Photoreaction on TiO_2(101) Anatase Single Crystal.

The effect of UV light exposure at 300 K in UHV on an anatase TiO_2(101) surface dosed with 50 L of ethanol was studied by STM; the results are shown in **Figure 6.4**. Exposure to UV light in the absence of O_2 showed negligible photoreaction products in the gas phase, namely, H_2, CH_3CHO, and CH_3 (radical), in line with previous similar studies on rutile TiO_2(110)[27,48] and other studies of the reactions of organic molecules on TiO_2(110) and TiO_2(011) single-crystal surfaces.[26,27] The photocatalytic reactions after UV exposure in the presence of molecular oxygen on an ethanol-covered surface at different partial pressures were studied. In each experiment, the freshly prepared surface had an identical exposure to ethanol prior to photocatalysis. For example, at an O_2 pressure of 3×10^{-8} mbar, the depletion of a fraction of the surface could be determined from the coverage of ethanol before and after UV irradiation. A reduction in the total surface coverage from 0.12 to 0.08 ML was observed after 13 min at an irradiation dosage of approximately 5 mW cm^{-2}. Considering that the Ti_{5c} density is ~5.2×10^{14} cm^{-2} for anatase TiO_2(101), a 0.04-0.06 ML decay (depletion rate) within 780 s gives a mean average surface depletion rate of ethanol/ethoxide of 2.7×10^{10} species s^{-1} cm^{-2}. The 5 mW cm^{-2} irradiation in the range of 320−390 nm corresponds to approximately 9.2×10^{15} photons s^{-1} cm^2, which translates into a reaction rate of about 3×10^{-6} (molecules removed per photon) at an oxygen pressure of 3×10^{-8} mbar.

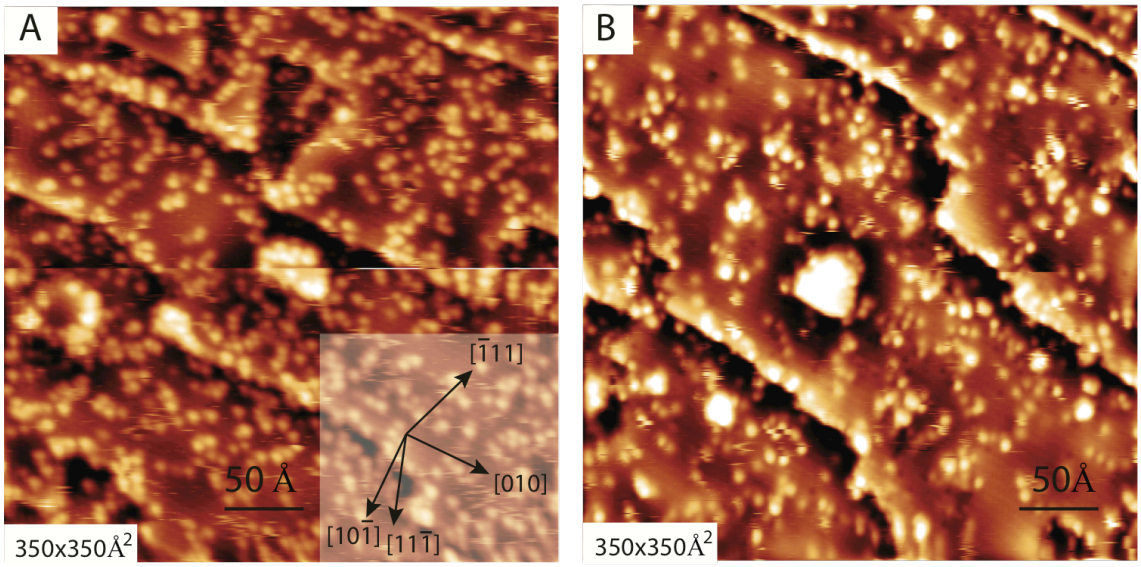

Figure 6.4: Representative STM images (350 × 350 Å^2) of anatase TiO_2(101) after exposure to 50 L of ethanol at 300 K. **(A)** Before UV illumination (sample bias +2.1 V, 0.64 nA) with an ethanol coverage of 0.12 ML. **(B)** After UV illumination in 3 × 10−8 mbar O_2 (sample bias +2.1 V, 0.29 nA) with an ethanol coverage of 0.08 ML [13 min of irradiation at 5 mW cm^{-2} (360 nm λ)]

6.3.4 Measurements of the Photoreaction Cross-Section by STM, Comparison with other Compounds and Surfaces.

Previous work by others has shown similar kinetics. For example, White and Henderson found that the photolysis of trimethylacetic acid (TMA) on rutile TiO_2(110) gave a yield of 1.5 × 10^{-5} (molecules depleted per photon) for the first 10 s of the reaction based on mass spectrometric data.[49] It is important to note that this type of evaluation is based on the results from a single crystal, which has the smallest possible surface area-to-bulk volume ratio, that is, one layer of adsorbate in the unit area exposed to light. In fact under real catalytic conditions, particles of nanometer size stacked on top of each other are expected to react with the same number of photons. In other words, assuming a homogeneous particle size distribution of 10 nm for TiO_2 and compact stacking perpendicular to the incident light, 100 layers of particles per 1 μm depth (at greater distances, the light will be strongly attenuated) would expose over 200 times the area (**Figure 6.4**).

An expression for the decay of the ethanol concentration as a result of the reaction can

be proposed $d[EtOH]/dt = -k[EtOH]^1[O_2]^{\sim 0}$[9] Integrated form: $C_t = C_0 \exp(-kt)$, where C_t is the number of ethanol molecules on the surface at time t and C_0 is the number at time t = 0. By rearrangement of the above expression, the rate constant (k in s^{-1}) of the decay can be extracted from the STM determination of surface coverage: $\ln(C_0/C_t)/t = k$ or ln(0.12/ 0.08)/(780 s) = 0.0012 s^{-1}. Because k = FA, where F is the photon flux and A is the cross-sectional area, a photon flux F of 9.2×10^{15} photons s^{-1} cm^{-2} gives a cross section of 1.3 × 10-19 cm^2. The cross-sectional areas for other reactions on TiO_2 rutile single crystals have been calculated previously using on-line mass spectrometry, reflection absorption infrared spectroscopy (RAIRS), and C 1s XPS. **Table 6.2** lists some of the values extracted from similar sets of experiments for comparison.

Table 6.2. Photooxidation of various oxygenates over the surfaces of oxide single crystals at the given O_2 pressures (P_{O_2}).

Molecule	**Surface**	**Cross section (cm^2)**	**P_{O2} (torr)**	**Comments**
O_2	TiO_2 (110) - rutile	1.5×10^{-15} - 8×10^{-17}	PSD	[50]
CO	TiO_2 (110) - rutile	3×10^{-18}	5×10^{-6}	[51]
Ethanol	TiO_2 (110) - rutile	2×10^{-18}	1×10^{-6}	[52]
Acetaldehyde	TiO_2 (011) - rutile	10^{-17} - 10^{-19}	Pre-dosed	[53]
Glycine	ZnO $(000\bar{1})$ - O	1.5-2.5×10^{-18}	5×10^{-6}	[54]
TMAA	TiO_2 (110) - rutile	ca. 10^{-18}	-	[4]
Acetic acid	TiO_2 (011) - rutile	9×10^{-22}	1×10^{-6}	[55]
Acetone	TiO_2 (011) - rutile	10^{-18} - 3×10^{-21}	5×10^{-7}	[56]
Ethanol	TiO_2 (101) - anatase	1×10^{-19}	4×10^{-8}	This work

[a]Cross section A defined as k/F, where k is the rate constant in s^{-1} and F is the light flux in (number of photons)/(cm^2 s). [b]PSD, photostimulated desorption; TMA, trimethylacetic acid.

[9] The validity of this equation is demonstrated in sections 6.3.6 and 6.3.7, the measured reaction order of 0.15 can be approximated as 0.

In another experiment, the results of which are shown in **Figure 6.5A,B**, the STM image of an ethanol-dosed surface after UV exposure at ~7 mW/cm^2 for 3600 s in the presence of 3 × 10^{-8} mbar oxygen indicated the existence of large (0.8 Å height) protrusions in the depression mode in addition to ethanol/ethoxides (bright-dark-bright features). These large 0.7-0.8 Å height protrusions were not observed prior to UV exposure. These features of 0.01−0.02 ML were arranged in a (1 × 2) formation along the [010] direction, where a row of three are displayed in **Figure 6.5B** (enlargement of **Figure 6.5A**), with the line profiles in **Figure 6.5C** indicating a separation of 10 Å. This individual feature is potentially attributable to a bi-dentate binding species, such as acetate.[39] Further work is required to investigate these adsorbates such as a study in the protrusion STM mode and the co-adsorption of acetic/formic acid and ethanol onto the surface.

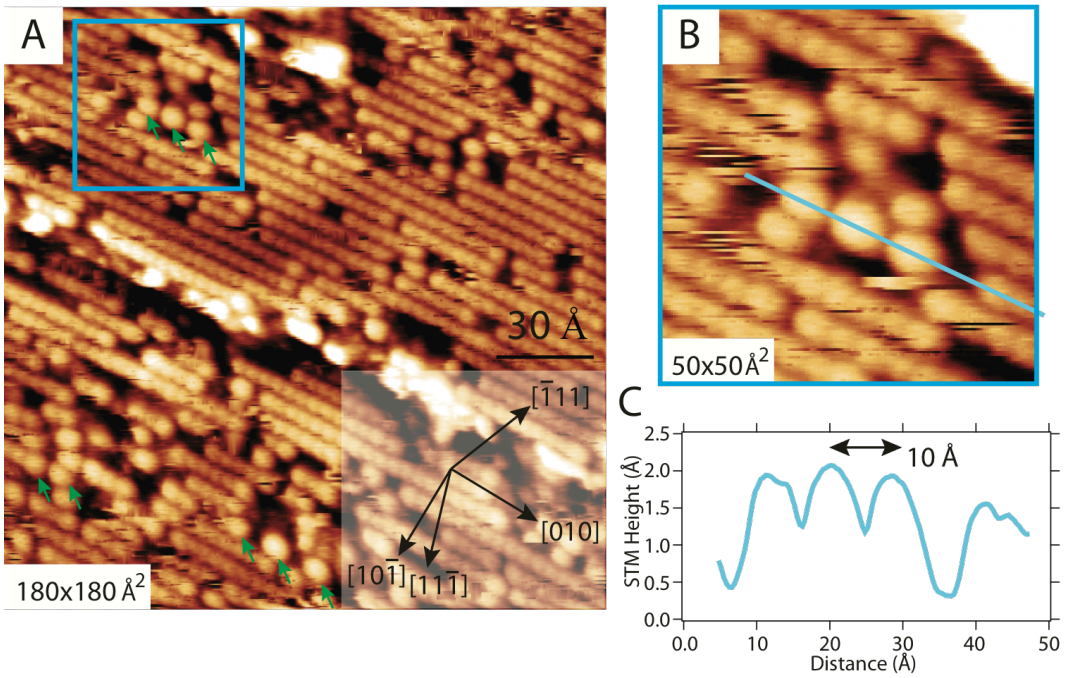

Figure 6.5: (A) Filtered and polynomial-flattened STM image (180 × 180 Å^2, +2.1 V, 0.25 nA) of anatase TiO_2(101) after exposure to 50 L of ethanol at 300 K and UV illumination in 3 × 10^{-8} mbar O_2. Green arrows outside the cyan box indicate small fractions of different spacing. **(B)** Enlargement (50 × 50 Å^2) of the region in image **(A)** identified by the cyan box, which contains features in a (1 × 2) arrangement. **(C)** Height profile of the line shown in image (**B**).

6.3.5 C 1s XPS of Ethanol on TiO_2(101) Anatase Before and After Photoreaction.

To further study the origin of this species, we utilized XPS. The cleanliness of the freshly prepared anatase TiO_2 surface was checked, and no significant contamination was found. A saturation coverage of ethanol was dosed onto the surface, after which the sample was subjected to UV exposure under 1×10^{-5} mbar O_2. To monitor the reaction products on the surface, C 1s core-level spectra were collected before and after the excitation with UV light. Due to the small size of the crystal mounted with Ta wire, the spectrum of the clean surface contained a contribution from tantalum carbide at 282 eV that could not be removed by many sputtering cycles and that was subtracted from both spectra, before and after the UV excitation (see **Figure 6.6**). The XPS spectrum before the reaction (**Figure 6.6A**) exhibited the signature of ethoxides, as evidenced by the spectral features fitted by Gaussian peaks with a polynomial baseline at 286.5 and 285 eV due to $–CH_2O$(a) and $–CH_3$ groups, respectively as these two peaks were present in the study by Jayaweera,[27] demonstrating no variation in core binding energy during heating to 440 K or UV light illumination. Therefore our spectral features and ratios are in accord with the XPS data reported for rutile TiO_2(110).[27] After UV exposure for 360 s in the presence of O_2, one can notice a decrease (of 50%) of the C 1s peaks attributed to ethoxides (**Figure 6.6B**) and the appearance of a peak at 289.5 eV representing about 10% of the total carbon species left on the surface. The latter is attributed to RCOO(a) species.[55,57] However, the decrease of the ethoxides was not mirrored by the increase in carboxylates. In other words, a large fraction of adsorbed ethanol/ethoxides was removed from the surface, whereas a small fraction was oxidized to carboxylates. This final point of the XPS findings is in line with the reaction of adsorbed ethanol under UV excitation studied by online mass spectrometry, which is presented in **Figure 6.7**.

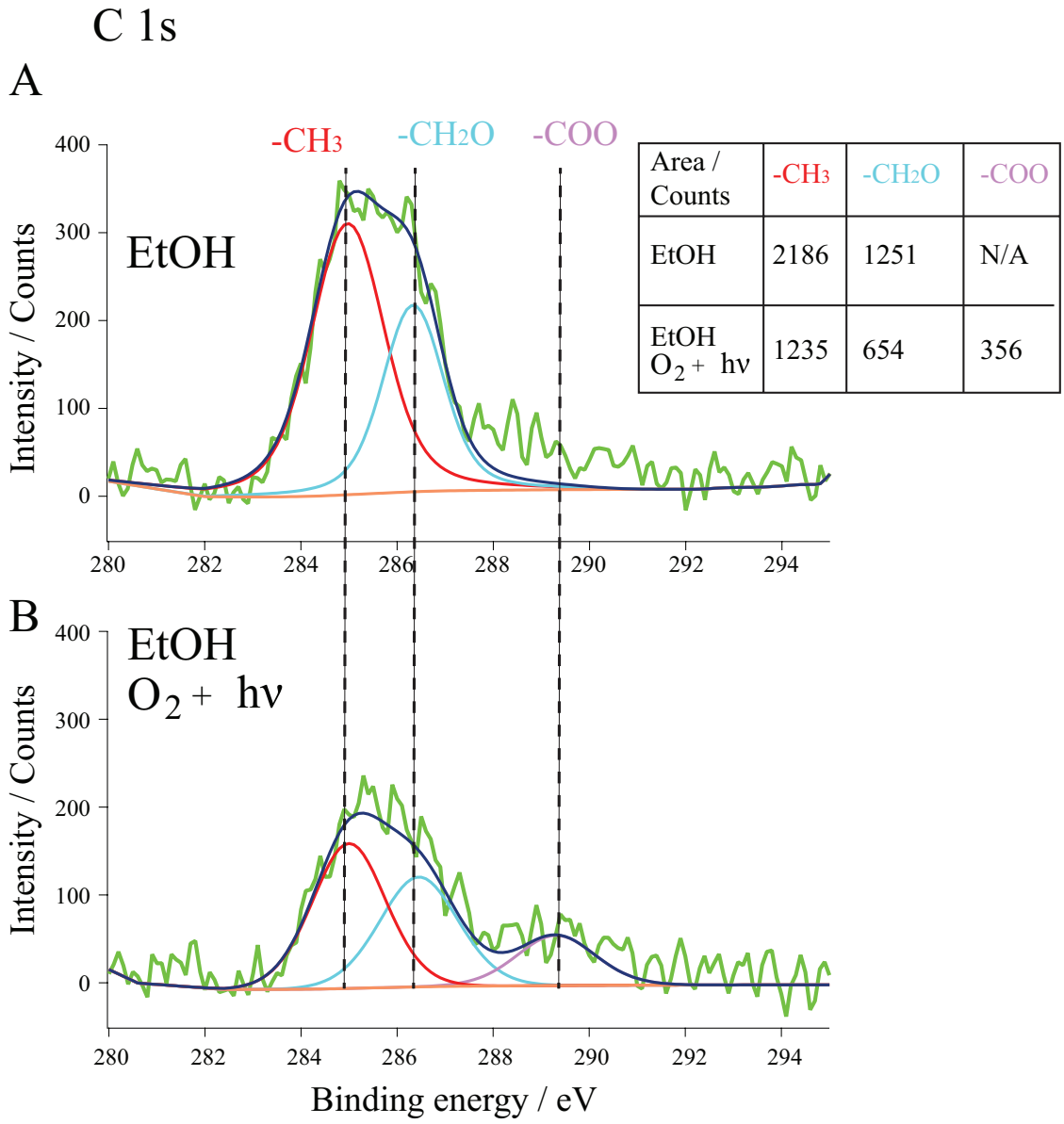

Area / Counts	-CH_3	-CH_2O	-COO
EtOH	2186	1251	N/A
EtOH O_2 + hν	1235	654	356

Figure 6.6: XPS of the anatase TiO_2(101) surface after a saturation exposure (ca. 100 L) to ethanol (**A**) before and (**B**) after exposure to UV light (light flux = 10^{17} photons cm^{-2} s^{-1} in the 360−400-nm range) at 1 × 10^5 mbar O_2. –CH_2O, 286.5 eV (blue); −CH_3, 285 eV (red); −COO, 289.5 eV (purple). [This XPS data was collected and fitted by Y. Alsalik at SABIC.]

6.3.6 Photooxidation of Ethanol on Single Crystal TiO_2(101) Studied with Mass spectrometry

To study the initial photoxidation reaction parameters, reaction rate, and reaction products, two sets of experiments were conducted. The first involved a saturation exposure of the anatase TiO_2(101) single-crystal surface to ethanol at 300 K, followed by UV exposure at ~5

mW/cm^2 in the presence of molecular oxygen at different partial pressures. In the second set of experiments, an O_2 partial pressure of 1×10^{-7} mbar was maintained as the surface coverage of ethanol was changed by the exposure of ethanol. For each experimental run, the surface was re-prepared and cleaned by repeated Ar^+ sputtering and annealing to 1000 K, and then surface cleanliness was checked with STM prior to each run.

Three sets of control experiments were conducted to rule out any contribution to the mass spectrometer signal from the background. The desorption products of ethanol were collected (by monitoring *m/e* 44, 31, 29, and 15) (i) from the back of the Ta sample holder pre-dosed with a saturation coverage of ethanol, (ii) from the surface of the clean anatase TiO_2(101) crystal at 1×10^{-7} mbar of O_2, and (iii) from the anatase surface in UHV pre-dosed with ethanol. In all three cases, the desorption products were negligible in quantity when compared to the signal detected from anatase TiO_2(101) under the surface reaction conditions. The main reaction products seen at 300 K were acetaldehyde and CO_2. This is based on their known fragmentation patterns of *m/e* 44, 31, 29, and 15 (CH_3CHO) and *m/e* 44 (CO_2), respectively, and thus, these values were monitored exclusively. Previous results on rutile TiO_2(110) related to the photooxidation of acetaldehyde indicated the formation of CH_3 radicals.[1] We checked this route on the anatase surface of this work and found a negligible contribution. The CH_3 radical (*m/e* 15) was determined after removal of the contribution from acetaldehyde (~39%).

The desorption of photochemically produced acetaldehyde in the gas phase was found to correlate strongly with the presence of oxygen in the UHV chamber and the initial coverage (θ) of ethanol on the surface. Because aldehydes are more weakly adsorbed than alcohols on metal oxides in general and on TiO_2 in particular[21] (see **Table 6.1**; $E_{ads,acetaldehyde}$ = 0.77 vs $E_{ads,EtOH}$ = 1.11 eV), the former will desorb into the gas phase as soon as they are formed from an ethanol-covered surface. **Figure 6.7A** shows the production of acetaldehyde (*m/e* 29) (deducting 10% for the *m/e* 31 intensity arising from ethanol) on the (101) surface of anatase TiO_2 as a function of O_2 partial pressure (mbar). After the UV shutter was opened (UV on), a

sharp rise in the response at *m/e* 29 was observed; this signal then decayed toward a background elevated from the baseline. After the UV shutter had been closed (UV off), the response decayed to a baseline that was determined by the background O_2 pressure and chamber pumping speed. Peak areas were computed by fitting a linear background in line with the pressure before and after UV light exposure and then integrating the total area as defined by the brown-shaded region in **Figure 6.7B**. A double-exponential fitting was found to best represent the desorption of acetaldehyde from the surface over the entire O_2 pressure range.

6.3.7 Effect of O_2 Pressure on the Photooxidation of Ethanol on TiO_2(101) Anatase Single Crystal

The plot of total integrated area against O_2 pressure (**Figure 6.7C**) displays a logarithmic function, indicating a limiting influence of gas-phase O_2 on the reaction rate at ~1×10^{-7} mbar, at which point the adsorption sites on the anatase TiO_2(101) surface would be saturated by O_2. Similar results obtained using XPS for the ethanol photoreaction on the rutile TiO_2(110) surface were reported. The finite nonzero intercept at 0 mbar O_2 pressure either is suggestive of a small production of acetaldehyde in the absence of O_2 or is simply due to the uncertainty of the fit. Shown in the inset of **Figure 6.7C** are the areas of the fast and slow decay processes (associated with the double-exponential fitting). The total area for the fast process was found to remain constant as a large fraction of ethanol was depleted within the first 100 s or more. The contribution of the slow process, however, increased with the O_2 pressure. The total rate of depletion, rate = $k[P_{O_2}]^a[\theta_{EtOH}]$, where k is the average of the rate constants of the fast k_1 and slow k_2 processes, was analyzed by plotting the natural logarithm of the peak area against the natural logarithm of the oxygen partial pressure [$\ln(PO_2)$] at a constant initial ethanol coverage (θ_{EtOH}) (**Figure 6.7D**). The reaction order of this photocatalytic reaction with respect to the O_2 partial pressure was found to be equal to 0.15.

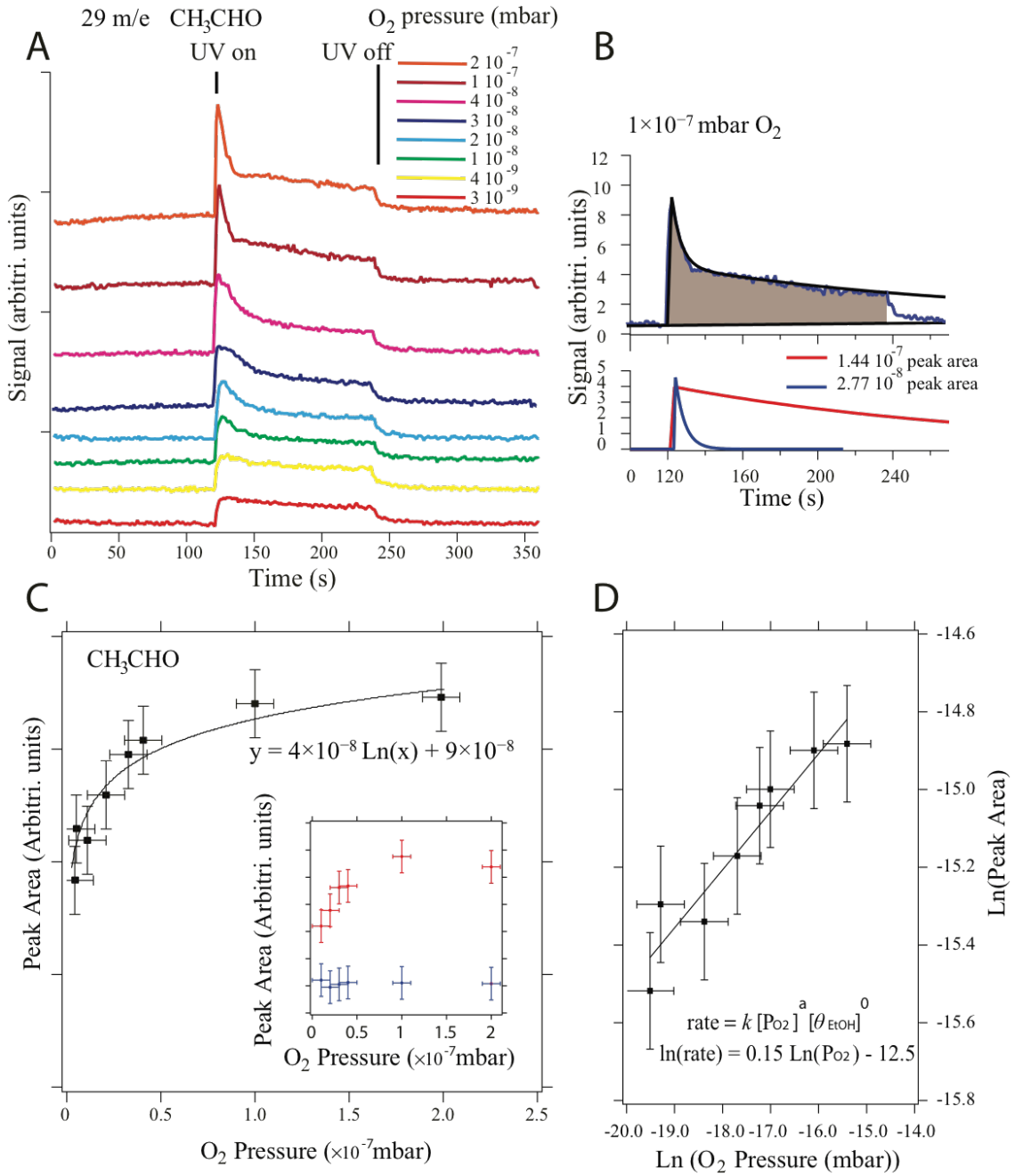

Figure 6.7: **(A)** Acetaldehyde formation upon photooxidation of ethanol on TiO_2(101) anatase single crystal at a saturation coverage of ethanol at 300 K and the indicated molecular O_2 pressures in mbar. UV excitation flux ≈ 5 mW/cm^2. **(B)** Example of an exponential fit for the 1 × 10^{-7} mbar O_2 run, with fast and slow exponential decays; the brown shaded region was used. (**C**) Computed peak areas from panel (**A**) as a function of O_2 pressure in mbar. Lower inset: computed areas of the exponential fitted function, slow (red) and fast (blue) processes. (**D**) ln(reaction rate) taken from panel A as a function of ln(P_{O2}). **[**The QMS mass spectrometry data was collected by Dr. K. Katsiev]

6.3.8 Effect of Ethanol Surface Coverage on the Photooxidation of Ethanol on TiO_2(101) Anatase Single Crystal.

Figure 6.8A shows the production of acetaldehyde on anatase TiO_2(101), where, in this case, the ethanol exposure to the anatase surface was varied in the range of 2.3−23 L at a constant O_2 pressure of 1×10^{-7} mbar. Given the chamber volume (3.6 L), the number of acetaldehyde molecules desorbed was obtained and converted into a fractional coverage (crystal area = 0.09 cm^3) desorption rate in (ML of ethanol) s^{-1} cm^{-2}, where 1 ML s^{-1} cm^{-2} = 5.2×10^{14} molecules s^{-1}. Further details are presented in Chapter 3. **Figure 6.8C** shows a graph of the (initial) rate, r (ML s^{-1} cm^{-2}) plotted against initial ethanol coverage, θ_{EtOH} on the surface. The rate can be expressed as

$$r = k\theta_{EtOH}^{a}\left[P_{O_2}\right]^{0.15}$$

or

$$\ln(r) = \ln(k) + a\ln(\theta_{EtOH}) + 0.15\ln\left(P_{O_2}\right)$$

Figure 6.8D presents a plot of ln(r) versus ln(θ_{EtOH}), giving a reaction order, a, of 1. The rate constant for the reaction could then be extracted and was found to equal 0.027 s^{-1}, giving a cross section of ~3×10^{-18} cm^2, which is roughly (given experimental error and approximations) in line with the value that we obtained (1×10^{-19} cm^2) from the change in surface coverage determined by STM at $P_{O2} = 4 \times 10^{-8}$ mbar (**Table 6.2**). The details of this calculation are shown below, with further explanation provided in Chapter 3.[10]

[10] $\ln(r\theta_{EtOH}(\mathrm{ML\,s^{-1}})) = \ln(k\mathrm{s^{-1}}) + 1{\times}ln(\theta_{EtOH}(ML)) + 0.15\ln(1E-07)$
$\ln(r\theta_{EtOH}ML) = \ln(k) + 1{\times}ln(\theta_{EtOH}ML) - 2.41$
$-6.0 = \ln(k) - 2.41$
exp(-6.0 + 2.41) = 0.027 s^{-1} = k

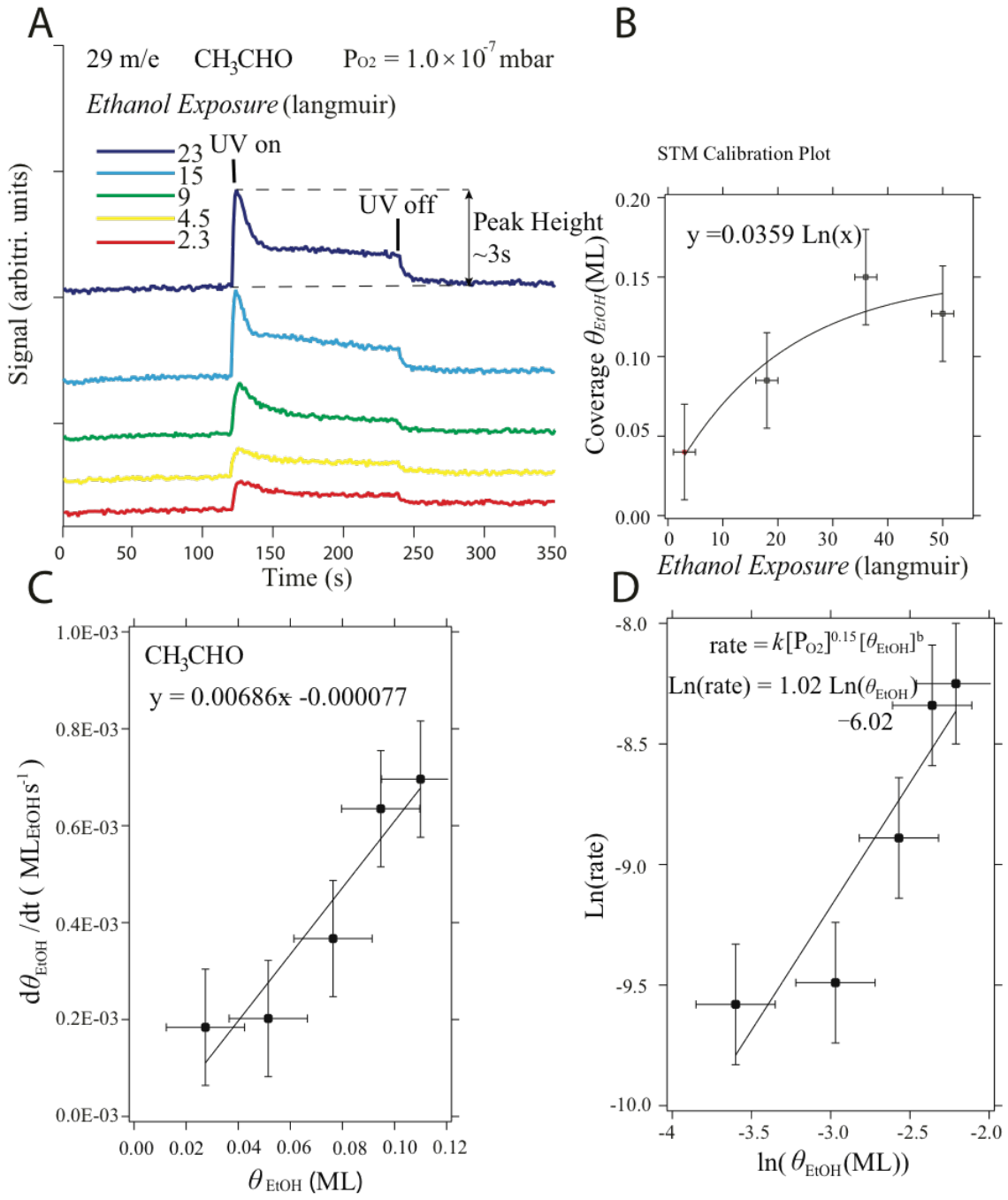

Figure 6.8: (A) Acetaldehyde formation upon photooxidation of ethanol on TiO_2(101) at 1 × 10^{-7} mbar O_2 pressure, 300 K, and ethanol exposure between 2.3 and 32 L. **(B)** Ethanol coverage plot as a function of exposure in Langmuir. **(C)** Initial rate of reaction (in ML_{EtOH} s^{-1}) with respect to the initial ethanol coverage (in ML), with a linear regression fit. UV excitation flux ≈ 5 mW/cm^2. **(D)** ln(rate) vs ln(θ_{EtOH}) plot. [The mass spectrometry traces were collected by Dr. K Katsiev]

6.3.9 Proposed Reaction Mechanism for the Photo-oxidation of Ethanol to Acetaldehyde over TiO_2(101) Anatase Single Crystal.

The above results suggest the following reaction scheme: According to the STM and C 1s XPS results, ethanol is first largely dissociatively adsorbed on Ti−O pairs as ethoxides and surface hydroxyls, the latter not identified or indistinguishable from ethoxides in STM.

$$CH_3CH_2OH(a) + O(s) \rightarrow CH_3CH_2O(a) + OH(a) \qquad \text{Eqs 6.2}$$

where the indexes a and s stand for adsorbed and surface, respectively.

Upon excitation with UV photons, electrons are excited from the VB of TiO_2 to its CB where CB represents the conduction band and VB represents the valence band.

$$2Ti-O + 2h\nu \rightarrow 2e^-(CB) + 2h^+(VB) \qquad \text{Eqs 6.3}$$

[also written as Ti^{3+} and $O^-(1)$]

In the presence of O_2, excited electrons lead to the formation of $O_2^{\cdot -}$ radicals

$$2e^- + 2O_2(a) \rightarrow 2O_2^{\cdot -}\,(radical) \qquad \text{Eqs 6.4}$$

which, in turn, give rise to $HOO^{\cdot}$ radicals, as previously observed in numerous work.

This allows for the first hole trapping by an ethoxide species to give a short-lived radical species.

$$h^+ + CH_3CH_2O(a) + O_s \rightarrow CH_3C^{\cdot}HO(a) + OH(a) \qquad \text{Eqs 6.5}$$

Molecularly adsorbed ethanol might behave similarly to dissociatively adsorbed ethanol (forming hydroxyl radical instead of an oxy radical). Idriss et al. has demonstrated the

favorability of this process in DFT studies[58] of hydrogen peroxide and ethanol[59] with the rutile TiO_2(110) surface. This finding is in line with other results for oxygen containing organic adsorbates on TiO_2 surfaces.[60]

The formation of the oxy radical species (Esq 6.5) is followed by a second hole trapping to give acetaldehyde

$h^+ + CH_3C^{\cdot}HO(a) \rightarrow CH_3CHO(g)$ Eqs 6.6

The two hydrogen atoms removed from ethanol **(**Eqs 6.2 and 6.5) would ultimately give water to close the cycle, although the initial pathway results in the formation of perhydroxyl radicals (Eqs. 6.7).

$2O_2^{\cdot-}$(anion radical) + 2OH(a) → 2HOO(radical) + $2O_s$ Eqs 6.7

2HOO(radical) → $2OH^{\cdot}$ (radical) + O_2 Eqs 6.8

The sum of Eqs. 6.2−6.8 gives $CH_2CH_2OH(a) + O_2 \rightarrow CHCHO(g) + 2OH$(radical). Oxygen-containing radicals would react with a small fraction of the acetaldehyde before desorption to (ultimately) convert the acetaldehyde to formate/acetate species. The dependence of the reaction rate with respect to P_{O2} was found to be approximately 0.15, which indicates that other limiting factors (in addition to the reaction stoichiometry as seen in the above equations) are involved, in particular the weak equilibrium (binding) constant of O on the surface of TiO_2, which requires increasing pressure for reaction. Oxygen molecules are very weakly adsorbed on TiO_2. In the case of rutile TiO_2(110), they completely desorb at about 60 K[61] and similarly on anatase TiO_2(101).

The formation of carboxylate species (as hinted by STM in **Figure 6.5**) and identified by C 1s XPS (**Figure 6.6**) is evidence of further reactions of the oxy radical species (as

previously seen in photo-oxidation studies of organic compounds[26,62]). This, in turn, indicates the participation of oxygen radicals in further reaction steps that ultimately lead to the production of CO_2 and H_2O for a complete catalytic cycle.

6.4 Conclusion

The photocatalytic reaction of ethanol over the (101) surface of an anatase TiO_2 single crystal was studied by STM and online mass spectrometry in the presence and absence of molecular oxygen. Upon dosing of ethanol at 300 K, two types of species with distinct STM heights were observed. These were attributed to two adsorption modes: molecular and dissociated. UV illumination in the presence of oxygen resulted in the partial depletion of ethanol from the surface. Furthermore, the appearance of large protrusions in the depression mode was observed. These were arranged in a (1 × 2) structure and oriented along the [010] direction, which strongly suggests that the species were adsorbed in a bi-dentate manner, such as carboxylate species. Upon UV excitation in the presence of O_2, the main reaction product of ethanol photooxidation at 300 K was found to be acetaldehyde. The reaction order with respect to O_2 at near-saturation coverage of ethanol/ethoxide was found to be approximately 0.15. The reaction order with respect to ethanol was found to be equal to 1. The photooxidation cross section was calculated as $(0.1-3) \times 10^{-18}$ cm^2 from STM and mass spectrometry measurements at O_2 partial pressures of $\sim(0.3-1.0) \times 10^{-7}$ mbar.

6.5 Perspectives

Further investigation of the species present on the ethanol/ anatase TiO_2(101) with low temperature (LT) ~78 K STM is required, combined with TPD to determine the species definitively where images at corresponding temperatures can be correlated with TPD desorption peaks for molecular and dissociative ethanol adsorbates. In particular the technique of inelastic tunneling spectroscopy could be used to identify the vibrational signature of ethanol and resolve the dissociated form from molecular, with the aid of simulation. A UV light flux dependent

photo-oxidation study of the ethanol/TiO_2(101) surface is required to resolve definitively the surface product species. The identification of the population of formate/acetate species in STM as a function of UV light flux would aided by TPD and XPS measurements.

As alluded to in Chapter 4, the ethanol adsorbed tip modified surface of anatase TiO_2(101) containing a rutile component could be studied in the dark and under UV light illumination with STM. Some qualitative and quantitative (photo-reaction cross-section) comparison could be made to the clean anatase TiO_2(101) surface studied in this Chapter. Unfortunately the mass spectrometry could not be employed for this study.

The dispersion of small Au clusters of ~ 10 Å height on the surface of anatase TiO_2(101) and its effect on the photooxidation of ethanol would also be of interest. A recent study conducted on Au/rutile TiO_2(110) within our group revealed the generation of H_2(g) by mass spectrometry upon UV illumination in UHV. A comparison to this study would be of value as the anatase TiO_2(101) surface makes a up a significant fraction of surfaces present in Au/TiO_2 nano materials photo-catalysts. The same combination of STM and mass spectrometry would be used to afford comparison between the rutile TiO_2(110) and anatase TiO_2(101) surfaces.

References

(1) Zehr, R. T.; Henderson, M. A. Acetaldehyde Photochemistry on TiO2(110). *Surf. Sci.* **2008**, *602*, 2238–2249.

(2) Connelly, K. A.; Idriss, H. Photoreaction of Au/TiO2 For Hydrogen Production From Renewables: a Review on the Synergistic Effect Between Anatase and Rutile Phases of TiO2. *Mater. Renew. Sustain. Energy* **2012**, *1*, 3–12.

(3) Henderson, M. A. A Surface Science Perspective on TiO2 Photocatalysis. *Surf. Sci. Rep.,* **2011**, *66*, 185–297.

(4) Carp, O.; Huisman, C. L.; Reller, A. Photoinduced Reactivity of Titanium Dioxide. *Prog. Solid State Chem.,* **2004**, *32*, 33–177.

(5) Al-Azri, Z. H. N.; Chen, W.-T.; Chan, A.; Jovic, V.; Ina, T.; Idriss, H.; Waterhouse, G. I. N. The Roles of Metal Co-Catalysts and Reaction Media in Photocatalytic Hydrogen Production: Performance Evaluation of M/TiO2 Photocatalysts (M=Pd, Pt, Au) in Different Alcohol-Water Mixtures. *J. Catal.* **2015**, *329*, 355–367.

(6) Tereshchuk, P.; Da Silva, J. Ethanol and Water Adsorption on Close-Packed 3d, 4d, and 5d Transition-Metal Surfaces: a Density Functional Theory Investigation with Van Der Waals Correction. *J. Phys. Chem. C* **2012**.

(7) Wang, Z.; Hao, Q.; Mao, X.; Zhou, C.; Dai, D.; Yang, X. Photocatalytic Chemistry of Methanol on Rutile TiO_2(011)-(2 × 1). *Phys. Chem. Chem. Phys.,* **2016**, *18*, 10224–

10231.
(8) Pang, C.-L.; Lindsay, R.; Thornton, G. Structure of Clean and Adsorbate-Covered Single-Crystal Rutile TiO_2 Surfaces. *Chem. Rev.* **2013**, *113*, 3887–3948.
(9) Weststrate, C. J.; Gericke, H. J. Ethanol Decomposition on Co (0001): C−O Bond Scission on a Close-Packed Cobalt Surface. J. *Phys. Chem. Lett.* **2010**.
(10) Alghamdi, H.; Idriss, H. Comparison of the Interaction of Hydrogen Peroxide and Ethanol with TiO_2 Rutile (110) Surface Within the Context of Water Splitting. (*in Preparation*)
(11) Idriss, H.; Seebauer, E. G. Reactions of Ethanol Over Metal Oxides. *J. Mol. Catal. A:,* **2000**, *152*, 201–212.
(12) Guo, Q.; Zhou, C.; Ma, Z.; Ren, Z.; Fan, H.; Yang, X. Elementary Photocatalytic Chemistry on TiO_2 Surfaces. *Chem. Soc. Rev.* **2016**, *45*, 3701–3730.
(13) Thomas, A. G.; Syres, K. L. Adsorption of Organic Molecules on Rutile TiO2 and Anatase TiO2 Single Crystal Surfaces. *Chem. Soc. Rev.* **2012**, *41*, 4207–4211.
(14) Tan, T. H.; Scott, J.; Ng, Y. H.; Taylor, R. A. Understanding Plasmon and Band Gap Photoexcitation Effects on the Thermal-Catalytic Oxidation of Ethanol by TiO_2-Supported Gold., *ACS Catal.*, **2016**, *6* (3), pp 1870–1879
(15) Yang, Y. Z.; Chang, C.-H.; Idriss, H. Photo-Catalytic Production of Hydrogen Form Ethanol Over M/TiO_2 Catalysts (M=Pd, Pt or Rh). *Appl. Catal. B,* **2006**, *67*, 217–222.
(16) Coronado, J. M.; Kataoka, S.; Tejedor-Tejedor, I.; Anderson, M. A. Dynamic Phenomena During the Photocatalytic Oxidation of Ethanol and Acetone Over Nanocrystalline TiO_2: Simultaneous FTIR Analysis of Gas and Surface Species. *J. Catal.* **2003**, 219, 1, 219-230
(17) Yu, Z.; Chuang, S. In Situ IR Study of Adsorbed Species and Photogenerated Electrons During Photocatalytic Oxidation of Ethanol on TiO_2. *J. Catal.,* **2007**, *246*, 118–126.
(18) Herman, G. S.; Dohnálek, Z.; Ruzycki, N. Experimental Investigation of the Interaction of Water and Methanol with Anatase-TiO_2(101). *J. Phys. Chem. B,* **2003**.
(19) Xu, C.; Yang, W.; Guo, Q.; Dai, D.; Chen, M. Molecular Hydrogen Formation From Photocatalysis of Methanol on Anatase-TiO_2(101). *J. Am. Chem. Soc.* **2014**.
(20) Xu, M.; Gao, Y.; Moreno, E. M.; Kunst, M.; Muhler, M. Photocatalytic Activity of Bulk TiO_2 Anatase and Rutile Single Crystals Using Infrared Absorption Spectroscopy. *Phys. Rev. Lett.* **2011**, 206, 393-405
(21) Geng, Z.; Chen, X.; Yang, W.; Guo, Q.; Dai, D. Photoinduced Carbonyl Coupling of Aldehydes on Anatase TiO_2(101)., J. Phys. Chem. C, **2016**, *120*, 9897–9903
(22) Zhang, R.; Liu, Z.; Ling, L.; Wang, B. The Effect of Anatase TiO_2 Surface Structure on the Behavior of Ethanol Adsorption and Its Initial Dissociation Step: a DFT Study. *Appl. Surf. Sci.,* **2015**, *353*, 150–157.
(23) Thompson, T. L.; Yates, J. T. Surface Science Studies of the Photoactivation of TiO_2 New Photochemical Processes. *Chem. Rev.* **2006**, 106, 4428-4453
(24) He, Y.; Dulub, O.; Cheng, H.; Selloni, A.; Diebold, U. Evidence for the Predominance of Subsurface Defects on Reduced Anatase TiO_2(101). *Phys. Rev. Lett.* **2009**, *102*, 106105–4.
(25) Kundu, S.; Vidal, A. B.; Nadeem, M. A. Ethanol Photoreaction on RuOx/Ru-Modified TiO_2(110). *J. Phys. Chem. C* **2013**, *117*, 11149–11158.
(26) Reztsova, T.; Chang, C. H.; Koresh, J.; Idriss, H. Dark- and Photoreactions of Ethanol and Acetaldehyde Over TiO_2/Carbon Molecular Sieve Fibers. *J. Catal.* **1999**, *185*, 223–235.
(27) Jayaweera, P. M.; Quah, E. L.; Idriss, H. Photoreaction of Ethanol on TiO_2(110) Single-Crystal Surface. *J. Phys. Chem. C,* **2007**, *111*, 1764–1769.
(28) Rismanchian, A.; Chen, Y. W.; Chuang, S. In Situ Infrared Study of Photoreaction of Ethanol on Au and Ag/TiO_2. *Catal. Today,* **2016**, 264, 16-22

(29) Panayotov, D. A.; DeSario, P. A.; Pietron, J. J. Ultraviolet and Visible Photochemistry of Methanol at 3D Mesoporous Networks: TiO_2 And Au–TiO_2. J. Phys. Chem. C, **2013**, 117, 15035-15049

(30) King, R.; Idriss, H. Acetone Reactions Over the Surfaces of Polycrystalline UO_2: A Kinetic and Spectroscopic Study. *Langmuir,* **2009**, *25*, 4543–4555

(31) Liao, L. F.; Wu, W. C.; Chen, C. Y.; Lin, J. L. Photooxidation of Formic Acid vs Formate and Ethanol vs Ethoxy on TiO2 and Effect of Adsorbed Water on the Rates of Formate and Formic Acid Photooxidation. *J. Phys. Chem. B* **2001**, 105, 32, 7678-7685

(32) Katsiev, K.; Harrison, G.; Alghamdi, H. Mechanism of Ethanol Photooxidation on Single-Crystal Anatase TiO_2(101). *J. Phys. Chem. C.,* **2017**, *121*, 2940–2950

(33) Giannozzi, P.; Baroni, S.; Bonini, N.; Calandra, M.; Car, R.; Cavazzoni, C.; Ceresoli, D.; Chiarotti, G. L.; Cococcioni, M.; Dabo, I.; et al. QUANTUM ESPRESSO: a Modular and Open-Source Software Project for Quantum Simulations of Materials. *J. Phys.: Condens. Matter* **2009**, *21*, 395502–395536.

(34) Garrity, K. F.; Bennett, J. W.; Rabe, K. M.; Vanderbilt, D. Pseudopotentials for High-Throughput DFT Calculations. *Comp. Maerial. Sci.* **2014**, *81*, 446–452.

(35) Murnaghan, F. D. The Compressibility of Media Under Extreme Pressures. Proc. Natl. Acad. Sci. U.S.A.**1944**, *30*, 244–247.

(36) Grimme, S. Semiempirical GGA-Type Density Functional Constructed with a Long-Range Dispersion Correction. *J. Comput. Chem.* **2006**. 27, 15, 1787-1799

(37) Gong, X.-Q.; Selloni, A.; Batzill, M.; Diebold, U. Steps on Anatase TiO_2(101). *Nat. Mater.,* **2006**, *5*, 665–670.

(38) Setvin, M.; Schmid, M.; Diebold, U. Aggregation and Electronically Induced Migration of Oxygen Vacancies in TiO_2 Anatase. *Phys. Rev. B,* **2015**, 195403–195409.

(39) Grinter, D. C.; Nicotra, M.; Thornton, G. Acetic Acid Adsorption on Anatase TiO_2(101). *J. Phys. Chem. C*., 2012, *116* (21), pp 11643–11651

(40) Setvin, M.; Daniel, B.; Aschauer, U.; Hou, W.; Li, Y.-F.; Schmid, M.; Selloni, A.; Diebold, U. Identification of Adsorbed Molecules via STM Tip Manipulation: CO, H_2O, and O_2 on TiO_2 Anatase (101). *Phys. Chem. Chem. Phys.* **2014**, *16*, 21524–21530.

(41) Stetsovych, O.; Todorović, M.; Shimizu, T. K. Atomic Species Identification at the (101) Anatase Surface by Simultaneous Scanning Tunnelling and Atomic Force Microscopy. *Nat. Comm., 7265,* **2015**.

(42) Setvin, M.; Hao, X.; Daniel, B.; Pavelec, J.; Novotny, Z.; Parkinson, G. S.; Schmid, M.; Kresse, G.; Franchini, C.; Diebold, U. Charge Trapping at the Step Edges of TiO_2 Anatase (101). *Angew. Chem. Int. Ed.* **2014**, *53*, 4714–4716.

(43) Hansen, J. Ø.; Huo, P.; Martinez, U.; Lira, E.; Wei, Y. Y. Direct Evidence for Ethanol Dissociation on Rutile TiO_2(110). *Phys. Rev. Lett.* **2011**, *107*, 136102–136104.

(44) Setvin, M.; Aschauer, U.; Hulva, J.; Simschitz, T.; Daniel, B.; Schmid, M.; Selloni, A.; Diebold, U. Following the Reduction of Oxygen on TiO_2 Anatase (101) Step by Step. *J. Am. Chem. Soc.* **2016**, *138*, 9565–9571.

(45) Dette, C.; Pérez-Osorio, M. A.; Mangel, S.; Giustino, F.; Jung, S. J.; Kern, K. Single-Molecule Vibrational Spectroscopy of H_2O on Anatase TiO_2(101). *J. Phys. Chem. C* **2017**, *121*, 1182–1187.

(46) Lazzeri, M.; Vittadini, A. Structure and Energetics of Stoichiometric TiO_2 Anatase Surfaces. *Phys. Rev. B* **2001**, *63*, 155409–155409.

(47) Labat, F.; Baranek, P.; Adamo, C. Structural and Electronic Properties of Selected Rutile and Anatase TiO 2Surfaces: an Ab Initio Investigation. *J. Chem. Theory Comput.* **2008**, *4*, 341–352.

(48) Nadeem, A. M.; Muir, J.; Connelly, K. A. Ethanol Photo-Oxidation on a Rutile TiO_2(110) Single Crystal Surface. *Phys. Chem. Chem. Phys.* **2011**, *13*, 7637–7637.

(49) White, J. M.; Henderson, M. A. Trimethyl Acetate on TiO_2(110): Preparation and

Anaerobic Photolysis. *J. Phys. Chem. B* **2005**, *109*, 12317–12430.
(50) Lu, G.; Linsebigler, A.; Yates, J. T., Jr. The Adsorption and Photodesorption of Oxygen on the TiO_2(110) Surface. *J. Chem. Phys.* **1995**.
(51) Rohmann, C.; Wang, Y.; Muhler, M.; Metson, J. Direct Monitoring of Photo-Induced Reactions on Well-Defined Metal Oxide Surfaces Using Vibrational Spectroscopy. *Chem. Phys. Lett.* **2008**.
(52) Jayaweera, P. M.; Quah, E. L.; Idriss, H. Photoreaction of Ethanol on TiO_2(110) Single-Crystal Surface. *J. Phys. Chem. C* **2007**, *111*, 1764–1769.
(53) Zehr, R. T.; Henderson, M. A. Acetaldehyde Photochemistry on TiO_2(110). *Surf. Sci*., **2008**, *602*, 2238–2249.
(54) Gao, Y. K.; Traeger, F.; Woll, C.; Idriss, H. Glycine Adsorption and Photo-Reaction Over ZnO (000$\bar{1}$) Single Crystal. *Surf. Sci.* **2014**, 624, 112-117
(55) Quah, E. L.; Wilson, J. N.; Idriss, H. Photoreaction of the Rutile TiO_2(011) Single-Crystal Surface: Reaction with Acetic Acid. *Langmuir* **2010**, 206, 393-405
(56) Henderson, M. A. Photooxidation of Acetone on TiO_2(110): Conversion to Acetate via Methyl Radical Ejection. *J. Phys. Chem. B* **2005**, *109*, 12062–12070.
(57) Idriss, H.; Légare, P.; Maire, G. Dark and Photoreactions of Acetates on TiO2(110) Single Crystal Surface. *Surf. Sci.* **2002**, *515*, 413–420.
(58) Muir, J. N.; Choi, Y.; Idriss, H. Computational Study of Ethanol Adsorption and Reaction Over Rutile TiO_2(110) Surfaces. *Phys. Chem. Chem. Phys.,* **2012**, *14*, 11910–11919.
(59) Connelly, K. A.; Idriss, H. The Photoreaction of TiO_2 And Au/TiO_2 Single Crystal and Powder Surfaces with Organic Adsorbates. Emphasis on Hydrogen Production From Renewables. *Green Chem.* **2012**, *14*, 260–280.
(60) Di Valentin, C.; Fittipaldi, D. Hole Scavenging by Organic Adsorbates on the TiO_2 Surface: a DFT Model Study. *J. Phys. Chem. Lett.*, **2013**, *4* (11), pp 1901–1906
(61) Dohnálek, Z.; Kim, J.; Bondarchuk, O. Physisorption of N_2, O_2, And CO on Fully Oxidized TiO_2 (110). *J. Phys. Chem. B* **2006**.
(62) Idriss, H.; Seebauer, E. G. Photooxidation of Ethanol on Fe−Ti Oxide Particulates. *Langmuir* **1998**, *14*, 6146–6150.
(63) He, Y.; Tilocca, A.; Dulub, O.; Selloni, A.; Diebold, U. Local Ordering and Electronic Signatures of Submonolayer Water on Anatase TiO_2(101). *Nat. Mater.* **2009**, *8*, 585–589.

A.0 Appendix

A.1 Chapter 4

A.1.1 Electron Bombardment of Anatase TiO_2(101)

Shown in **Figure A.1 (**large-scale**)** and **Figure A.2** (zoomed-in) are STM images recorded of the centre of the anatase TiO_2(101) sample after 5 minutes electron irradiation. Features (black circle identify depressions, green circles protrusions) qualitatively similar to the outer edge of the e-beamed surface after 5 + 10 minutes are apparent.

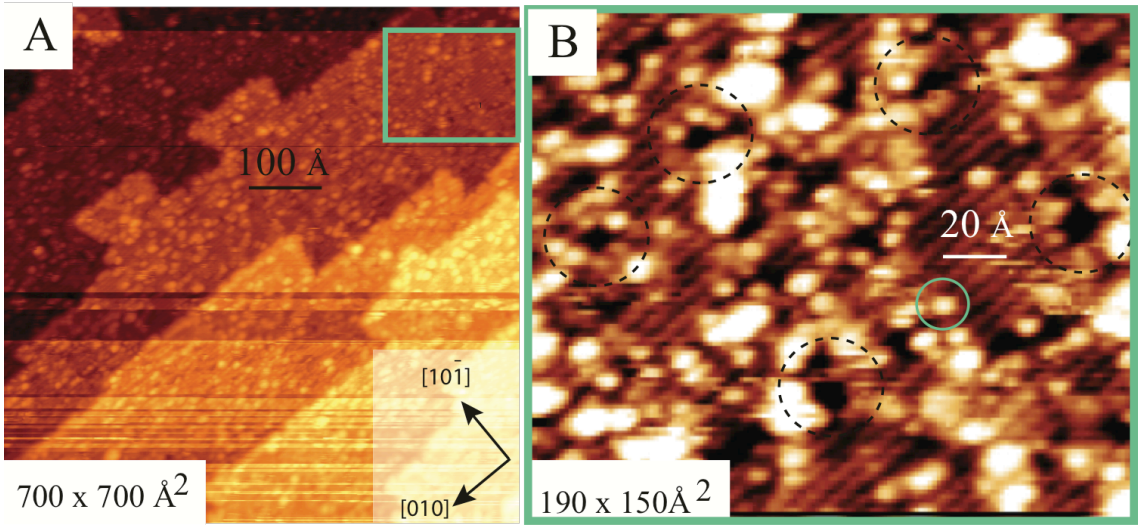

Figure A.1: The centre of the anatase TiO_2(101) surface after electron bombardment for 5 minutes at a flux of 1.5×10^{15} electrons $s^{-1}cm^{-2}$. (**A**) A 700 × 700 $Å^2$ image (+1.6 V, 0.1 nA) Shown in the inset are azimuths with respect to the (101) surface. (**B**) A zoomed-in area 190 × 150 $Å^2$ image where dark depressions (black dashed circles) and protrusions (green circles) are identified.

Shown in **Figure A.2** are STM images recorded at the outer edge of the e-beamed surface after a total electron irradiation for 5 + 10 minutes. It is apparent that the dark depressions aligned in the [010] direction in the topographic image of 5-10 Å width are present at both +1.6 V sample bias empty states imaging and –1 V sample bias filled states images. Identical features are identified by the green dashed lines in the blue ovals.

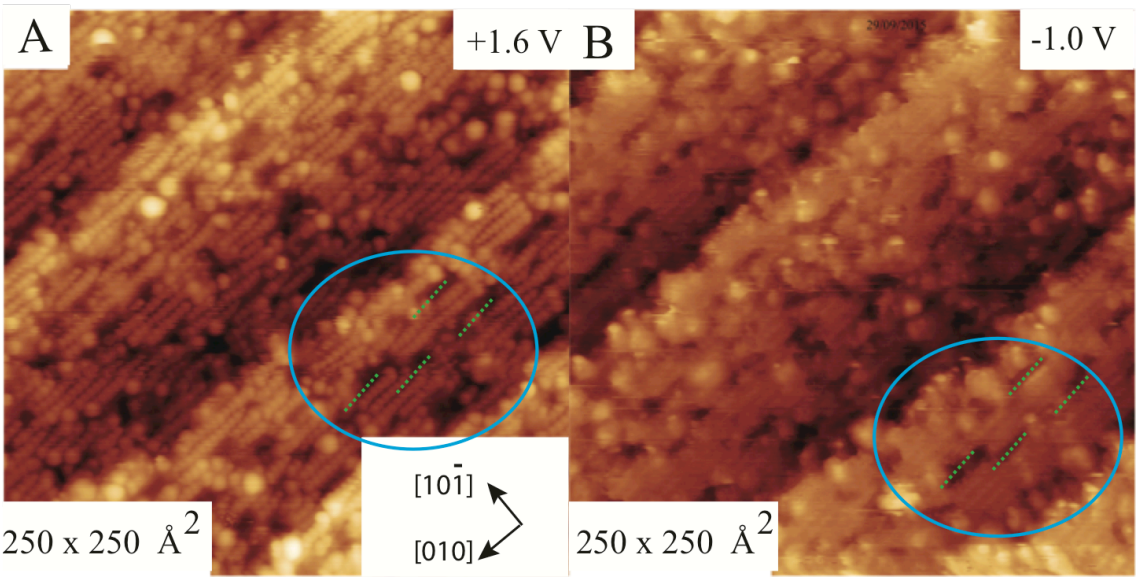

Figure A.2: STM image of the outer edge of the anatase TiO_2(101) after e-beaming with an electron flux of 1.5×10^{15} electrons $s^{-1}cm^{-2}$ for 5 + 10 minutes. (**A**) A 250 × 250 $Å^2$ (+1.6 V sample bias, 0.1 nA), dark strips are present elongated in the [$\bar{1}$01] direction. (**B**) A 250 × 250 $Å^2$ (-1.0 V, 0.1 nA) with identical dark strips. In both imags several representative depressions are identified by the green dashed lines in the blue ovals.

A.1.2 Example image calibration

Figure A.3 details an example calibration protocol used in Chapter 4 to analyse a tip modified anatase TiO_2(101) surface. A large-scale tunneling current (+1.6V, 0.1 nA) image **Figure A.3A** displays a tip modified anatase TiO_2(101) surface. The (100)-(1 × 3) region is visible in the top left hand corner. The lattice parameter of a region of the underlying anatase (101)-(1 × 1) surface was measured, as shown by the zoomed in **Figure A.3B** image where pink and blue line profiles overlaid on the image in the anatase TiO_2(101) [010] and (101) [$\bar{1}$01] directions. To determine the correction factors to apply to vertical and horizontal image dimensions, the lattice parameters are extracted from the row spacing as shown in line profiles **Figure A.3C** and **Figure A.3D** and compared to the known anatase lattice parameters (3.78 × 10.24 $Å^2$), (taking into account the angle of the [010] and [$\bar{1}$01] directions with respect the horizontal and vertical directions). A zoom of the calibrated STM image is shown in **Figure A.3E.** Measurements of line profiles across the rows of the rutile (100)-1 × 3 determined a

lattice parameter of 14.2 Å with a corresponding error of 0.4 Å estimated from the minimum (blue line) and maximum (pink line) distances.

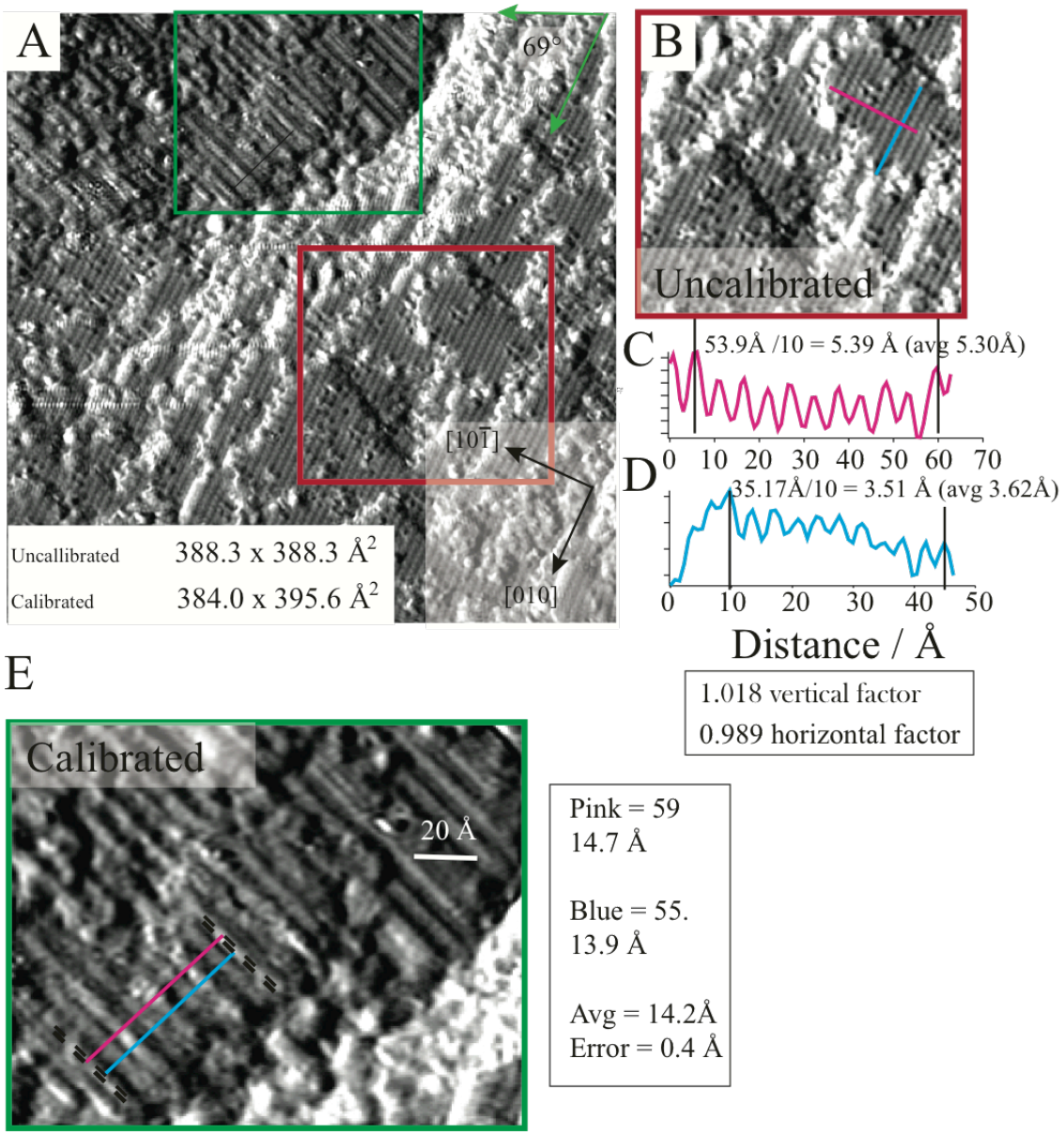

Figure A.3: An example of the calibration procedure performed on the tip modified STM images in Chapter 4. (**A**) A 300 K 388.3 × 388.3 Å^2 STM tunneling current image (+1.6 V, 0.1 nA) of a tip modified region of anatase TiO_2(101). The green square is the region zoomed in image (**E**). The red square is the region zoomed-in in image (**B**). The green arrows identify the angle between the [010] anatase direction and the horizontal image direction (vertical is 21°). Bottom inset: The (101) azimuths are shown.(**B**) Zoomed-in image of the anatase TiO_2(101)-(1 × 1) surface. Pink and blue line profiles are overlaid in the [10$\bar{1}$] and [010] direction respectively. (**C**) A line profile in the [10$\bar{1}$] direction. (**D**) A line profile in the [010] direction. (**E**) A zoomed-in image of the modified region defined by green square in (**A**). Overlaid are lines across the length of four unit cells of the (1 × 3) from which the maximum (pink line) and minimum (blue line) can determine a (1 × 3) lattice parameter 14.2 Å ± 0.4 Å.

A.1.3 Additional Structures Formed by Tip Modification: No. 1

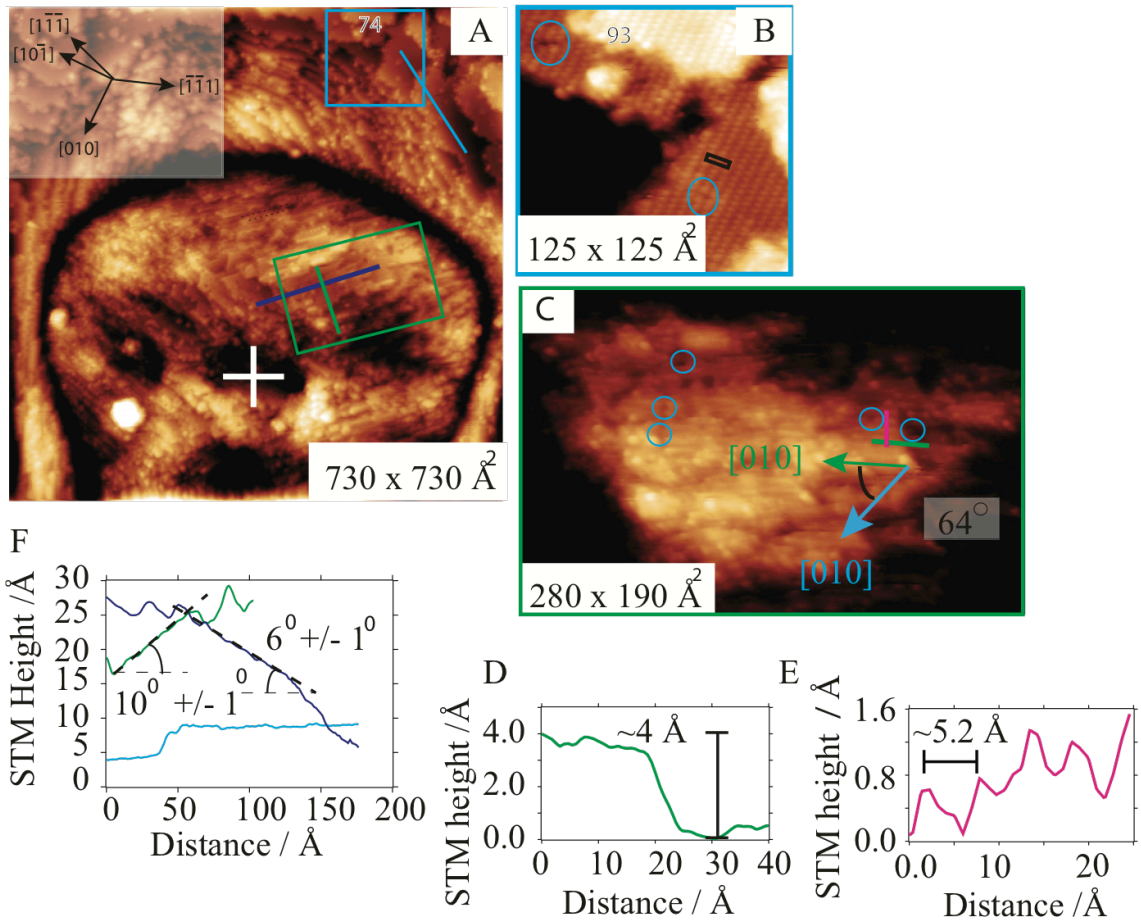

Figure A.4: 300 K STM images (+1.6 V, 0.1 nA) of a tip modified (+10 V 200 ms, 50 nA) anatase TiO_2(101) surface. **(A)** A (730 × 730 Å^2) STM image, white cross indicates the centre of pulse. Top inset: the anatase TiO_2(101) azimuths are identified. Blue box identifies an area zoomed-in in (**B**). The green rectangle indicates the area zoomed in in (**C**) **(B)** A (125× 125 Å^2) STM image of an outer 'healed' region. Blue ovals identify bright-dark-bright point defects. Black rectangle identifies the anatase (101) unit cell. **(C)** A 280 × 190 Å^2 area of the surface identified by the green box in (**A**). Blue circles identify bright-dark-bright point defects. Pink and green lines profiles are overlaid. **(D)** Line profile of step height (4 Å) in (**C**). **(E)** Pink line profile as defined in (**C**), where rows (5.2 Å) are identified. **(F)** Height line profiles from lines in (**A**) an angle of 10° ± 1° (green) [101] an angle of 6° ±1° (dark blue) [010] and substrate 0° (light blue) are shown.

A pulse (+10 V, 200 ms 50 nA) produced a mound/hole structure containing a large crystalline domain. **Figure A.4A** displays a large-scale 730×730 Å^2 (polynomial deducted) image of the modified region. The mound contains a central region of small (~100 Å) rectangular terraces, faceted into a dome shape (~23000 Å^2 area). Blue and green lines are overlaid to compare the angle of a region of the structure with respect to the (101) substrate. The (1 × 1) healed outer region is shown in the atomically resolved zoomed in 250×250 Å^2

image (**Figure A.4B**). The (10.24 × 3.78 Å^2) unit cell is identified (black rectangle). Point defects with a bright-dark-bright motif in the empty state image, spanning three Ti_{5c}-O_{2c} units are identified (blue circles).

One representative area of the new modified surface is shown in the zoomed-in image **Figure A.4C** identified by the green box in **Figure A.4A**. Structural measurements were performed by extracting and measuring line profiles from the image and these are shown in **Figure A.4D** and **Figure A.4E**. It is apparent that; i) The steps edge height (30 line profiles on three steps) is of approximately 4 Å ± 1 Å as shown in **Figure A.4E;** ii) The lattice row spacing as shown in **Figure A.4F** is 5.2 Å ± 0.2 Å (average of 10 measurements).

From STM characterisation a likely assignment is that of anatase TiO_2(101)–(1 × 1) surface grown on-top of the (101) substrate. In addition depressions centred on the rows of ~2-3 Å length in the empty state image are identified (blue circles). Theses features on the new surface are similar to the defects present also on anatase TiO_2(101).(see Chapter 4 and references therein)

An analysis of row direction indicates that the modified anatase (101) substrate [010] direction is rotated by 64° with respect to the underlying (101) [010] direction (see **Figure A.4C)**. The relationship with the underlying surface is further assessed by line profiles (**Figure A.4F**) drawn though a region of the newly formed surface in the (modified (101)) [010] direction (dark blue) and [$\bar{1}$01] (green), inclined from horizontal by angles of 6 ° ± 2° and 10 ° ± 2° respectively. This indicates a tilted relationship between the underlying (101) surface and the tip modified anatase surface. (see Chapter 4 and references therein)

A.1.4 Additional Structure Formed by Tip Modification: No. 2

A tip pulse modified region (+8 V, 100 ms, 50 nA) is presented in **Figure A.5**. The **Figure A.5A** STM image (1400 × 1200 Å^2) indicates a large mound within a hole formed in the surface surrounded by cleared anatase TiO_2(101). A crystalline domain (10000 Å^2) exists in a hollow disc at the outer region of this mound, as seen in the zoomed in image **Figure A.5B.** In

Figure A.5A a black line height profile is overlaid on both the newly formed crystalline region and the outer anatase TiO_2(101) surface, demonstrating a co-planar relationship. This profile is shown in **Figure A.5C** The lattice spacing of the newly formed crystalline region is distinct from anatase TiO_2(101). In the zoomed in image **Figure A.4D**, the anatase TiO_2(101) (1 × 1) surface can be identified (green dashed oval) where a line profile (blue) is drawn in the (101) [$\bar{1}$01] direction. An exposed region of new (white dashed oval surface) show resolved rows aligned with the substrate (101) [010] direction (~±2°). A representative height line profile in **Figure A.5E** (green line) indicates a mean average calibrated lattice constant of 9 Å ± 0.2 Å and corrugation of ~1 Å. These ordered regions are apparently all of the same row spacing size, in registry and orientated in the same direction. The black dashed circles in **Figure A.5B** identify example areas. In the high-resolution STM image (**Figure A5B** inset**)** a step edge with adjacent terraces formed of rows are identified by the black dashed ovals. It is apparent that the terraces above and below this step edge are directly out of phase as the dashed lines overlaid on the STM image for two step-edges indicate. It is not clear what this structure is and further data is required to characterise it. The co-planar relationship and alignment with the [010] direction would suggest an epitaxial arrangement to the surface. (see Chapter 4 and references therein)

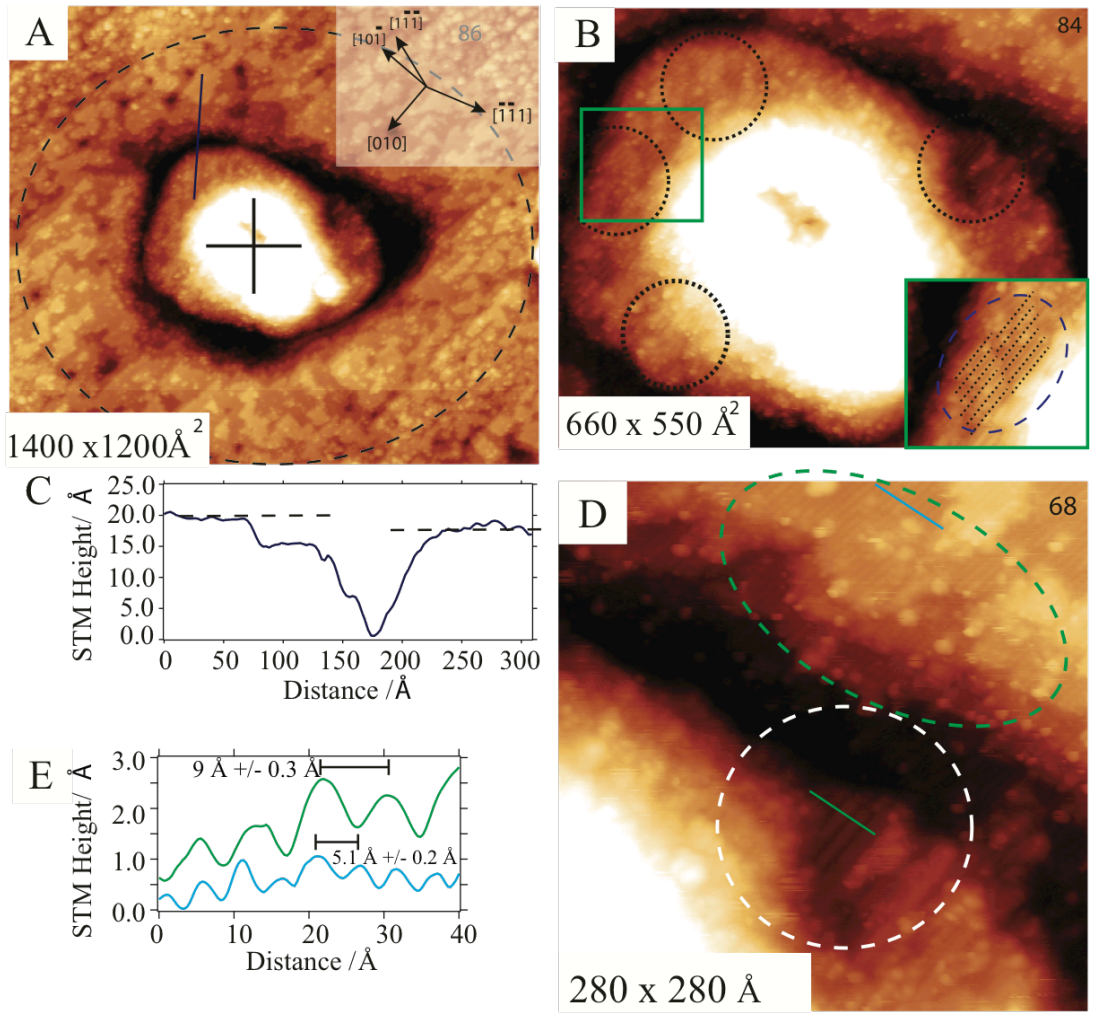

Figure A.5: STM images (+1.6 V, 0.1 nA) of a (+8 V 100 ms, 50 nA) tip pulse modified e-beamed (35 minutes total) anatase TiO_2(101) surface. **(A)** 1400 × 1200 Å^2 large scale image of the tip pulse, black dashed circle identifies the outer effected area, black cross depicts the centre of the pulse and the dark blue line a height line profile over a region of crystalline surface of the outer 'healed' surface. **(B)** An STM image of the tip pulsed region where multiple crystalline areas can be observed (black dashed circle). Inset: region defined by the green box zoom indicates surface above and below a step edge are directly out of phase **(C)** A line profile from **(A) (D)** 280 × 280 Å^2 STM image where a region of anatase (101) is identified (green oval) and modified surface white circle with blue and green line profiles overlaid. **(E)** Blue and green line profiles as defined in (**D**).

A.2 Chapter 5

A.2.1 Lepidocrocite-like TiO_2/ W(100) Surface after Annealing

Shown in **Figure A.6** is an image of lepidocrocite-like TiO_2 / W(100) surface after annealing to 1000 K for 10 minutes. The lepidocrocite-like TiO_2 nanosheet (blue dashed boxes) demonstrates a thermal instability and now has a diminished area coverage of 3%. The rutile surface is identified by the rows of 6.5 Å (high resolution image **Figure A.6B** and line profile **Figure A.6C.**

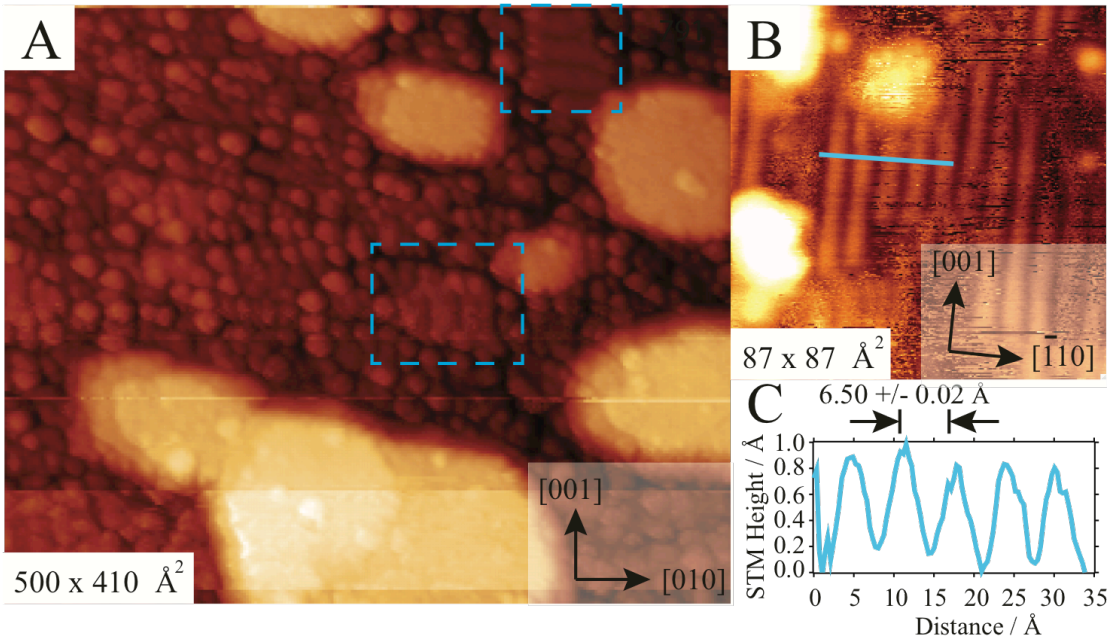

Figure A6.: 300 K STM images of the lepidocrocite-like TiO_2/ W(100) surface after annealing to 1000 K for 10 minutes. (**A)** A large scale (500 × 410 Å^2) STM image (+1.6 V, 0.1 nA). The blue dashed boxes identify remaining lepidocrocite-like islands of coverage 0.03 MLE. The higher islands are rutile TiO_2(110)-(1 × 1). The principal W(100) azimuths are indicated in the lower inset. (**B**) A high resolution (87 × 87 Å^2) image on top of one of the rutile TiO_2(110)-(1 × 1) islands, where rows of 6.5 Å separation are present. A blue line identifies a line height profile. (**C**) Height line profile where rows of 6.5 Å are present.

A.3 Chapter 6

A.3.1 Monitoring CH_3CH_2OH Adsorbate STM Contrast Changes on Ethanol/Anatase TiO_2(101)

Shown in **Figure A.7** are STM images of ethanol/anatase TiO_2(101) recorded before and after a tip apex change resulting in a reversal of contrast of the ethanol adsorbates on the surface of anatase TiO_2; where features can be identified in depression mode (**Figure A.7A**) with a bright-dark-bright motif and in the protrusions mode as protrusions (**Figure A.7B**). Two diagonal rows (green dashed lines) and a single adsorbate (blue box) are identified in both images, with the contrast resulting from identical species in both images. A double tip is present in **Figure A.7B**.

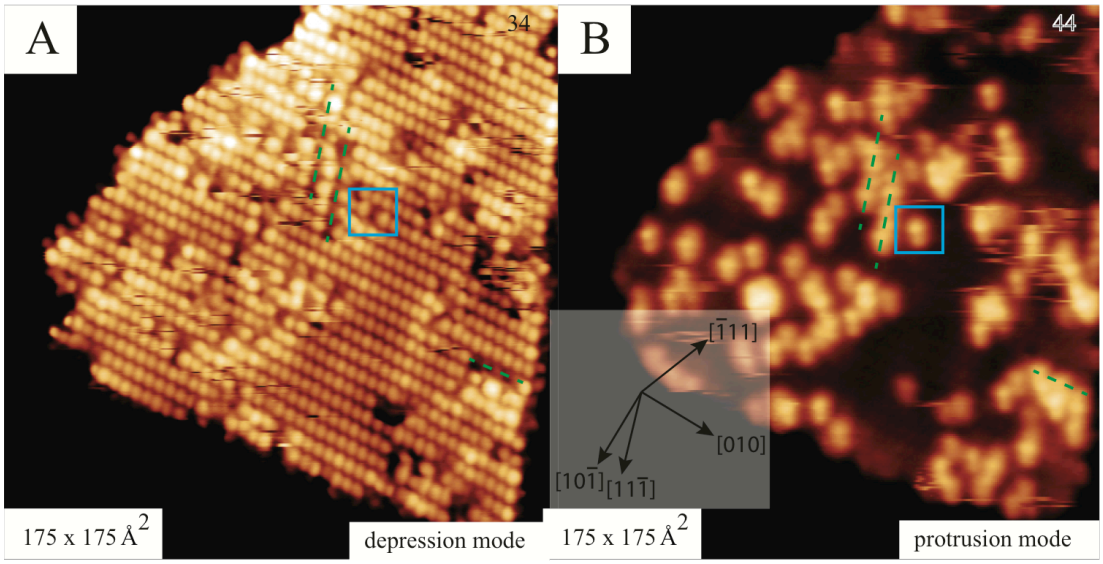

Figure A.7: 300 K STM images of anatase TiO_2(101) after exposure to 50 L of ethanol at 300 K. (**A**) 175 × 175 Å^2 image recorded at +1.0 V sample bias 0.17 nA, in the depression mode, two rows of ethanol molecules in the bright-dark-bright mode are arranged in the [11$\bar{1}$] and [010] direction are identified by the green dashed line, a single feature is identified by the blue square. (**B**) 175 × 175 Å^2 image recorded at +1.0V sample bias and 0.18 nA, matching features of ~1.6 Å height in the protrusion mode are identified by the green dashed line and blue square. Lower inset: the principal azimuths of anatase TiO_2(101). A double tip is present in image (**B**).

A.3.2 CH_3CH_2OH Adsorbate Coverage on Anatase TiO_2(101) as a Function of Exposure

Shown in **Figure A.8** are representative STM images of the ethanol/anatase TiO_2(101) surface after a range of exposures (3-50 Langmuir). The ML coverage is defined with respect to the number of surface Ti_{5c}-O_{2c} pairs with individual bright round features attributed to single ethanol molecules. More images were used to determine average coverage for ethanol exposure, with the standard deviation used to determine the error bar.

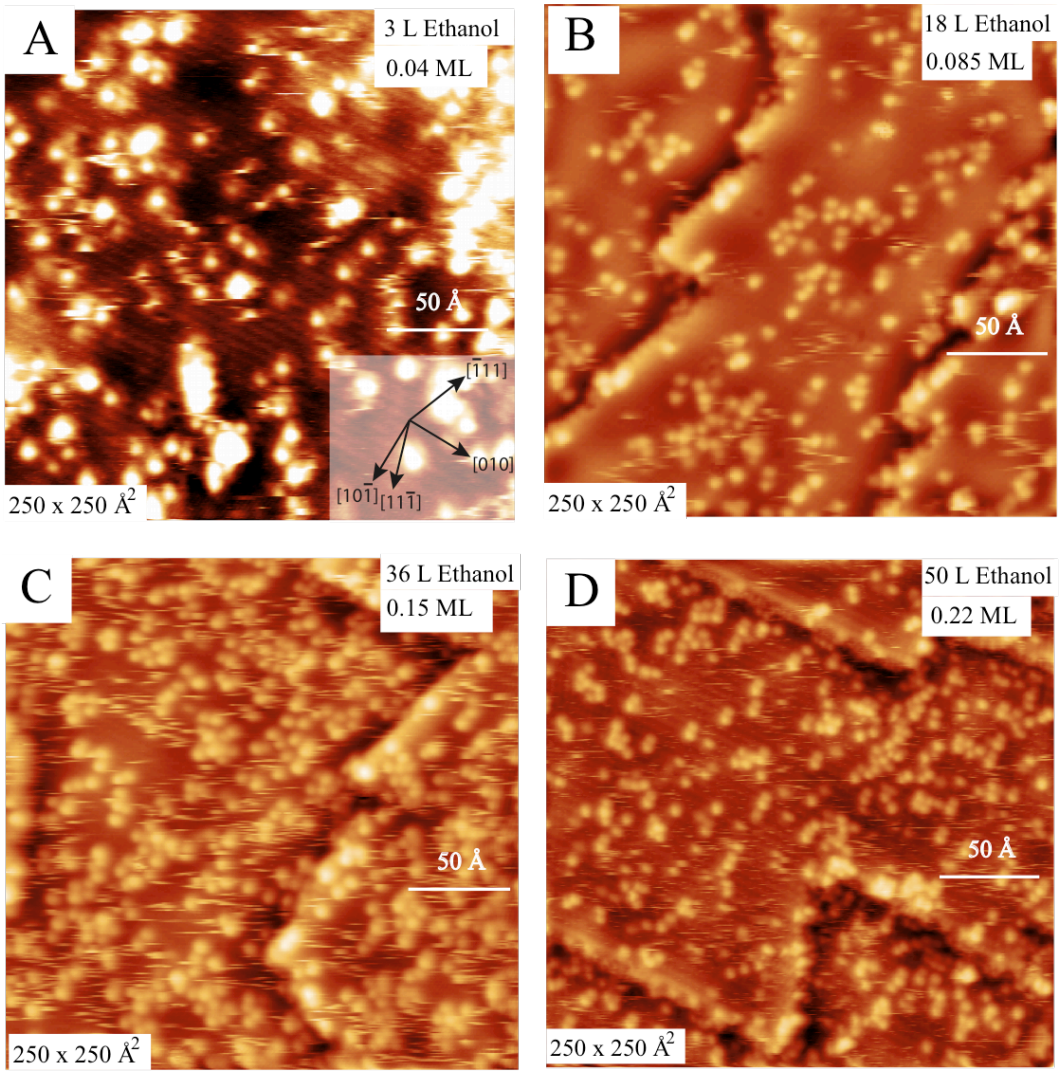

Figure A.8: 300 K STM images (+2V, 0.2 nA) of anatase TiO_2(101) are shown after various exposures to ethanol. (**A**) 250 × 250 Å^2 STM image after 3 L ethanol exposure, 0.04 ML ethanol. Insets: the principal (101) surface azimuths. (**B**) A 250 × 250 Å^2 STM image after 18 L ethanol exposure, 0.085 ML ethanol. (**C**) A 250 × 250 Å^2 STM image after exposure to 36 L of ethanol, 0.15 ML. (**D**) A 250 × 250 Å^2 STM image after exposure to 50 L of ethanol.